# Magnetic monolayers on semiconducting substrates: an *in situ* FMR study of Fe-based heterostructures

Vom Fachbereich Physik
der Universität Duisburg-Essen
(Campus Duisburg)

zur Erlangung des akademischen Grades eines
Doktors der Naturwissenschaften (Dr. rer. nat.)
genehmigte Dissertation von

**Khalil Zakeri Lori**

aus Sirjan–I.R. Iran

Referent: Prof. Dr. rer. nat. Michael Farle
Korreferent: Prof. Dr. rer. nat. Claus M. Schneider
Tag der mündlichen Prüfung: 18.10.2007

Dedicated To My Dear Parents

# Abstract

The growth, magnetic anisotropy, $g$-factor, and magnetization of Fe monolayers grown on GaAs(001), InAs(001), and InP(001) are investigated by a combination of *in situ* ferromagnetic resonance and SQUID magnetometry as a function of temperature and film thickness. The effect of stress caused by the lattice mismatch and the surface reconstruction on the magnetic anisotropy is quantified. An in-plane spin reorientation transition as a function of film thickness is observed at room temperature for all systems. A magneto-elastic model is used to explain the direction of the easy axis, the spin reorientation transition, and the contributions to the magnetic anisotropy terms using the stress components measured directly by *in situ* IV-low-energy electron diffraction. While the model gives a quantitative explanation of the out-of-plane magnetic anisotropy, changes of the electronic interface structure have to be taken into account for the in-plane magnetic anisotropy. The influence of Ag and Au buffer and cap layers on the magnetic anisotropy terms are determined. The temperature dependence of the total magnetic anisotropy, as well as the surface-interface and volume contribution to the magnetic anisotropy are determined for Fe monolayers on GaAs(001). It is demonstrated that the temperature dependence of the magnetic anisotropy is correlated with the temperature dependence of the magnetization according to the Callen-Callen model. The temperature dependence of the volume contribution to the perpendicular magnetic anisotropy is fully explained by the temperature dependence of the magneto-elastic anisotropy. A temperature-driven morphological transformation occurring at a temperature higher than 550 K depending on the film thickness is observed.

The thin $Fe_3Si$ binary Heusler structure epitaxially grown on MgO(001) is investigated. In addition to the structural properties, magnetic anisotropy, magnetization, $g$-factor, spin, and orbital magnetism, the magnetic relaxation mechanisms are determined as a function of Si concentration, sample treatment, and film thickness. The Arias and Mills model is confirmed yielding a quantitative explanation for the magnetic relaxation parameters from the ferromagnetic resonance linewidth. Two relaxation channels, i.e. dissipative isotropic Gilbert damping as well as anisotropic two-magnon scattering are simultaneously identified. It is demonstrated that changing the film thickness from 8 to 40 nm and slightly modifying the Fe concentration influences the relaxation channels and can be used to tune the relaxation rates.

# Kurzfassung

Das Wachstum, die magnetische Anisotropie, der $g$-Faktor und die Magnetisierung von auf GaAs(001), InAs(001) und InP(001) gewachsenen Fe-Monolagen wurden durch eine Kombination von *in situ* UHV ferromagnetischer Resonanz und SQUID-Magnetometrie als Funktion der Temperatur und Schichtdicke untersucht. Gitterfehlanpassung und Oberflächenrekonstruktion verursachen eine Gitterverspannung, deren Einfluß auf dei magnetische Anisotropie quantifiziert wurde. Bei allen Systemen wurde bei Zimmertemperatur ein Spinreorientierungsübergang in der Ebene beobachtet. Um die leichte Richtung, den Spinreorientierungsübergang und die Anisotropiebeiträge zu erklären, wurde ein magnetoelastisches Modell herangezogen, für das mit Hilfe niederenergetischer Elektronenbeugung die Gitterverspannung direkt gemessen worden ist. Während dieses Modell eine quantitative Erklärung für die senkrechte Anisotropie gibt, muss man für die Anisotropie in der Ebene die veränderte elektronische Struktur an der Grenzfläche mit berücksichtigen. Der Einfluss von Ag- und Au-Puffer- und Abdeckschichten auf die magnetischen Anisotropiebeiträge wurde untersucht. Hierzu wurden die temperaturabhängige magnetische Anisotropie, die Oberflächen-/Grenzflächen und Volumenbeiträge zur magnetischen Anisotropie von Fe-Monolagen auf GaAs(001) bestimmt. Im Rahmen des "Callen-Callen" Modells wurde der erwartete Zusammenhang zwischen magnetischer Anisotropie und Magnetisierung in dünnen Filmen bestätigt. Die Temperaturabhängigkeit des Volumenbeitrages zur senkrechten magnetischen Anisotropie wurde durch die Temperaturabhängigkeit der magnetoelastischen Anisotropie vollständig erklärt. Es wurde beobachtet, dass Fe-Filme eine temperaturgesteuerte, morphologische Umwandlung zeigen, die in Abhängigkeit von der Schichtdicke bei Temperaturen von mehr als 550 K auftritt.

Ferner wurden die auf MgO(001) epitaktisch gewachsene, dünne, binäre, $Fe_3Si$ Heuslerlegierung untersucht. Zusätzlich zu den strukturellen Eigenschaften wurden die magnetische Anisotropie, die Magnetisierung, der $g$-Faktor, der Spin- und Bahnmagnetismus, und die magnetischen Relaxationsmechanismen als Funktion der Si-Konzentration, Probenbehandlung und Schichtdicke untersucht. Das "Arias-Mills" Modell wurde bestätigt und benutzt, um die magnetischen Relaxationsparameter zu bestimmen. Zwei unterschiedliche Relaxationskanäle, die dissipative, isotrope Gilbert-Dämpfung sowie die anisotrope Zwei-Magnonenstreuung wurden gleichzeitig identifiziert. Es konnte gezeigt werden, dass sowohl eine Änderung der Schichtdicke von 8 zu 40 nm als auch eine Modifikation der Fe-Konzentration die Relaxationskanäle beeinflussen, und somit dazu verwendet werden können, die Relaxationsraten festzulegen.

# List of acronyms and abbreviations

| | |
|---|---|
| AES | Auger electron spectroscopy |
| bcc | body-centered cubic |
| BLS | Brillouin light scattering |
| CEMS | conversion electron Mössbauer spectroscopy |
| DFT | density functional theory |
| EDX | energy dispersive X-ray analysis |
| FM | ferromagnet or ferromagnetic |
| FMR | ferromagnetic resonance |
| LDA | local density approximation |
| LEED | low-energy electron diffraction |
| LL | Landau-Lifshitz |
| LLG | Landau-Lifshitz-Gilbert |
| LT | low temperature |
| MAE | magnetic anisotropy energy |
| ML | monolayer(s) |
| MOKE | magneto-optical Kerr effect |
| MTJ | magnetic tunnelling junction |
| RPA | random phase approximation |
| RT | room temperature |
| RHEED | reflection high-energy electron diffraction |
| SC | semiconductor or semiconducting |
| SQUID | superconducting quantum interference device |
| SRT | spin reorientation transition |
| STM | scanning tunnelling microscopy |
| TBKKR | tight-binding Korringa-Kohn-Rostoker |
| $T_a$ | annealing temperature |
| $T_C$ | Curie temperature |
| TMR | tunnelling magnetoresistance |
| UHV | ultrahigh vacuum |
| VSM | vibration sample magnetometry |

| | |
|---|---|
| XMCD | X-ray magnetic circular dichroism |
| XPS | X-ray photoemission spectroscopy |
| XRD | X-ray diffraction |

# List of symbols

| | |
|---|---|
| $a$ | lattice constant |
| A | amplitude of the ferromagnetic resonance absorption spectra |
| $B$ | induction magnetic field |
| $B_{\text{eff}}$ | effective field |
| $B_i$ | *i-th* magneto-elastic coupling constant |
| $B_{\text{res}}$ | resonance field |
| $c$ | velocity of light in free space (3·$10^8$m/s) |
| $d$ | film thickness |
| $D$ | exchange stiffness |
| $d_c$ | critical thickness |
| e | elementary charge (= 1.602·$10^{-19}$ C) |
| $E$ | energy, electrical field |
| $f$ | frequency |
| $F$ | free energy density |
| $g$ | $g$-factor |
| $g_{\text{electron}}$ | $g$-factor of a free electron (= 2.0023193043718) |
| $G$ | Gilbert damping parameter |
| $h$ | Planck's constant (=$6.626069 \cdot 10^{-34}$ Js) |
| $H$ | magnetic field strength |
| $\widehat{i}, \widehat{j}, \widehat{k}$ | unit vectors in Cartesian coordinate system |
| $\vec{k}$ | electron wave vector |
| $K_{2\perp}$ | perpendicular uniaxial magnetic anisotropy constant |
| $K_{2\parallel}$ | in-plane uniaxial magnetic anisotropy constant |
| $K_4$ | cubic anisotropy constant |
| $K_i^{\text{si,eff}}$ | effective surface-interface contribution to the magnetic anisotropy constant |
| $K_i^v$ | volume contribution to the magnetic anisotropy constant |
| $\vec{M}$ | magnetization vector |
| $m_e$ | mass of electron (=$9.10938188 \cdot 10^{-31}$ kg) |
| $M_s$ | saturation magnetization |
| $\vec{q}$ | magnons wave vector |

| | |
|---|---|
| $T_1(T_2)$ | longitudinal (transverse) relaxation rate |
| $U(t-t')$ | unit step function |
| $V$ | inner potential |
| $V_g$ | band gap |
| $\alpha$ | dimensionless damping parameter |
| $\alpha_i$ | direction cosines |
| $\beta$ | bulk spin asymmetry |
| $\epsilon$ | lattice mismatch |
| $\epsilon_{ij}$ | strain components |
| $\gamma$ | spectroscopic splitting factor |
| $\Delta B_{\mathrm{HWHM}}$ | half width at the half maximum of the ferromagnetic resonance spectrum |
| $\Delta B_{pp}$ | peak-to-peak ferromagnetic resonance linewidth |
| $\hbar$ | Dirac's constant (=$1.054571 \cdot 10^{-34}$ Js) |
| $\lambda$ | Landau-Lifshitz damping parameter or wavelength |
| $\lambda_{sd}$ | spin diffusion length |
| $\mu_{S(L)}$ | spin (orbital) magnetic moment |
| $\mu_0$ | vacuum permeability (=$4\pi \cdot 10^{-7}$ H/m or kg·m·s$^{-2}$·A$^{-2}$) |
| $\mu_0 M_{\text{eff}}$ | effective out-of-plane anisotropy field |
| $\mu_B$ | Bohr magnetron(=9.274096·$10^{-24}$ J/T) |
| $\theta(t-t')$ | Heaviside step function |
| $\rho$ | electrical resistivity |
| $\sigma$ | electrical conductivity or roughness parameter |
| $\xi$ | correlation length |
| $\chi''$ | imaginary part of the susceptibility |
| $\chi_P$ | Pauli susceptibility |
| $\tau_{el}$ | electron orbital relaxation time |
| $\tau_{sf}$ | electron spin-flip relaxation time |
| $\nu_F$ | Fermi velocity |
| $\omega$ | angular frequency |

# Contents

# 1. Introduction

In the emerging field of semiconductor spin transfer electronics (‘*spintronics*’) one seeks to exploit the spin of electrons injected into semiconductors. It is widely expected that new functionalities for electronics and photonics can be derived, if the injection, transfer, manipulation, and detection of the electron spin can be controlled above room temperature. The spin polarized electrons can be realized by employing conventional ferromagnets with a high degree of spin polarization at the Fermi level (see Fig. 1.1(a)) or by a second class of materials so called half metallic Heusler alloys. Half metallic means that one spin channel is metallic whereas the other one is semiconducting (a schematic half metallic band structure is shown in Fig. 1.1(b)). A number of experiments reported successful and efficient spin injection from a ferromagnetic metal into a semiconductor even at room temperature by ballistic transport (i.e. Schottky barriers and tunnelling) [1–7].

In order to get high spin polarization at room temperature one should use materials with a high Curie temperature. A low Curie temperature leaves only a small fraction of the full spin polarization at room temperature (RT). Due to their high Curie temperature and technological importance Fe-based ferromagnets (i.e. Fe and $Fe_3Si$) on different semiconducting substrates were investigated in this thesis.

The main goal of this work is to understand the interplay between crystal structure and magnetism in well ordered magnetic monolayers on the (001)-surface of different types of III-V semiconducting substrates. In order to control the magnetic anisotropy, two different groups of semiconductors with different lattice mismatches (positive and negative, see Fig. 1.1(c)) were used as substrates: As-based semiconductors (i.e. GaAs, InAs) and In-based semiconducting substrates (i.e. InAs, InP).

The Fe/GaAs system has a lattice mismatch of $\epsilon =$-1.6%. Numerous works on *covered* Fe layers were carried out *ex situ* [8–15], and only just a few works [16] were performed on uncapped Fe/GaAs. Its magnetic properties and the influence of buffer and capping layers in the monolayer regime were not well understood at the begining of this thesis. The Fe/GaAs samples studied here were grown, characterized and measured *in situ* under a UHV condition and in a wider range of temperature and thickness than in any previous experiment. The absolute value of the magnetic anisotropy terms has been determined by performing *in situ* FMR and *in situ* SQUID measurements on the same samples.

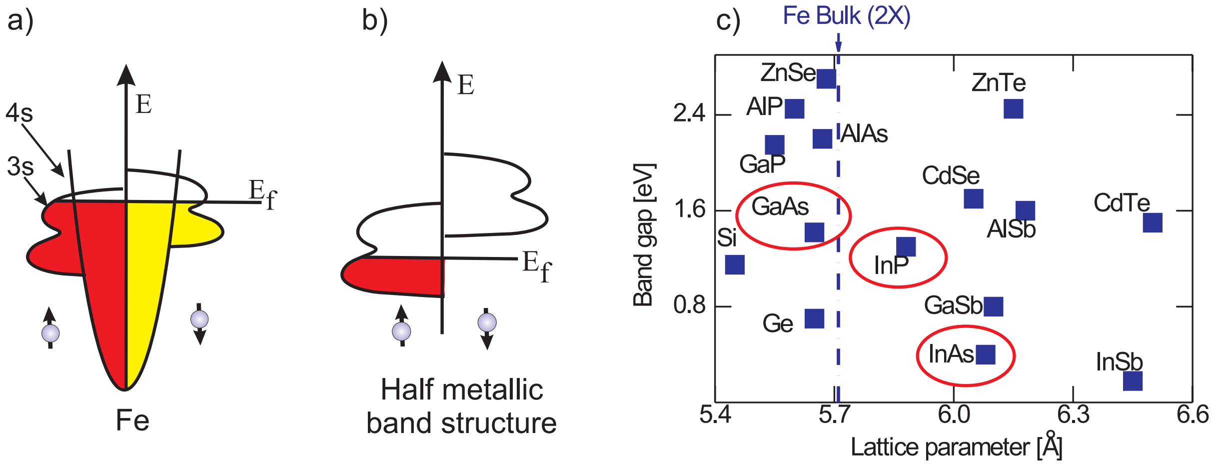

**Figure 1.1.:** (a) Schematic representation of the Fe band structure. (b) Half metallic band structure. (c) Band gap versus lattice parameter of various semiconductors. The marked semiconductors are used in this work as substrates.

Since interface modification is the key for *spintronics* and it is well-known that the Ag/GaAs interface is thermodynamically much more stable than the Fe/GaAs interface [17], Fe/Ag/GaAs(001) was investigated. Moreover, it has been predicted that the Ag/Fe(100) has a strong spin dependence of the interface resistance and should therefore be a good polarizer [18] and consequently, a strong spin transfer effect can be expected in systems including an Fe/Ag interface [19]. The Ag/Fe/GaAs(001) system was studied as well.

The second candidate for *spintronics* is Fe/InAs(001). The spin injection through an Fe/InAs interface has been predicted by Zwierzycki *et al.* [20] and later demonstrated by Ohno *et al.* [21] who found a circular polarization of about -12% at T=6.5 K and an applied magnetic field of 10 T. InAs has a narrow band-gap (less than 0.4 eV) and therefore, the Fe/InAs is an ideal ohmic contact as reported by Xu *et al.* [22]. Moreover, InAs is a very good candidate for high speed electronics and infrared optoelectronics, due to its large electron mobility (larger than 3.5 $\frac{m^2}{Vs}$) and considerably high Rashba effect. In this work the epitaxial growth and the magnetic anisotropy of Fe monolayers grown on $\{4\times2\}$InAs were studied *in situ*, i.e. under UHV conditions. As mentioned above the Fe/InAs is an ideal ohmic contact. Since a Schottky barrier is needed for *spintronic* applications [23], the different possibilities to produce a Schottky contact between Fe and InAs has been proposed. The barrier height of the *clean* Au/InAs interface was found by Oher *et al.* to be 10±5 meV [24] and an extraordinary magnetoresistance effect was observed in a hybrid device consisting of an Au film with an InAs-based two-dimensional electron system [25]. Therefore a technological relevant device can be realized by growing an atomically ordered Au layer between Fe and InAs. In order to better understand the role of the Au/Fe interface in our layered structure both Fe/Au/InAs(001) and Au/Fe/Au/InAs(001) systems are investigated.

The third candidate for *spintronic* devices is Fe/InP. InP has a band gap of $V_g = 1.34$ eV very close to the one of GaAs $V_g = 1.43$ eV (which is relevant for magneto-electronic applications). The lattice mismatch is positive in contrast to GaAs with a value of $\epsilon = +2.2\%$. This yields a tensile strain in the film plane along a particular direction and consequently changes the magnetic properties at the interface. The thickness dependence of the different anisotropy contributions as well as the magnetization is determined and discussed. Moreover, it will be demonstrated how the strain at the interface influences the interfacial properties of the magnetic anisotropy.

$Fe_3Si$, which is a binary Heusler alloy with a cubic $D0_3$ structure is another interesting material for spin injection into semiconductors. It has a spin polarization of 43% and a high Curie-temperature $T_c$ =820 K [26–28]. In order to use of $Fe_3Si$ in future magneto-electronic and *spintronic* devices the growth of well ordered ultrathin magnetic structures is required and the magnetic properties as a function of the temperature and thickness need to be understood.
In contrast to bulk samples the epitaxial growth and magnetic properties of $Fe_3Si$ films on semiconducting substrates has been investigated by a few groups only, i.e. $Fe_3Si$/Si(Ge) [29–34] and $Fe_3Si$/GaAs(001) [35–43]. According to our knowledge no data on growth and/or magnetic characterization of $Fe_3Si$/MgO(001) has been reported in literature. The growth of $Fe_3Si$ films on MgO(001) substrates is of interest in conjunction with the tunnel magnetoresistance (TMR) effect. The TMR effect results from the quantum mechanical tunnelling effect with spin-splitted transition probabilities. The TMR can be illustrated well by a simple system of two ferromagnetic layers separated by an insulating spacer layer. It has been predicted [44] and later demonstrated [45–47] that the TMR effect can be enhanced just by replacing the amorphous $Al_2O_3$ spacer layer by a crystalline MgO layer in FM/MgO/FM magnetic tunnelling junctions (MTJ).
In this work the structural, static and dynamic magnetic properties of $Fe_3Si$ films epitaxially grown on MgO(001) are investigated as a function of the film thickness, sample treatment, and Si concentration. The magnetic anisotropy, magnetization, $g$-factor, spin and orbital magnetic moments as well as magnetic relaxation parameters are quantitatively determined for the first time.
The thesis is organized as follows: **Chapter 2** includes some theoretical aspects to provide a background which is relevant for this thesis. **Chapter 3** provides a short overview of the different experimental setups which are designed, developed and employed during this work and the focus will be put on the *in situ* ferromagnetic resonance setup.

The experimental results and discussion for Fe/GaAs(001) and Ag/Fe/GaAs(001) are presented in **Chapter 4** whereas in **Chapter 5** the results for Fe/Ag/GaAs(001) are discussed.

The magnetic anisotropies of the Fe/InAs and Fe/Au/InAs systems are outlined in **Chapter 6** and those of Fe/Au/InAs(001) and Au/Fe/Au/InAs(001) are presented in **Chapter 7**.

**Chapter 8** discuss the results of Fe/InP(001) where the thickness dependence of the magnetic anisotropy constants as well as the onset of ferromagnetic ordering of Fe/InP(001) are of concern.

**Chapter 9** provides a comparison among the magnetic parameters of the Fe/semiconductor structures investigated in this thesis.

In **Chapter 10** the results of *ex situ* structural and magnetic characterizations of $Fe_3Si$/MgO(001) are presented. Both static and dynamic magnetic properties are discussed. The magnetic anisotropy, magnetization, $g$-factor, spin, and orbital moments are discussed in detail. The spin dynamics in this binary Heusler structure are understood by proposing a general model. Moreover, the Si concentration dependence around the optimum concentration of 25% Si:75% Fe on the magnetic properties is investigated. The experimental results of spin and orbital magnetic moment are compared to the calculated results of density functional theory.

# 2. Theoretical background

*In this chapter the basic aspects of ferromagnetism in ultrathin magnetic structures are summarized. The different contributions to the magnetic anisotropy are discussed. The resonance equations, which satisfy the resonance condition in the small angle limit of precessional motion are described. The relaxation mechanism is explained in terms of different contributions to the ferromagnetic resonance linewidth.*

## 2.1. Magnetocrystalline anisotropy

The magnetocrystalline anisotropy energy (MAE) is the difference in the free energy associated with different directions of the magnetization with respect to the crystallographic axes of the crystal. The orientation of the magnetization is therefore given by the equilibrium condition where the magnetic part of the total energy of the system is minimal. In the following, we briefly review the intrinsic contributions to the overall measured phenomenological magnetocrystalline anisotropy constants $K_i$.

In principle, only two origins for MAE exist, (i) the so-called *shape anisotropy* due to dipolar interactions and (ii) MAE resulting from the spin-orbit interactions. In terms of quantum mechanics both mechanisms are relativistic corrections to the Hamiltonian-operator of the system that break the rotational symmetry of the spin quantization axis, thus coupling the spin to the real space, i.e. the crystal lattice. Note, that exchange interaction within the widely used Heisenberg model is isotropic, since the corresponding Hamiltonian contains no spatial coordinates.

### Magnetic anisotropy due to dipolar interaction

One source for magnetic anisotropy results from the fact that a single magnetic dipole $\vec{\mu}_i$ creates a magnetic field, which at the position $\vec{r}_i$ is given by:

$$\vec{B}_i(\vec{r}_i) = \frac{\mu_0}{4\pi}\left(\frac{3(\vec{r}_i \cdot \vec{\mu}_i) \cdot \vec{r}_i}{r_i^5} - \frac{\vec{\mu}_i}{r_i^3}\right) \tag{2.1}$$

Another magnetic dipole $\vec{\mu}_j$ at the distance $\vec{r}_{ij}$ in the field of the first dipole has the energy

$$E_{\mathrm{dip}} = -\vec{\mu}_j \cdot \vec{B}_i = \frac{\vec{\mu}_i \cdot \vec{\mu}_j}{r_{ij}^3} - \frac{3(\vec{r}_{ij} \cdot \vec{\mu}_i) \cdot (\vec{r}_{ij} \cdot \vec{\mu}_j)\vec{r}_{ij}}{r_{ij}^5} \tag{2.2}$$

Due to the periodic ordering of the dipoles within a crystal lattice, the magnetic interaction energy according to Eq. (2.2) depends on the orientation of the dipoles relative to the crystal lattice.

### Magnetic anisotropy due to spin-orbit coupling

The spin-orbit coupling is the direct source of MAE. The orbital moment of bulk 3d metals is almost quenched due to cubic symmetry. Therefore, the magnetism of bulk 3d metals is mainly due to the spin moment, which can be understood from measurements of the $g$-factor ($g = 2.0023$ indicating complete quenching of the orbital moment). The $g$-factor for bulk 3d metals is close to the *'spin-only'* value, which means that the magnetism in these transition metals can be ascribed mainly to the spin of the delocalized 3d electrons. The electron spin, however, is weakly coupled to the orbital moment via spin$-$orbit coupling, and consequently the energy of the system depends on the relative orientation between the magnetization (spin orientation) and crystal axes.

To see how the spin couples to the lattice, consider a free atom: an electron travelling with a velocity $\vec{v}$ on a classical trajectory around the nucleus, experiences the electric field $\vec{E}$ generated by the screened nucleus in the form of a magnetic field (from the screened nucleus), $\vec{B} = \frac{1}{c}\vec{E} \times \vec{v}$. This field will couple to the magnetic (spin) moment $\vec{\mu}$ of the electron as $-\vec{\mu} \cdot \vec{B}$ [1]. If we assume that in a solid the crystal field forces the electron to move in a certain crystallographic plane, the electron spin will be aligned in a direction normal to this plane. In such a way, a uniaxial anisotropy can arise regardless of the shape of the crystal. To treat this quantitatively on a quantum-mechanical basis, it is necessary to start from the Dirac equation (see Ref. [48] for more details). This is because the Dirac equation like the Schrödinger equation contains no term that differentiates between the various magnetization directions even for a magnetic system. But if we include the relativistic mass-velocity term from the Pauli equation (a two-component approximation to the Dirac equation) in a simple case for a free atom we get the following correction term to the Hamiltonian:

$$\vec{\sigma} \cdot \left(\vec{E}(\vec{r}) \times \vec{p}\right) = \vec{\sigma} \cdot \left(\vec{\nabla} V(r) \times \vec{p}\right) = \frac{1}{r}\frac{dV(r)}{dr}\vec{\sigma} \cdot (\vec{r} \times \vec{p}) = \frac{1}{r}\frac{dV(r)}{dr}(\vec{\sigma} \cdot \vec{L}) = \xi\vec{\sigma} \cdot \vec{L} \tag{2.3}$$

It is a relativistic correction (factor $1/c$ ) that leads to the coupling between spin-space ($\vec{\sigma}$) and $\vec{E}(\vec{r})$. $\vec{L}$ is the orbital momentum operator. The term $\xi\vec{\sigma} \cdot \vec{L}$ is called the spin-orbit coupling

---

[1] Although this interaction has the form of a Zeeman term (the interaction of the spin with an external magnetic field), due to kinematical effects, this spin-orbit interaction is smaller by a factor of two. The origin of this effect is called Thomas-precession.

(SOC) term with the spin-orbit coupling constant $\xi$. Since the radial derivative of the potential in a crystal will be largest in the vicinity of a nucleus, we can expect that the major contribution to the spin-orbit interaction will come from this region.

A large MAE can be expected in ultrathin films due to the reduced symmetry of distorted lattices, interfaces, surfaces, and the presence of microscopic roughness. It is shown by a perturbation theory approach that the energy difference between easy and hard direction $\Delta\varepsilon$ is linked to the anisotropy of the orbital moment, and for a more than half-filled d-shell

$$\Delta\varepsilon \propto \jmath \frac{\xi}{4\mu_B} \left( \mu_L^{\parallel} - \mu_L^{\perp} \right) \tag{2.4}$$

where the factor $\jmath$ depends on the details of the band structure and also on the magnitude of the orbital moment [49].

In order to calculate the magnetic anisotropy energy for thin films one usually calculates the electronic structure by means of the local spin density approximation (LSDA) using a parametrization for the exchange correlation energy and potential [50]. This part of the MAE (the electronic part) is defined as the difference in total energy of the system for two different directions of the magnetization $\vec{M}$. To make an accurate calculation the fully relativistic spin-polarized version of the tight-binding Korringa-Kohn-Rostoker (TBKKR) method has to be applied because of the very small contribution of the MAE to the total energy of the system.

### Magneto-elastic anisotropy

Once one realizes that the MAE is a quantity describing the interaction between the electron spin and the lattice, it is intuitively clear that changes of the lattice constant will affect the magnetic properties. In a magnetized body one has energy terms that depend both on the strain and the magnetization direction: the magneto-elastic energy. Although resulting from the same origin, namely the spin-orbit interaction, magneto-elastic anisotropies only exist when stress is exerted on the magnetic system. For instance in iron, the effect of tension on a single crystal is to create a preferred direction of magnetization parallel to the direction of stress. The experimentally obtained magneto-elastic constants are significantly larger than the crystalline anisotropy constants [51]. As a consequence, even small strain may give rise to an important anisotropy contribution. Moreover, this phenomenon may be of importance in epitaxial structures, where considerable strain may result from the epitaxial growth of the film on a substrate or adjacent layers having different lattice parameters. If the lattice mismatch is not too large, below a critical thickness $d_c$ (coherent regime), the misfit is accommodated by introducing a tensile strain in one layer and a compressive strain in the other, such that both adopt the same in-plane lattice parameter. So, for relatively thin films the strain and the magneto-elastic coupling are independent of thickness. Above the critical thickness $d_c$, it becomes energetically more favorable to introduce misfit dislocations which partially accommodate the lattice misfit, allowing the uniform strain to be reduced (incoherent regime). In the incoherent regime, the contribution to the magneto-elastic energy is given by a reciprocal thickness dependence.

Generally, the magneto-elastic part of the magnetic anisotropy for a cubic system can be written as [52]:

$$\begin{aligned}
F_{\mathrm{MEL}} &= B_1\left(\alpha_1^2\epsilon_{11} + \alpha_2^2\epsilon_{22} + \alpha_3^2\epsilon_{33}\right) \\
&+ 2B_2\left(\alpha_1\alpha_2\epsilon_{12} + \alpha_2\alpha_3\epsilon_{23} + \alpha_3\alpha_1\epsilon_{31}\right) \\
&+ B_3\left(\alpha_1^4\epsilon_{11} + \alpha_2^4\epsilon_{22} + \alpha_3^4\epsilon_{33}\right) \\
&+ B_4\left(\alpha_2^2\alpha_3^2\epsilon_{11} + \alpha_3^2\alpha_1^2\epsilon_{22} + \alpha_1^2\alpha_2^2\epsilon_{33}\right) \\
&+ 2B_5\left(\alpha_3^2\alpha_1\alpha_2\epsilon_{12} + \alpha_2^2\alpha_1\alpha_3\epsilon_{13} + \alpha_1^2\alpha_2\alpha_3\epsilon_{23}\right) \\
&+ \ldots .
\end{aligned} \tag{2.5}$$

where $\epsilon_{ij}$ are the strain components, $B_i$ the magneto-elastic coupling constants and $\alpha_i$ the direction cosines (see coordinate system in Fig. 2.2) given by

$$\begin{aligned}
\alpha_1 &= \sin\theta\cos\phi \\
\alpha_2 &= \sin\theta\sin\phi \\
\alpha_3 &= \cos\theta
\end{aligned} \tag{2.6}$$

In order to calculate the magneto-elastic part one needs to measure $B_i$. If $i = j$ in Eq. (2.5) the strain is along the cubic $\langle 100 \rangle$ axes, for $i \neq j$ the strain is along the $\langle 110 \rangle$ axes. While the former type of strain leads to a change of the volume of the unit cell, the latter is equivalent to a shearing of the lattice keeping the volume constant. The strain components $\epsilon_{ij}$ are related to each other. For cubic symmetry the out-of-plane strain component $\epsilon_{33}$ is related to the in-plane ones by elastic constants, $c_{ij}$ [52,53]:

$$\begin{aligned}
&(100) \implies \epsilon_{33} = -\frac{c_{12}}{c_{11}}(\epsilon_{11} + \epsilon_{22}); && 1:[100], 2:[010] \\
&(110) \implies \epsilon_{33} = -\frac{(c_{11} + c_{12} - 2c_{44})(\epsilon_{11} + 2c_{12}\epsilon_{22})}{(c_{11} + c_{12} + 2c_{44})}; && 1:[\bar{1}10], 2:[001] \\
&(111) \implies \epsilon_{33} = -\frac{(c_{11} + 2c_{12} - 2c_{44})}{(c_{11} + 2c_{12} + 4c_{44})}(\epsilon_{11} + \epsilon_{22}); && 1,2:\perp \text{ arbitrary axes}
\end{aligned} \tag{2.7}$$

## 2.2. Landau-Lifshitz-Gilbert equation of motion

The motion of an exited magnetization $\vec{M}$ in general can be described by

$$\frac{1}{\gamma}\frac{\partial \vec{M}}{\partial t} = -\left[\vec{M} \times \vec{B}_{\text{eff}}\right] + \vec{R} \tag{2.8}$$

where $\vec{B}_{\text{eff}}$ is the effective field[2] which consists of external as well as internal fields, $\gamma$ is the gyro-magnetic ratio given by $g\mu_B/\hbar$ where $g$ is the $g$-factor. The first term on the right hand side represents the precessional torque and the last one represents the damping term which may be written in different phenomenological forms (e.g. Gilbert, Landau-Lifshitz, Bloch-Bloembergen, see Sec. 2.3).

For the uniform precession in the classical limit without any dephasing of the spins, the spin motion can be described by the well-known Landau-Lifshitz (LL) equation of motion

$$\frac{1}{\gamma}\frac{\partial \vec{M}}{\partial t} = -\left[\vec{M} \times \vec{B}_{\text{eff}}\right] + \frac{\lambda}{\mu_0 \gamma^2 M^2}\left(\vec{M} \times \vec{M} \times \vec{B}_{\text{eff}}\right) \tag{2.9}$$

Here $\lambda$ is the LL damping parameter. For small damping the LL term can be replaced by the Gilbert damping term resulting in the Landau-Lifshitz-Gilbert (LLG) equation of motion [54]

$$\frac{1}{\gamma}\frac{\partial \vec{M}}{\partial t} = -\left[\vec{M} \times \vec{B}_{\text{eff}}\right] + \frac{\alpha}{\gamma M}\left(\vec{M} \times \frac{\partial \vec{M}}{\partial t}\right) \tag{2.10}$$

where $\alpha$ is the damping parameter and is related to the Gilbert damping parameter $G$, according to: $\alpha = G/\gamma M$.

## 2.3. Uniform ferromagnetic resonance

The resonance equation can be derived by solving the *‘complete’* ferromagnetic resonance (FMR) theory and considering the dynamical effects of exchange/conductivity and of surface anisotropy (for more details see [55]).

Here we use the free energy approach developed by Smit and Beljers [56] in order to derive the resonance equations [57–60]. We assume that the sample is statically and dynamically homogeneously magnetized i.e. we neglect the influence of exchange energy and we approximate the surface magnetic energy by an effective volume anisotropy[3]. To consider the symmetry of the

---

[2] Throughout this thesis $\vec{H}$ and $\vec{M}$ are given in Ampere per meter [A/m] and $\vec{B}$ is given in Tesla [T], $\vec{B} = \mu_0(\vec{H} + \vec{M})$.

[3] In order to support this assumption we have also calculated the dynamical effects of exchange/conductivity and of surface anisotropy (assumed as uniaxial with symmetry axis along the sample normal) on the resonance field intensities using the "complete" FMR theory. The field differences between the results of the "complete" theory and the Smit and Beljers approach are less than the accuracy of the resonance field measurement (less than 0.1 mT), for the applied magnetic field along the film normal and parallel to the film plane for the used ranges of film thicknesses and microwave frequencies.

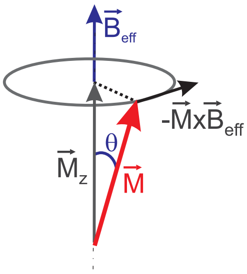

**Figure 2.1.:** Schematic drawing of the precession of the magnetization in resonance condition without magnetic damping effect.

given lattice it is always helpful to use polar coordinates. In the first step we neglect the magnetic damping effect, therefore, the precession of the total magnetic moment in the resonance condition can be described by the first term in LLG equation of motion. In Fig. 2.1 a schematic illustration of this mechanism is given.

According to Fig. 2.1 the motion of magnetization can be described as:

$$\dot{\theta} = \gamma B_{\text{eff},\phi} \qquad \dot{\phi} = -\frac{\gamma}{\sin\theta} B_{\text{eff},\theta} \tag{2.11}$$

The different contributions to $B_{\text{eff}}$ have to be taken into consideration through the free energy $F$.

$$dF = \vec{B}_{\text{eff}} \cdot d\vec{M} \tag{2.12}$$

Now let us define the free energy partial derivatives at the equilibrium conditions

$$F_\theta \equiv \frac{dF}{d\theta}\,|_\theta \overset{!}{=} 0 \qquad F_\phi \equiv \frac{dF}{d\phi}\,|_\phi \overset{!}{=} 0 \tag{2.13}$$

For a small precession angle we have

$$\delta_\theta = \theta(t) - \theta \qquad \delta_\phi = \phi(t) - \phi \tag{2.14}$$

By combining Eq. (2.11) and (2.14) together with Eq. (2.13) one can write

$$-\frac{M}{\gamma}\sin\theta\frac{\partial\,(\delta\theta)}{\partial t} = F_{\phi\theta}\delta\theta + F_{\phi\phi}\delta\phi \qquad \frac{M}{\gamma}\sin\theta\frac{\partial\,(\delta\phi)}{\partial t} + F_{\theta\theta}\delta\theta + F_{\theta\phi}\delta\phi \tag{2.15}$$

By assuming $\delta\theta,\ \delta\phi \sim \exp(i\omega t)$, the precession of a total magnetic moment with free energy $F$ occurs at the resonance frequency $f = \frac{\omega}{2\pi}$ given by

$$\left(\frac{\omega}{\gamma}\right)^2 = \frac{1}{M^2 \sin^2\theta}\left[\frac{\partial^2 F}{\partial\theta^2}\frac{\partial^2 F}{\partial\phi^2} - \left(\frac{\partial^2 F}{\partial\theta\partial\phi}\right)^2\right] \tag{2.16}$$

One can do the same calculation without neglecting the damping effect. Consequently, the resonance equation will include the damping parameter.

$$\left(\frac{\omega}{\gamma}\right)^2 = \frac{1+\alpha^2}{M^2 \sin^2\theta}\left[\frac{\partial^2 F}{\partial\theta^2}\frac{\partial^2 F}{\partial\phi^2} - \left(\frac{\partial^2 F}{\partial\theta\partial\phi}\right)^2\right] \tag{2.17}$$

Although Eq. (2.17) is mathematically correct, it is physically not convenient, because the origin of the different terms in $F$ is obscured by an angular-dependent mixing. This mixing was avoided by Baselgia *et al.* [61] who derived the following relation:

$$\left(\frac{\omega}{\gamma}\right)^2 = \frac{1+\alpha^2}{M^2}\left[\frac{\partial^2 F}{\partial\theta^2}\left(\frac{1}{\sin^2\theta}\frac{\partial^2 F}{\partial\phi^2} + \frac{\cos\theta}{\sin\theta}\frac{\partial F}{\partial\theta}\right) - \left(\frac{1}{\sin\theta}\frac{\partial^2 F}{\partial\theta\partial\phi} - \frac{\cos\theta}{\sin^2\theta}\frac{\partial F}{\partial\phi}\right)^2\right] \tag{2.18}$$

The partial derivatives are evaluated at the angles $\theta$ and $\phi$ which minimize $F$. Note, that the resonance frequency is given by the second derivatives of $F$, and thus is essentially a measure of the *curvature* of $F$, or the stiffness of $M$. In a conventional ferromagnetic resonance (FMR) experiment the magnetization is perturbed at a constant microwave frequency $\omega_m$ and $F$ is modified by varying an applied external field. The field needed to change $F$ such that $\omega = \omega_m$ is referred to as the resonance field, $B_{\text{res}}$. If the magnetization is oriented along a free energy minimum or *easy* direction of the added energy, the curvature of $F$ is increased and the applied field needed to make the resonance frequency equal to the microwave frequency $B_{\text{res}}$ is decreased. Similarly, if the magnetization is oriented along a free energy maximum, (the *hard* direction of the additional energy) $B_{\text{res}}$ is increased. An increased value of $B_{\text{res}}$ with respect to the resonance field of the *easy* direction therefore corresponds to a hard direction and a decreased value of $B_{\text{res}}$ corresponds to an easy direction. For a ferromagnetic film with cubic symmetry the free energy density $F$ includes the Zeeman energy, the demagnetizing energy, the perpendicular uniaxial $K_{2\perp}$ as well as the cubic $K_4$ anisotropy energy density:

$$\begin{aligned} F &= -\vec{M}\cdot\vec{B} + \left(\frac{1}{2}\mu_0 M^2 - K_{2\perp}\right)\alpha_z^2 + K_4(\alpha_x^2\alpha_y^2 + \alpha_x^2\alpha_z^2 + \alpha_y^2\alpha_z^2) \\ &= -MB\left[\sin\theta\sin\theta_B\cos(\phi-\phi_B) + \cos\theta\cos\theta_B\right] \\ &- \left(\frac{\mu_0}{2}M^2 - K_{2\perp} - K_4\right)\sin^2\theta - \frac{K_4}{8}(7+\cos 4\phi)\sin^4\theta \end{aligned} \tag{2.19}$$

Here $\theta_B(\phi_B)$ is the polar (azimuthal) angle of the external field $\vec{B}$ with respect to the [001]([100])-direction, $\theta$ ($\phi$) is the polar (azimuthal) angle of the magnetization with respect

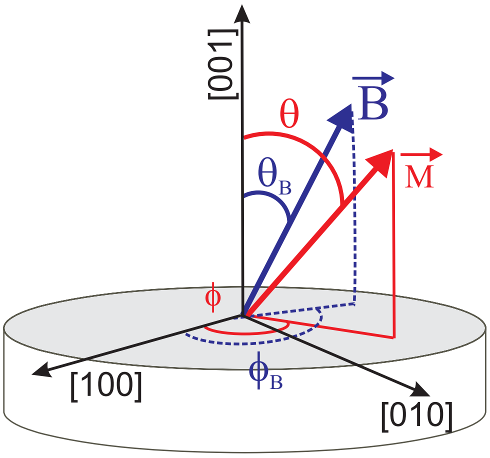

**Figure 2.2.:** Schematic drawing of the coordinate system used to analyze the FMR data.

to the [001]([100])-direction and the $\alpha_i$ are the direction cosines according to the coordinate system shown in Fig. 2.2. In the case of ultrathin ferromagnetic films on semiconducting substrates in addition to the anisotropy terms which are included in Eq. (2.19) a strong in-plane anisotropy ($K_{2\|}$) of uniaxial character has been observed, which has to be added to the phenomenological free energy, (2.19) leading to:

$$\begin{aligned}
F = & - \vec{M}\cdot\vec{B} + \left(\frac{1}{2}\mu_0 M^2 - K_{2\perp}\right)\alpha_z^2 + K_{2\|}\alpha_{\text{e.a.}}^2 + K_4(\alpha_x^2\alpha_y^2 + \alpha_x^2\alpha_z^2 + \alpha_y^2\alpha_z^2) \\
= & - MB\left[\sin\theta\sin\theta_B\cos(\phi-\phi_B) + \cos\theta\cos\theta_B\right] \\
& - \left(\frac{1}{2}\mu_0 M^2 - K_{2\perp}\right)\cos^2\theta + K_{2\|}\sin^2\theta\cos^2(\phi-\delta) \\
& + K_4\sin^2\theta - \frac{K_4}{8}(7+\cos 4\phi)\sin^4\theta
\end{aligned} \qquad (2.20)$$

$\delta$ is the angle between the easy axis of the twofold in-plane anisotropy $K_{2\|}$ with respect to the easy axis of the fourfold anisotropy, $\alpha_{\text{e.a.}}$ is the direction cosine with respect to the easy *in-plane* direction. In case that the sample cannot be treated as a quasi infinite film, demagnetizing effects in the film plane have to be considered. For an ultrathin film and following the approach of [56] that considers the equilibrium condition of the magnetization under a steady field and neglecting magnetic damping effects, the resonance condition (2.18) for the out-of-plane geometry, for which the external field is varied from the film normal [001] to the $[1\bar{1}0]$-direction is given by the following equation [62]:

$$\begin{aligned}\left(\frac{\omega}{\gamma}\right)^2 &= \Bigg\{B_{\mathrm{res}\perp}\cos\Delta\theta+\left[\mu_0M_{\mathrm{eff}}+\frac{K_4}{2M}+\frac{2K_{2\|}}{M}\cos^2\left(\frac{\pi}{4}+\delta\right)\right]\cos 2\theta_{eq}\\ &+ \frac{3K_4}{2M}\cos 4\theta_{eq}\Bigg\}\cdot\Bigg\{B_{\mathrm{res}\perp}\cos\Delta\theta+\left[\mu_0M_{\mathrm{eff}}+\frac{K_4}{M}+\frac{2K_{2\|}}{M}\cos^2\left(\frac{\pi}{4}+\delta\right)\right]\\ &\times \cos^2\theta_{eq}+\frac{3K_4}{M}\cos^4\theta_{eq}-\frac{2K_4}{M}+\frac{2K_{2\|}}{M}\sin 2\delta\Bigg\}-\left[\frac{K_{2\|}}{M}\cos\theta_{eq}\cos 2\delta\right]^2 \quad (2.21)\end{aligned}$$

Here $\Delta\theta=\theta_{eq}-\theta_B$ and $\mu_0M_{\mathrm{eff}}=\frac{2K_{2\perp}}{M}-\mu_0M$ denotes the effective out-of-plane anisotropy field. For $\mu_0M_{\mathrm{eff}}<0$ ($>0$) the easy axis of the system lies in (normal to) the film plane. For the in-plane configuration and for $\theta_B$=90 the resonance condition becomes

$$\begin{aligned}\left(\frac{\omega}{\gamma}\right)^2 = &\left\{B_{\mathrm{res}\|}\cos\Delta\phi-\mu_0M_{\mathrm{eff}}-\frac{2K_4}{M}+\frac{K_4}{2M}\left[7+\cos 4\phi_{eq}\right]+\frac{2K_{2\|}}{M}\cos^2(\phi_{eq}-\delta)\right\}\\ \times&\left\{B_{\mathrm{res}\|}\cos\Delta\phi+\frac{2K_4}{M}\cos 4\phi_{eq}+\frac{2K_{2\|}}{M}\cos 2(\phi_{eq}-\delta)\right\} \qquad (2.22)\end{aligned}$$

where $\Delta\phi=\phi_{eq}-\phi_{\mathrm{B}}$, $B_{\mathrm{res}\|}$ is the resonance field, and $\theta_{eq}(\phi_{eq})$ is the polar (azimuthal) equilibrium angle of the magnetization with respect to the film normal ([001]-direction), which is determined by the minimum of the free energy density (2.20). In order to determine the anisotropy fields, which are defined by the anisotropy values $K_i$ divided by $M$, one needs to perform a full polar and azimuthal angular dependence of the resonance field at a fixed frequency and fit the data points with Eq. (2.21) and Eq. (2.22) (the fitting parameters are the anisotropy fields).

In the special case that the magnetic field is oriented in the film plane and along the [1$\bar{1}$0]- or [100]-direction Eq. (2.22) can be simplified to [62]:

$$B\parallel[1\bar{1}0]\Longrightarrow\left(\frac{\omega}{\gamma_\|}\right)^2=\left(B_{\mathrm{res}\|}-\frac{2K_4}{M}-\frac{2K_{2\|}}{M}\right)\left(B_{\mathrm{res}\|}-\mu_0M_{\mathrm{eff}}+\frac{K_4}{M}\right) \qquad (2.23)$$

$$\vec{B}\parallel[100]\Longrightarrow\left(\frac{\omega}{\gamma_\|}\right)^2=\left(B_{\mathrm{res}\|}+\frac{2K_4}{M}\right)\left(B_{\mathrm{res}\|}-\mu_0M_{\mathrm{eff}}+\frac{2K_4}{M}\right) \qquad (2.24)$$

and for the [001]-direction ($\vec{B}$ is applied parallel to the film normal) Eq. (2.21) can be written as:

$$\vec{B}\parallel[001]\Longrightarrow\frac{\omega}{\gamma_\perp}=B_{\mathrm{res}\perp}+\left(\mu_0M_{\mathrm{eff}}+\frac{2K_4}{M}\right) \qquad (2.25)$$

One should note that Eqs. (2.23), (2.24) and (2.25) are only valid for the saturated condition, i.e., $\vec{B}$ is strong enough to align all magnetic moments parallel to its direction ($\phi_B=\phi_{eq},\theta_B=\theta_{eq}$).

In an FMR experiment, however, for specific anisotropy values the resonance condition can also be fulfilled when the magnetization is not parallel to the external magnetic field direction $\vec{B}$. This causes an additional signal at smaller fields with lower intensity (unsaturated mode). Such unsaturated resonance modes have been observed in our samples and will be discussed later. In order to find the dispersion relation (frequency versus field) for the unsaturated mode (unsaturated branch) numerical calculation is needed.

Equations (2.23) and (2.24) indicate that the squared resonance frequency versus the resonance field is a parabolic function for the in-plane $\langle 100 \rangle$- and $\langle 110 \rangle$-directions but for the perpendicular configuration ($\vec{B}\ \|[001]$) the frequency is linear with $B_{res\perp}$ (see Eq. (2.25)). Therefore, in order to precisely determine the $g$-factor one needs a frequency dependent measurement to suppress the effect of anisotropy fields on the determination.

In order to separate the different anisotropy contributions into volume and surface-interface contributions one also needs to do a full thickness dependent measurement. The thickness dependence of each anisotropy constant can be fitted by a constant term representing a volume contribution ($K_i^v$) and an effective surface-interface contribution ($K_i^{s,\mathrm{eff}}$) being proportional to $1/d$ where $d$ is the thickness of the film.

$$K_i = K_i^v + \frac{K_i^{s,\mathrm{eff}}}{d} \qquad\qquad i = 2, 4, 6 \tag{2.26}$$

## 2.4. Relaxation mechanisms

The magnetic relaxation process can be described by the LLG equation of motion (Sec. 2.2). In an FMR experiment the homogeneous microwave field couples to the uniform mode of magnetization, for which all spin rotate in phase (wave vector $\vec{k} = 0$). This uniform mode may not only decay via direct dissipation to the lattice, but also via dissipation to the other spin-wave ($\vec{k} \neq 0$) modes (i.e. keeping the energy within the spin system), which then dissipate the energy to the lattice. The viscous damping is a direct energy dissipation to the lattice and is irreversible. Figure 2.3 shows the possible processes during magnetization dynamics. Path (1) indicates the viscous damping and path (2) denotes a decay into nonuniform spin-waves ($\vec{k} \neq 0$), which finally decay to the lattice via path (3). In other words path (2) indicates that the energy of the uniform precession might dissipate to the lattice via an intermediate reversible state. This state may include high energy magnons or Stoner excitation for instance (for better understanding see the schematic illustration of the spin-wave dispersion curve in Fig. 2.6 and also Sec. 2.4.2 ).

A description for such a process can be given by the Bloch-Bloembergen [64,66] description:

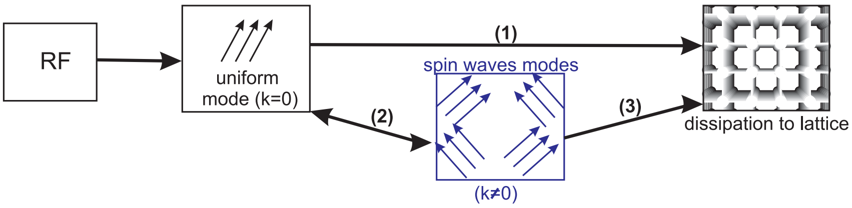

**Figure 2.3.:** Schematic drawing of the possible paths of the relaxation of the magnetization precession [63–65].

$$\frac{1}{\gamma}\frac{\partial\vec{M}}{\partial t} = -\left[\vec{M}\times\vec{B}_{\text{eff}}\right] - \frac{M_x}{\gamma T_2}\hat{i} - \frac{M_y}{\gamma T_2}\hat{j} - \left[\frac{M_z - M_s}{\gamma T_1}\right]\hat{k} \tag{2.27}$$

Here $T_1$ denotes the direct dissipation to the lattice, the so-called longitudinal relaxation rate, whereas $T_2$ is the transverse relaxation (in this case the energy is scattered to the transverse components of the magnetization). A schematic illustration of both phenomena is given in Fig. 2.4. The magnetization vector according to the LLG equation spirals towards direction of the effective magnetic field (Fig. 2.4 (a)). The length of $\vec{M}$ staying constant, while $M_z$ increases, whereas in the Bloch-Bloembergen case the z-component stays constant if $T_1 \gg T_2$, since the energy is scattered into the transverse components of the magnetization (Fig. 2.4 (b)).

In the following we introduce two different mechanisms, which are important for understanding the relaxation mechanisms shown as path (1) and (2) in Fig. 2.3.

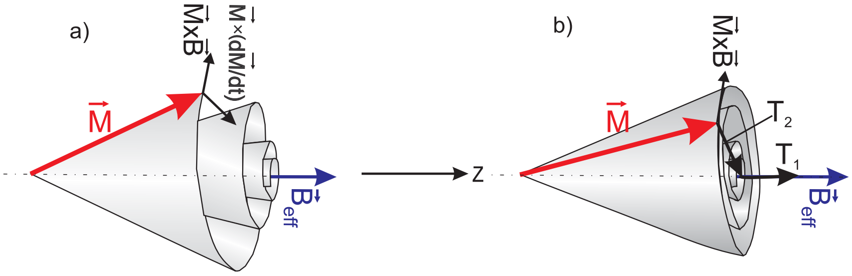

**Figure 2.4.:** Schematic illustration of (a) LLG and (b) Bloch-Bloembergen damping.

## 2.4.1. Gilbert mechanism

Following the free energy approach discussed in the last section the *intrinsic* part of the FMR linewidth can be derived from Eq. (2.17) as [67]:

$$\Delta\omega = \frac{\gamma\alpha}{M}\left(\frac{\partial^2 F}{\partial\theta^2} + \frac{1}{\sin^2\theta}\frac{\partial^2 F}{\partial\phi^2}\right); \qquad \Delta B_{\text{HWHM}} = \frac{dB}{d\omega}\Delta\omega \tag{2.28}$$

Assuming an perfectly uniform magnetized sample with no variation of the local anisotropy fields, the FMR linewidth can be roughly expressed as [67]:

$$\Delta B_{\mathrm{HWHM}} \approx \frac{\alpha}{\gamma} \frac{\omega}{\cos \beta} \tag{2.29}$$

where $\beta$ is the angle between $\vec{M}$ and $\vec{B}$, i.e. for in-plane configuration $\beta = \phi_B - \phi_{eq}$ and for out-of-plane configuration $\beta = \theta_B - \theta_{eq}$. It should be noted that $\Delta B_{\mathrm{HWHM}}$ introduced here is the half width at half maximum of the FMR absorption spectra.

In the following we will discuss the spin-orbit relaxation as the origin for the spin-lattice relaxation in metallic ferromagnets. Both spin-flip and ordinary processes will be briefly introduced.

### Spin-orbit relaxation

*The following section is based on the book by Bland and Heinrich [60] .*

One mechanism for spin relaxation has been proposed by Heinrich *et al.* [68] in 1967, which is based on the s-d exchange interaction.

In this model the interaction of itinerant s-p like electrons with localized d-spins can be obtained by integrating the s-d exchange energy density function.

$$H_{sd} = \sum_j \int_V J(\vec{r}_j - \vec{r}) \vec{S}_{j,d} \cdot \vec{S}_S(\vec{r}) dr^3 \tag{2.30}$$

where $J(\vec{r}_j - \vec{r})$ is the s-d exchange interaction between the spin density, $\vec{S}_S$, of s-p like itinerant electrons and the localized spins of the d-electrons, $\vec{S}_{j,d}$. $j$ is the lattice site. Two groups of electrons have to be considered. Those that are mostly localized (here denoted as d-electrons) and those that are itinerant (here denote as s electrons). In reality the itinerant electrons are hybridized states of s-p and d electrons. The transverse interaction Hamiltonian involving only the rf-components of magnetization vectors is described by three particle collision terms:

$$H_{sd} = \sqrt{\frac{2S}{N}} \sum_{\vec{k}} J(\vec{q}) a_{\vec{k},\uparrow} a^{\dagger}_{\vec{k}+\vec{q},\downarrow} b_{\vec{q}} + h.c. \tag{2.31}$$

where $N$ is the number of atomic sites, $a$ ($b$) annihilates an electron (a magnon ) and $a^{\dagger}$ ($b^{\dagger}$) creates an electron (a magnon). The arrows ↑ and ↓ as subscripts show the spin direction (up and down, respectively). A schematic illustration of this process is shown in Fig. 2.5

In principle, Eq. (2.31) indicates that the magnons and itinerant electrons are coherently scattered by the s-d exchange interaction, which results in an electron-hole annihilation pair.

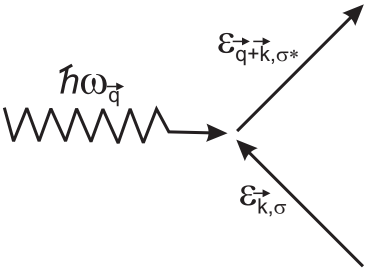

**Figure 2.5.:** Schematic illustration of the spin-flip scattering process. Here $\vec{q}$ ($\vec{k}$) denotes the magnon (electron) wave vector, $\sigma$ and $\sigma^*$ represent the spin states.

This scattering (Fig. 2.5) does not lead to magnetic damping of magnons with the uniform mode ($\vec{q} = 0$). The coherent scattering of magnons with itinerant electrons has to be disrupted by incoherent scattering with other excitations. The spin-flip hole-electron pairs can be incoherently scattered by thermally excited phonons. One can account for incoherent scattering by including a finite lifetime for the electron-hole pair excitation. Therefore, the electron-hole pair energy has an additional imaginary term

$$\Delta\varepsilon_{\vec{k},\vec{k}+\vec{q}} = \varepsilon_{\vec{k}+\vec{q},\uparrow} - \varepsilon_{\vec{k},\uparrow} + i\frac{\hbar}{\tau_{\text{eff}}} \tag{2.32}$$

where $\tau_{\text{eff}}$ is the effective lifetime and given by the spin-flip time of the electron-hole pair, $\tau_{\text{sf}}.\tau_{\text{sf}}$. It is enhanced compared to the momentum relaxation time $\tau_m$ which enters in the conductivity. The reason is that one needs to invoke spin-orbit interaction to flip the spin during the relaxation process of electron-hole pairs by phonons. For simple normal metals $\tau_{\text{sf}} = \tau_m/\Delta g^2$ [69], where $\Delta g$ is the deviation of the $g$-factor from the free electron value. Another estimation of $\tau_{\text{sf}}$ can be given via the spin diffusion length. The spin diffusion length is a part of the spin accumulation process which occurs in the current perpendicular to plane giant magnetoresistance (CPP GMR) investigations [70–72] and is given by

$$l_{sd} = \sqrt{\frac{\lambda^m_{FM}\nu_F\tau_{\text{sf}}}{6}}; \qquad \frac{1}{\lambda^m_{FM}} = \frac{1}{2}\left(\frac{1}{\lambda_\uparrow} + \frac{1}{\lambda_\downarrow}\right) = \frac{ne^2\rho^*}{m\nu_F} \tag{2.33}$$

where $\lambda^m_{FM}$ is the effective momentum mean free path resulting from the momentum mean free paths of the majority $\lambda_\uparrow$ and minority $\lambda_\downarrow$ electrons. $\upsilon_F$ is the Fermi velocity of the electrons participating in the spin accumulation, $n$ is the total density of conduction electrons. $\rho^* = \rho_{FM}(1-\beta^2)$ where $\rho_{FM}$ is the measured resistivity of the ferromagnet and $\beta$ is a bulk spin asymmetry coefficient.

The rf susceptibility can be calculated by using the Kubo Green function formalism in the random phase approximation (RPA) [73].

$$G_{\vec{q},\vec{q}'} = \langle b_{\vec{q}} | b^{\dagger}_{\vec{q}'} \rangle = -i\theta(t-t') \left\langle \left[ b_{\vec{q}}(t), b^{\dagger}_{\vec{q}'}(t') \right] \right\rangle \tag{2.34}$$

Here, $\theta(t-t')$, the Heaviside step-function denotes averaging over a grand-canonical ensemble. Please note that brackets '[...]' represent the commutative operator. The infinite chain of higher-order Green functions is determined using contraction over operators $a$ and $b$. By defining an additional Green function,

$$F_{\vec{k},\vec{k}',\vec{q}} = \langle a_{\vec{k},\uparrow} a^{\dagger}_{\vec{k}',\downarrow} | b_{\vec{q}} \rangle \tag{2.35}$$

the effective damping field can be given by the imaginary part of the Green function. After some simplifications and assuming a sharp Fermi energy the Gilbert damping field can be written as (for more details see [68])

$$H^{\text{s-f}}_{\text{eff}} = \frac{2\langle S \rangle}{N g \mu_B} \sum_{\vec{k}} |J(\vec{q})|^2 \delta(\varepsilon_{\vec{k}} - \varepsilon_F) \hbar\omega_{\vec{q}} \frac{\hbar}{\tau_{\text{sf}}} \frac{1}{\left(\hbar\omega + \varepsilon_{\vec{k},\uparrow} - \varepsilon_{\vec{k}+\vec{q},\downarrow}\right)^2} \tag{2.36}$$

where $\langle S \rangle = M_s(T)/M_s(0)$ denotes the reduced spin, $n$ is the density of states, and $g\mu_B = \gamma\hbar$ is a conversion factor, which converts the energy into a field. According to the fact that the excitation energy of electron-hole pairs is dominated by the exchange energy in an uniform ferromagnetic resonance, the Gilbert damping field can be written as

$$H^{\text{s-f}}_{\text{eff}} = \frac{\hbar^2 \omega_{\vec{q}}}{2 M_s \tau_{\text{sf}}} \sum_{\vec{k}} \delta(\varepsilon_{\vec{k}} - \varepsilon_F) \tag{2.37}$$

Comparing this equation with the Gilbert term in the LLG equation one can easily derive the Gilbert parameter as

$$G = \frac{\chi_P}{\tau_{\text{sf}}}; \qquad \chi_P = \left(\frac{\hbar\gamma}{2\pi}\right)^2 \int \vec{k}^2 \delta(\varepsilon_{\vec{k}} - \varepsilon_F) d\vec{k} = 2\mu_B^2 n\left(\varepsilon_F\right) \tag{2.38}$$

where $\chi_P$ is the Pauli susceptibility of itinerant electrons and $n(\varepsilon_F)$ is the density of itinerant electrons at the Fermi level.

Another model for spin-lattice relaxation has been proposed by Kamberský [74,75]. He showed that the intrinsic damping in metallic ferromagnets can be derived from the spin-orbit interaction Hamiltonian.

$$H_{so} = \frac{1}{2}\sqrt{\frac{2S}{N}} \xi \sum_{\vec{k}} \sum_{\alpha,\alpha',\sigma} \langle \beta | L_+ | \alpha \rangle \, c^{\dagger}_{\beta,\vec{k}+\vec{q},\sigma} c_{\alpha,\vec{k},\sigma} b_{\vec{q}} + h.c. \tag{2.39}$$

where $\xi$ denotes the spin-orbit interaction coefficient, $L_+ = L_x + iL_y$ is the right handed component of the atomic transverse angular momentum, $c_{\beta,\vec{k}+\vec{q},\sigma}$ ($c^\dagger_{\beta,\vec{k}+\vec{q},\sigma}$), which annihilates (creates) electrons in the appropriate Bloch states with the spin $\sigma$. $b_{\vec{q}}$ annihilates the spin-wave with the wave-vector $\vec{q}$. The $\alpha$ and $\beta$ subscripts represent the projected local orbitals of Bloch states. In order to calculate the rf susceptibility one can use the Kubo Green function formalism in RPA. The effective damping field is given by the imaginary part on the dominator of the circularly polarized susceptibility.

$$\begin{aligned}\frac{G}{\gamma M_s}\frac{\omega}{\gamma} = \frac{\langle s\rangle^2}{2M_s}\xi^2\left(\frac{1}{2\pi}\right)^3 \int d\vec{k}^3 \sum_{\alpha,\beta,\sigma} \langle\beta|L_+|\alpha\rangle\langle\alpha|L_-|\beta\rangle \times \\ \delta\left(\varepsilon_{\alpha,\vec{k},\sigma} - \varepsilon_F\right)\hbar\omega \frac{\hbar/\tau_m}{\left(\hbar\omega + \varepsilon_{\alpha,\vec{k},\sigma} - \varepsilon_{\beta,\vec{k}+\vec{q},\sigma}\right)^2 + (\hbar/\tau_m)^2}\end{aligned} \tag{2.40}$$

Here again $\langle S\rangle = M_s(T)/M_s(0)$ is the reduced spin. The relaxation time $\tau_{sf}$ is replaced by the momentum relaxation time, $\tau_m$ which enters the conductivity of the ferromagnet.

For *intraband* electron transitions for low frequency spin-waves ($q \ll k_F$), the electron energy balance $\hbar\omega + \varepsilon_{\alpha,\vec{k},\sigma} - \varepsilon_{\alpha,\vec{k}+\vec{q},\sigma} = \hbar\omega - (\hbar^2/2m)\left(2\vec{k}\cdot\vec{q} + q^2\right)$ in the dominator of Eq. (2.40) can be significantly less than $\hbar/\tau_m$. After integration over the Fermi surface the Gilbert parameter can be approximated by

$$G \simeq \langle S\rangle^2 \left(\frac{\xi}{\hbar}\right)^2 \left(\sum_\alpha \chi_P^\alpha \langle\alpha|L_+|\alpha\rangle\langle\alpha|L_-|\alpha\rangle\right)\tau_m \tag{2.41}$$

$\chi_P^\alpha$ is the Pauli susceptibility of those states which participate in *intraband* electron transitions. Equation (2.41) indicates that the Gilbert damping in this regime is proportional to the inverse of the relaxation time, $1/\tau_m$, and therefore scales with the conductivity.

*Interband* transitions are associated with energy gaps $\Delta\varepsilon_{\beta,\alpha}$. The electron-hole pair energy can be dominated by these gaps. For gaps larger than the relaxation frequency $\hbar/\tau_m$, the Gilbert damping can be approximated by

$$G \simeq \langle S\rangle^2 \sum_\alpha \chi_P^\alpha (\Delta g_\alpha)^2 \frac{1}{\tau_m} \tag{2.42}$$

One should notice that in this limit the spin-orbit interaction results in a Gilbert damping coefficient similar to that found for s-d exchange interaction, if one assumes Elliot's formula for the spin-flip relaxation time, $\tau_{sf} = \tau_m/\Delta g^2$ [69].

The Gilbert parameter introduced within these models (Eqs. (2.38) and (2.41)) is temperature independent.

### 2.4.2. Two-magnon scattering mechanism

In addition to the Gilbert mechanism there exists another relaxation process which contributes to the damping mechanism. The uniform FMR mode can be scattered to nonuniform modes ($\vec{k} \neq 0$) as denoted in Fig. 2.3 by the path (2). This scattering process is referred to as two-magnon scattering. It is extensively used to explain the extrinsic damping in different kinds of magnetic structures [63,76–80].

The two-magnon scattering contribution can be extracted from the torque term (first) in Eq. (2.8) and consequently, does not result from the second term. The dispersion relation for spin-waves can be derived from Eq. (2.8). The only consideration is that the dipolar field, which includes $k \neq 0$ magnons has to be added to the exchange field. Therefore, the effective field can be expressed as (for detailed analysis see for example [80])

$$\vec{B}_{\text{eff}} = \vec{B}_{\text{Exchange}} - \frac{\mu_0}{k^2}\vec{k}\left(\vec{k}\cdot\vec{m}\right); \qquad \vec{m} = \vec{m}_0 exp\left(i\vec{k}\cdot\vec{r}\right) \tag{2.43}$$

In Fig. 2.6 a schematic illustration of the bulk spin-wave dispersion relation for different orientations of the applied magnetic field is given. It indicates a shift of the band by changing the measurement configuration from the perpendicular to the parallel orientation of the external field. In perpendicular configuration the bottom of the spin-wave band at $k = 0$ coincides with the FMR frequency and there exist no degenerate non-zero $k$ spin-wave states at this frequency. In the parallel configuration the band has dropped down so that the top of the spin-wave band at $k = 0$ equals the FMR frequency. In this configuration there is an extended range of wave numbers degenerate with the uniform FMR mode.

In the ultrathin film regime the wave vectors $\vec{k}$ are confined to the film plane. For a thin film with an effective out-of-plane anisotropy field, $\mu_0 M_{\text{eff}} = \frac{2K_{2\perp}}{M} - \mu_0 M$, the magnon energies are given by Damon-Eshbach modes [81–85]. For simplicity let us assume that the magnetic field is

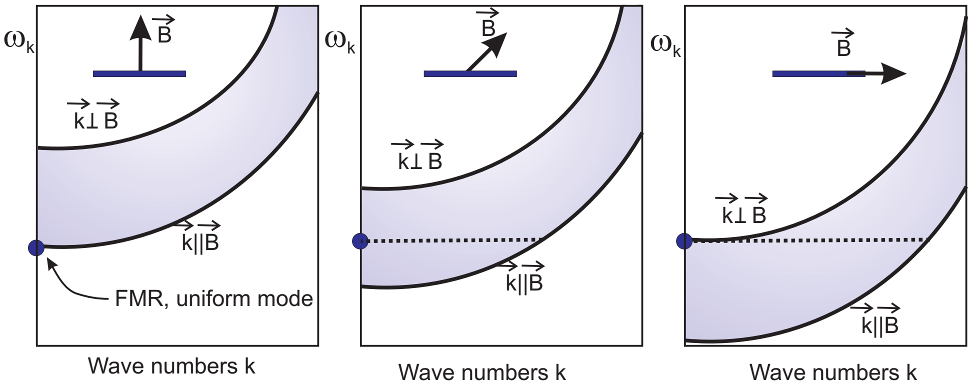

**Figure 2.6.:** Schematic illustration of the spin-wave dispersion curve for different orientations of the applied magnetic field.

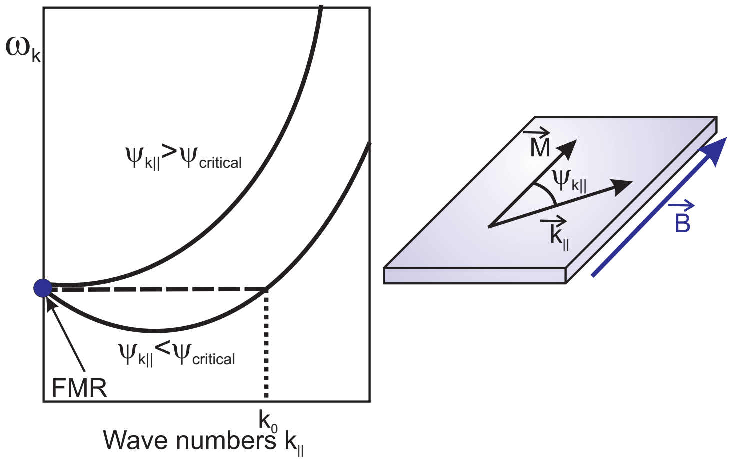

**Figure 2.7.:** Schematic illustration of the in-plane spin-wave dispersion curve of an ultrathin film.

applied along the easy in-plane magnetization direction. Therefore, the dispersion relation can be expressed as

$$\left(\frac{\omega_{k_\parallel}}{\gamma}\right)^2 = \left(\frac{\omega}{\gamma}\right)^2 - \frac{1}{2}\mu_0 M d\left[B - (B+\mu_0 M_{\text{eff}})\sin^2\psi_{k_\parallel}\right]k_\parallel + (2B+\mu_0 M_{\text{eff}})Dk_\parallel^2 \quad (2.44)$$

where, $D$ is the exchange stiffness and $\psi_{k_\parallel}$ is the angle between the in-plane component of wave vector $\vec{k}$ and $\vec{M}$.

Equation (2.44) indicates that in addition to the quadratic term there exists another linear term which is angle dependent. Moreover, this indicates that *below* a critical angle $\psi_{\text{critical}}$ given by

$$\sin^2\psi_{\vec{k}_\parallel} < \frac{B}{B+\mu_0 M_{\text{eff}}} \Longrightarrow |\psi_{k_\parallel}| < \arcsin\left(\left(\frac{B}{B+\mu_0 M_{\text{eff}}}\right)^{\frac{1}{2}}\right) \quad (2.45)$$

the spin-wave band could be changed so that the minimum is not anymore at $k=0$ and there are non-zero $k$ spin-wave states degenerate with the uniform FMR mode. A schematic illustration of the spin-wave dispersion curve of an ultrathin film is given in Fig. 2.7.

In contrary to the Gilbert contribution the frequency dependence of the linewidth due to two-magnon scattering is nonlinear. Arias and Mills have calculated the frequency dependence of the FMR linewidth due to two-magnon scattering [81,85]. They have employed the Green's function formalism and defined a Green's function as

$$S_{\alpha,\beta}\left(\vec{k}_\parallel, \vec{k'}_\parallel, t\right) = i\frac{\theta(t)}{\hbar}\left\langle\left[m_\alpha\left(\vec{k}_\parallel, t\right), m_\beta^\dagger\left(\vec{k'}_\parallel, 0\right)\right]\right\rangle \quad (2.46)$$

Here it is assumed that the $z$-axis is along the film normal, the operators are in Heisenberg representation and $\alpha$ and $\beta$ represent the range over $y$ and $z$. After relatively complicated mathematical steps the authors derived the frequency dependence of the FMR linewidth due to the two-magnon scattering mechanism.

$$\Delta B_{pp}^{2mag}(\omega) = \Gamma \arcsin\left(\sqrt{\frac{\sqrt{\omega^2 + (\omega_0/2)^2} - \omega_0/2}{\sqrt{\omega^2 + (\omega_0/2)^2} + \omega_0/2}}\right)$$
$$\omega_0 = \gamma\left(\mu_0 M - \frac{2K_{2\perp}}{M}\right) = -\gamma\mu_0 M_{\text{eff}} \tag{2.47}$$

Here $\Gamma$ represents the strength of the two-magnon scattering mechanism. In Fig. 2.8 the calculated frequency dependence of the FMR linewidth caused by different mechanisms is plotted. In this calculation $\Gamma = 50$ mT, $-\mu_0 M_{\text{eff}}$=2.1 T, $g$=2.09, $G = 6 \cdot 10^7$ Hz is used, and $\vec{B}$ is applied along the [100]-direction. $\Delta B_{pp}(0)$ represents the frequency and angle independent linewidth. The FMR linewidth due to the Gilbert mechanism is a linear function, whereas the contribution caused by two-magnon scattering is nonlinear.

The two-magnon scattering needs scattering centers of the order of spin-wave wavelength. This means that $\Gamma$ is isotropic and that it depends on the crystallographic directions because eventually the misfit dislocations in the crystal can be formed along individual direction(s) or in other words two-magnon scattering is angle dependent and depends on the direction of the network of misfit dislocations. In order to identify the angular dependence of two-magnon scattering, knowledge of the lattice structure is necessary (detailed information can be found in Sec. 10.8).

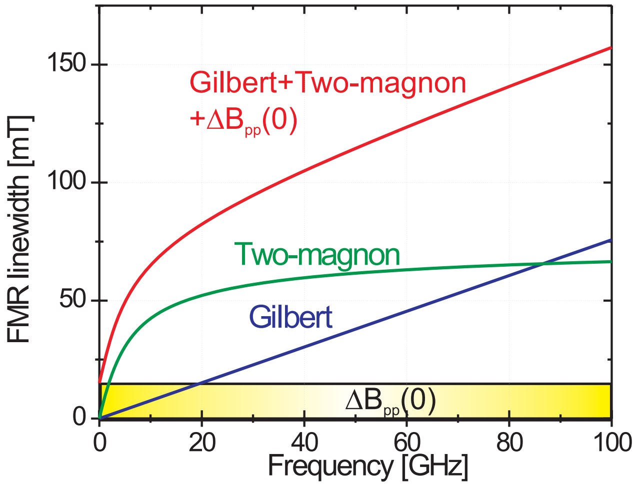

**Figure 2.8.:** Calculated frequency dependence of the FMR linewidth for an ultrathin film with in-plane magnetization. In this calculation $\Gamma = 50$ mT, $-\mu_0 M_{\text{eff}} = 2.1\ T$, $g$=2.09, $G = 6 \cdot 10^7$ Hz, and $\vec{B}$ applied along [100]-direction ($\phi_B = 0°$, $\theta_B = 90°$). $\Delta B_{pp}(0)$ represents the frequency independent linewidth.

# 3. Experimental methods

*In this chapter the experimental setups, which are constructed and used to measure the different physical properties of the samples, are described. While most results of this thesis are determined by in situ FMR, the focus will be put on the description of the UHV-FMR technique, which is uniquely combined with UHV-SQUID magnetometry and structural and chemical characterization techniques.*

## 3.1. MBE apparatus

All samples discussed in this work were prepared by molecular beam epitaxy (MBE). The Fe/semiconductor structures were prepared, characterized and measured under ultrahigh vacuum (UHV) conditions. The MBE system consists of a single UHV chamber directly connected to several pumps. The base pressure of the UHV chamber was about $1 \times 10^{-10}$ mbar. It is equipped with a 4-pocket e-beam evaporator, an Auger electron spectroscopy device, an ion-beam sputter gun, and a low-energy electron diffraction device. A schematic drawing of our MBE chamber is shown in Fig. 3.1. Detailed technical information can be found in [86]. In the following section we briefly introduce the different parts of our MBE system, which were constructed, developed and used during this work.

### The sample holder

Inside the UHV-chamber, the substrates were mounted on the sample holder, which is composed of three different pieces with individual functionalities: (i) a stabilizer made from oxygen-free copper to connect the other pieces to the liquid-He cryostat by a thin ceramic electrical insulator. All electrical connections were made via this part. (ii) an arm made from oxygen-free copper contains a thermocouple and heating wires (having the capability to heat the substrate to a temperature of 1000 K). This part was designed such that the head can be located exactly at the center of the cavity. Also, the amount of material was minimized in order to achieve a higher cavity's quality factor. (iii) a molybdenum rotatable head. This enables us to perform full in- and out-of-plane angle dependent FMR measurements. A schematic representation of the designed sample holder is given in Fig. 3.2. The head can be manipulated using a UHV rotary feedthrough. A schematic picture of this mechanism is given in Fig. 3.3.

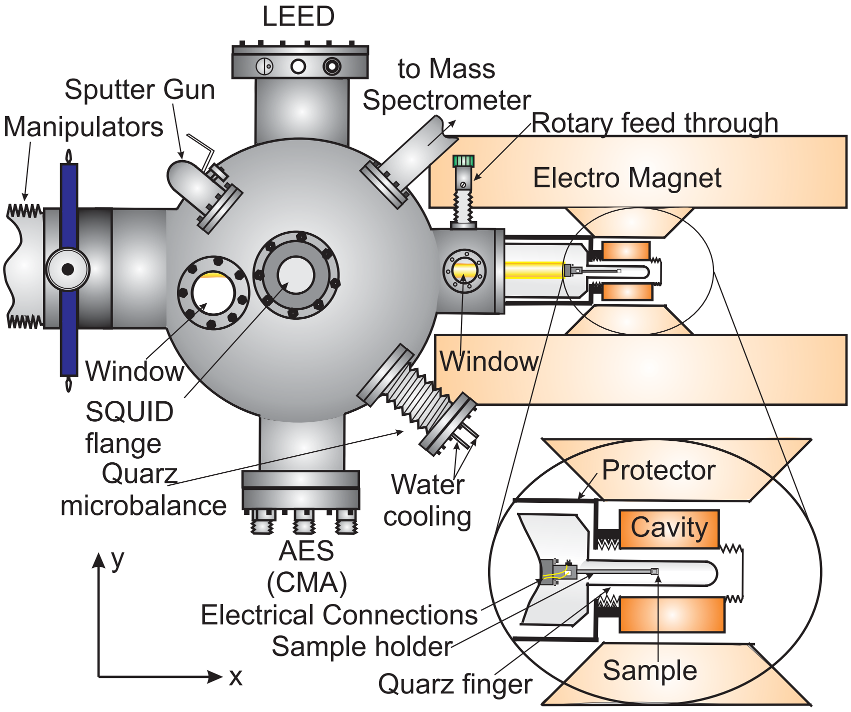

**Figure 3.1.:** Schematic illustration of the UHV chamber and *in situ* FMR configuration.

### 3.1.1. Auger electron spectroscopy

The chemical purity of the samples is checked with Auger electron spectroscopy (AES). The method basically uses the Auger effect: if ions, electrons or high energy photons hit a surface, there is a definite probability that an electron will be knocked out of the inner shell of a surface atom. The vacancy is occupied by an electron from an outer shell. This transition corresponds to an energy release, which can lead to the removal of a second electron from the outer shell. This latter electron is detected as an ‘*Auger electron*’. Since these transitions originate from atomic energy levels, they are element specific and the method is suitable to prove the composition of a surface and the region close to the surface. The nomenclature for the Auger transition is given by the electron shells contributing to the process. For example in LMM Auger transitions L- electrons are ejected from the surface and the vacancies in the L-shells are occupied by M-electrons, causing an energy gain which is finally transferred to other M-electrons. The intensity loss $dI$ of the primary electron beam upon penetrating a slab of material with thickness $dx$ is a function of the incoming intensity $I_0$ and the factor $1/\lambda$, which describes the cross section of the material, where $\lambda$ is the electron mean free path. This leads to the following dependency: $I(x) = I_0 exp(x/\lambda)$. This dependence between the Auger electron intensity and the thickness $x$ of a material slab allows the determination of the amount of coverage and of the growth character. Also it gives information of possible out-(inter-) diffusion of the substrate materials. Therefore the intensity changes of the Auger signals originating from the substrate and the

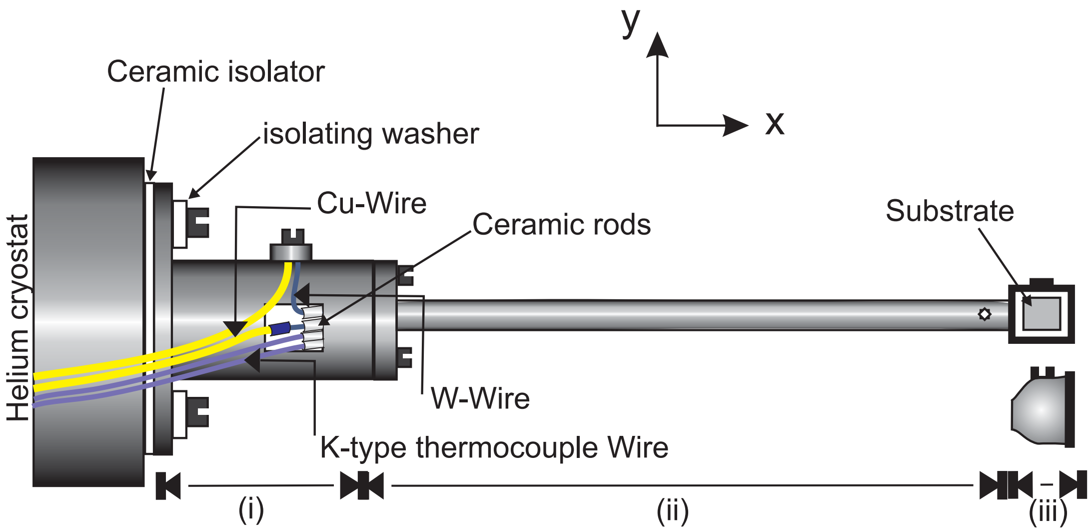

**Figure 3.2.:** Schematic illustration of the designed sample holder. The numbers denote the three different pieces of the sample holder (see text).

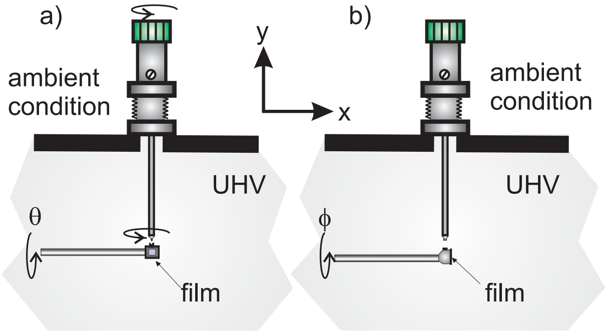

**Figure 3.3.:** Schematic drawing of the designed rotation mechanism to change the sample situation from out-of-plane (a) to in-plane configuration (b).

deposited layer have to be compared as a function of the thickness of the deposited layer. The primary electron energy used in AES is generated by an electron gun and is of the order of 3 to 5 keV. The type of analyzer used is a cylindrical mirror analyzer (CMA), where the electron source for the excitation of Auger electrons is situated on the cylinder axis of the CMA. The primary electrons generated by the electron gun penetrate the sample and the resulting Auger electrons can subsequently be detected by the CMA [87].

### 3.1.2. Low-energy electron diffraction

The characterization of the crystal structure can be achieved with low-energy electron diffraction (LEED). In this technique an electron beam of an energy between 10 and 1000 eV is scattered coherently from a crystalline surface. This energy range corresponds to a de-Broglie wavelength $\lambda_{Broglie}$ comparable to the atomic distances. An electron gun generates a collimated electron beam directed at the sample. The sample is located at the focal point of a system of spherical grids and a fluorescent screen. If electrons are scattered coherently, an interference pattern of the two- dimensional lattice can be observed on the fluorescent screen. The LEED pattern is an image of the surface symmetry in reciprocal space [88,89].

$$\vec{k} - \vec{k_0} = \vec{G}_{hkl} \tag{3.1}$$

where $\vec{k}$ ($\vec{k_0}$) is the scattered (incident) wave vector, and $\vec{G}_{hkl}$ represents the reciprocal lattice vector. Here $h; k; l$ are integers which do not necessarily have to coincide with the indices of real crystal planes. This technique does not give information about the third spatial direction, i.e. the lattice spacing perpendicular to the sample surface. The LEED pattern facilitates the determination of the two-dimensional symmetry of the crystalline surface.

### 3.1.3. IV-Low-energy electron diffraction

IV-Low-energy electron diffraction is based on the well known Bragg condition

$$2d \sin(\theta) = n\lambda \tag{3.2}$$

where $d$ is the distance between lattice points in a two-dimensional surface and $2\theta$ is the angle between the incoming and the diffracted electron beams. According to Eq. (3.2) by changing the de-Broglie wavelength of the incident beam one can get information about the perpendicular lattice spacing. This is possible by sweeping the energy of the incident electron beam and monitoring the intensity of the (0,0) LEED spot. The brightness of the (0,0) spot is maximum when the Bragg condition is fulfilled. One can easily write

$$E = \frac{h^2}{8m_e d^2 sin^2(\theta)} n^2 + V \tag{3.3}$$

where $h$ is Planck's constant, $m_e$ is the mass of the electron, $\theta$ is the angle of the incident electrons with respect to the film plane and $V$ is the inner potential, which is of the order of a few eV. During the experiment $\theta$ was about $2^\circ$ with respect to the film normal. By plotting the incident beam energy versus the square of the order of the Bragg peaks one gets the vertical layer spacing. The lowest order Bragg peak to be evaluated is of third order since for high energy electrons the influence of the inner potential V is negligible. Their band structure approaches that of free electrons. This technique has a relative good accuracy (1-2%) and unlike X-ray diffraction methods, it is sensitive for investigations of surfaces since the penetration length of the primary electrons is only a few monolayers.

## 3.2. *In situ* ferromagnetic resonance

One of the most established techniques to study the magnetic anisotropy, $g$-factor, and relaxation mechanisms is FMR [58,67,90]. In a conventional FMR experiment a magnetic system is exposed to a sinusoidal electromagnetic radiation at a fixed frequency typically in the Gigahertz range. As shown in Sec. 2.3 the resonance frequency is determined by the effective field which includes both external and internal fields. Therefore, the magnetic system can be driven through the resonance condition by sweeping a static external field. When measuring the absorption of the microwave radiation by the sample, the resonance field is found at maximum absorption. In order to enhance the signal to noise ratio, the magnetic field is modulated to allow for lock-in technique. As a consequence, the measured FMR signal is proportional to the field derivative of the imaginary part of the susceptibility ($d\chi''/B$). In the other words the FMR technique is based on measuring microwave losses in a magnetic sample as a function of the external dc magnetic field. In Fig. 3.4 the block diagram of an FMR spectrometer is shown.

The microwaves are mostly generated by klystrons which are operating in the frequency range from 10 to 72 GHz. The studied sample is mounted inside a cavity, located between the poles of the electromagnet.

In this work FMR was integrated in the UHV system and the samples were grown under ultrahigh vacuum condition and directly transferred into the quartz finger where the resonant cavity is installed from the outside. A cylindrical cavity with $\mathrm{TE}_{012}$ mode (suffixes represent

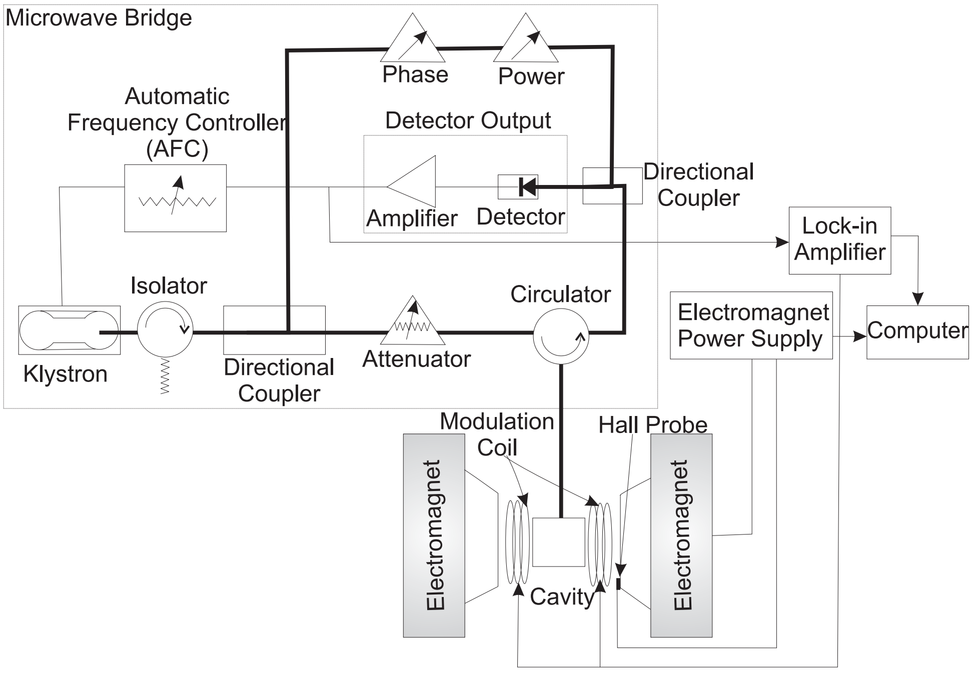

**Figure 3.4.:** Block diagram of an FMR spectrometer.

the number of half wavelength variations in the standing wave pattern in the angular, radial, and longitudinal direction, respectively) was used to perform the measurements. The cavity is coupled to the rectangular wave guide by a small coupling hole (iris), which is directly connected to the microwave bridge. This setup allowed us to measure the resonance field and the FMR linewidth continuously from the in-plane to the perpendicular orientation. The full in-plane angular dependence is possible by changing the sample configuration using the rotational mechanism (see Fig. 3.3).

Normally, the reflected power from the microwave cavity is monitored by a microwave diode detector. The reflected microwave power is proportional to the absorption of microwaves in the magnetic sample. The absorbed power $P$ is directly proportional to the imaginary part of the transversal rf-susceptibility.

By assuming only small deviations of the magnetization from equilibrium one can easily write $\vec{M} = (M_x, M_y, M_z) \approx (M_s, m_y, m_z) \approx\simeq \vec{M}_s + \vec{m}(y,z,t)$ where $\vec{m}(y,z,t)$ is the rf component of $\vec{M}$. In order to simplify the situation let us consider only the linear response of the rf driving field $\vec{h}_{\text{rf}} = (0, h_y = h_0, 0)$. Higher order terms in $\vec{B}_{\text{eff}}$ can be neglected. By assuming a simple $\exp(-i\omega t)$ for time dependence of the oscillatory field the LLG equation of motion results in

$$\begin{aligned} -i\frac{\omega}{\gamma}M_y^s + \left[B_{\text{eff}}^s - \frac{i\alpha\omega}{\gamma}\right]M_z^s &= 0 \\ \left[B^* - i\frac{\alpha\omega}{\gamma}\right]M_y^s + i\frac{\omega}{\gamma}M_z^s &= M_s d b_0 \end{aligned} \tag{3.4}$$

where $M_x^s$ and $M_y^s$ are the rf magnetization components and $B_{\text{eff}}^s$ and $B^*$ are related to the anisotropy fields according to

$$\begin{aligned} B_{\text{eff}}^s &= B - \mu_0 M_{\text{eff}} - \frac{2K_4}{M_s} + \frac{K_4}{2M_s}(7+\cos 4\phi) + \frac{2K_{2\|}}{2M_s}\cos^2(\phi-\delta) \\ B^* &= B + \frac{2K_4}{M_s}\cos 4\phi + \frac{2K_{2\|}}{2M_s}\cos 2(\phi-\delta) \end{aligned} \tag{3.5}$$

The rf-susceptibility can be easily derived from the Eq. (3.4)

$$\chi_y = \frac{M_y^s}{h_0} = \frac{\mu M_s d\left[B_{\text{eff}}^s - i\frac{\alpha\omega}{\gamma}\right]}{\left[B_{\text{eff}}^s - i\frac{\omega}{\gamma}\right]\left[B^* - i\frac{\alpha\omega}{\gamma}\right] - \left(\frac{\omega}{\gamma}\right)^2} \tag{3.6}$$

where $\mu$ is the permeability of the material. The absorbtion curve in well-ordered epitaxial films is almost Lorentzian. This can be shown by replacing $B^*$ by $B_{res} + \delta B$ in Eq. (3.6), utilizing the resonance condition (2.22) to simplify the resulting denominator and then keeping terms that are linear with $\delta B + (\omega/\gamma)(G/\gamma M_s)$. The susceptibility becomes

$$\chi_y = \frac{\mu M_s d}{B^s_{\text{eff, res}} + B^*_{res}} \frac{B^s_{\text{eff,res}} + \delta B - i\frac{\alpha\omega}{\gamma}}{\delta B - i\frac{\alpha\omega}{\gamma}} \tag{3.7}$$

The suffix *'res'* represents the resonance condition. The imaginary part of $\chi_y$ can be easily expressed as

$$\text{Im}\left[\chi_y\right] = \mu M_s d \frac{B^s_{\text{eff, res}}}{B^s_{\text{eff,res}} + B^*_{res}} \frac{1}{\Delta B_{\text{HWHM}}} \times \frac{1}{1 + \left(\frac{B - B_{\text{res}}}{\Delta B_{\text{HWHM}}}\right)^2} \tag{3.8}$$

By comparison of Eq. (3.8) with a conventional Lorentzian function $(A/(1+x^2))$ the amplitude of the absorption peak can be given by

$$A = \mu M_s d \frac{B^s_{\text{eff, res}}}{\left[B^s_{\text{eff,res}} + B^*_{res}\right]} \frac{1}{\Delta B_{\text{HWHM}}} \tag{3.9}$$

Equation (3.9) indicates that the FMR intensity is proportional to the magnetization, film thickness and an ellipticity factor ($B^s_{\text{eff, res}}/\left[B^s_{\text{eff,res}} + B^*_{res}\right]$) which can be simply calculated using the anisotropy fields extracted from the angle dependent measurements for each sample. The FMR absorption line is characterized by the resonance field $B_{res}$ , the resonance linewidth $\Delta B_{\text{HWHM}}$ (half width at half maximum) and the intensity which is proportional to the sample magnetization and the ellipticity factor. In Fig. 3.5 a schematic FMR spectrum is shown. The signal-to-noise ratio is improved by using a small ac modulation of the external field. The amplitude of the modulation has to be much smaller than the FMR linewidth. The measured signal corresponds to the field derivative of the imaginary part of the transversal susceptibility. In this case it is almost easy to measure the peak-to-peak linewidth, $\Delta B_{pp}$ which is related to $\Delta B_{\text{HWHM}}$ according to

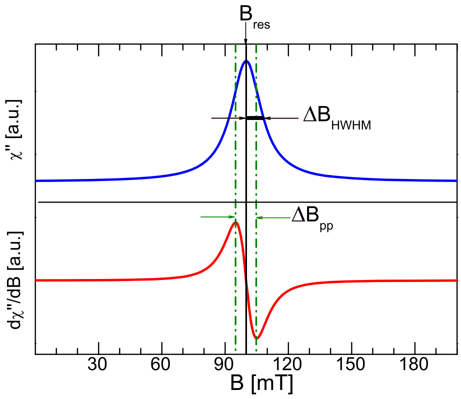

**Figure 3.5.:** Schematic illustration of an FMR spectrum.

$$\Delta B_{pp} = \frac{2}{\sqrt{3}} \Delta B_{\mathrm{HWHM}} \tag{3.10}$$

The FMR sensitivity is large so that it is able to detect the ferromagnetic signal of $10^{13}$ spins (a single atomic layer of a ferromagnetic material) [58]. Since the resonance condition includes internal field as well as external ones (see Eq. (2.17)) it is able to measure anisotropy fields. In order to determine the absolute value of the magnetic anisotropy values one needs the absolute value of the saturation magnetization.

In this work the magnetization of the samples was measured *in situ* under UHV by SQUID magnetometry. In the next section we will give just a brief introduction to the SQUID magnetometry under UHV. A full description of our *in situ* SQUID setup can be found in [86,91,92].

## 3.3. *In situ* SQUID magnetometry

The high-$T_c$ rf-SQUID detects the z-component of the magnetic stray field of the uniformly magnetized sample. By moving the sample below the SQUID sensor one can measure a 3D distribution of the magnetic stray field of the sample. This can be fitted with an analytical expression of the stray field for a given sample geometry yielding the magnetization of the sample in absolute units.

A schematic representation of the SQUID sensor and a typical three dimensional plot of the z-component of the stray field is shown in Figs. 3.3 (a) and (b) respectively. One important parameter needed to determine the magnetization is the exact distance between SQUID sensor and the sample. It is measured by an insulated W-wire loop of rectangular shape integrated inside the sample holder. At a current of ∼5 mA the induced magnetic stray field at a typical

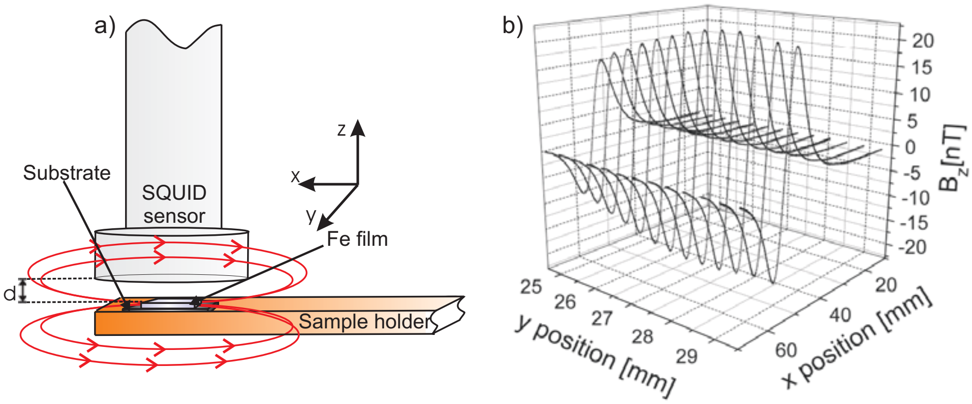

**Figure 3.6.:** (a) Schematic drawing of the configuration for SQUID measurement. (b) A typical stray field distribution in the x-y plane of a sample of a 20 ML Fe/GaAs(001) at a distance of z=5 mm taken from [91].

distance of 5 mm is in the range of 100 nT and can easily be detected by SQUID. Therefore, within this method one can easily measure the distance between the SQUID sensor and the sample.

# 4. Fe monolayers on GaAs(001)

*In this chapter the results of the in situ FMR experiments of epitaxial Fe monolayers grown on {4×6} reconstructed GaAs(001) are presented. The easy axis of magnetization is parallel to the [110]-direction for film thicknesses below 15 ML and rotates by 45° towards the [100]-direction for thicker Fe layers. The perpendicular magnetic anisotropy is strongly thickness dependent with a large surface-interface contribution (favoring an easy axis perpendicular to the film plane). Since the volume contribution to the cubic anisotropy was found to be very close to the Fe-bulk value, the surface-interface term is relatively large and favors an easy axis along the* $\langle 1\bar{1}0\rangle$*-direction. A strong uniaxial in-plane anisotropy was found for films with a thickness of 2.8 up to 40 ML originating from the Fe-GaAs interface which favors an easy axis along the [110]-direction . The different anisotropy contributions were ascribed to be the effect of the magneto-elastic anisotropy, but cannot be quantitatively explained. Especially the in-plane interface anisotropy can be understood only, when hybridization effects at the interface of Fe and GaAs are taken into account. The temperature dependence of the magnetic anisotropy and the magnetization were determined indicating that the temperature dependence of the perpendicular uniaxial anisotropy follows precisely the Calen-Callen model. Furthermore, the temperature dependence of the surface-interface and the volume terms were determined yielding the anisotropy contributions at zero Kelvin. It was observed that the Fe films exhibit a temperature-driven morphological transformation occurring at temperatures higher than 550 K depending on the film thickness. Finally, the effect of an Ag over-layer on the magnetic anisotropy was quantitatively determined.*

## 4.1. Introduction

The interface magnetic properties of ultrathin magnetic films grown on semiconductor substrates are of great scientific and technological interest for integration of magnetic materials with III-V semiconductors. The first candidate for such an application is the Fe ultrathin film on GaAs due to the high Fe magnetic moment and possible adaptability of GaAs for integration [1–4,6]. Although numerous works on covered Fe layers were carried out, just a few were performed on uncapped Fe/GaAs, and the magnetic properties of this system in the monolayer regime are not well understood yet. In particular the origin of the different anisotropy contributions observed in all experiments is not known. The room temperature magnetic anisotropy of uncapped Fe layers is studied by Madami *et al.* [16] using *in situ* Brillouin light scattering (BLS). Covered Fe/GaAs have been studied by other authors using various *ex situ* techniques: BLS [9], Alternating Gradient Field Magnetometery (AGFM) [10–12], Vibration Sample Magnetometery (VSM) [13], and FMR [14,15]. However, the Fe/GaAs samples studied here were grown, characterized, and measured *in situ* under UHV conditions and in a wider range of temperature and thickness than in any previous experiment. Furthermore, the absolute value of the magnetic anisotropy terms were determined by performing *in situ* FMR and *in situ* SQUID measurements on the same samples. whereas, FMR experiments yield the anisotropy fields, SQUID yields the magnetization in absolute units with sub-monolayer sensitivity [92,93]. The main goals of this chapter are: (i) to characterize the magnetic properties of high quality ultrathin Fe/GaAs, (ii) to determine the absolute values of anisotropy constants, (iii) to shed light on the origin of the different anisotropy contributions, (iv) to determine the temperature dependence of magnetic anisotropy, (v) to determine magnetic properties in the vicinity of the ferro- and superparamagnetic transition, and (vi) to investigate the effect of an Ag over-layer on the magnetic anisotropy.

## 4.2. Sample preparation

In the following section the sample preparation of Fe/{4×6}GaAs(001) and Ag/Fe/{4×6} GaAs(001) structures is described.

### 4.2.1. Substrate preparation

A 4×4 mm$^2$ (20×5 mm$^2$) cut from commercially available n-type GaAs(001) wafers was used as substrate. Before inserting into UHV, the crystals were ultrasonically cleaned using pure acetone and isopropanol. After transfer into the UHV chamber the substrates were first outgassed by slowly rising the temperature to about 900 K, so that the pressure did not exceed $1\times10^{-8}$ mbar, and subsequently annealed in UHV at 900 K for 60 min. Cycles of low energy Ar$^+$ sputtering (0.5-0.6 keV) at 900 K for 30 min were performed which resulted in a clean GaAs substrate as revealed by Auger electron spectroscopy (AES). At a partial Ar$^+$ pressure of about $1\times10^{-5}$ mbar, an Ar$^+$ current density of about 2 $\mu$ A/cm$^2$ was measured. A typical AES spectrum of a clean GaAs surface is shown in Fig. 4.1(a).

This substrate preparation yields a {4×6} well-ordered reconstruction of the GaAs(001) surface as revealed by our LEED pattern with a surface roughness of approximately 3 Å as confirmed by scanning tunnelling microscopy (STM). A typical LEED pattern and STM image of the clean GaAs(001) are shown in Figs. 4.1(b) and (c) respectively.

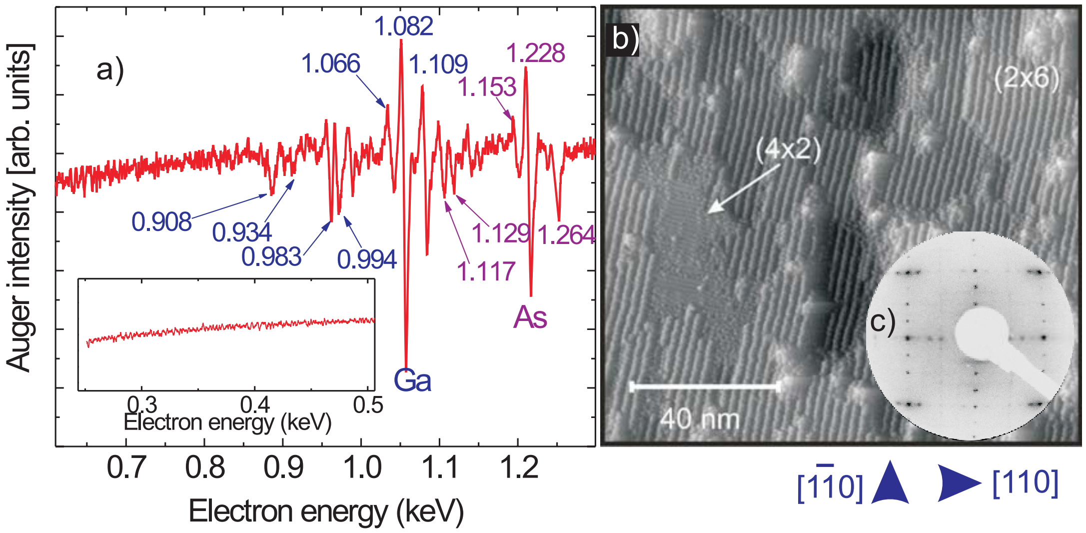

**Figure 4.1.:** (a) A typical AES spectrum of a clean Ga-rich GaAs substrate. The numbers show the detailed position of the Ga and As peaks [87]. The inset shows the spectrum of the same substrate recorded at low energies confirming the non-existence of surface contaminations, i.e. C and O. (b) STM-image of a clean GaAs(001) surface after cleaning procedure, recorded by C. Urban. (c) A LEED-pattern taken at an electron energy of about 52 eV showing the well ordered {4×6}reconstruction of the GaAs substrate.

## 4.2.2. Growth of Fe on GaAs(001)

The Fe layers were grown at room temperature (RT) by MBE with a deposition rate of 0.5 ML/min which was monitored by a quartz microbalance while the characteristic changes were observed in the LEED pattern. The base pressure of the chamber was about $2\times10^{-10}$ mbar which rose during Fe-deposition up to about $1.0\times10^{-9}$ mbar. A LEED analysis was performed after deposition to verify the good epitaxial growth. It was observed that the LEED pattern disappears immediately after the deposition of about 0.5 ML of Fe and reappears around the nominal thickness of 4 ML (see Zakeri *et al.* [94] for more details). Such an observation has also been reported by Xu *et al.* [95] and Madami *et al.* [16]. Our AES results show no diffusion of Ga(As) into the Fe films, since the LMM peaks of the Ga and As disappear near a thickness of 8 ML (see Fig. 4.2).

As mentioned in Sec. 4.2.1 the GaAs substrate has a surface roughness of approximately 3 Å which is around the height of the surface reconstruction.

In order to study the initial growth of Fe on $\{4\times6\}$ reconstructed GaAs(001), Fe was deposited on a $\{4\times6\}$ surface at RT in several steps inside the STM chamber by C. Urban at the University of Bochum during this work. The same region of the surface was repeatedly imaged by STM before and after deposition of few amounts of Fe. The STM results show that from the beginning, 3D islands are formed which appear as bright bumps. Their height is 1–3 ML

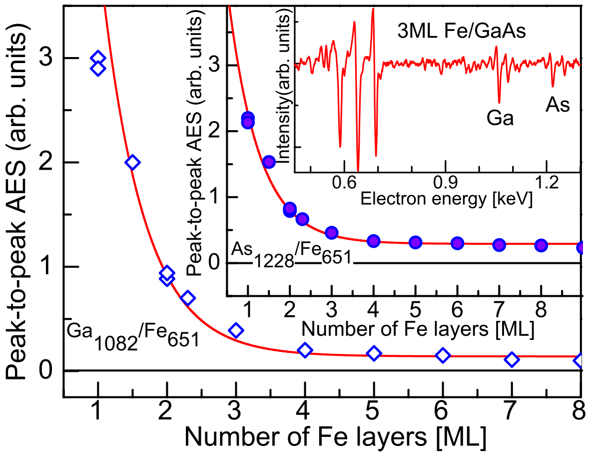

**Figure 4.2.:** The ratio of AES peak-to-peak amplitudes of the Ga LMM line at 1082 eV over Fe LMM line at 651 eV (open diamonds), along with the ratio of the AES peak-to-peak amplitudes of the As LMM line at 1228 eV over Fe LMM line at 651 eV (solid circles), measured for films grown at RT. The solid curves are guide to eyes. The inset shows a typical Auger spectrum of a 3 ML sample

and their diameter is on the order of a nanometer, meaning that the growth of Fe on $\{4 \times 6\}$ reconstructed GaAs proceeds via nucleation of 3D islands (Volmer–Weber growth) followed by quasi-layer-by-layer growth. This is in good agreement with our LEED observations. The 3D growth of Fe on Ga-rich GaAs is reported by various groups mainly using RHEED oscillations [10,14,95–98]. The first few monolayers grow as separate paramagnetic islands. At an average coverage of approximately 3.1 ML the material becomes superparamagnetic at room temperature, which is attributed to each island becoming ferromagnetic. At around 4.8 ML the islands merge and the material undergoes a transition to become ferromagnetic with a relatively high Curie temperature. The critical exponent of the susceptibility at the superparamagnetic to ferromagnetic transition is close to that of a 2D percolation transition [99]. Furthermore, the STM results reveal that on $\{4 \times 6\}$ reconstructed surfaces, the Fe nuclei are arranged in rows along $[1\bar{1}0]$. Therefore, the sites of nucleation are influenced by the specific reconstruction, since the direction of the rows corresponds to the previous substrate surface reconstruction. This is exactly the direction of the in-plane uniaxial magnetic anisotropy. We will come back to this point in Sec. 4.7.3.

### 4.2.3. The vertical lattice parameter and its temperature dependence

The vertical layer spacing was determined in an IV-LEED experiment by applying the Bragg equation (3.3) [100]. The energy of the primary electrons was varied in range of 20–900 eV. Fig

4.3 (b) shows a typical Bragg reflection of a 20 ML thick sample. The vertical lattice spacing was determined directly from the slope of the peak position as a function of the squared order of the Bragg reflection (see Fig 4.3 (c)). Figure 4.3 (a) shows that the vertical lattice parameter below 20 ML is approximately 3% larger than the Fe-bulk value meaning a tensile strain in the perpendicular direction and consequently in-plane compression in the film plane. The in-plane stress is also reported by Wedler *et al.* [101,102] using *in situ* stress evaluation during film formation. The vertical lattice parameter decreases slowly as the film thickness increases and relaxes to the Fe-bulk value above 65 ML.

The temperature dependence of the vertical lattice parameter was studied for a 20 ML sample between 40 and 400 K. The results are shown in Fig. 4.4. Interestingly, seven Bragg reflection peaks were observed at low temperatures, which increases the accuracy of the measurements with respect to the RT measurements (see Fig. 4.4 (b) and (c)). Clearly, the vertical lattice parameter increases with temperature. This expansion of the vertical lattice parameter is however much larger than the thermal expansion of bulk Fe. According to the fact that Fe-Ga(As) forms strong interface bonds and that the thermal expansion coefficient of Fe is two times larger than that of GaAs [103], we assume that the Fe lattice is fixed to the GaAs and can expand mainly in the vertical direction. This means that the perpendicular strain component increases as temperature increases. The temperature dependence of the strain will be discussed

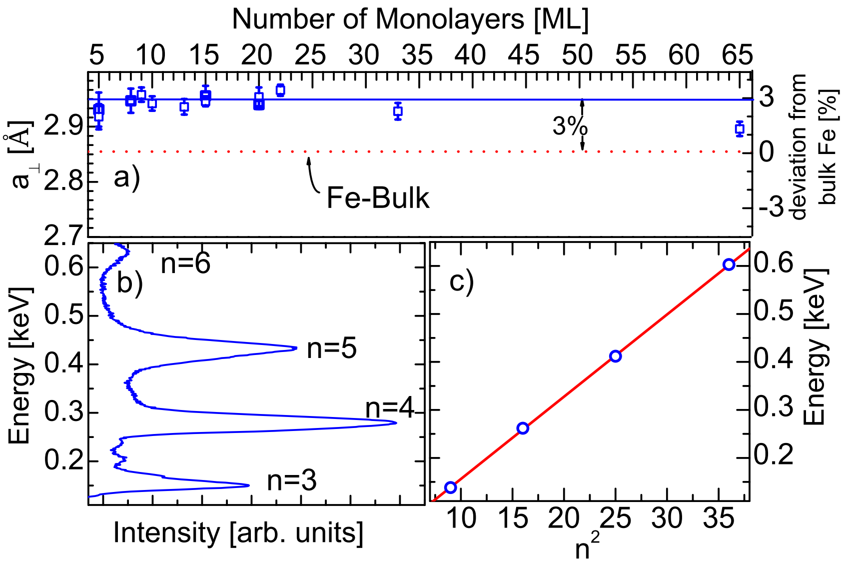

**Figure 4.3.:** (a) Room temperature vertical lattice parameter as a function of Fe thickness. The dotted line represents the lattice parameter of bulk Fe. (b) A typical I(V) profile of a 20 ML sample. The integers represent the order of the Bragg peaks. (c) The energy of the Bragg peaks as a function of the squared Bragg peak order. The solid line is the linear fit to the experimental data. The slope of the linear fit yields the inter-layer distance directly.

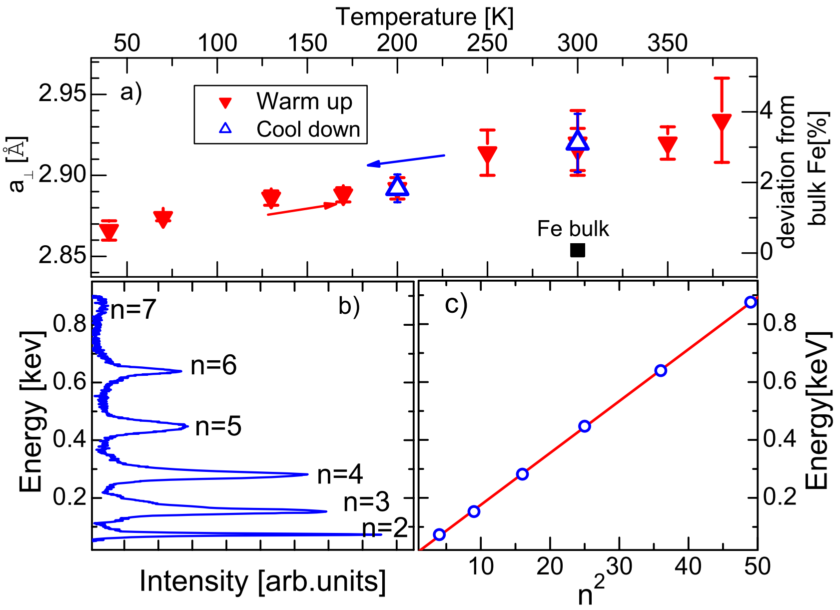

**Figure 4.4.:** (a) Temperature dependence of the vertical lattice parameter of a 20 ML Fe film epitaxially grown on {4×6}GaAs(001). The RT lattice parameter of bulk Fe is shown as a solid square. Both cooling down and heating up yields the same results. (b) Typical Bragg reflections observed for a 20 ML sample measured at 70 K. 7 Bragg peaks are observable. The integers denote the order of the Bragg peaks. (c) The energy of Bragg peak positions as a function of the squared order of the Bragg peaks at 70 K.

in Sec. 4.9.1.

### 4.2.4. Growth of Ag on Fe/GaAs(001)

The growth of Ag on Fe seems to satisfy the structural and thermodynamic criteria expected for a perfect layer-by-layer growth (Frank–van der Merwe growth mode) [104–106]. The lattice mismatch $\epsilon$ between fcc Ag (001) (space group Fm-3m, $a_{Ag}$= 4.0853 Å) and bcc Fe (001) (space group Im-3m, $a_{Fe}$= 2.8665 Å) is small, $\epsilon \approx -0.8\%$ (if the Ag lattice is rotated by 45° with respect to the one of Fe), and this suggests that the elastic energy of the epitaxially strained film will be only of minor importance for the resulting growth mode as compared to kinetic arguments. The lower surface free energy of Ag (001), $\xi$=1.2 J/m$^2$ [107], in comparison to Fe (001), $\xi$=2.2 J/m$^2$, also favors the wetting of the Fe (001) surface by Ag.

Epitaxial Ag were grown on top of the Fe layers at RT in the thickness of 1, 2, 5, 10, and 30 ML. A quadratic LEED pattern was observed for 10 ML Ag, showing a cubic (fcc) structure. A typical LEED pattern of an fcc Ag film is shown in Fig. 4.5. Furthermore, our IV-LEED measurements reveal that the lattice parameter of 10 ML Ag grown on 20 ML Fe/GaAs is very close to the lattice parameter of bulk fcc Ag, i.e. no substantial strain is present in the Ag layer.

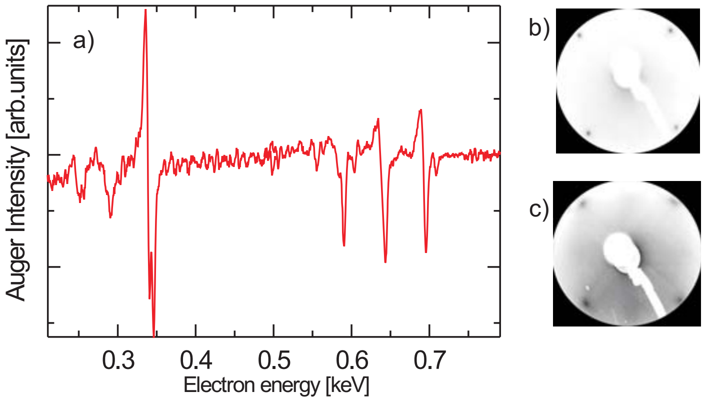

**Figure 4.5.:** (a) Typical AES spectrum of 2 ML Ag/20 ML Fe/{4×6}GaAs. (b) LEED-pattern of 20 ML Fe/{4×6}GaAs at an electron energy of 124 eV showing a well ordered bcc structure and (c) LEED-pattern of 10 ML Ag/20 ML Fe/{4×6}GaAs taken at an electron energy of about 172 eV showing a well ordered fcc structure.

## 4.3. *In situ* magnetic characterization

In order to determine the magnetic anisotropy, *in situ* FMR measurements were carried out immediately after growth at $f$=4.02 and 9.3 GHz. For each film thickness the resonance fields were recorded for polar angles $-90^\circ \leq \theta_B \leq 90^\circ$, i.e. within the ([1$\bar{1}$0], z) plane, see Fig. 4.6. The in-plane angle was varied within $-48^\circ \leq \phi_B \leq -42^\circ$ and $132^\circ \leq \phi_B \leq 138^\circ$ with respect to the [100]-direction to record additional FMR spectra in the in-plane geometry around the hard-direction in the film plane. Additionally, a polar angle dependence was measured at 4.02 GHz to confirm the anisotropy terms obtained from the measurement at 9.3 GHz and to enhance the accuracy of the results. It should be noted that the complete in- and out-of-plane angle dependent measurements were necessary to determine the anisotropy constants of the sample. The anisotropy constants were determined using the formulas derived in Sec. 2.3. The results for samples measured near the ferromagnetic and the superparamagnetic transition (0<film thickness<4) are discussed in Sec. 4.8.

In the case of 20 and 15 ML thick films two resonances were observed and for films thinner than 15 ML one resonance was observed in the in-plane configuration ($B||$[1$\bar{1}$0]) at 9.3 GHz. At a resonance frequency of 4.02 GHz two modes were observed for all films.

In Fig. 4.7 typical FMR spectra at 9.3 GHz and 4.02 GHz with the external field parallel to the [1$\bar{1}$0]-direction are shown for (a) 5 ML, (b) 10 ML , (c) 15 ML, and (d) 20 ML thick Fe films. Note the very small linewidth $\Delta B$=1.8 mT of the 20 ML film shown in the inset of Fig. 4.7(d), which confirms the excellent magnetic homogeneity of the layers. In accordance with the equations derived in Sec. 2.3, just a single resonance mode is expected for an ultrathin ferromagnetic

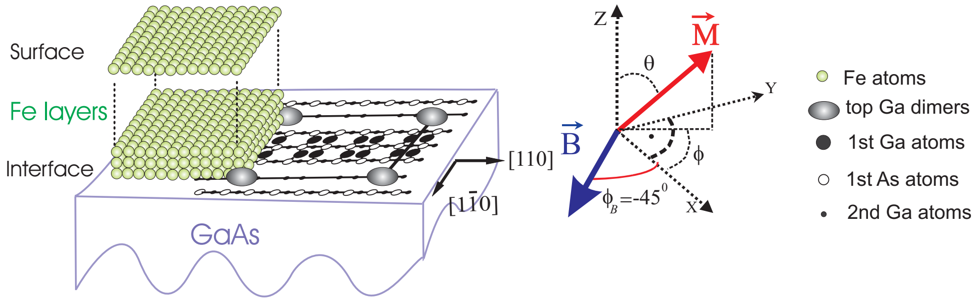

**Figure 4.6.:** Measurement geometry in parallel configuration. The model for the {4×6} reconstructed GaAs surface was taken from Ref. [108]. $1^{st}$ and $2^{nd}$ refers to Ga atoms at the top and below.

layer. However, for specific anisotropy values and magnetic field direction it is possible to see two and even three resonance modes as were observed in our Fe films on {4×6}GaAs(001). These modes are collective excitations of the spin system, in which the spins precess around the internal anisotropy fields instead of the external one. The inset of Fig. 4.7 shows that two resonance modes are observable for all film thicknesses by measurement at 4.02 GHz if the external magnetic field is applied very close to the [1$\bar{1}$0]-direction. The measurements at 9.3 GHz shows two resonance modes for 15 and 20 ML films only. The high-field signal has the largest intensity and can be identified as the saturated mode (Eqs. (2.23) and (2.24)), and the low-field signal as the unsaturated mode. There can be more than one mode and they will slightly overlap if the magnetic field is not perfectly aligned along the [1$\bar{1}$0]-direction.

The separation between saturated and unsaturated modes steadily increases when approaching the film normal. The occurrence of unsaturated resonance modes yields a possibility to increase the accuracy of the measurements, as two or even three modes can be used for fitting.

In order to determine the magnetic anisotropy constants the FMR data were analyzed as follows:

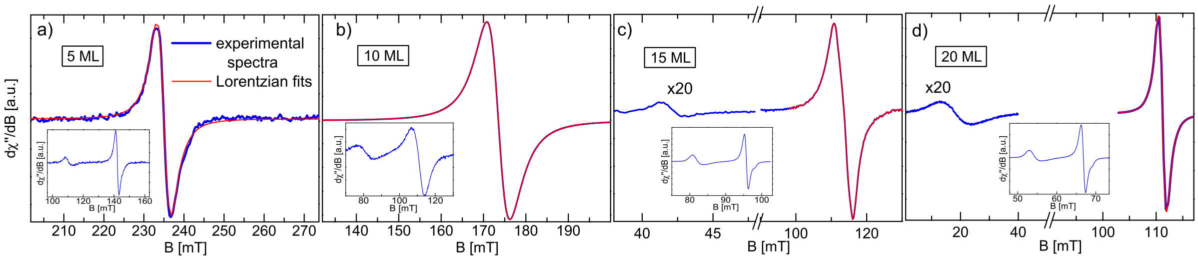

**Figure 4.7.:** FMR spectra recorded at RT and at a frequency of 9.3 GHz with an external magnetic field applied along [1$\bar{1}$0]-direction for (a) 5, (b) 10, (c) 15, and d) 20 ML Fe/{4×6}GaAs(001). The red curves are the Lorentzian fits to the experimental spectra (blue one). The insets show the spectra for the same films by measurements at a microwave frequency of 4.02 GHz (S-band).

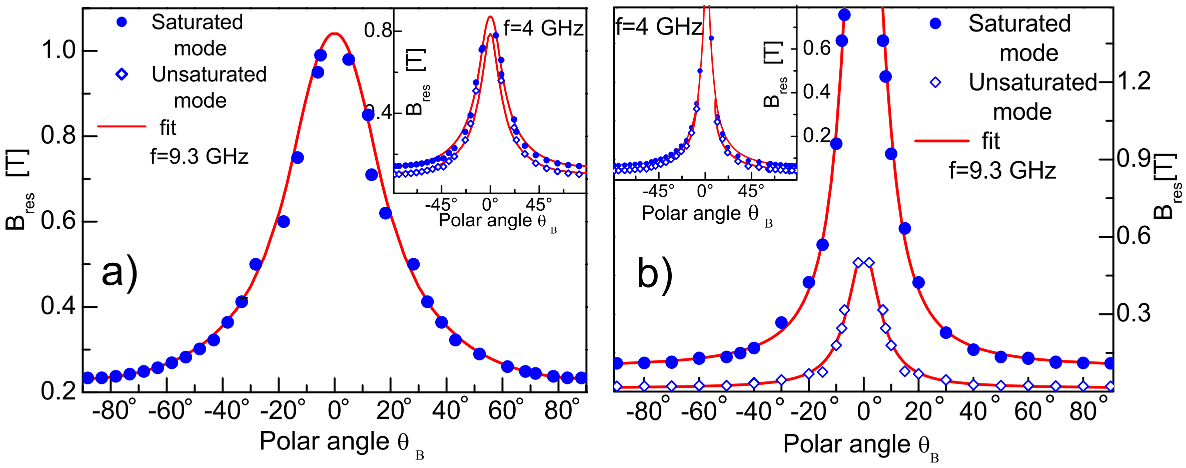

**Figure 4.8.:** Typical polar angular dependence of the resonance field for (a) a 5 ML and (b) a 20 ML Fe film on {4×6}GaAs(001) at a resonance frequency of 9.3 GHz. Insets show the polar angular dependence recorded at 4 GHz. The solid lines are fits to the experimental data. For the 20 ML sample the angular dependence of both saturated and unsaturated resonance modes are shown. In the case of the 5 ML sample just the saturated resonance mode is observable by a measurement at 9.3 GHz, but a measurement at 4 GHz yields both saturated and unsaturated resonance modes.

(i) The FMR spectra were fitted by a Lorentzian function for each in-plane and out-of-plane angle and also for spectra measured at 9.3 and 4.02 GHz. The fit was performed for both saturated as well as unsaturated resonance modes. This Lorentzian fit yields the FMR resonance fields, linewidth, and intensity.

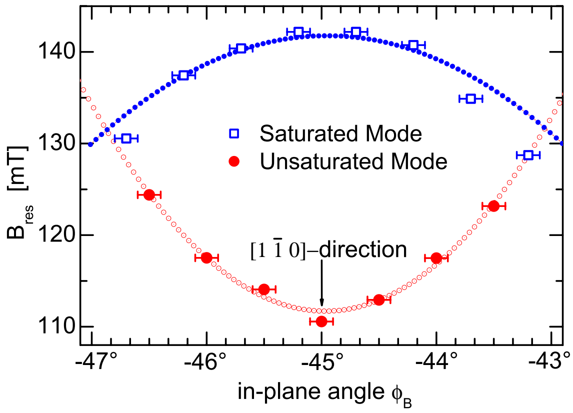

**Figure 4.9.:** Azimuthal angular dependence of the resonance field for 5 ML Fe/GaAs. The open squares denote the saturated resonance modes, whereas the solid circles denote the unsaturated modes. The dotted lines are the theoretical curves according to Eq. (2.22) (see text).

(ii) The resonance fields were plotted as a function of polar and azimuthal angle and were fitted by the fitting program which is based on Eqs. (2.21) and (2.22) with the same parameters obtained from (i). The $g$-value was chosen to be $g = 2.09$ which is the Fe-bulk value and has also been reported for thin Fe films on GaAs by McPhail [109]. Relative changes of the $g$-factor of $\pm 0.05$ do not yield significant differences in anisotropy constants. It should be noted that in principle the analysis of the saturated FMR field alone is sufficient to extract all information on the anisotropy values, however, the analysis of the unsaturated modes yields higher accuracy. A typical polar and azimuthal angular dependence of the saturated and unsaturated resonance signal, $B_{res}$, for (a) 5 ML Fe and (b) 20 ML Fe measured at RT is shown in Fig. 4.8 and 4.9, respectively. In Fig. 4.8 the solid lines are fits according to Eq. (2.21). One can directly learn from Fig. 4.8 that the maximum of the resonance field occurs when the external magnetic field is applied along the film normal indicating an in-plane alignment for magnetization direction. This has been observed for all film thicknesses. For the 20 ML film the difference between the resonance fields in parallel and perpendicular configuration is larger than for the 5 ML film implying that the thin film has a larger out-of-plane anisotropy. The fits for 4.02 and 9.3 GHz were performed using the same set of parameters.

To investigate the in-plane anisotropy in more detail we measured the in-plane angular dependence of the resonance field close to the $[1\bar{1}0]$-direction. In Fig. 4.9 the resonance field as a function of the in-plane angle is plotted for the 5 ML sample. By rotating the magnetic field in the film plane the saturated resonance mode (open squares) shifts to lower fields, whereas the unsaturated resonance mode (solid circles) moves to higher field values and within $2^\circ$ of rotation the FMR signal disappears. This directly shows that the $[1\bar{1}0]$-direction is the hard (in-plane) axis of the system. The fitting procedure has been performed using the anisotropy constants which have been determined by the out-of-plane angle dependent measurements according to Eq. (2.22). The fits for both saturated (closed circles) as well as unsaturated (open circles) modes reproduce the in-plane angular dependence around the hard direction very well.

## 4.4. Magnetization

The only way to extract the absolute value of the magnetic anisotropy constants is first to determine the absolute value of the saturation magnetization $M$ of the sample. It was determined by *in situ* SQUID magnetometry on the same samples [91]. The *in situ* SQUID yields the magnetization of the monolayers in absolute units. A detailed discussion of the SQUID results can be found elsewhere [91]. Furthermore, the magnetization was determined by analyzing the FMR intensity. Perfectly Lorenzian and noise free FMR spectra, which were observed for the samples, allow a detailed analysis of the FMR intensity as discussed in Sec. 3.2. Note that a 30 ML thick sample was chosen as reference for bulk magnetization. And other magnetization values

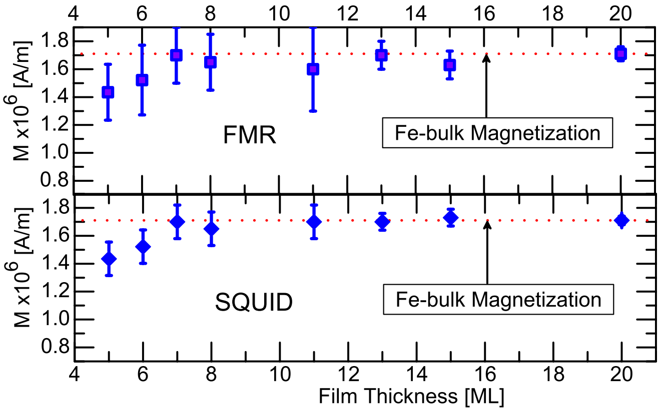

**Figure 4.10.:** Thickness dependence of the magnetization of the Fe films on {4×6}GaAs. The SQUID results (lower panel) are taken from Ref. [91].

were scaled accordingly. The results of FMR and SQUID are shown in Fig. 4.10. These data are in good agreement with the magnetization data for capped Fe/GaAs samples studied by McPhail *et al.* [109].

Both SQUID and FMR data show that the magnetization for samples with a thickness above 7 ML is close to the Fe-bulk value (M$_s$ $= 1.71 \times 10^6$A/m). The magnetization of the samples with a thickness of below 7 ML is slightly decreased in comparison to the bulk magnetization. This is attributed to the reduced Curie temperature and the growth mode of Fe on GaAs. A detailed discussion of the thickness and temperature dependence of the magnetization can be found in [91].

## 4.5. Magnetic anisotropy

The results of the magnetocrystalline anisotropy constants are listed in Tab. 4.1 for 5 to 30 ML of Fe on GaAs(001). In the following sections we discuss the different magnetic anisotropy contributions.

The perpendicular uniaxial anisotropy $K_{2\perp}$ in the first column of Tab. 4.1 is smaller than the shape anisotropy $\frac{1}{2}\mu_0 M^2$=18.35 J/m$^3$ (for $M$=1.71×10$^6$A/m). Consequently, the magnetization lies in the film plane for all thicknesses. The cubic anisotropy $K_4$ (the second column of Tab. 4.1) is positive for all films meaning that the favorable easy magnetization direction is the [100]-direction within the thicker Fe layers which is the easy axis of bulk-Fe (because thicker layers have a dominating cubic anisotropy). For thinner Fe layers, $d \leq$7 ML we find a large in-plane uniaxial anisotropy $K_{2\parallel}$ (the last column of Tab. 4.1) with a negative sign favoring an easy axis along the [110]-direction. The interplay between $K_4$ and $K_{2\parallel}$ leads to a change of the easy

| Thickness (ML) | $K_{2\perp}$ ($10^5$J/m$^3$) | $K_4$ ($10^5$J/m$^3$) | $K_{2\parallel}$ ($10^5$J/m$^3$) | $\frac{\mu_0 M_{\mathrm{eff}}}{2}$ (mT) | $\frac{K_4}{M}$ (mT) | $\frac{K_{2\parallel}}{M}$ (mT) |
|---|---|---|---|---|---|---|
| Fe-Bulk | 0 | 0.48 | 0 | -1072 | 27.5 | 0 |
| 30 | 1.00 | 0.47 | -0.04 | -1009 | 27.4 | -2.35 |
| 20 | 2.68 | 0.46 | -0.043 | -910 | 27 | -2.5 |
| 15 | 2.88 | 0.44 | -0.08 | -900 | 26 | -4.7 |
| 13 | 4.00 | 0.35 | -0.22 | -832.8 | 20.6 | -12.9 |
| 11 | 4.8 | 0.30 | -0.29 | -786 | 17.65 | -17.0 |
| 10 | 6.00 | 0.25 | -0.38 | -715 | 14.71 | -22.4 |
| 8 | 7.80 | 0.12 | -0.55 | -609.3 | 7.06 | -32.4 |
| 7 | 11.10 | 0 | -0.59 | -420 | 0 | -34 |
| 6 | 11.52 | 0 | -0.85 | -390 | 0 | -50 |
| 5 | 11.53 | 0 | -1.02 | -390 | 0 | -60 |

**Table 4.1.:** The measured magnetocrystalline anisotropy constants of uncapped Fe monolayers on $\{4\times6\}$GaAs(100). The integers in the first column represent the number of monolayers. All samples were measured *in situ* and at RT. The conversion to $\mu$eV/atom can be given by $1\times10^5$ J/m$^3$ =7.4 $\mu$eV/atom (see Appendix A for more details). The bulk value is given from [88].

axis from the [110]- towards the [100]-direction above $d$ ≈12 ML as will be discussed in detail in Sec. 4.7. Qualitatively, the strong uniaxial in-plane anisotropy may be understood by considering the twofold surface symmetry of the Fe-GaAs interface due to the $4\times6$ reconstruction (see Fig. 4.6). The rectangular surface cell is directly connected to the Fe-Ga and Fe-As bonds at the interface and thus to the atomic configuration [108]. As the STM images in Fig. 4.1(b) show the surface of the GaAs(001) substrate contains wide flat terraces with rows of atoms elongated along the $[1\bar{1}0]$-direction. The formation of small clusters of Fe above the surface is clearly visible at the initial stage of growth; these clusters seem to be formed along the atomic rows of the substrate (Fig. 4.1 (b)). These clusters become bigger as the nominal film thickness increases while their separation gets much smaller. This is likely the origin of the in-plane uniaxial anisotropy. The uniaxial anisotropy could also be related to an uniaxial stress within the Fe film as well as to a change of the Fe band structure at the interface due to hybridization. We will discuss this point in detail in Sec. 4.7.3.

## 4.6. The contributions to the magnetic anisotropy

In order to separate the volume and the surface-interface anisotropy contributions we have plotted in Fig. 4.11 the anisotropy constants as a function of reciprocal film thickness according to

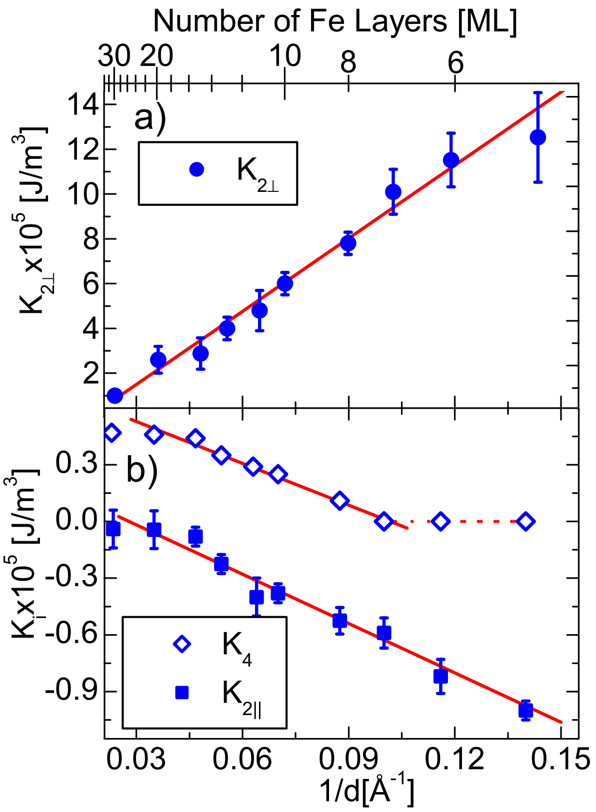

**Figure 4.11.:** The out-of-plane uniaxial (a), the in-plane cubic, and in-plane uniaxial (b) magnetocrystalline anisotropy constants of the Fe monolayers on $\{4\times6\}$GaAs(001) as a function of the reciprocal film thickness, determined at RT.

Eq. (4.2). The volume and surface-interface anisotropy constants resulting from these analyses are summarized in Tab. 4.2 and are compared to the other studies.

We start the discussion of Tab. 4.2 with the contributions to the uniaxial out-of-plane anisotropy $K_{2\perp}$. The volume contribution $K^v_{2\perp}$ = -1.7±0.8×10$^5$ J/m$^3$ (-13±6 $\mu$eV/atom) is very small, even smaller than the value which has been reported by Platow *et al.* [113] for Fe films on Cu(001) ($K^v_{2\perp}$ = 10.5±0.3×10$^5$ J/m$^3$ = 77.7±3 $\mu$eV/atom) [113], but it is close to the value for Au capped Fe/GaAs reported by McPhail *et al.* [109]. The negative sign of our $K^v_{2\perp}$ indicates a preferential alignment of the magnetization in the film plane due to this volume term. In previous studies of capped Fe/GaAs samples this contribution is neglected and McPhail *et al.* [109] is the only one who reported a value for $K^v_{2\perp}$ using polar magneto-optical Kerr effect (pMOKE). Note that in [109] a different sign convention was used yielding an in-plane orientation for positive $K^v_{2\perp}$. The much larger surface-interface term $K^{s,\mathrm{eff}}_{2\perp}$=1.17±0.1×10$^{-3}$ J/m$^2$ (600±50 $\mu$eV/atom) is a superposition of the Fe-vacuum and Fe-GaAs interface anisotropy. As shown by the positive sign of $K^{s,\mathrm{eff}}_{2\perp}$ the interface anisotropy favors an easy axis out-of-plane, which is well-known also to be the case for thin Fe films on Cu(001) [113]. As the interface

| | $K^v_{2\perp}$ ($10^5$J/m$^3$) | $K^v_4$ ($10^5$J/m$^3$) | $K^v_{2\parallel}$ ($10^5$J/m$^3$) | $K^{s,\mathrm{eff}}_{2\perp}$ ($10^{-3}$J/m$^2$) | $K^{s,\mathrm{eff}}_4$ ($10^{-5}$J/m$^2$) | $K^{s,\mathrm{eff}}_{2\parallel}$ ($10^{-5}$J/m$^2$) |
|---|---|---|---|---|---|---|
| **This work†** | **-1.7±0.8** | **0.66±0.1** | **0.18±0.25** | **1.17±0.1** | **-6.1±0.1** | **-8.9±0.4** |
| [16]† | – | 0.34±0.03 | 0.005±0.01* | 0.8±0.2 | -2.4±0.8 | -4.4±0.2* |
| [109]‡ | -1.2 ±0.7 * | 0.37±0.03 | – | 0.9±0.1* | -3.3±0.5 | 10±1 |
| [14]§ | – | 0.46±0.03 | – | 1.7±0.1 | -5.1±0.05 | 3.2±0.12 |
| [110]§§ | – | 0.47±0.03 | – | 0.58±0.01 | -2±0.1 | 10±1 |
| [15,110]‡ | – | 0.43±0.01 | – | 0.78 ±0.05 | -2.8±0.1 | 14±1 |
| [111,112] ‡ | – | 0.43±0.02 | – | -1.1±0.2 | -2.1±0.2 | 12±2 |

**Table 4.2.:** The surface-interface and volume contributions to the magnetocrystalline anisotropy of uncapped Fe monolayers on {4×6}GaAs(001) measured at RT.

†: Uncapped, ‡: Au-capped, §: Cu-capped, §§: Cr-capped.

$\ast$ In [109] and [16] a different definition of the free energy was used which yields opposite signs. The values have been adapted to the anisotropy model of this work.

contribution gets more important for thinner layers, the reduced value of $\mu_0 M_{\mathrm{eff}}$ at lower film thicknesses is a direct result of the interface anisotropy of uniaxial character. Interestingly, our value is only slightly larger than the value which has been found for the Fe-vacuum interface in Fe films on Ag by Urquhart *et al.* ($K^{s,\mathrm{vac}}_{2\perp}$ =0.96×$10^{-3}$J/m$^2$=490 $\mu$eV/atom) [106,114]. Taking this value for the Fe-vacuum contribution results in a very small value for the Fe-GaAs interface anisotropy ($K^{s,\mathrm{GaAs}}_{2\perp}$ =0.21±0.1×$10^{-3}$J/m$^2$=110±50 $\mu$eV/atom). This value is smaller than the value which is claimed by Monchesky *et al.*($K^{s,\mathrm{GaAs}}_{2\perp}$ =1.1$\pm0.1$ ×$10^{-3}$J/m$^2$=570±50 $\mu$eV/atom) [14] for Cu-capped films. We note, however, that the contribution of the vacuum interface does not have to be the same as for Fe on Ag, since it is known that the growth mode of Fe/Ag –unlike Fe/GaAs– proceeds layer-by-layer [106]. Therefore, the difference might be related to the difference of the surface morphology and also to the nature of the Fe-Ga and Fe-As bonds at the interface and to the substrate and surface roughness.

The analysis of Fig. 4.11 (b) shows that the cubic anisotropy vanishes below 7 ML indicating a transition from cubic to predominantly uniaxial symmetry. The thickness at which the cubic anisotropy vanishes has been reported to be 6-8 ML for capped films [14,111,115] and 5.2 ML for uncapped films studied by *in situ* BLS [16]. The thickness dependence of the cubic anisotropy constant (Fig. 4.11(b)) yields a negative surface-interface contribution ($K^{s,\mathrm{eff}}_4$ = -6.1±0.1×$10^{-5}$J/m$^2$=-31±1 $\mu$eV/atom) and a positive volume contribution ($K^v_4$ = 0.66±0.1×$10^5$ J/m$^3$ = 4.8±0.75 $\mu$eV/atom) close to bulk iron ($K_{4,\mathrm{bulk}}$ = 0.48×$10^5$ J/m$^3$=3.5 $\mu$eV/atom), which is similar to the values reported for other studies on capped and uncapped films (see Tab. 4.2 for details) indicating that the interior part of the thinner films is only moderately strained. $K^v_4$ is responsible for the alignment of the magnetization parallel to the [100]-direction (d>7ML) which is the easy axis for bulk-Fe. The decrease of $K_4$ at smaller film thickness results from the negative interface contribution $K_4^{s,\text{eff}}$. The negative sign indicates that the $\langle 110 \rangle$ directions are the favored easy axes, which are different from the bulk easy axes $\langle 100 \rangle$ (positive $K_4$).

Similar to $K_{2\perp}$, the thickness dependence of the uniaxial in-plane anisotropy $K_{2\|}$ shows a very small value for the volume contribution $K_{2\|}^v$ = 0.18±0.25×$10^5$J/$m^3$(1.3±1.85 $\mu$eV/atom), proving that $K_{2\|}$ is an interface effect. It should be noted that within the error bar $K_{2\|}^v$ is approximately zero. However, the surface-interface contribution is large. From the fit in Fig. 4.11 (b) one gets $K_{2\|}^{s,\text{eff}}$ = -8.9 ±0.4×$10^{-5}$ J/$m^2$ (-46.3±2 $\mu$eV/atom). This value is 2.8 times larger than the value for Cu covered Fe/GaAs which was found by Monchesky *et al.* ($K_{2\|}^{s,\text{efff}}$ = 3.2 ±1.2×$10^{-5}$ J/$m^2$=16±7 $\mu$eV/atom) [14] but it is in excellent agreement with Au capped samples studied by McPhail *et al.* ($K_{2\|}^{s,\text{eff}}$ = 10 ±1×$10^{-5}$J/$m^2$=52±6 $\mu$eV/atom) [109] and also by Brockmann *et al.* ($K_{2\|}^{s,\text{eff}}$ = 12 ±2×$10^{-5}$J/$m^2$=62±11 $\mu$eV/atom) [111]. The negative sign of $K_{2\|}^{s,\text{eff}}$ shows that the easy axis given by the uniaxial in-plane anisotropy is the [110]-direction, whereas the [1$\bar{1}$0] is the hard in-plane direction of our Fe films. One should note that some confusion concerning the identification of the crystallographic in-plane directions occurred in the literature (see e.g. [10,109]), where the [1$\bar{1}$0]- and [110]-directions were erroneously exchanged). The correct description was given by Madami *et al.* [16], then later by Zakeri *et al.* [62] and finally it was well explained in the review by Wastelbauer and Bland [8]. The change of the easy axis for thicker films towards the [100]-direction results, therefore, from the increasing influence of $K_4^v$ and decreasing influence of $K_{2\|}^{s,\text{eff}}$.

## 4.7. Discussion of the origin of the anisotropy contributions

The analysis of the FMR measurements revealed that the magnetic anisotropy of the Fe films is governed by strong interface contributions, whereas the volume contribution is almost bulk-like and only slightly altered by contributions, which are not expected in cubic Fe. In the following section we discuss possible sources of the various anisotropy contributions based on our experimental results.

### 4.7.1. The perpendicular uniaxial anisotropy

#### The volume contribution

As shown by our IV-LEED experiments (see Fig. 4.2.3), the room temperature vertical lattice parameter of the epitaxial Fe films on GaAs is approximately 3% larger than the lattice parameter of Fe-bulk thus implying a tensile strain perpendicular to the film plane. This out-of-plane strain expected to be accompanied with an in-plane one. Indeed an in-plane compressive strain is confirmed by the measured in-plane atomic distance by other groups by employing extended X-ray absorption fine structure experiments [116], which showed that a 10 ML thick film is compressed by -1.1% in the film plane. Since our experiments show that even 60 ML Fe have a vertical lattice parameter that enhanced by 3% with respect to the Fe bulk, we suggest that the stress in the volume is governed by compressive tension of uniaxial character. This is consistent with the tetragonally distorted environment of the films observed by IV-LEED for all samples.

According to elasticity theory (see [52,53] for details) we have $\epsilon = \epsilon_{11} = \epsilon_{22}$ for an isotropic compression in the film plane . The in-plane stress component $\epsilon$ is related to the perpendicular one by $\epsilon = -\frac{1}{2}\frac{c_{11}}{c_{12}}\epsilon_{33}$ where $c_{ij}$ are the elastic constants of the material. For Fe $c_{12} \approx c_{11}$, so that $\epsilon_{33} \approx -2\epsilon$ yielding a perpendicular uniaxial anisotropy term given by $K^v_{2\perp} \approx 3B_1\epsilon$ or $K^v_{2\perp} \approx -\frac{3}{2}B_1\epsilon_{33}$ (see Eq. (2.5)). Using the experimental value of $B_1 = 3.5 \times 10^6$ J/m$^3$ from [101] and $\epsilon_{33} \approx 3\%$ from our IV-LEED experiments one can calculate a value of $K^v_{2\perp} \approx -1.6{\times}10^5$ J/m$^3$ very closed to the value, which has been determined from our *in situ* FMR data. Furthermore, the perpendicular magneto-elastic anisotropy can be calculated using the in-plane strain component according to the fact that $K^v_{2\perp} \approx 3B_1\epsilon$. Using the reported value for $\epsilon$ by Gordon *et al.* ($\epsilon$=1.1%) [116] and $B_1 = 3.5 \times 10^6$ J/m$^3$ by Wedler *et al.* [101] one can calculate a magneto-elastic anisotropy of $K^v_{2\perp} \approx$ -1.0×10$^5$ J/m$^3$. Within the error bar this is the same value as the experimental one measured by our *in situ* FMR experiments ($K^v_{2\perp}$ =-1.7±0.8×10$^5$ J/m$^3$) with the same negative sign supporting that strain is the origin of $K^v_{2\perp}$. One should note that the calculation of $K^v_{2\perp}$ has been performed using the first order magneto-elastic coupling constant of the Fe film on GaAs measured by Wedler *et al.* [101], which has a positive sign in contrast to the Fe-bulk value. With the bulk magneto-elastic coupling constant it is impossible to calculate a reasonable value.

### The surface-interface contribution

The uniaxial surface term $K^{s,\mathrm{eff}}_{2\perp}$ which prefers an easy axis along the film normal cannot be explained by stress considerations. Thus, this term must have a different origin. One possibility could be the Fe-vacuum interface, which in the case of Fe/Cu(001) also leads to an easy axis perpendicular to the film plane. It is known that the Fe-vacuum surface anisotropy for bcc structures has a very large contribution to the perpendicular anisotropy [90]. It is mainly due to the symmetry breaking of the Fe atoms at the Fe-vacuum interface. The authors of [90] suggest that the 3d valence electron states confined to the surface possess very different magnetic properties than those that are fully itinerant. It has been shown in [90] that the broken symmetry at the Fe film interfaces causes large uniaxial perpendicular anisotropies [106]. The strongest surface uniaxial anisotropy was found for the Fe/vacuum interface (K$_{\mathrm{Fe-Vacuum}} \approx 1.0$ J/m$^2$ $\approx 738\mu$eV/atom) followed by Fe/Ag, Fe/Cu, Fe/Au and Fe/Pd. Therefore, we conclude that this surface-interface term mainly comes from the Fe-vacuum —not the Fe-GaAs— interface and, similar to the other Fe-vacuum interface anisotropies of bcc Fe films on metallic substrates, is due to the fact that the 3d and 4s/p valence states at the surface strongly enhance the contribution of the spin-orbit interaction to the interface valence band energies. This results in a large interface magnetic surface anisotropy with out-of-plane easy axis.

## 4.7.2. The cubic anisotropy

### The volume contribution

The IV-LEED experiments show that the vertical lattice parameter becomes smaller as the thickness of the film increases and relaxes towards the Fe-bulk value, when the film becomes thicker. The fact that the film strain becomes smaller for thicker films is confirmed by the observation of the cubic volume anisotropy term $K_4^v$ that is very close to the Fe-bulk value. The magneto-elastic *biaxial* anisotropy appearing in higher order within the Taylor expansion (2.5) is expected to be negligible due to the small lattice mismatch between Fe and GaAs.

### The surface-interface contribution

The cubic surface-interface contribution $K_4^{s,\mathrm{eff}}$ has an opposite sign in comparison to the volume contribution and leads to an in-plane reorientation of the fourfold easy and hard axes by $45^\circ$ below a critical thickness. However, the magneto-elastic anisotropy plays no role in cubic surface-interface anisotropy as shown in [52]. The fact that $K_4^{s,\mathrm{eff}}$ has the opposite sign of the cubic bulk value, favoring the $\langle 110 \rangle$-directions, indicates that hybridization at the GaAs interface or symmetry breaking at the Fe-vacuum interface are likely the sources for this contribution.

## 4.7.3. The in-plane uniaxial anisotropy

### The surface-interface contribution

Quantitative studies of the stress evolution during Fe deposition by Wedler *et al.* [101] show that the Fe films are under compressive stress of -3.5 GPa at the initial stage of growth (first 2–3 ML). This stress is even larger than the one resulting from an ideal coherent growth for which the stress would be given by the 1.36$\%$ misfit between Fe ($a$ =0.2866 nm) and GaAs ($a/2$ =0.2827 nm) yielding a compressive stress of -2.8 GPa. This enhancement was explained in terms of surface stress changes when the substrate reconstruction changes to the new interface consisting of Fe, Ga and As atoms. Considering the structural results from the STM investigation [108] (see model in Fig. 4.6), Fe is expected to be uniaxially strained at the interface. The compression of the lattice parallel to the [110]-direction results in a contribution of the magneto-elastic energy $F_{\mathrm{MEL}}$ per unit volume to the overall free energy density. For cubic

systems $F_{\mathrm{MEL}}$ is given by Eq. (2.5).
The in-plane strain leads to a uniaxial anisotropy contribution in the film plane. Using Eq. (2.5) and the fact that the in-plane stress is given by $\epsilon_{12}$ parallel to the [110]-direction, $F_{\mathrm{MEL}}$ can be written as $2B_2\alpha_1\alpha_2\epsilon_{12}$. Note that $\epsilon_{12}$ is negative in our case due to the compressive stress. In [102] the magneto-elastic constants of Fe on Ga-terminated GaAs(001) were measured. For 25 nm thick Fe films a value of $B_2 = 7.2 \times 10^6$ J/m$^3$ was obtained, whereas the Fe-bulk value is given by $B_2 = 7.62 \times 10^6$ J/m$^3$. Using the direction cosines $\alpha_1 = \sin\theta\cos\phi$ and $\alpha_2 = \sin\theta\sin\phi$ one gets $F_{\mathrm{MEL}} = +B_2\epsilon_{12}$ along the [110]-direction ($\alpha_1 = \alpha_2 = \sqrt{2}/2$) and $F_{\mathrm{MEL}} = -B_2\epsilon_{12}$ along the [1$\bar{1}$0]-direction ($\alpha_1 = -\alpha_2 = \sqrt{2}/2$). With $B_2 > 0$ and $\epsilon_{12} < 0$ a total energy reduction along the [110]-direction results, and the [1$\bar{1}$0]-direction becomes a hard one in excellent agreement with our results. The contribution of the magneto-elastic anisotropy is directly given by the energy difference for the two directions, i.e. $K_{2\|}^{\mathrm{MEL}} = F_{[110]}^{MEL} - F_{[1\bar{1}0]}^{MEL} = 2B_2\epsilon_{12}$. For $\epsilon_{12} = -1.7\%$ (corresponding to a stress of -3.5 GPa) $K_{2\|}^{\mathrm{MEL}} = -2.6 \times 10^5$ J/m$^3$ results. The in-plane magneto-elastic energy density can be written as $K_{2\|}^{\mathrm{MEL}} = -B_2\epsilon_{33}$ (because $\epsilon_{12} = -\frac{1}{2}\frac{c_{11}}{c_{12}}\epsilon_{33} \approx -\frac{1}{2}\epsilon_{33}$). The value of $\epsilon_{33} = 3\%$ measured by IV-LEED results in $K_{2\|}^{\mathrm{MEL}} = -2.3 \times 10^5$ J/m$^3$.
Now both values have to be compared to the measured uniaxial interface anisotropy $K_{2\|}^{s,\mathrm{eff}}/d$ = -6.2×10$^5$J/m$^3$ extracted from FMR data where $d$ is the thickness of the monolayer ($d = 0.1433$ nm). The values are of the correct order of magnitude and thus it is likely that strain at the interface plays a crucial role for the uniaxial anisotropy in the film plane. The fact that the experimental value is larger than the strain induced anisotropy indicates that other sources contribute to the uniaxial interface anisotropy as well. One reason could be hybridization of the Fe bands with the ones of Ga and As, in particular when interface intermixing is present. This anisotropy is strictly an interface term, which only involves the interface or the first atomic layer of Fe. The variation of the anisotropy with the direction of the dangling bonds is difficult to predict; it requires a full relativistic band structure calculation. Such a calculation of the anisotropy terms has been performed by Kŏsuth *et al.* [117]. However, the authors use a unreconstructed surface of GaAs. They have concluded that this anisotropy is caused primarily from the anisotropic Fe chemical bond to the GaAs.

Although the interface obviously exhibits a strain of uniaxial character, in the volume of the films no uniaxial strain persists as can be concluded from the vanishing value of $K_{2\|}^{v}$.

In summary, by considering the compressive stress at the interface one can understand the interface contribution to the in-plane $K_{2\|}^{s,\mathrm{eff}}$ as well as the volume contribution to the out-of-plane uniaxial anisotropy $K_{2\perp}^{v}$.

## 4.8. The onset of the long-range ferromagnetic order

In order to investigate the onset of ferromagnetism sub-monolayers of Fe were grown from 0.5 to 5 ML in steps of 0.3 ML and the FMR experiments were performed as a function of temperature. Fig. 4.12 shows the thickness dependence of (a) the FMR resonance field $B_{res}$ and (b) the FMR linewidth $\Delta B_{pp}$ measured at $T$ =50 K and f=9.3 GHz with an external magnetic field applied along the [1$\bar{1}$0]-direction. FMR signals were observed from a film thickness of 2.3 ML onwards. A significant change for both $B_{res}$ and $\Delta B_{pp}$ was observed at 4 ML. This phenomenon is likely related to the growth mode of Fe on $\{4{\times}6\}$GaAs which proceeds by the nucleation of 3D islands (Volmer-Weber growth) followed by a quasi layer-by-layer growth above a coverage of several ML (see Sec. 4.2.2). At an average coverage of approximately 2.3 ML the material behaves superparamagnetic above $T = 50$ K. At around 2.8 ML the islands merge and the material undergoes a ferromagnetic transition, showing a large in-plane uniaxial anisotropy. At the film thicknesses of 2.3–2.7 ML the total magnetic anisotropy of the system is zero which is shown by the isotropic resonance field $B_{res}$ of about 330.7 mT. 2.7 ML is the thickness where the transition from superparamagnetism to ferromagnetism occurs. Furthermore, *in situ* SQUID measurements showed that these Fe clusters have a Curie-temperature, which exponentially decays with decreasing thickness [91]. The corresponding critical exponent was determined by Bensch *et al.* to be $\beta = 0.26$ for Au capped samples, implying that the Curie temperature decreases by 270 K per ML [118]. The large value of the resonance linewidth $\Delta B_{pp}$ observed in the transition region (Fig. 4.12 (b)) can be correlated to the large size distribution of the Fe clusters [10,96,97]. A change in the spin-wave frequency and the broadening of BLS spectra has been reported by Steinmüller *et al.* [119] at RT for a film thickness of 3.4 ML, which is in good agreement with our finding using FMR.

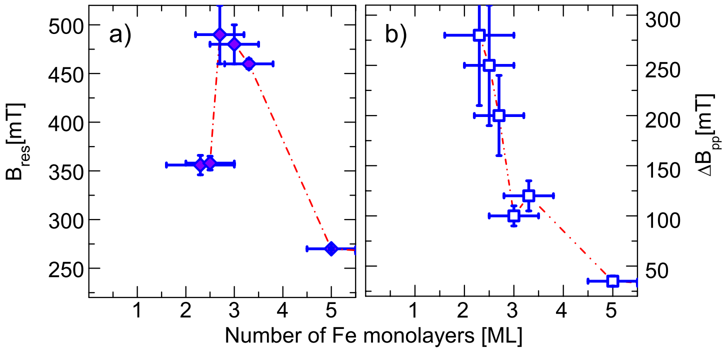

**Figure 4.12.:** Evolution of (a) the FMR resonance field and (b) linewidth with nominal number of Fe layers recorded at a microwave frequency of 9.3 GHz and temperature of 50 K.

## 4.9. Temperature dependence of the magnetic anisotropy

In the following section we focus on the temperature dependence of the magnetic anisotropy of uncovered Fe monolayers on $\{4\times6\}$GaAs. The temperature dependence of covered Fe films was measured previously [118,120]. One should note that the magnetic anisotropy terms are sensitive to the metallic over-layers especially if the thickness of the Fe film is just a few monolayers (see Sec. 4.11). Figure 4.13 shows the temperature dependence of the FMR spectra of a 20 ML sample. All spectra are recorded at the microwave frequency of 9.3 GHz with the external field applied along the hard in-plane axis ($[1\bar{1}0]$-direction). Note that an additional unsaturated resonance mode at low field appears below 200 K, which is due to the temperature dependent change of the in-plane magnetic anisotropy terms.

The anisotropy terms were determined by angle dependent measurements at different temperatures for 5, 6, 7, 15, and 20 ML Fe. The temperature variation of the magnetic anisotropy parameters is given in Fig. 4.14. Both in-plane uniaxial and cubic anisotropy constants are large and dominate the Zeeman energy causing such an unusual and surprising triple-line FMR spectra in the single ferromagnetic layer (Fig. 4.13). It can be seen from Fig. 4.14 that all magnetic anisotropy parameters strongly depend on temperature. As the temperature decreases the

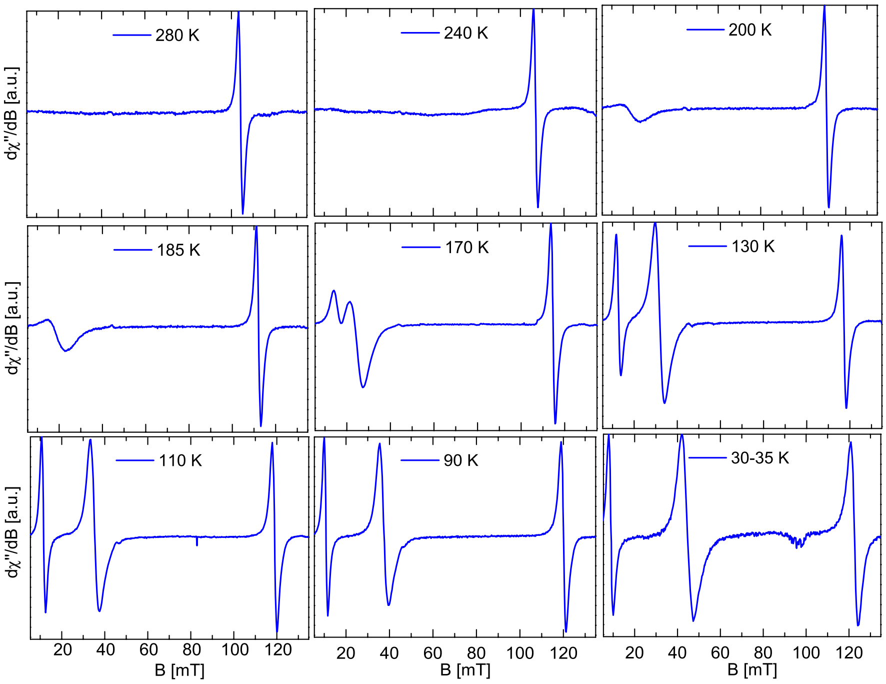

**Figure 4.13.:** Temperature dependence of the FMR spectra of 20 ML Fe on $\{4\times6\}$GaAs(001) recorded at 9.3 GHz with the external field applied along the $[1\bar{1}0]$-direction.

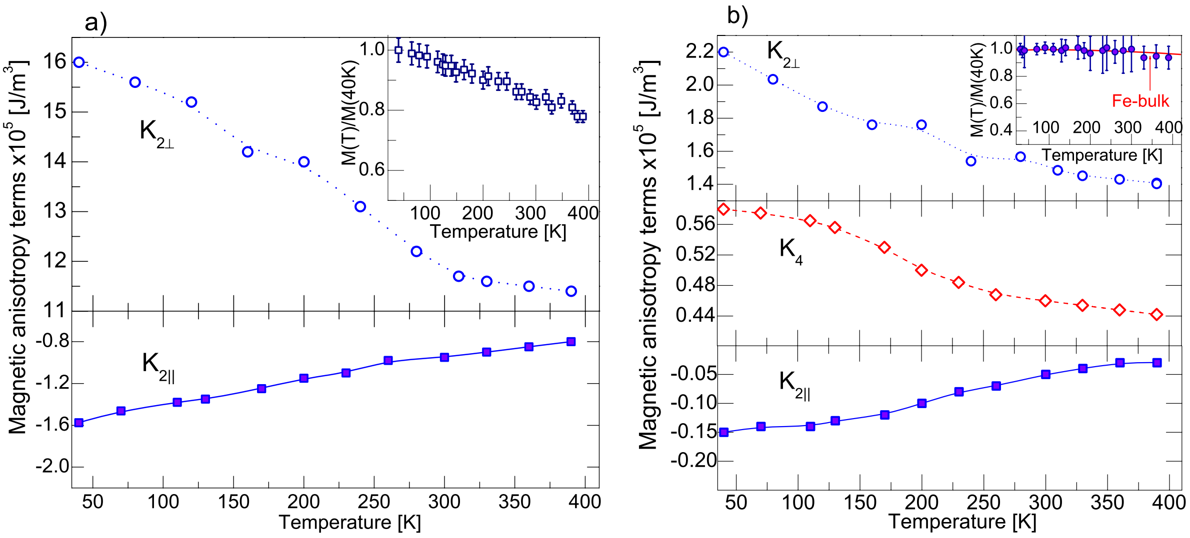

**Figure 4.14.:** Temperature dependence of the magnetic anisotropy ($K_{2\perp}$, $K_{2\|}$, and $K_4$) for (a) 5 ML and (b) 20 ML of uncovered Fe monolayers grown on {4×6}GaAs(001). The insets show the temperature dependence of the magnetization.

anisotropy terms increase. The magnetization curve is shown as inset of Fig. 4.14. It shows the slight increase of the saturation magnetization according to the Bloch law ($\propto T^{3/2}$). The ferromagnetic transition temperature of bulk iron is about 1044 K, that is why even at RT the magnetization is almost fully saturated. Using the temperature dependence of the magnetization data measured by SQUID one can determine the temperature dependence of the absolute value of the anisotropy terms. As supposed in Sec. 4.7.3 the strong uniaxial anisotropy in Fe films on GaAs originates from the interface and is induced by hybridization of the interface electronic states in the first Fe layer and the valence electrons in the surface reconstructed GaAs substrate. Therefore, it is possible that a contraction of interatomic distances, which changes the degree of the metal-substrate hybridization, may also contribute to the temperature dependence of the magnetic anisotropy parameters. This is probably the reason for the strong temperature dependence of $K_{2\|}$ for the 5 ML sample.

## 4.9.1. Temperature dependent correlation of the magnetic anisotropy and magnetization

The correlation between the temperature dependence of the magnetic anisotropy and the magnetization has been described by Callen and Callen [121] and others [122–124] in terms of spin fluctuation theory and random-phase approximation (RPA) [125] considering the spin-orbit interaction as a small perturbation to the exchange coupling for a bulk magnet.

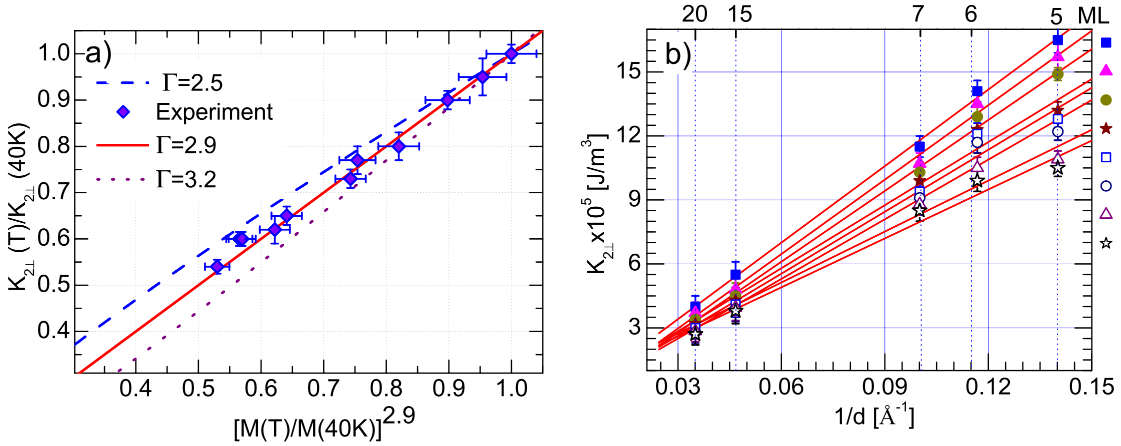

**Figure 4.15.:** (a) Comparison between $K_{2\perp}(T)/K_{2\perp}(40)$ and $(M(T)/M(40))^{2.9}$ for a 5 ML thick film. The solid line is a linear fit with a slope of 1 indicating $\Gamma = 2.9$ confirming the validity of the single-ion anisotropy for Fe films on GaAs. The dashed and dotted lines represent $\Gamma = 2.5$ and $\Gamma = 3.2$, respectively. (b) Temperature and thickness dependence of $K_{2\perp}(T)$ in Fe films on GaAs. The linear fits to the reciprocal thickness dependence of $K_{2\perp}(T)$ yield the surface-interface and volume contributions to $K_{2\perp}(T)$.

Within these theoretical approximations one obtains for the cubic thin film symmetry the anisotropic part of the free energy due to ligand field effects, which can be written as: $\mathrm{F}(\theta,\phi)$=$k_{2\perp}\mathrm{Y}_2^0(\theta,\phi)$+$k_4[\mathrm{Y}_4^0(\theta,\phi)$+ $\mathrm{Y}_4^4(\theta,\phi)$+$\mathrm{Y}_4^{-4}(\theta,\phi)]$+$k_{2\|}[\mathrm{Y}_2^2(\theta,\phi-\delta)$+ $\mathrm{Y}_2^{-2}(\theta,\phi-\delta)]$, where $\mathrm{Y}_l^m$ are spherical harmonics (see appendix A) and the angle $\theta$ $(\phi,\delta)$ is measured with respect to the [001] ([100])-direction. The different anisotropy coefficients $k_i$ and the magnetization $M$ are related by [121]:

$$\frac{k_i(T)}{k_i(0)} \propto \left(\frac{M(T)}{M(0)}\right)^{i(i+1)/2} \tag{4.1}$$

where $i$ represents the order of the spherical harmonic coefficients $k_i$. Within the experimental analysis most authors use an expansion in terms of the direction cosines, i. e. F=$K_{2\perp}\alpha_z^2$+$K_{2\|}\alpha_{[110]}^2$+$K_4(\alpha_x^2\alpha_y^2$+$\alpha_x^2\alpha_z^2$+$\alpha_y^2\alpha_z^2)$ [58], the z-direction being the film normal. By comparing the two different expansions the experimental second and fourth order anisotropy values, $K_{2\perp}$, $K_{2\|}$ and $K_4$—for the [110]-direction (the equilibrium magnetization direction)—are related to the coefficients $k_i$ (see Appendix A for more details). For vanishing in-plane anisotropy terms, one expects an exponent $\Gamma = i(i+1)/2 = 3$ for the experimentally measured uniaxial perpendicular anisotropy term $K_{2\perp}$. In previous experimental works an exponent Γ=2.6(5) for 5.6 monolayer (ML) Fe on Cu(100) [126] and Γ=6.5 for W(110)/Fe 60Å/W(110) [127] was reported. While the value for Fe on Cu(100) shows reasonable agreement with the single-ion anisotropy theory, the large difference in the case of Fe on W(110) remains unclear. An unusual exponent $\Gamma$=2.1 was also reported for bulk like FePt films [128,129] and found to be the result of induced Pt moments leading to a two-ion anisotropy [130]. This result has been confirmed by *ab initio* electronic structure theory for $\mathrm{L1_0}$ ordered FePt [131].

A benefit in the case of Fe/GaAs is that by changing the thickness in the monolayer range one can analyze the influence of different strength contributions of $K_4$, since $K_4$ becomes smaller for thinner Fe layer and vanishes at 6±1 ML (Sec. 4.5). In this section, we will show by independent *in situ* FMR and *in situ* SQUID measurements that the temperature dependence of the experimental out-of-plane uniaxial anisotropy and the magnetization obey the expected power-law only in the case of vanishing $K_4$ that is for 5 ML. In addition, we present the temperature dependence of the effective surface-interface ($K_{2\perp}^{s,\mathrm{eff}}$) and the volume contribution ($K_{2\perp}^{v,\mathrm{eff}}$) of the out-of-plane uniaxial anisotropy constant. The extrapolation to T⟶0 K yields the surface and the volume anisotropy which can be compared to *ab initio* calculations.

The out-of-plane uniaxial anisotropy constant $K_{2\perp}$ was determined from polar angular dependent measurements which were performed at twelve different temperatures between 40 and 400 K for 5, 6, 7, 15, and 20 ML thick films. The anisotropy constants were obtained using Eq. (2.21). Since $K_{2\parallel}$ is one order of magnitude smaller than $K_{2\perp}$ whereas $K_4$ is negligible we do not include the temperature dependence of $K_{2\parallel}$ in the analysis by means of the Callen-Callen's model. Figure 4.15 shows the results of the analysis according to the Callen-Callen's model.

The temperature dependence of $K_{2\perp}$ normalized with respect to its value at 40 K, $K_{2\perp}(T)/K_{2\perp}(40)$, is plotted versus $(M(T)/M(40))^{\Gamma}$ with $\Gamma = 2.9$±0.2 for a 5 ML film. The exponent $\Gamma$=2.9±0.2 is very close to $\Gamma$=3, which is expected according to the Callen-Callen's model [121]. One may note that our direct measurement of $M(T)$ and $K_{2\perp}(T)$ results in a much better accuracy than the indirect determination from the competition of shape and magnetocrystalline anisotropies at the spin reorientation temperature for 5.6 ML Fe on Cu(100) [126]. The temperature dependence of the out-of-plane uniaxial anisotropy for a thicker film (20 ML) is shown in the upper panel of Fig. 4.14 (b). The curvature of the data increases, which indicates the existence of a non-negligible $K_4$ contribution, which becomes stronger as film thickness increases. As mentioned above, an evaluation of a small $K_4$ from the measured out-of-plane angular dependence is not precise enough for a quantitative analysis in terms of a power-law behavior.

Please note that the Callen-Callen model does not identify the microscopic origin of the anisotropy contributions, but includes the contributions from magneto-elastic as well as magnetostrictive properties entering into the spin hamiltonian through the combination of spin-orbit coupling and ligand field splitting.

### 4.9.2. Temperature dependence of the surface-interface & volume contributions

In addition to the analysis of the power-law relation of the magnetization and $K_{2\perp}$ we also determined the temperature dependence of the surface-interface $K_{2\perp}^{s,\text{eff}}$ and the volume $K_{2\perp}^{v}$ contribution to the perpendicular twofold anisotropy according to: $K_{2\perp}(T)$=$K_{2\perp}^{v}(T)+K_{2\perp}^{s,\text{eff}}(T)/d$ [58] in order to obtain an insight into the microscopic origins. As mentioned in Sec. 4.7 $K_{2\perp}^{s,\text{eff}}(T)$ is given by the superposition of the Fe-GaAs interface ($K_{2\perp}^{s,\text{GaAs}}$) and the vacuum-Fe surface anisotropy ($K_{2\perp}^{s,\text{vac}}$). Fig. 4.15 (b) shows the reciprocal thickness dependence of $K_{2\perp}(T)$. A linear fit for each temperature has been performed to separate the anisotropy contributions. The resulting temperature dependence of $K_{2\perp}^{s,\text{eff}}(T)$ and $K_{2\perp}^{v}(T)$ are shown in Fig. 4.16 (a) and (b) respectively. One may note that the magnitude of $K_{2\perp}^{s,\text{eff}}(T)$ increases by a factor of 2 and the one of $K_{2\perp}^{v}(T)$ decreases roughly by a factor of 3 when decreasing the temperature between 300 and 40 K. At RT, $K_{2\perp}^{v}$ has been explained in terms of a magneto-elastic model, (see Sec. 4.7). Its temperature dependent behavior is most likely due to the temperature dependence of the magneto-elastic and the elastic constants. The temperature dependence of the vertical lattice parameter was shown in Fig. 4.3. It was mentioned that this strong temperature dependence of the vertical lattice parameter is likely related to the nature of the strong bonding at the interface, which fixed the in-plane lattice of the Fe to the one of GaAs and also the difference of the thermal expansion coefficients of Fe and GaAs where the one of Fe is two times larger than the one of GaAs [103]. Therefore, it has been assumed that the Fe lattice can be expanded in the vertical direction only. This assumption led us to calculate the temperature dependence of the magneto-elastic contribution to $K_{2\perp}$ according to $K_{2\perp}^{MLE}=\frac{3}{2}B_1\epsilon(T)$ using the $\epsilon(T)$ values measured by IV-LEED (inset of Fig. 4.16(a)) and the value of $B_1=3.5\times10^6$J/m$^3$ reported by Wedler *et al.* [101]. The results are shown as open squares in Fig. 4.16(b), which are in good agreement with the $K_{2\perp}^{v}$ measured by *in situ* FMR.

The temperature dependence of $K_{2\perp}^{s,\text{eff}}$ can be extrapolated to T⟶0 K, yielding $K_{2\perp}^{s,\text{eff}}(T\longrightarrow0)$=(1.26±0.1)×10$^{-3}$ J/m$^2$ (649±51.5 $\mu$eV/atom), and one of $K_{2\perp}^{v}(T\longrightarrow0)$=(4±9)×10$^4$ J/m$^3$ (3±6.7 $\mu$eV/atom). These data allow a correct comparison with *ab initio* (T=0) band structure calculations.

In conclusion the magnetic anisotropy and magnetization of uncapped 5-20 ML Fe films on $\{4\times6\}$GaAs(001) in the temperature range of 40-400 K have been studied using *in situ* FMR and SQUID. The out-of-plane uniaxial anisotropy increases as the temperature decreases and follows the $\left[\frac{M(T)}{M(0)}\right]^{\Gamma}$ power-law with Γ=2.9±0.2 for a 5 ML film. Different temperature dependencies of the surface-interface ($K_{2\perp}^{s,\text{eff}}$) and the volume contribution ($K_{2\perp}^{v}$) are observed. The extrapolation of the temperature dependence of $K_{2\perp}^{s,\text{eff}}$ and $K_{2\perp}^{v}$ yields the surface-interface and volume contributions: $K_{2\perp}^{s,\text{eff}}(T\longrightarrow0)$=(1.26±0.1)×10$^{-3}$ J/m$^2$=649±36 $\mu$eV/atom and

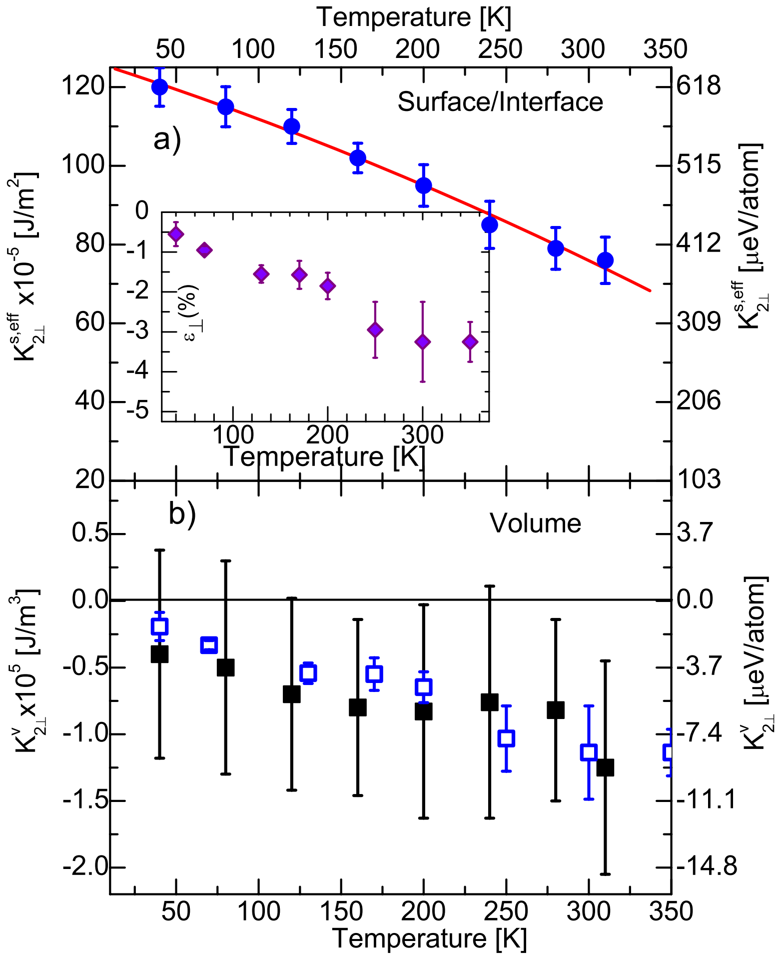

**Figure 4.16.:** Temperature dependence of (a) the effective surface-interface and (b) the volume magnetic anisotropy. The inset shows the perpendicular strain component as a function of temperature. The open squares in (b) are the calculated values of the magneto-elastic contribution to $K_{2\perp}$ according to $K_{2\perp}^{MLE} = \frac{3}{2}B_1\epsilon(T)$ using the measured $\epsilon(T)$ values by means of IV-LEED (inset (a)) and the value of $B_1$ reported by Wedler *et al.* [101] to be $B_1 = 3.5 \times 10^6$J/m$^3$. For $K_{2\perp}^v$ and $K_{2\perp}^{s,\mathrm{eff}}$ the conversion to $\mu$eV/atom is given by 1×10$^5$ J/m$^3$ =7.4 $\mu$eV/atom and 1×10$^{-5}$ J/m$^2$ =5.15 $\mu$eV/atom, respectively.

$K_{2\perp}^v(T \longrightarrow 0)$=(4±9)×10$^4$ J/m$^3$=3±6.7 $\mu$eV/atom, respectively.

## 4.10. Temperature-driven morphological transformation

In this section the results of higher temperatures (between 400 and 650 K) are discussed which were motivated by the study of Shaw *et al.* [132,133]. By employing *ex situ* BLS and polar-

MOKE the authors observed a change in the spin-wave frequency and coercivity in samples capped by 1.5 nm of Al which were annealed at 573 K. The effect was not observed in high temperature grown samples and may be related to the formation of the $Fe_{1.8}Ga_{0.2}As$+$Fe_2As$ alloy, which was observed after annealing a 5 nm Fe film to 723 K [134].

Here, we report on a morphological transformation in uncapped Fe films on GaAs(001), which causes significant changes of magnetic anisotropy fields whereas the magnetization remains unchanged. In extend to the work by Shaw *et al.* [132,133] the complete magnetic, structural, and chemical characterization of uncapped 5 and 10 ML Fe films was performed *in situ* under UHV conditions. The change of the anisotropy constants and the magnetization is quantitatively determined and correlated to the change of the topography, crystal structure and chemical composition observed by STM, LEED, and AES. The morphology and microstructure was studied by *in situ* STM in another UHV-chamber with a base pressure of $1 \times 10^{-10}$ mbar.

The temperature dependent FMR measurements were performed in the following sequence: the sample was cooled down to 40 K and subsequently warmed up to 650 K in steps of 10 K. FMR spectra were recorded at each temperature. In order to check the reversibility of the experiment, the sample was cooled down once more to RT, again in steps of 10 K, at which FMR spectra were recorded.

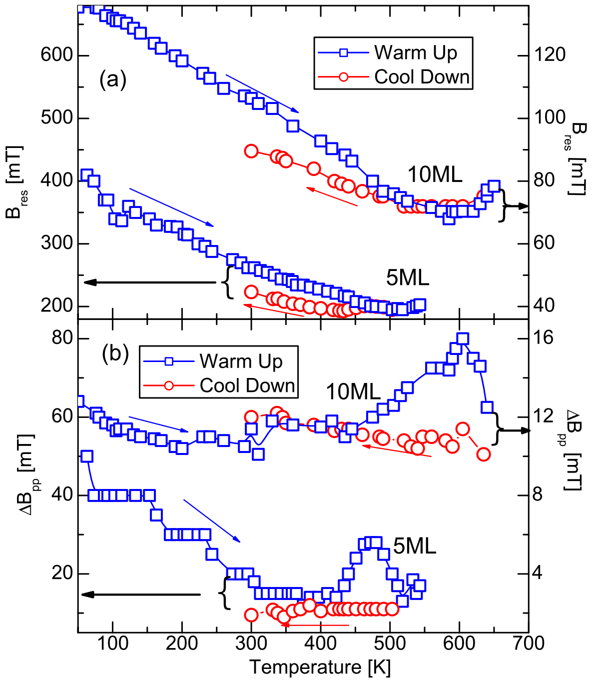

**Figure 4.17.:** The temperature dependence of (a) the FMR resonance field and (b) FMR linewidth for 5 and 10 ML Fe films on GaAs(001). The measurements have been performed at 9.26 GHz with the external magnetic field applied along the $[1\bar{1}0]$-direction. The error bar is smaller than the symbol size.

For all FMR measurements performed *below* a thickness dependent critical temperature the resonance field $B_{res}$ and the linewidth $\Delta B_{pp}$ were the same for cooling and heating cycles. If the samples are heated *above* that critical temperature the FMR resonance fields were irreversible, and a maximum in the temperature dependence of the FMR linewidth was observed. In Fig. 4.17 (a) the temperature dependence of the FMR resonance field $B_{res}$ for the 5 ML and 10 ML sample measured at $f = 9.26$ GHz with an external magnetic field applied along the [1$\bar{1}$0] crystallographic direction is shown. The [1$\bar{1}$0] direction is the hard in-plane axis for Fe films on GaAs(001). The temperature dependence of $B_{res}$ is related to the temperature dependence of the anisotropy constants and the magnetization according to [58,59]:

$$\begin{aligned}\left(\frac{\omega}{\gamma}\right)^2 &= \left\{B_{\mathrm{res}\|}(T) - B_4(T) - B_{2\|}(T)\right\} \times \\ &\times \left\{B_{\mathrm{res}\|}(T) - \mu_0 M_{\mathrm{eff}}(T) + B_4(T)\right\}\end{aligned} \tag{4.2}$$

where $B_i$ $(i = 2, 4)$ are anisotropy fields defined by the corresponding anisotropy constants divided by the magnetization ($B_i = 2K_i/M$). $\mu_0 M_{\mathrm{eff}} = \left(\frac{2K_{2\perp}}{M} - \mu_0 M\right)$ denotes the effective out-of-plane anisotropy field of the sample. The resonance field of the two samples initially decreases with increasing temperature and increases again (Fig. 4.17 (a)) above 500 K (580 K) for the 5 (10) ML film. This behavior can be directly understood from Eq. (4.2). The decrease of the resonance field is due to the decrease of the anisotropy constants, since the magnetization far below the Curie temperature is nearly constant. Above 500 K (for 5 ML) and 580 K (for 10 ML) the temperature dependence of the magnetization overcomes the temperature dependence of the anisotropy constants and the resonance field increases again as described in Sec. 4.9. Finally, at the Curie temperature ($T = T_C \gg 600$ K) the anisotropy fields would vanish ($B_i = \mu_0 M_{\mathrm{eff}} = 0$), which in turn yields $B_{res} = \frac{\omega}{\gamma} = 330.7$ mT, being the so-called *'isotropic resonance field'*. The decrease of $B_{res}$ from low temperatures to a minimum at $T_{min} \simeq 500$ K for the 5 ML thick sample and $T_{min} \simeq 580$ K for the 10 ML one is due to the temperature dependence of the magnetic anisotropy and can be quantitatively reproduced by Eq. (4.3) as has been discussed in Sec. 4.9. When the films are cooled down to RT (open circles) again, the resonance fields (Fig. 4.17(a)) and also the linewidths (Fig. 4.17 (b)) strongly deviate from their initial values (open squares) indicating that the anisotropy fields and the homogeneity of the structure have changed irreversibly.

For both films we observe an initial reduction of $\Delta B_{pp}$ with increasing temperature followed by a peak-like maximum at 480 K for the 5 ML and 610 K for the 10 ML thick sample. In general, $\Delta B_{pp}$ of films with magnetic inhomogeneities show a larger linewidth than magnetically homogeneous films of the same material [135]. Consequently, the peak of $\Delta B_{pp}$ suggests a transformation of the film's morphology and microstructure and the reduced $\Delta B_{pp}$ for the 5 ML sample at lower temperatures an improved magnetic homogeneity after the annealing step.

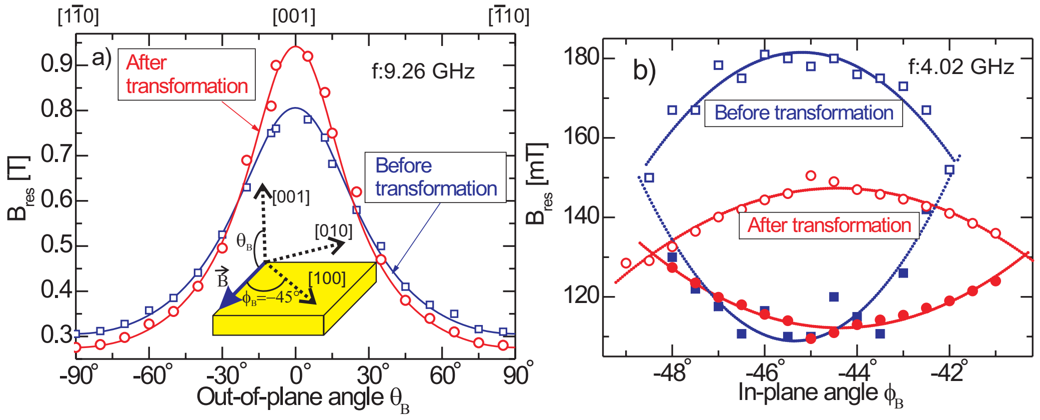

**Figure 4.18.:** Polar (a) and azimuthal (b) angular dependence of the resonance field of a 5 ML Fe film on GaAs before and after the transformation. The open and closed symbols in (b) represent the saturated and unsaturated resonance modes. Both measurements were carried out at RT. The inset of (a) shows the coordinate system used in our FMR measurements and data analysis.

In order to quantify the anisotropy fields for both films, angle dependent FMR measurements with the magnetic field applied at polar angles $-90^\circ \leq \theta_B \leq 90^\circ$ within the (1$\bar{1}$0) plane (see the inset of Fig. 4.18) were performed at 9.26 GHz. The in-plane angle was varied within the range -48° $\leq\phi_B\leq$-42° with respect to the [100]-direction and FMR spectra were recorded at 4.02 GHz. In Fig. 4.18 the polar and azimuthal angular dependencies of the resonance field at RT before and after the transformation are plotted for the 5 ML thick sample. The absolute value of the saturation magnetization $M$ (see Eq. (4.3)) was determined by *in situ* HTS-SQUID measurements at RT before and after this transformation. Interestingly, the RT value of the magnetization does not change even when the sample is warmed up to higher values than the critical temperature (transformation temperature) and cooled down again to RT. The anisotropy fields were calculated according to the resonance equations (Eqs. (2.21) and (2.22)).

The room temperature magnetic anisotropy constants as well as the magnetization values are listed in Tab. 4.3. The cubic anisotropy is enhanced by a factor of 2 for the 10 ML sample and by a factor of 5 for the 5 ML one after the temperature-driven transformation. The in- and out of-plane uniaxial anisotropy for both films decreased by about 20% and 10%, respectively.

The effect of annealing on the morphology of the Fe layers was studied by STM. The films were annealed for 10 minutes at different temperatures and imaged by STM at RT. Figure 4.19 shows a typical STM image after heating the iron film to 670 K. The inset shows the morphology at RT with typical cluster sizes of 4 nm. The transition proceeds in a first step by island coalescence forming a nearly closed iron layer. In a second step at a slightly higher temperature the continuous layer breaks up into larger rectangular islands (type A in Fig. 4.19) and smaller islands with an oval shape and a diameter of roughly 15 nm (type B in Fig. 4.19).

| | Thickness<br>(ML) | $K_{2\perp}$<br>($10^5$J/m$^3$) | $K_4$<br>($10^5$J/m$^3$) | $K_{2\parallel}$<br>($10^5$J/m$^3$) | $M$<br>($10^6$A/m) |
|---|---|---|---|---|---|
| before | 10±0.5 | 6.0 | 0.15 | -0.55 | 1.7 |
| after | 10±0.5 | 4.4 | 0.32 | -0.41 | 1.7 |
| before | 5±0.5 | 11.1 | 0.04 | -1.20 | 1.5 |
| after | 5±0.5 | 9.8 | 0.20 | -1.00 | 1.5 |

**Table 4.3.:** Room temperature magnetic anisotropy constants of Fe on GaAs(100) before and after the morphological transformation. The error bar of the magnetic anisotropy parameter is $0.05 \times 10^5$ J/m$^3$.

The large rectangular islands form mesas with a height of 4-5 nm and a width of several hundred nanometers. The oval islands (type B) are embedded in the substrate surface. Due to the much larger magnetic volume of the type A islands, they dominate the magnetic behavior of the Fe film. The directions of the edges of island type A are along [110] and [$1\bar{1}0$], where an elongation along [$1\bar{1}0$] seems to be present. The effect of the morphology change can be seen clearly at annealing temperatures above 580 K. Moreover, the type A islands show a surface reconstruction which results from Gallium segregation (see below).

In the following we will discuss the possible sources of the change in the anisotropy values based on our structural investigation together with the compositional and morphological

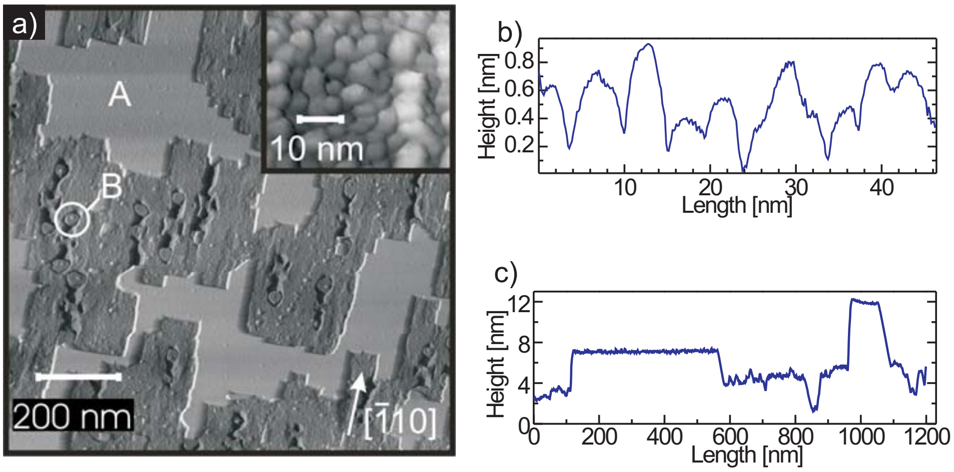

**Figure 4.19.:** (a) Room temperature STM image of a 5 ML Fe/GaAs(001) after heating up to 670 K showing big, flat, rectangular Fe islands (marked as A) as well as small oval islands, which are embedded into the surface (marked as B). The inset shows the morphology of the typical 3D-cluster-like Fe growth on GaAs(001) at RT before the transformation. (b) and (c) are the typical line scans of the structures before and after the transformation respectively. Tunnelling current and bias voltage were 25 pA, and 2.4 V. Images were recorded by C. Urban.

characterization of the films.

The enhancement of the cubic anisotropy during the transformation can be explained by the fact that the formation of the rectangular island (type A in Fig.4.19) leads to a development of defined island edges along the [110]- and [1$\bar{1}$0]-direction. In addition, the cubic structural order within these islands increases as evidenced by the observation of a sharper LEED pattern. At the same time the Auger peak-to-peak ratio of the Ga MLL transition to the Fe LMM transition increases indicating that the Fe film has broken up exposing large GaAs areas to the electron beam. As a result the enhancement of the cubic anisotropy could result also from the segregation of the substrate materials on the surface (most likely Ga) which has direct impact on the surface-interface contribution of the cubic anisotropy. As the surface contribution for the Fe/GaAs(001) system was found to have the opposite sign compared to the volume part [62], the enhanced overall cubic anisotropy could thus be related to a reduction of its surface-interface contribution. From the enhanced Ga AES intensity we conclude that a Ga segregation towards the film surface seems to be a probable source for the surface anisotropy modification.

The in-plane uniaxial anisotropy is reduced after the transformation (see column 5 of Tab. 4.3). Since the in-plane uniaxial anisotropy results mostly from the interface properties [8,62], the decrease of the in-plane uniaxial anisotropy $K_{2\|}$ could also be the result of the Ga segregation that was evidenced by our AES study. XPS measurements by Shaw *et al.* [132,133] show that more Ga had reacted with Fe in annealed samples at 573 K, thus confirming this scenario. Another source for the reduced value of $K_{2\|}$ is found from the STM images that show that the rectangular Fe islands are mostly elongated along the [1$\bar{1}$0]-direction (see Fig. 4.19). Consequently, this particular direction has a geometrical preference over other directions after the morphological transformation. As the [110]-direction was found to be the easy axis of $K_{2\|}$ in as-prepared Fe/GaAs(001) films (see [62] and references therein for details), the anisotropic island shape favors the [1$\bar{1}$0]-direction and might weaken the uniaxial anisotropy further. A change in the film strain can be ruled out since our IV-LEED experiment shows that the interlayer distance does not change during the transformation. Therefore, the part of $K_{2\|}$ caused by stress at the interface is almost unaffected during the transformation. This confirms our previous explanation of the origin of $K_{2\|}$ using a magneto-elastic model *and* a hybridization at the interface [62]. The magneto-elastic contribution to $K_{2\|}$ does not change according to our IV-LEED strain analysis. The change of the uniaxial in-plane anisotropy must therefore be due to the changes of the electronic structure at the interface along preferential crystallographic directions.

The IV-LEED result also leads to the conclusion that the reduction of the perpendicular uniaxial anisotropy $K_{2\perp}$ must be due to a reduction of its surface contribution, since its volume contribution, being much smaller, was found to result exclusively from in-plane stress in the film (see Sec. 4.7). The change in the surface contribution to $K_{2\perp}$ could either be the result of the Ga segregation or of a change in the surface roughness as observed in our STM images (Fig. 4.19). Such a morphological influence, i.e. the change of the surface roughness, on the perpendicular magnetic anisotropy of ferromagnetic layers on metallic substrates was already reported previously [136,137]. Theoretically, the roughness has two effects on the perpendicular surface anisotropy: (i) *dipolar anisotropy* and (ii) *magnetocrystalline step anisotropy* [138]. The roughness creates in-plane demagnetizing fields at the edges of the terraces, thereby reducing the shape anisotropy and favoring a perpendicular magnetization direction. The magnitude of this effect can be calculated using our experimentally determined roughness parameter $\sigma$ and the lateral correlation length $\xi$:

$$K_s = E_{\text{Shape}} \cdot \frac{3}{4} \cdot \sigma \{1 - f[2\pi(\frac{\sigma}{\xi})]\} \tag{4.3}$$

$E_{\text{Shape}} = \frac{1}{2}\mu_0 M^2$ is the shape anisotropy. The function $f[2\pi(\frac{\sigma}{\xi})]$ is defined in Ref. [138] and becomes 1 if $\frac{\sigma}{\xi} \longrightarrow 0$ (for a very smooth surface) and $\sim 0.1$ if $\frac{\sigma}{\xi} \longrightarrow 1$ (for a surface with a roughness parameter being of the order of the lateral correlation length). The SQUID data yield the same value $E_{\text{Shape}} = 14.13 \times 10^5$J/m$^3$ before and after the transformation, i.e. no change of the magnetization itself is observed. Our STM images show a roughness parameter of $\sigma_{\text{before}}$=0.6 nm and a correlation length of $\xi_{\text{before}}$=7 nm ($\frac{\sigma}{\xi} \simeq 0.85$) for the 5 ML sample before the transformation, which are changed to $\sigma_{\text{after}}$ =4 nm, $\xi_{\text{after}}$ =500 nm after the transformation ($\frac{\sigma}{\xi} \simeq 0.99$). This means that the surface becomes smoother after the transformation, yielding a reduction of the surface contribution to the perpendicular magnetic anisotropy of about $\Delta K^s_{2\perp} = 0.953 \times 10^{-4}$ J/m$^2$. Correspondingly, the total perpendicular anisotropy is reduced by about $\Delta K_{2\perp} = 1.34 \times 10^5$ J/m$^3$, which is about the value determined by our FMR experiments. Using the pair interaction model, Bruno [139] showed that steps reduce the surface magnetocrystalline anisotropy. The reduction for a simple cubic (100) surface is given by $-2\sigma/\xi$. In our case this origin is of minor importance because our films become smoother after the transformation. We conclude that the reduction of $K_{2\perp}$ is mainly due to the annihilation of in-plane demagnetizing fields at the edges of terraces, thereby increasing the shape anisotropy and consequently, reducing $K_{2\perp}$.

In conclusion, the change in the magnetic parameters of 5 and 10 ML of Fe grown on GaAs(001) caused by a temperature induced morphological transformation has been studied by means of *in situ* FMR and *in situ* SQUID magnetometry. The structure and chemical composition of the films have been investigated using *in situ* STM, (IV)-LEED and AES. The morphological change is accompanied by a drastic change of the magnetic anisotropy, whereas the saturation magnetization is found to remain almost unaffected. The change in magnetic anisotropy is quantitatively explained by the observed changes of the structure, morphology and the chemical composition of the films.

## 4.11. The effect of an Ag over-layers on the magnetic anisotropy

The surface magnetic moment and the magnetic anisotropy of Fe monolayers on W(011) have been investigated by Elmers [140,141]. Interestingly, no significant changes of the surface magnetic moment and the surface anisotropy of Fe/W(011) were observed when covering with Ag. The magnetic surface anisotropy of vacuum/Fe(001) thin films has been reported to be larger than the other interfaces (i.e. Ag/Fe(100), Au/Fe(100), Cu/Fe(100)) [106,114] meaning that the existence of the cover layers on Fe(001) surface decrease the surface anisotropy. In order to study the effect of the over-layers on the magnetic anisotropy of Fe/GaAs, FMR experiments were carried out before and after deposition of different layers of Ag ranging from 1 to 5 ML. All measurements were performed *in situ*. The FMR signal of the 2.8 ML thick sample disappeared when one ML of Ag was deposited. The temperature dependent measurements on this sample show that the Curie temperature is reduced to about $T_c$=195 K. The ferromagnetic signal reappears for 1 ML Ag/Fe/GaAs at RT only for Fe films thicker than 3.1 ML. The reduction of the Curie temperature in the presence of the Ag over-layer most likely results from a change of the electronic band structure of the Fe film due to the presence of Ag atoms (either on top or inside the Fe film). A change of the band structure would in turn change the magnetic moments, the magnetic anisotropy, and/or the exchange interaction between the Fe atoms. All these quantities are strongly related to the Curie temperature so that a change of its value due to Ag is very likely. However, theoretical support is needed to verify this scenario. Furthermore, it was found that the FMR resonance field shifts to lower fields as the first layer of Ag is deposited meaning that mainly the first layer of Ag changes the anisotropy terms. In order to quantitatively determine the change of the magnetic anisotropy in the presence of the Ag over-layer, the magnetic anisotropy was studied for four different thicknesses of Fe layers (4, 10, 20, and 30 ML) and the results are summarized in Tab. 4.4.

Figure 4.20 shows the magnetic anisotropy constants as a function of Ag over-layer indicating that the most prominent change happens when the first ML of Ag is added. This behavior can be understood from the fact that Fe and Ag are immiscible in the bulk. The change of $K_{2\perp}$ is due to a change of the surface contribution to $K_{2\perp}$, which was found to mainly result from the Fe/vacuum interface (see Sec. 4.7). In the following we discuss the change of the anisotropy terms in the presence of Ag.

As the first atomic layer of Ag is deposited, $K_{2\parallel}$ is changed by about 10% for a 4 ML thick Fe layer while it remains unchanged up to a 20 ML thick Fe layer. This clearly indicates the Fe/GaAs-interface nature of $K_{2\parallel}$ as discussed in Sec. 4.7.3.

A change of the cubic anisotropy ($K_4$) is observed for all Fe thicknesses, i.e., volume and surface contribution to $K_4$ are affected due to the presence of Ag. We propose that a change of

| Investigated Systems | $K_{2\perp}$ ($10^5$J/m$^3$) | $K_4$ ($10^5$J/m$^3$) | $K_{2\parallel}$ ($10^5$J/m$^3$) | $\frac{\mu_0 M_{\mathrm{eff}}}{2}$ (mT) | $\frac{K_4}{M}$ (mT) | $\frac{K_{2\parallel}}{M}$ (mT) |
|---|---|---|---|---|---|---|
| 1 Ag/30 Fe/{4×6}GaAs | 0.8 | 0.46 | -0.04 | -1021 | 27 | 2.35 |
| 2 Ag/30 Fe/{4×6}GaAs | 0.8 | 0.46 | -0.04 | -1021 | 27 | 2.35 |
| 5 Ag/30 Fe/{4×6}GaAs | 0.8 | 0.46 | -0.04 | -1021 | 27 | 2.35 |
| 1 Ag/20 Fe/{4×6}GaAs | 1.5 | 0.4 | -0.05 | -980 | 23.5 | 2.35 |
| 2 Ag/20 Fe/{4×6}GaAs | 1.4 | 0.38 | -0.05 | -985 | 22.4 | 2.35 |
| 5 Ag/20 Fe/{4×6}GaAs | 1.3 | 0.35 | -0.05 | -991 | 20.1 | 2.35 |
| 1 Ag/10 Fe/{4×6}GaAs | 4.7 | 0.16 | -0.58 | -790 | 9.4 | 33.53 |
| 2 Ag/10 Fe/{4×6}GaAs | 4.6 | 0.14 | -0.55 | -798 | 8.24 | 32.35 |
| 5 Ag/10 Fe/{4×6}GaAs | 4.5 | 0.13 | -0.55 | -803 | 7.65 | 32.35 |
| 1 Ag/ 4 Fe/{4×6}GaAs | 10.7 | -0.04 | -1.15 | -386 | -2.35 | 67.7 |
| 2 Ag/ 4 Fe/{4×6}GaAs | 10.4 | -0.07 | -1.1 | -398 | -4.12 | 64.7 |
| 5 Ag/ 4 Fe/{4×6}GaAs | 10.3 | -0.07 | -1.1 | -398 | -4.12 | 64.7 |

**Table 4.4.:** The measured magnetocrystalline anisotropy constants of Fe monolayers in Ag/Fe/{4×6} GaAs(100) structures for different numbers of Fe and Ag layers. The integers in the first column denote the number of monolayers. All samples are measured *in situ* and at RT. The conversion to $\mu$eV/atom can be given by $1\times10^5$ J/m$^3$ =7.4 $\mu$eV/atom.

the density of states of the Fe is the reason for the slight change of the volume contribution to the cubic anisotropy. The relative change of $K_4$ is, however, largest for the 4 ML Fe film. This implies that the influence on the surface contribution is the dominating one.

## 4.12. Frequency dependent measurements and g-factor

Now we turn to the frequency dependent results. Figure 4.21 shows the resonance frequency as a function of the resonance field for the magnetic field applied along the [1$\bar{1}$0]-direction. The solid, pointed, and dashed lines show the dispersion relation (2.23), for 5, 15, and 20 ML uncapped samples. The magnetic anisotropy constants of Tab. 4.1 were used to simulate the dispersion relation. The experimental data points (symbols) fall onto the fit curves as expected. At 9.3 GHz the low field (unsaturated) resonance of 5 ML film cannot be excited due to the relative high in-plane uniaxial anisotropy. While the open squares represent the measurements at 4 GHz (S-band), the full circles and diamonds show the measurements at 9.3 GHz (X-band) and 24 GHz (K-band). The point at $f = 24$ GHz was obtained for a 20 ML Ag capped Fe film

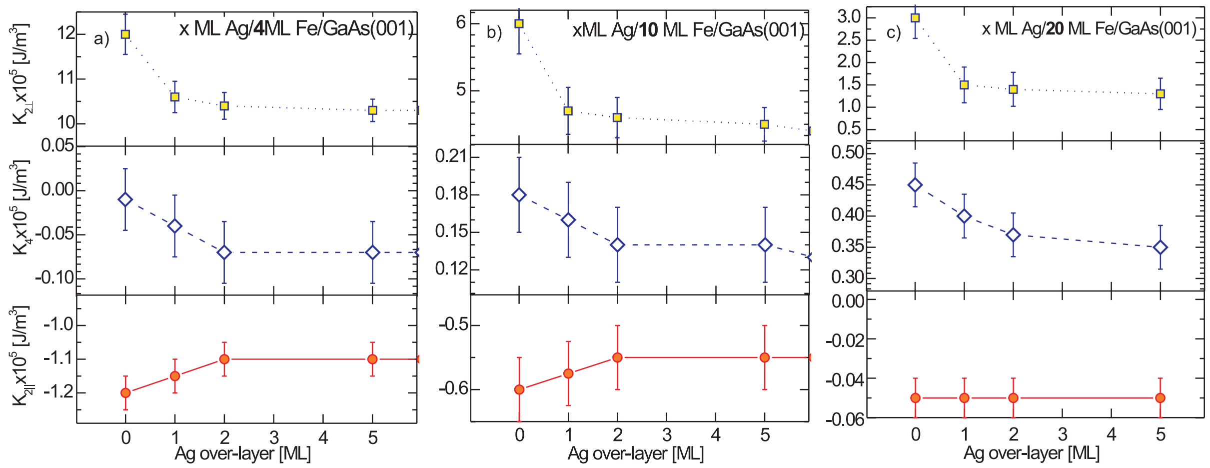

**Figure 4.20.:** The magnetic anisotropy terms as a function of the thickness of the Ag over-layer. (a) 4 ML (b) 10 ML and (c) 20 ML Fe grown on {4×6}GaAs(001).

which has been measured *ex situ*.

As described in Sec. 2.3 the frequency dependence of the FMR resonance field can be used to determine the $g$-factor. Since the deviation of the $g$-factor from the free electron value ($g_{\text{electron}} = 2.0023$) is usually very small, a frequency dependent measurement over a wide

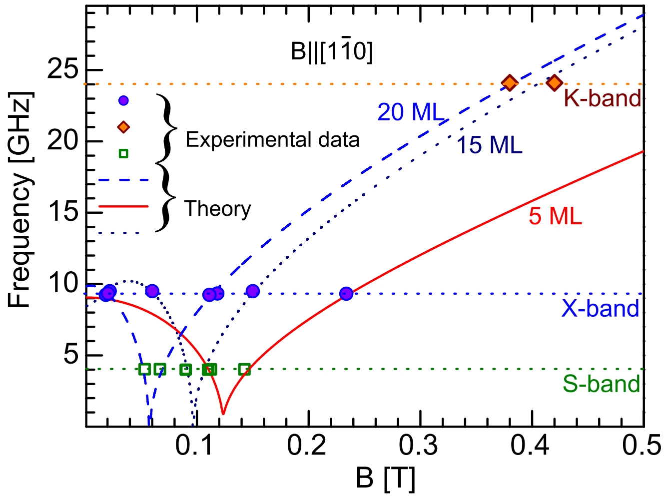

**Figure 4.21.:** Dispersion relation for 5, 15, and 20 ML Fe films on {4×6}GaAs(001) using the magnetic anisotropy constants of Tab. 4.1 in Eq. (2.23). The external magnetic field is applied along the [$\bar{1}$10]-direction. The points near 24 GHz for 15 and 20 ML films are measured *ex situ* for samples capped with 3 nm Ag.

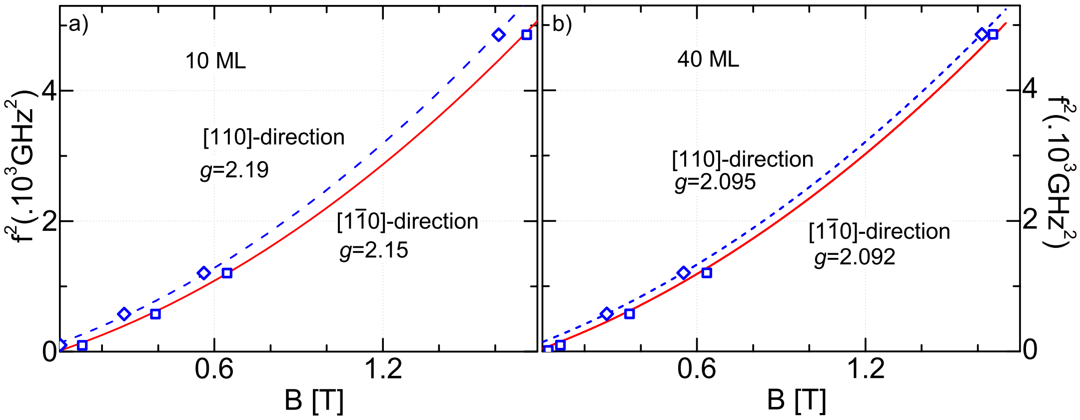

**Figure 4.22.:** The square of the resonance frequency versus the resonance field. The solid and dashed lines are fits according to Eq. (2.23).

range of microwave frequencies is needed. The $g$-factor of the 10 and 40 ML thick samples was measured by performing a frequency dependent measurement in the frequency range of 1-70 GHz.

In Fig. 4.22, the square of the frequency versus resonance field is plotted and fitted according to Eqs. (2.23) and (2.24). In the case of the 40 ML sample the $g$-factor is very close to the Fe-bulk value ($g = 2.09$); for the 10 ML sample the $g$-factor is enhanced ($g = 2.19 \pm 0.05$).

The enhanced $g$-factor indicates an increased orbital moment. According to Kittel's formula the deviation of the $g$-factor from the free electron value in 3d elements can be written as [58]

$$g - 2 = 2\left(\frac{\mu_L}{\mu_S}\right) \tag{4.4}$$

where $\mu_S$ and $\mu_L$ are spin and orbital moments respectively. We note that Kittel's formula is valid only for the small value of $\mu_L/\mu_S$ but for the large value, it should be modified. However, it yields the lower limit of $\mu_L/\mu_S$. Therefore, we were led to approximate $\mu_L/\mu_S$ with lower limit using Kittel's formula (4.4). This results in a ratio of orbital to spin moment of $\mu_L/\mu_S = 0.095 \pm 0.02$ for the 10 ML sample. This means that the orbital moment is enhanced by more than 200% whereas the spin moment is found to be unchanged and very close to the bulk value (see Fig. 4.10). We conclude that this enhancement is related to the individual properties of the Fe/GaAs interface. Fully relativistic band structure calculations showed that the 3% distortion of the Fe lattice does not affect the orbital and spin moment and consequently the $g$-factor [142]. Therefore, a strain induced change of the $g$-factor can be ruled out. Our results are in good agreement with the observation of the enhanced orbital moment measured by X-ray magnetic circular dichroism (XMCD) [143]. The authors have found a ratio of $\mu_L/\mu_S = 0.117 \pm 0.011$ for 8 ML Fe/GaAs(001) [143]. They suggested that the enhanced orbital moment is due to an increased electron localization of the Fe atoms at the interface in contact with Ga (or As) atoms.

## 4.13. Summary

A detailed study of the growth and *in situ* magnetic characterization of Fe monolayers was presented. The magnetic anisotropy and the magnetization were determined in absolute units and the origin of the different anisotropy contributions was ascribed to be the effect of magneto-elastic anisotropy. A magneto-elastic model was employed to explain the anisotropy contributions using the direct stress components measured *in situ* by IV-LEED.

The temperature dependence of the different anisotropy contributions was determined and the power-law relation between the temperature dependence of the perpendicular magnetic anisotropy and the magnetization was investigated, which reveals that the single-ion magnetic anisotropy is the dominating microscopic origin in the ultrathin magnetic structure. It was found that the perpendicular magnetic anisotropy (similar to the cubic magnetic anisotropy) obeys the single-ion-anisotropy model. Moreover, the temperature dependence of each anisotropy contribution was determined and extrapolated to zero Kelvin, which allows quantitative comparison with first principle calculations.

It was observed that the Fe films exhibit a temperature-driven morphological transformation occurring at temperatures higher than 550 K depending on the film thickness. During this transformation the cubic anisotropy increases by a factor of more than 2, while the perpendicular and in-plane uniaxial anisotropies decrease by about 15 and 10%, only.

The effect of a Ag over-layer (1–5 and 30 ML) was studied. It was demonstrated that a single layer of Ag increases the critical thickness for the onset of ferromagnetism from 2.8 ML Fe/GaAs to 3.1 ML for 1 ML Ag/Fe/GaAs at room temperature. This can be related to the suppression of the surface contribution to the perpendicular magnetic anisotropy by about 20%. The Ag capping has only minor effects on the in-plane magnetic anisotropy.

Finally, an enhanced orbital moment for thinner Fe layers on GaAs was observed, which is attributed to the nature of the Fe-GaAs interface and the enhanced spin-orbit coupling of the Fe atoms at the interface.

# 5. Fe monolayers on Ag/GaAs(001)

*In this chapter the experimental results of the in situ FMR experiments of ultrathin Fe films grown on {4×6} reconstructed GaAs(001) with a buffer layer of silver will be presented. The role of the silver buffer layer is to modify the interface stability and also the magnetic behavior at the interface. while the interface uniaxial in-plane anisotropy decreases as the thickness of the Ag buffer layer increases, no significant change is observed for other anisotropy terms.*

## 5.1. Introduction

Control of the interface is the key for *'spintronics'*. The spin injection efficiencies reported for Fe/GaAs [1] as well as for Fe/AlGaAs (up to 32% at 4.5K) [144] are lower than for all semiconductor structures at low temperatures. A significant increase in spin injection efficiency can be achieved by optimizing the interface structure. For example, it has been shown that for the case of Fe/AlGaAs structures a decrease in interface roughness significantly increases the spin injection efficiency [144]. In order to get an insight into this issue the magnetic parameters of Fe films grown on Ag buffer layers of varying thickness were studied. It is well-known that the Ag/GaAs interface is thermodynamically more stable than the Fe/GaAs interface [17]. Furthermore, the Ag/Fe(100) interface has been predicted to have a strong spin dependence of the interface resistance and should therefore be a good polarizer [18]. Consequently, a strong spin transfer effect can be expected in systems with an Fe/Ag interface [19]. The only problem, which arises, is the formation of electrical shunts due to the Ag layer. This can be prevented if the chosen buffer layer is thin enough (1-5 ML) [17]. The thickness of the Fe film was chosen to be 10 ML and the thickness of the Ag layer was varied.

## 5.2. Sample preparation

The substrate preparation for this structure follows the procedure, which has been reported in Sec. 4.2.1. The growth of Fe/Ag/{4×6}GaAs(001) is shortly reviewed below.

### 5.2.1. Growth of Ag on GaAs

The Ag buffer layers were grown in thicknesses of 1, 2, and 5 ML at RT with a deposition rate of 0.8 ML/min. The pressure rises during evaporation to about $1.0 \times 10^{-9}$ mbar while Ag was evaporated from a molybdenum crucible. A LEED experiment was carried out immediately after the growth. The substrate LEED pattern disappears after the deposition of the first atomic layer of Ag. No LEED pattern was observed for 1 and 2 ML Ag. A quadratic LEED pattern was observed for a 5 ML Ag film (see Fig. 5.1 (b)).

While the LEED patterns of bcc and fcc structures are not directly distinguishable, we were performed an IV-LEED experiment in order to obtain an insight into the structure of the Ag layer. The IV-LEED data are shown in Fig 5.1 indicating an fcc structure with a lattice parameter close to Ag-bulk. Furthermore, the crystallographic axes of Ag are rotated by 45° with respect to the ones of the substrate. Bulk-Ag with fcc structure has a lattice parameter of 0.409 nm whereas the one of GaAs is 0.5654 nm and one would expect a rotation of the crystallographic axes. A schematic illustration of growth relationship in Ag/GaAs is shown in Fig. 5.2.

The AES data show that LMM peaks of the Ga (As) disappear after deposition of a 2 ML Ag, confirming no out-diffusion of the Ga(As). This observation is also a confirmation that the Ag/GaAs interface is thermodynamically more stable than the Fe/GaAs interface.

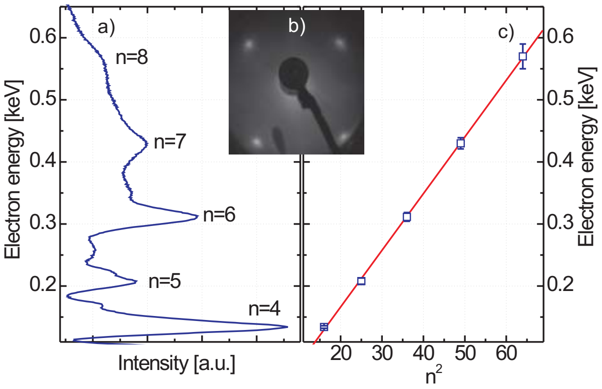

**Figure 5.1.:** (a) A typical Bragg reflection observed for 5 ML Ag/GaAs. The integers show the order of the Bragg peaks. (b) LEED-pattern recorded at an electron energy of 117 eV. (c) The energy of Bragg peak position as a function of the square of the order of the Bragg peak positions. The solid line is the best linear fit to the experimental data. The slope of the linear fit directly yields the vertical layer spacing. The measurements are performed at RT.

### 5.2.2. Growth of Fe/Ag bilayer structures

A 10 ML Fe film was deposited directly onto Ag/GaAs with a deposition rate of 1 ML/min at RT. The sample was immediately characterized by LEED and AES indicating a well-ordered bcc structure. In Fig. 5.2 a schematic illustration of the growth relationship of Fe/Ag/GaAs(001) structure is shown. Although the Ag lattice is rotated by 45° with respect to the GaAs lattice the Fe lattice is parallel to the one of GaAs.

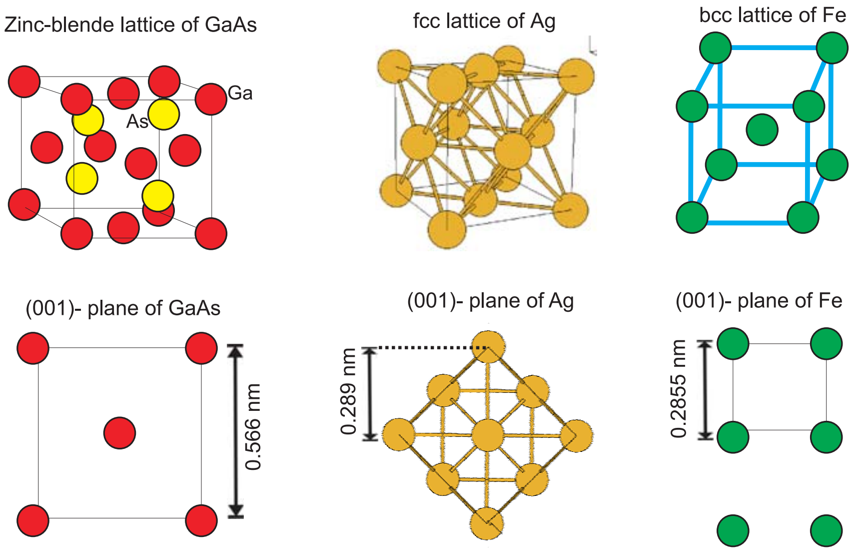

**Figure 5.2.:** A schematic illustration of the substrate and over-layer lattice structure in Fe/Ag/GaAs. The upper parts show the bulk structure whereas the lower parts show the atomic structure of the (001)-plane. The unit cells are shown as rectangles.

## 5.3. The effect of the Ag buffer layer on the magnetic anisotropy

In Fig. 5.3 the FMR dispersion relation of 10 ML Fe/Ag/{4×6}GaAs for different thicknesses of Ag buffer layers is plotted. The resonance field moves to lower fields as the thickness of the Ag buffer layer increases indicating a change in the magnetic anisotropy constants.

The magnetic anisotropy of the 10 ML Fe/Ag/{4×6}GaAs was determined by performing polar and azimuthal angle dependent measurements of the resonance field as discussed in Sec. 2.3.

Fig. 5.4 shows the magnetic anisotropy of 10 ML Fe/Ag/{4×6}GaAs structure as a function of the Ag buffer layers. Interestingly, only $K_{2\|}$, is affected by the Ag buffer layer. This again indicates that the uniaxial anisotropy is an interfacial effect as described in Sec. 4.7.3. A single layer of Ag suppresses $K_{2\|}$ by 15%. This effect becomes stronger as the thickness of Ag buffer

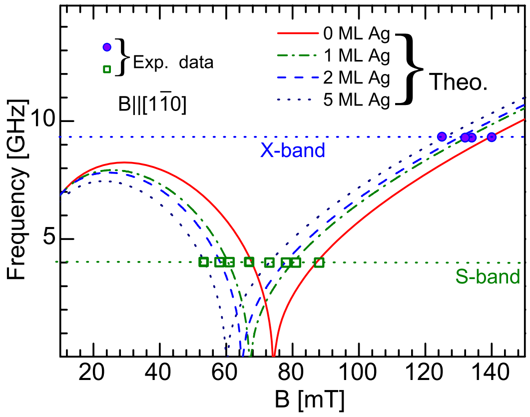

**Figure 5.3.:** The resonance frequency as a function of the resonance field of 10 ML Fe/Ag/{4×6}GaAs for different thicknesses of the Ag buffer layer at RT.

layer increases. $K_{2\|}$ for a sample with 5 ML Ag buffer layer, is reduced by approximately 25% with respect the samples without buffer layer.

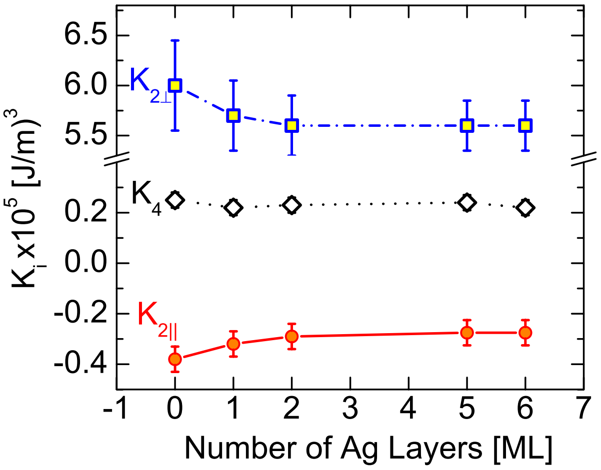

**Figure 5.4.:** The magnetic anisotropy constant of 10 ML Fe in Fe/Ag/{4×6}GaAs layered structure as a function of the Ag buffer layer.

## 5.4. Summary

In summary, the magnetic anisotropy of Fe layers grown on 1, 2, and 5 ML thick Ag buffer layers of were studied. The Ag/GaAs interface is thermodynamically more stable than the Fe/GaAs interface. A rotation of the crystallographic axes of the Ag buffer layer with respect to the ones of the GaAs substrate was found. A single atomic layer of Ag decreases $K_{2\|}$ by almost 15%. This effect becomes stronger as the thickness of the Ag layer increases; for example a 5 ML

Ag layer reduces the in-plane uniaxial anisotropy by about 25%. It is interesting to notice that the other anisotropy contributions are just slightly affected by the existence of the Ag layer, again due to the FM/SC interface nature of $K_{2\|}$. Our investigation demonstrates that this kind of structure has, in principle, the capability to be used in future spintronic devices while the thickness of the buffer layer is thin enough to prevent the electrical shunts.

# 6. Fe monolayers on InAs(001)

*In this chapter the experimental results of the in situ FMR experiments of Fe monolayers (3–30 ML) grown on* $\{4 \times 2\}$ *reconstructed InAs(001) are presented. It is observed that both surface-interface and volume contributions to the perpendicular magnetic anisotropy favor an easy axis perpendicular to the film plane. The cubic surface-interface anisotropy is relatively large with an easy axis along the* $\langle 1\bar{1}0\rangle$*-directions in contrast to the volume contribution, which favors an easy axis along the* $\langle 110\rangle$*-directions. The volume contribution is found to be larger than the Fe bulk cubic anisotropy. A thickness independent uniaxial anisotropy was found for all films. The volume contributions to the uniaxial in- and out-of-plane, as well as cubic anisotropy are ascribed to be the effect of magneto-elastic anisotropy.*

## 6.1. Introduction

Another candidate for *'spintronics'* is the Fe/InAs(100) structure. InAs has a narrow band-gap (less than 0.4 eV), which makes Fe/InAs an ideal ohmic contact as reported by Xu *et al.* [22]. Moreover, InAs is a very good candidate for high speed electronics and infrared optoelectronics, due to its large electron mobility [larger than 3.5 $\frac{m^2}{Vs}$] and considerably large Rashba effect.

The epitaxial growth of Fe on $\{4\times2\}$InAs has been studied over last few years [22,95,145–149]. It has been shown that As and In react partially with the Fe layer at the interface and a segregation of the substrate materials (mainly In) on the surface has been observed [146,147]. It has been demonstrated by Teodorascu *et al.* that the Fe/InAs interface is much less reactive than the one of Fe/GaAs and the interface formation has been found to be restricted to only 0.6 ML [150–152].

The spin injection into InAs has been predicted by Zwierzycki *et al.* [20] and later demonstrated by Ohno *et al.* [21] who found a circular polarization of about -12% at $T$=6.5 K and an applied magnetic field of 10 T. The phase diagram of an InAs(001) surface structure studied by Yamaguchi and Horikoshi [153] using reflection high-energy electron diffraction (RHEED), STM and Monte carlo simulation shows a phase transition between As-stabilized $\{2 \times 4\}$ and In-stabilized {4×2} surface reconstructions. According to their studies a $\{4 \times 2\}$ surface reconstruction is more In-rich. In order to avoid the possible formation of FeAs alloys (magnetically dead layers) the $\{4 \times 2\}$ surface reconstruction (In-rich) was chosen for our investigation.

In this chapter the epitaxial growth and the magnetic anisotropy of Fe monolayers grown on {4×2}InAs are presented and all structural and magnetic characterizations are performed *in situ* under UHV conditions.

## 6.2. Sample preparation

In the following section the sample preparation of Fe/{4×2}InAs(001) is described.

### 6.2.1. Substrate preparation

A 4×4 mm$^2$ piece cut from commercially available n-type InAs(001) wafers has been used as substrate. It was cleaned in an ultrasonic bath using pure acetone and isopropanol and immediately transferred into the UHV chamber. Inside the UHV chamber the substrates were first outgassed by slightly rising the temperature to about 550 K, so that the pressure did not exceed $1{\times}10^{-9}$ mbar. In order to obtain the {4×2} surface reconstruction the substrate was sputtered and subsequently annealed several times. The annealing temperature was about 580 K and a low energy Ar$^+$ sputtering (0.5 keV) with a partial Ar$^+$ pressure of about $1{\times}10^{-5}$ mbar and an Ar$^+$-ion current density of about $2\mu A/$cm$^2$ was used. The cleanliness of the substrates was revealed by AES. Although the intensity of the In MNN transition with respect to As LMM transition is very large, a comparison of our AES measurements with the spectra taken from the pure elements [87] shows an In-rich surface. An AES spectrum and a typical LEED pattern of a clean {4×2}InAs surface are shown in the inset of Fig. 6.1 (a). Streaky of middle spots in ×2-direction is due to the random combination of domains of {4×2} and other reconstructions (more likely c{2×8}). In Fig. 6.1 (b) the schematic representations of the {4×2} reconstructions taken from Ref. [153] are shown. It should be noticed that a confusing notation was given in the literature [146,149,154]. The notation {4×2} specifies the orientation of the pattern, with the ×2-direction along [011] and the ×4-direction along [0$\bar{1}$1]. This notation is consistent with that used to define the {4×2} and {2×4} reconstructions of GaAs(100) [153]. It is essential to know the orientation of the LEED pattern, since the [011]- and [0$\bar{1}$1]-directions are inequivalent with respect to the bulk [155]. In the [100] direction, zincblende structure III-V semiconductors consist of alternating layers of anions (e.g. As) and cations (e.g. In). If the crystal is terminated with a layer of anions, their dangling bonds lie in the (110) plane (i.e. oriented along [1$\bar{1}$0]). If the crystal is terminated with a layer of cations, their dangling bonds lie in the (1$\bar{1}$0) plane (i.e. oriented along [110]). A schematic illustration of the anions and cations dangling bonds at the (001) surface is given in Fig. 6.1 (b). For the {4×2} pattern, the periodicity is doubled along the direction of the indium dangling bonds, and quadrupled along the direction of the arsenic dangling bonds.

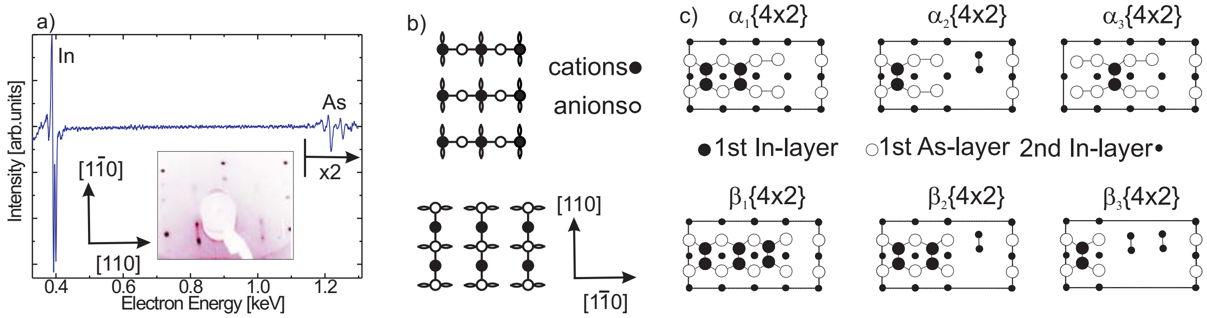

**Figure 6.1.:** (a) A typical AES spectrum of a clean InAs substrate. The inset shows a LEED pattern taken at an electron energy of 81 eV showing a well ordered {4×2} reconstruction. (b) Schematic representation of the direction of the dangling bonds at the (001)-plane of a III-V semiconductor surface [155]. (c) Schematic illustration of the possible atomic structure of {4×2}InAs(001) (taken from Ref. [153]).

## 6.2.2. Growth of Fe on InAs(001)

The Fe films were grown at RT by MBE with a deposition rate of 0.5 ML/min monitored by a quartz micro balance. The base pressure of the chamber was about $1\times10^{-10}$ mbar and rose during Fe-deposition up to about $6\times10^{-10}$ mbar. A LEED and an AES analysis were performed to verify the film quality. The LEED pattern disappeared immediately after the deposition of the first Fe layer, and a diffuse LEED pattern appeared with broad spots around 30 ML. Such an observation has been reported also by other groups [22,145]. Our AES results show segregation of In on top of the Fe films, since the MNN peak of In does not disappear even for Fe layers thicker than 30 ML (see Fig. 6.2).

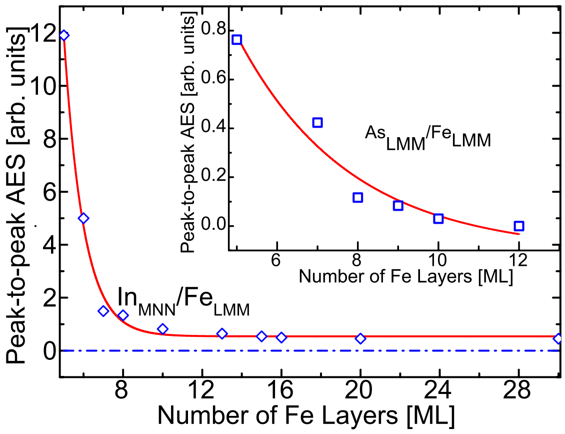

**Figure 6.2.:** The ratio of AES peak-to-peak intensities of the In MNN line to the Fe LMM line. Inset shows the AES peak-to-peak intensities of the As LMM line with respect to the Fe LMM line. The solid curves are the guides to the eyes.

## 6.3. Magnetic anisotropy

In order to determine the magnetic anisotropy *in situ* FMR measurements have been carried out immediately after growth as described in Sec 4.3. In this case a *full* in-plane angular dependent measurement was performed *in situ* at a microwave frequency of 9.3 GHz.

A typical polar and azimuthal angular dependence of the FMR resonance field, $B_{res}$, measured at RT is shown in Fig. 6.3. The solid curves in Fig. 6.3 are fits according to Eqs. (2.21) and (2.22).

For a film thickness above 20 ML an unsaturated resonance mode was observed very close to the hard axis (similar to the one of Fe/GaAs system, see Sec. 4.3).

The magnetocrystalline anisotropy constants are listed in Tab. 6.1 for different film thicknesses ($d$=5–30 ML). As capped Fe films on InAs measured by McPhail *et al.* showed a bulk like magnetization [109] the bulk magnetization ($M$=1.71×10$^6$A/m) was used to extract the anisotropy constants from the measured anisotropy fields.

The value of the perpendicular uniaxial anisotropy $K_{2\perp}$ in the second column of Tab 6.1 does not overcome the one of the shape anisotropy given by $E_{\text{Shape}} = \frac{1}{2}\mu_0 M^2$ (for $M = 1.71 \times 10^6 A/m$, $E_{Shape}$=18.35 J/m$^3$ ). Consequently, the magnetization lies in the film plane for all thicknesses as can be seen from the out-of-plane angular dependence of the resonance field (see Fig. 6.3 (a)). The cubic anisotropy $K_4$ is positive for all films meaning that the favorable easy magnetization direction should be the $\langle 100 \rangle$-direction within the thicker films (because thicker films have a dominating cubic anisotropy). For a film thickness below 7 ML the in-plane uniaxial anisotropy $K_{2\|}$ (the fourth column of Tab. 6.1) is the dominating in-plane term. The positive sign means that the favored easy axis is the [1$\bar{1}$0]-direction. The interplay between

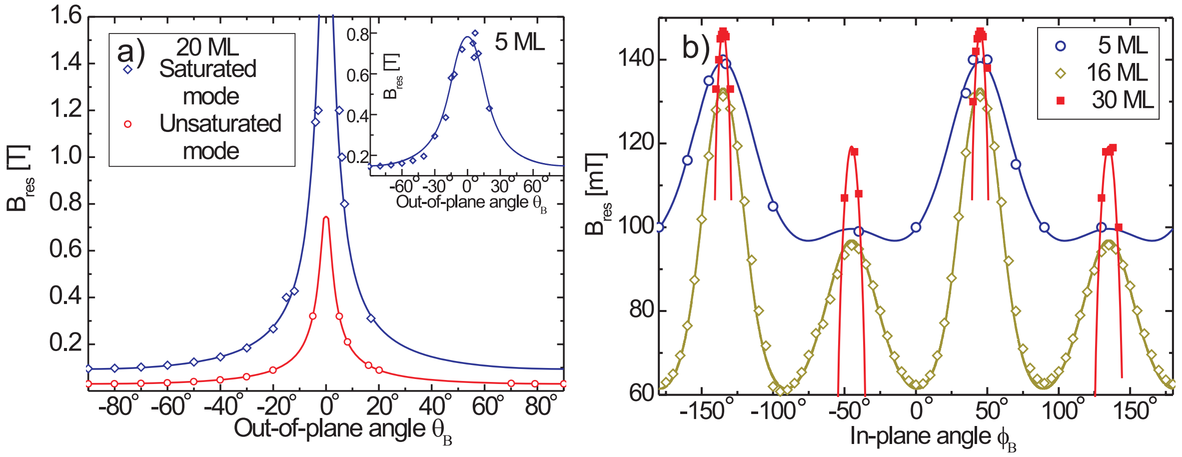

**Figure 6.3.:** (a) Polar and (b) azimuthal angular dependence of the resonance field measured at 9.3 GHz for different thicknesses of Fe layers grown on {4×2}InAs. The solid curves are fits to the experimental data.

| Thickness (ML) | $K_{2\perp}$ ($10^5$J/m$^3$) | $K_4$ ($10^5$J/m$^3$) | $K_{2\parallel}$ ($10^5$J/m$^3$) | $\frac{\mu_0 M_{\mathrm{eff}}}{2}$ (mT) | $K_4/M$ (mT) | $K_{2\parallel}/M$ (mT) |
|---|---|---|---|---|---|---|
| Fe-Bulk | – | 0.48 | – | -1072 | 27.5 | – |
| 30 | 5 | 0.58 | 0.10 | -774 | 34 | 5.8 |
| 20 | 6 | 0.52 | 0.11 | -715 | 31 | 6.5 |
| 16 | 7 | 0.500 | 0.11 | -656 | 29 | 6.5 |
| 15 | 8 | 0.47 | 0.11 | -597 | 28 | 6.5 |
| 12 | 8.8 | 0.40 | 0.11 | -550 | 24 | 6.5 |
| 10 | 9.8 | 0.35 | 0.11 | -491 | 21 | 6.5 |
| 8 | 11 | 0.28 | 0.12 | -421 | 16 | 7.1 |
| 7 | 12 | 0.20 | 0.13 | -362 | 12 | 7.6 |
| 5 | 14 | 0.12 | 0.15 | -244 | 7.0 | 8.8 |

**Table 6.1.:** The measured magnetic anisotropy constants of uncapped Fe layers on {4×2}InAs(100). All samples were measured *in situ* at RT. The conversion to $\mu$eV/atom can be given by $1\times10^5$ J/m$^3$ =7.4 $\mu$eV/atom. The bulk value is taken from Ref. [88].

$K_4$ and $K_{2\parallel}$ leads to a change of the easy axis from the [100]- towards the [110]-direction as the thickness of the Fe layer is increased.

The evolution of the magnetization angle with increasing number of Fe monolayers was determined from the equilibrium condition where the free energy density is minimal. The measured anisotropy constants were used to simulate the free energy density. Figure 6.4 shows how the in-plane spin reorientation transition takes place. The easy axis is along the [1$\bar{1}$0]-direction

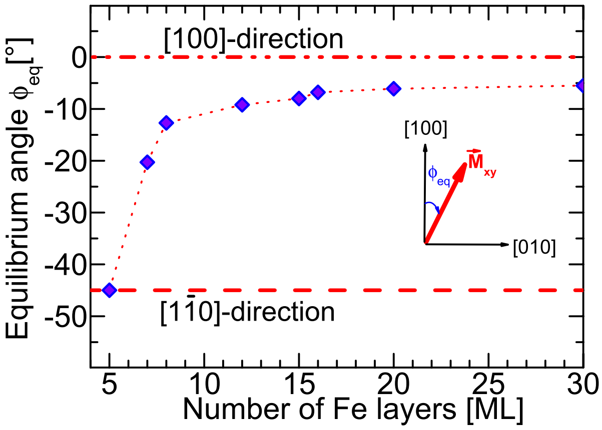

**Figure 6.4.:** In-plane reorientation of the easy axis of the magnetization as a function of the Fe thickness.

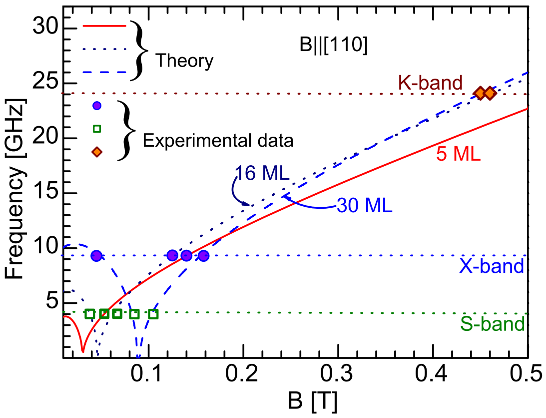

**Figure 6.5.:** Resonance frequency as a function of the resonance field for a 5, 16, and 30 ML Fe film on {4×2}InAs(001). The measurements were performed at RT with an external magnetic field applied along the [110]-direction.

and rotates by 45° towards the [110]-direction for a film thickness above 7 ML. The fact that the rotation of the easy axis is faster than the one of Fe/GaAs is related to the more strongly changing ratio of $K_4$ and $K_{2\|}$.

## 6.4. FMR dispersion relation

The resonance frequency versus resonance field (dispersion relation) is shown in Fig. 6.5 for the magnetic field applied along the [110]-direction. The curves show the numerically calculated dispersion relation based on Eq. (2.23) for a 5, 16, and 30 ML sample, respectively. The calculated dispersion relation predicts an unsaturated branch as was observed experimentally. At 9.3 GHz the low field (unsaturated) resonance of the 5 and 16 ML sample cannot be excited due to the smaller cubic anisotropy. The point at $f$=24 GHz is for a 3 nm Au capped film, which has been measured *ex situ*.

### 6.4.1. The surface-interface & volume magnetic anisotropy

The surface-interface anisotropy contributions to the different anisotropy constants were determined by plotting the anisotropy terms versus the reciprocal film thickness (Fig. 6.6). The volume and surface-interface anisotropy constants resulting from this analysis and the ones of a capped film [109] are shown in Tab. 6.2.

We start the discussion with the contributions to the uniaxial out-of-plane anisotropy $K_{2\perp}$. The volume contribution $K_{2\perp}^{v}$ = (3.1±0.7)×$10^5$ J/m$^3$ (22±5 $\mu$eV/atom) is positive, favoring an

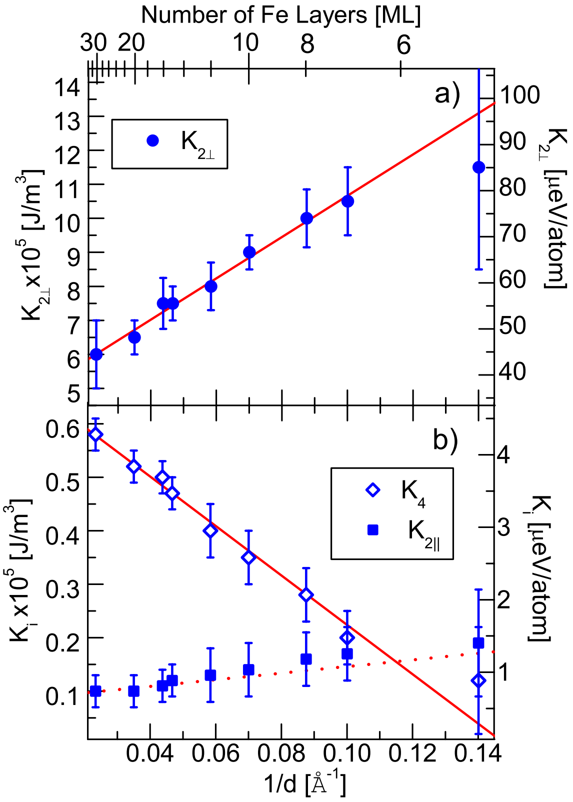

**Figure 6.6.:** Reciprocal thickness dependence of the anisotropy constants of Fe/{4×2}InAs(001). The perpendicular magnetic anisotropy is shown in the upper, panel whereas in the lower panel the in-plane anisotropy constants are plotted.

alignment of the magnetization out of the film plane (unlike to the one of Fe/GaAs). Although our value is larger and has an opposite sign in comparison to the value of Au-capped films measured by p-MOKE [109], it has the same sign as the value measured by FMR [156] for a thick film. Note that in [109] a different sign convention was used yielding an in-plane orientation for positive $K^v_{2\perp}$. This was considered and the anisotropy contributions measured by McPhail are converted to our coordinate system (see Tab. 6.2).

The surface-interface term $K^{s,\mathrm{eff}}_{2\perp}$=(0.92±0.12)×10$^{-3}$ J/m$^2$ (474±62 $\mu$eV/atom) includes both Fe-vacuum and Fe-InAs interface anisotropies. This contribution favors an easy axis out-of-plane, similar to the one of the Fe/GaAs system but it is also slightly smaller than the $K^{s,\mathrm{eff}}_{2\perp}$ of Fe/GaAs, and is smaller than the value reported by McPhail *et al.* [109] for Au-capped films. It should be noted that the surface anisotropy strongly depends on the surface morphology (see Sec. 4.10) and intermixing of the film and the cap layer. Therefore, the difference between our values and the ones of the other studies might result from changes at the interfaces of the substrate and capping layers.

Both surface-interface and volume contributions favor an out-of-plane magnetization di-

| | $K^{v}_{2\perp}$ ($10^5$J/m$^3$) | $K^{v}_{4}$ ($10^5$J/m$^3$) | $K^{v}_{2\parallel}$ ($10^5$J/m$^3$) | $K^{s,\mathrm{eff}}_{2\perp}$ ($10^{-3}$J/m$^2$) | $K^{s,\mathrm{eff}}_{4}$ ($10^{-5}$J/m$^2$) | $K^{s,\mathrm{eff}}_{2\parallel}$ ($10^{-5}$J/m$^2$) |
|---|---|---|---|---|---|---|
| **This work** | **3.1±0.7** | **0.68±0.03** | **0.12±0.05** | **0.92±0.12** | **-4.6±0.5** | **0.08±0.05** |
| [109]* | -2.2 ±1.3 | 0.65±0.03 | 0.025±0.01 | 1.4±0.1 | -7.9±0.6 | — |

**Table 6.2.:** Surface-interface and volume contribution to the magnetic anisotropy of uncapped Fe/{4×2} InAs(001) (upper part), and of Au capped Fe/InAs measured by BLS [109] (lower part).

* Note that in [109] a different definition of the free energy was used, which yields opposite signs. The values have been adopted to the anisotropy model of this work.

rection but they are dominated by the larger shape anisotropy yielding a negative $\mu_0 M_{\mathrm{eff}}$ and consequently an in-plane alignment of the magnetization, which one can see from the polar angular dependence of the resonance field (Fig. 6.3 (a)).

The thickness dependence of the cubic anisotropy constant (Fig. 6.6 (b)) yields a negative surface-interface contribution $K^{s,\mathrm{eff}}_{4}$ = (-4.6±0.5)×$10^{-5}$ J/m$^2$=-23.7±2.6 $\mu$eV/atom and a positive volume contribution $K^{v}_{4}$ = (0.68±0.03)×$10^5$ J/m$^3$ = 5±0.2 $\mu$eV/atom, slightly larger than for Fe-bulk ($K_{4,\mathrm{bulk}}$ = 0.48×$10^5$ J/m$^3$=3.5 $\mu$eV/atom). The slight enhancement of $K^{v}_{4}$ indicates the existence of a biaxial strain due to biaxial compression caused by the lattice mismatch. We will come back to this issue in Sec. 6.5.2.

The nearly thickness independent in-plane anisotropy $K_{2\parallel}$ (unlike to the one of Fe/GaAs) indicates that this term is mainly a volume term. According to the linear $1/d$ fit in Fig. 6.6 (b) one gets $K^{v}_{2\parallel}$ =(0.12±0.05)×$10^5$J/m$^3$=1.5±0.37 $\mu$eV/atom and $K^{\mathrm{s,\,eff}}_{2\parallel}$=(0.08±0.05)×$10^5$J/m$^3$=0.4±0.26 $\mu$eV/atom. $K^{\mathrm{s,\,eff}}_{2\parallel}$ is negligible and in good agreement with the previous studies of capped Fe/InAs films. Our $K^{v}_{2\parallel}$ is larger than the value reported by McPhail [109] but it is in excellent agreement with the value measured by Toliński *et al.* [156]. This is attributed to the difference of the sample preparations [156].

## 6.5. Origin of the anisotropy contributions

The FMR measurements revealed that the magnetic anisotropy of the Fe/InAs films is governed by both surface-interface and volume contributions (unlike to the case of Fe/GaAs for which the surface-interface contributions dominate). In the following we discuss the possible sources of the various anisotropy contributions based on our experimental results.

### 6.5.1. The perpendicular uniaxial anisotropy

#### The volume contribution

As discussed in Sec. 4.7 strain can result in a perpendicular anisotropy with uniaxial character. Either lattice mismatch or the atomic structure of the reconstructed surface or both can be the origin of this strain contribution. The RHEED experiment by Xu *et al.* [154] shows that the Fe films on InAs are under a large in-plane strain up to a thickness of 5 ML. This observation is attributed to the pseudomorphic growth at the initial stage. Afterwards the films start to relax towards the bulk Fe lattice at a thickness of about 25 ML. The magneto-elastic anisotropy due to the strain can be written as: $K_{2\perp}^{MEL}= B_1(\epsilon - \epsilon_{33})$. By assuming a cubic environment of the Fe film the perpendicular strain component $\epsilon_{33}$ is related to the in-plane one $\epsilon$ by: $\epsilon_{33} = -\frac{2c_{12}}{c_{11}}\epsilon \sim -2\epsilon$ [52,53].

Using this ansatz with $\epsilon = 5.4\%$, one can see that $B_1$ has to be positive as in the case of Fe/GaAs. With $B_1 = 3.5 \times 10^6$ J/m$^3$ for the Fe/GaAs system [101] the magneto-elastic anisotropy can be calculated accordingly, $K_{2\perp}^{MEL} = 3.8 \times 10^5$ J/m$^3$, in good agreement with the measured one. However, a direct measurement of the elastic constants of Fe/InAs is needed to verify this hypothesis.

#### The surface-interface contribution

Similar to the volume contribution, $K_{2\perp}^{s,\,eff}$ favors an out-of-plane magnetization direction. Although $K_{2\perp}^{s,\,eff}$ is smaller than the one of Fe/GaAs, all descriptions of the origins of this contribution remain valid. The main origin is the symmetry breaking at the surface and interface and the role of valence 3d and 4s/p electron states confined to the surface, which are exposed to a reduced lattice symmetry that strongly enhances the contribution of the spin-orbit interaction to the surface valence band energies (see Heinrich and Cochran [114] for more details). The fact that this term is smaller than the one of Fe/GaAs is likely related to the different surface morphology of the film and In on top of the Fe layer.

### 6.5.2. The cubic anisotropy

#### The volume contribution

As described before $K_4^v$ is larger than the bulk Fe value. The enhanced value may result from the biaxial strain contribution in the films. RHEED experiments [95] showed that the thickness, which is needed for the complete relaxation, is about 25 ML. This strain includes both uniaxial as well as biaxial terms. The biaxial strain results in a magneto-elastic anisotropy, which enhances the cubic anisotropy. The biaxial magneto-elastic anisotropy can be calculated by considering the higher order Taylor expansion in Eq. (2.5). A quantitative explanation of this term needs, however, detailed information of the higher order contribution of the magneto-elastic coupling constants ($B_3$), which according to our knowledge has not been measured, neither for Fe/GaAs nor for Fe/InAs. It should be noticed that this term for the case of Fe/GaAs is very small and almost negligible.

### The surface-interface contribution

The cubic surface-interface contribution $K_4^{s,\text{eff}}$ has sign opposite to the volume contribution (similar to the one of Fe/GaAs). The negative sign means that the favored easy axes are the $\langle 1\bar{1}0 \rangle$-directions. Since the strain has no surface-interface contribution to the magneto-elastic anisotropy with biaxial character [52,53], the strain induced anisotropy can be ruled out. Since this contribution is smaller for the uncapped sample, a possible explanation is that it originates mainly from the Fe surface.

## 6.5.3. The in-plane uniaxial anisotropy

### The volume contribution

As mentioned before, the Fe films are under in-plane strain. RHEED measurements showed that the lattice relaxation is *anisotropic* meaning that the Fe lattice relaxation along the [1$\bar{1}$0]-direction is significantly faster than that along the [110]-direction [154]. This observation is supposed to be related to the atomic scale of the reconstructed InAs surface. Using Eq. (2.5) and the fact that the in-plane strain parallel to the [110]-direction is given by $\epsilon_{12}$ and parallel to the [1$\bar{1}$0]-direction by $\epsilon_{21}$, leads to a contribution $F_{MEL}^{[110]} = 2B_2\alpha_1\alpha_2\epsilon_{12}$=$B_2\epsilon_{12}$. Using the same notation as in Sec. 4.7.3 the magneto-elastic anisotropy along the [1$\bar{1}$0] is given by $F_{MEL}^{[1\bar{1}0]} = -B_2\epsilon_{21}$. Therefore, the magneto-elastic anisotropy can be calculated as $K_{2\|}^{\text{MEL}} = F_{\text{MEL}}^{[110]} - F_{\text{MEL}}^{[1\bar{1}0]} = B_2(\epsilon_{12} + \epsilon_{21})$.

According to the RHEED data measured by Xu *et al.* [154] the film is nearly relaxed along the [1$\bar{1}$0]-direction ($\epsilon_{21} \sim 0$) but in the [1$\bar{1}$0]-direction it has a small deviation from the bulk Fe of about $\epsilon_{12}$ =0.5%. Using the magneto-elastic coupling constant of the Fe bulk $B_2 = 7.2 \times 10^6$ J/m$^3$ [102] (which is the same as Fe/GaAs [52,53]), one gets $K_{2\|}^{MEL} = 0.36 \times 10^5$ J/m$^3$, which is roughly 3 times larger than our measured value using *in situ* FMR. This means that strain plays a crucial role for the in-plane uniaxial anisotropy. However, the fact that the experimental value is smaller than the estimated one due to strain indicates that the magneto-elastic coupling constant of Fe/InAs might be smaller than the one of bulk Fe. Another possible explanation is that other sources may contribute to the uniaxial anisotropy as well, but negatively. Although the interface reaction was found to be negligible in comparison to the Fe/GaAs [150–152] and Fe/InP [157], the hybridization of the Fe atoms at the interface might also play a role.

## 6.6. The onset of room temperature ferromagnetic order

In order to obtain an insight into the onset of long range ferromagnetic order Fe was grown in thicknesses of 1 to 5 ML. FMR experiments were performed as a function of the nominal number of Fe layers at RT and a microwave frequency of 9.3 GHz. The external magnetic field was applied along the $[1\bar{1}0\ ]$-direction (easy axis). The results are shown in Fig. 6.7, where (a) the thickness dependence of the FMR resonance field $B_{res}$ and (b) the FMR linewidth $\Delta B_{pp}$ are shown. A ferromagnetic signal was observed from a film thickness of 2.7 ML onwards with the lowest resonance field and largest FMR linewidth. The small value of $B_{res}$ is due to the fact that for this thickness $K_4 \sim 0$. Consequently, the ferromagnetic resonance along $[1\bar{1}0]$-direction occurs at lower fields. The large $\Delta B_{pp}$ can be attributed to the large size distribution of the 3D-like clusters. The Fe clusters coalescence and form a continuous film at about around 5 ML as found by RHEED [154] and STM studies [149].

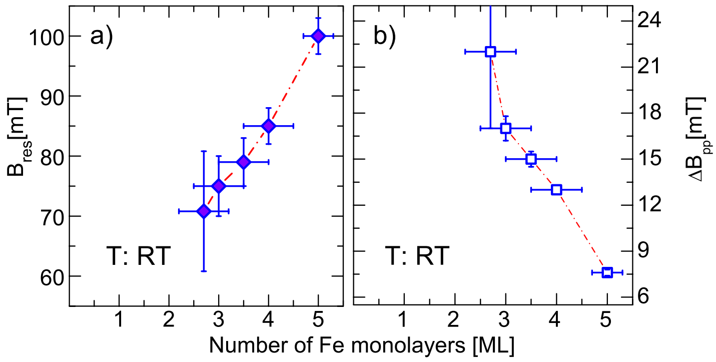

**Figure 6.7.:** (a) FMR resonance field and (b) linewidth as a function of monolayer equivalents, recorded at RT and an external magnetic field applied along the $[1\bar{1}0]$-direction.

## 6.7. Summary

Fe monolayers were grown on {4×2}InAs(001) by MBE. The epitaxial relationship was observed to be $[100]_{Fe} \parallel [100]_{InAs}$. Indium floats on top of the Fe layers as observed by AES. The magnetocrystalline anisotropy was determined by *in situ* FMR and compared to the one of Fe/GaAs. The origin of different anisotropy contributions were discussed. The volume contribution to the in-plane as well as the out-of-plane uniaxial anisotropy is proposed to be the effect of the in-plane strain. The enhanced cubic term is attributed to biaxial strain in the volume of the film. The cubic surface-interface term mainly originates from the Fe surface and might be related to the reduced symmetry of the upper Fe atomic layer.

# 7. Fe monolayers on Au/InAs(001)

*In this chapter the results of the in situ FMR experiments of Fe monolayers grown on a 5 ML buffer layer of gold on InAs(001) are presented. The role of the gold layer is supposed to decrease the mismatch of the band structure between Fe and InAs, and modify the interface stability and the interface magnetic properties. Although our magnetic characterization shows that the perpendicular uniaxial anisotropy is not affected, the in-plane uniaxial and cubic anisotropy are suppressed by 100% and 80%, respectively. Furthermore, the onset of ferromagnetic long-range order at room temperature is shifted to larger thicknesses, which is attributed to a disordered structure or to the diffusion of Au on top of the Fe layers.*

## 7.1. Introduction

As discussed in chapter 6, the interface of Fe/InAs is an ideal Ohmic contact. A Schottky barrier, however, is needed for *'spintronic'* applications [23]. One possible way to form a Schottky contact between Fe and InAs is to use gold. The barrier height at the *clean* Au/InAs interface was found by Ohler *et al.* to be 10±5 meV [24]. Moreover, a extraordinarily huge magnetoresistance effect was observed in a hybrid device consisting of an Au film on an InAs-based two-dimensional electron system [25]. A technological relevant device might be realized by growing an atomically ordered Au layer between Fe and InAs. Another advantage of this structure is that the thickness of the Au buffer layer can be chosen to be thin enough in order to prevent the presence of possible electrical shunts.

In this chapter the growth and the magnetic anisotropy of Fe monolayers in Fe/Au/InAs and Au/Fe/Au/InAs structures are presented, and all structural and magnetic characterizations are performed *in situ* under UHV conditions. The thickness of the Au layer is kept constant (5 ML) and the thickness of the Fe layers is varied.

## 7.2. Sample preparation

In the following section the sample preparation of Fe/Au/{4×2}InAs(001) and Au/Fe/Au/{4×2}InAs(001) is shortly reviewed. The InAs substrate preparation for this structure follows the same procedure, which has been reported in Sec.6.2.1.

### 7.2.1. Growth of Fe/Au bilayers and Au/Fe/Au sandwiches on InAs(001)

5 ML Au films were grown at RT with a deposition rate of 0.8 ML/min. The evaporation pressure was about $5\times10^{-9}$ mbar while Au was evaporated from a PBN-crucible. LEED and AES experiments were carried out immediately after the growth. The substrate's LEED pattern disappears after deposition of the Au layer. 1–25 ML Fe layers were grown directly after deposition of the Au at RT. The deposition rate was about 1 ML/min. No LEED pattern was observed from the Fe layers. The AES analysis (Fig. 7.1) shows that although the peak-to-peak ratio of the In MNN transition to the Fe LMM transition is decreased in comparison to the Fe/InAs system (see Fig. 6.2), the peak-to-peak ratio of the Au NVV transition with respect to the Fe LMM transition indicates an intermixing and diffusion of Au to the surface of the Fe layer. Similar surface alloying, and surface segregation of Au is well-known in Fe/Au(100) [158–160] and Au/Fe(100) [161]. After performing the magnetic characterization, the Fe layer was covered by a 5 ML thick Au layer at RT under the same conditions and characterized by LEED and AES.

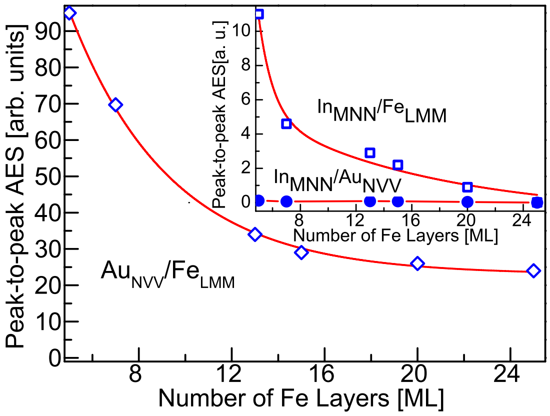

**Figure 7.1.:** The ratio of AES peak-to-peak amplitudes of the Au NVV line at 69 eV to the Fe LMM line at 651 eV (open diamonds), along with the ratio of the AES peak-to-peak amplitudes of the In MNN at 400 eV line over Fe LMM line at 651 eV (open squares) and Au NVV line (closed circles), for Fe films grown on 5 ML Au on InAs at RT. The solid curves are guides to the eyes.

## 7.3. Magnetic anisotropy of Fe/Au/InAs(001) bilayers

The magnetocrystalline anisotropy constants of Fe/Au/InAs measured by *in situ* FMR are listed in Tab. 6.1. As compared to Fe/InAs (Tab. 6.1), all in-plane anisotropy constants are drastically decreased by the presence of the Au buffer layer whereas the perpendicular magnetic anisotropy is mostly not affected.

| Thickness (ML) | $\frac{\mu_0 M_{\mathrm{eff}}}{2}$ (mT) | $K_{2\perp}$ ($10^5$J/m$^3$) | $\frac{K_{2\parallel}}{M}$ (mT) | $K_{2\parallel}$ ($10^3$J/m$^3$) |
|---|---|---|---|---|
| 25 | -774 | 4.9 | 1.1 | 1.9 |
| 20 | -740 | 5.6 | 1.2 | 2.0 |
| 15 | -686 | 6.5 | 1.1 | 1.9 |
| 12 | -600 | 8.0 | 1.1 | 1.8 |
| 10 | -530 | 9.3 | 0.5 | 0.8 |
| 7 | -356 | 12.1 | 0.5 | 1.2 |

**Table 7.1.:** The measured magnetocrystalline anisotropy constants and the corresponding anisotropy fields of Fe/5Au/{4×2}InAs. All samples were measured *in situ* at RT. The bulk magnetization ($M$=1.7×$10^6$A/m) was used to extract the magnetocrystalline anisotropy constants.

The latter is due to the fact that $K_{2\perp}$, mainly originates from the Fe-vacuum interface. Its small decrease with respect to the Fe/InAs value is due to the change of the volume contribution. In Fig. 7.2 (a) the reciprocal thickness dependence of $K_{2\perp}$ is plotted. Although the surface-interface contribution ($K_{2\perp}^{\mathrm{s,\,eff}} = (1 \pm 0.13) \times 10^{-3}$J/m$^2$) is not affected, the volume contribution is reduced by almost 40% which might be attributed to the change of the strain in the film ($K_{2\perp}^{v} = (1.8 \pm 0.7) \times 10^5$J/m$^3$).

Our FMR experiments demonstrate that the cubic anisotropy $K_4$, is suppressed completely by the Au layer. This is likely due to the fact that the Au layer is more polycrystalline than monocrystalline because of the large lattice mismatch between Au and InAs. On top of the Au layer the Fe layer likely grows polycrystalline and therefore a random orientation of the easy axes in the film plane is the reason for the suppression of $K_4$. Furthermore, the alloying and out-diffusion of Au on Fe certainly play a role.

The small in-plane uniaxial anisotropy $K_{2\parallel}$, indicates a preferential easy axis along the $[1\bar{1}0]$-direction. Although the films are polycrystalline, there is a preferential direction of crystallinities along which the Au layer and consequently the Fe layer are under tensile strain. This yields to an uniaxial anisotropy term.

### The onset of the room temperature ferromagnetic order

A ferromagnetic signal was detected at RT from Fe thickness of 7 ML onwards. This delay in the long range ferromagnetic order is likely due to alloying and intermixing (out-diffusion) of Au into the Fe layer as evidenced by our AES analysis (see Fig. 7.1). A similar delay in long range ferromagnetic order (9.8 ML) has been reported by Zhang *et al.* for Fe/3.5 ML Au/GaAs [162]. Although the authors explain their observation by formation of a superparamagnetic phase of Fe clusters on this structure, the alloy formation and intermixing (out-diffusions) cannot be ruled

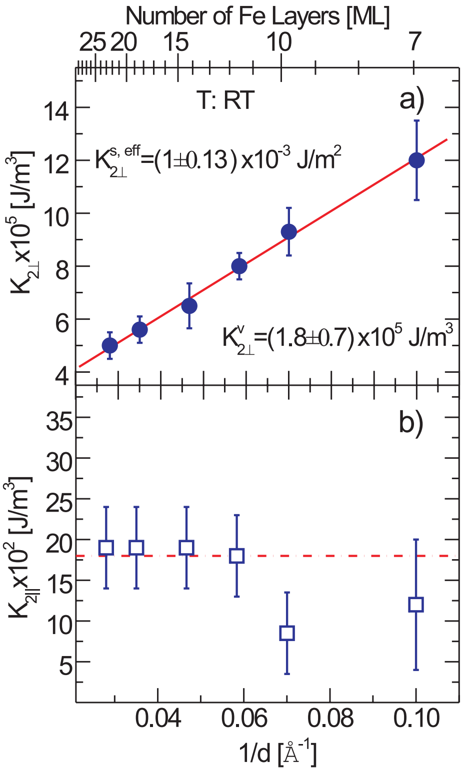

**Figure 7.2.:** Reciprocal thickness dependence of (a) $K_{2\perp}$ and (b) $K_{2\|}$ of Fe/Au/{4×2}InAs(001). The solid line is the linear fit to the experimental data and the dashed line is a guide to the eyes.

out.

### 7.3.1. Au/Fe/Au/InAs(001) sandwiches

In order to investigate the Au/Fe interface in more detail, an additional 5 ML of Au were deposited on top of 7Fe/5Au/{4×2}InAs and 20Fe/5Au/{4×2}InAs samples (the integers represent the number of atomic layers, ML). The magnetic anisotropy fields measured *in situ* at RT of 5Au/7Fe/5Au/{4×2}InAs and 5Au/20Fe/5Au/{4×2}InAs sandwiches are listed in Tab. 7.2.

The anisotropy fields of 5Au/20Fe/5Au/{4×2}InAs are not significantly changed because the thickness of the Fe layer is large enough, so that an additional Au layer has no significant effect. The possible explanations for the reducing of the out-of-plane anisotropy field $\mu_0 M_{\text{eff}}$, and enhancement of in-plane uniaxial anisotropy field in the 5Au/7Fe/5Au/{4×2}InAs structure are: (i) the formation of an Au-rich alloy which reduces the magnetization and consequently $\mu_0 M_{\text{eff}}$ or (ii) enhancement of $K_{2\perp}$ and $K_{2\|}$. However, finding a morphological characterization by STM is proposed for verifying this hypothesis.

| Thickness (ML) | $\frac{\mu_0 M_{\mathrm{eff}}}{2}$ (mT) | $\frac{K_{2\parallel}}{M}$ (mT) |
|---|---|---|
| 20 | -750 | 1.1 |
| 7 | -88 | 1.1 |

**Table 7.2.:** The measured magnetic anisotropy fields of 5Au/20Fe/5Au/{4×2}InAs and 5Au/7Fe/5Au/{4×2}InAs. The first column represents the thickness of the Fe layer in the sandwich structure. All samples were measured *in situ* at RT.

## 7.4. Summary

The magnetocrystalline anisotropy of Fe/Au/{4×2}InAs(001) bilayers and Au/Fe/Au/{4×2}InAs(001) sandwiches were presented. The in-plane cubic and uniaxial anisotropy terms are suppressed by 100% and 80%, respectively. Furthermore, the initial thickness of onset of the RT ferromagnetic long range order increases from 2.8 to 7 ML. All observations are attributed to a disordered structure, alloying, intermixing, and out-diffusion of Au into the Fe layers.

# 8. Fe monolayers on InP(001)

*In this chapter the results of the in situ FMR experiments of 1–21 ML Fe grown on* $\{2 \times 4\}$ *reconstructed InP(001) are presented. For all thicknesses the magnetization is found to favor an in-plane alignment. The easy axis of magnetization is parallel to the* $[1\bar{1}0]$*-direction for film thicknesses below 7 ML, and rotates by* $45^\circ$ *towards the* $[100]$*-direction for thicker Fe layers. The magnetic anisotropy energy of the system has been quantitatively determined as a function of film thickness. The perpendicular magnetic anisotropy is strongly thickness dependent revealing the presence of a large surface-interface term, which is comparable to the values of Fe grown on GaAs. The cubic anisotropy, however, is relatively small compared to the cubic anisotropy of bulk Fe over the whole thickness regime and almost thickness independent. In contrary to the cubic anisotropy the in-plane uniaxial anisotropy is strongly thickness dependent and originates from the Fe/InP interface. A part of the perpendicular magnetic anisotropy and the uniaxial interface anisotropy is related to the strain resulting from the mismatch between the film and the substrate. Our quantitative magnetic measurements indicate well ordered magnetic structures.*

## 8.1. Introduction

Besides Fe/GaAs there exist other promising systems for spin injection such as Fe/InP. The growth and structural investigation of Fe on InP has been restricted to a few works [157,163–165]. Zavaliche *et al.* [165] is the only one who reported magnetic measurements of Fe films on InP(001) using *in situ* MOKE. InP has a band gap of $V_g = 1.34$ eV very close to the one of GaAs $V_g = 1.43$ eV, which can be used for relevant magneto-electronic applications. The lattice mismatch is positive with a value of $\epsilon = (a_{\text{InP}} - 2a_{Fe})/2a_{Fe} = +2.2\%$ in contrary to GaAs ($\epsilon = a_{\text{GaAs}} - 2a_{Fe})/2a_{Fe} = -1.6\%$). This yields a tensile strain in the film plane and consequently changes the magnetic properties at the interface.

In this chapter the epitaxial growth and the magnetic anisotropy of Fe monolayers grown on {2×4}InP(001) will be discussed. The thickness dependence of the different anisotropy contributions as well as the magnetization will be quantified. It will be demonstrated how the strain at the interface plays a role for the interface magnetic anisotropy.

## 8.2. Sample preparation

A 5×10 mm$^2$ piece cut from commercially available n-type InP(001) wafers was used as substrate. It was cleaned by acetone and isopropanol in an ultrasonic bath for approximately 5 minutes until an optical microscope revealed a clean surface. The substrate was sputtered after transfer into the UHV chamber with $Ar^+$ ions at an $Ar^+$ pressure of $1 \times 10^{-7}$ mbar and an ion energy of 0.5 keV until no contaminations of carbon and oxygen were detectable by AES. The substrate temperature was increased to 580-600 K while the substrate was sputtered as mentioned above for about 30 minutes. After this procedure AES reveals a clean InP surface. Figure 8.1(a) shows an Auger spectrum of a clean InP substrate indicating a P-rich surface. This treatment results in a well ordered {2×4} reconstruction of the InP(001) surface. A typical LEED pattern of {2×4}InP(001) is shown in Fig. 8.1(b). Such an observation has also been reported by Zavaliche *et al.* [165].

The LEED patterns were always obtained with sharp $\frac{1}{4}$-order spots but streaky $\frac{1}{2}$-order spots. Streaky $\frac{1}{2}$-order spots in a $\{2 \times 4\}$ LEED pattern have been attributed to the random combination of $\{2 \times 4\}$ and c$\{2 \times 8\}$ domains [155]. In Fig. 8.1(c) and (d) the models proposed by Sung *et al.* [166] and Mitchell [155] are shown. The Sung model (Fig. 8.1(c)) predicts an In-terminated surface with a coverage of 0.75 ML. The P-adatom trimer model proposed by Mitchell (Fig. 8.1(d)), in which the trimers are due to threefold coordinated P-adatoms, is based on both STM and photoemission studies. This model predicts a P-terminated surface with a coverage of 0.5 ML (for more details see [155]). A detailed STM study together with calcula-

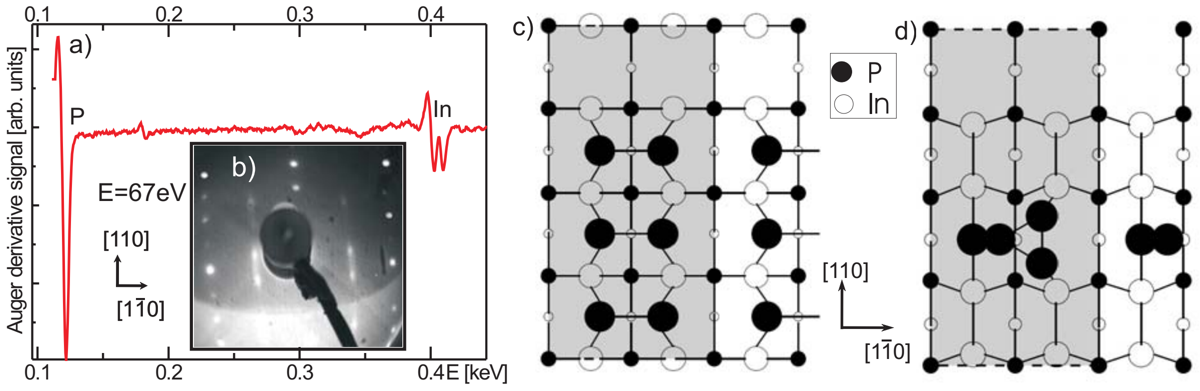

**Figure 8.1.:** (a) Auger spectrum of a clean InP substrate showing a P-rich surface. (b) LEED pattern of a $\{2 \times 4\}$ reconstructed InP surface recorded at E=67 eV. Structural models of a $\{2 \times 4\}$ reconstructed InP surface: (c) the missing row trimer-dimer model of Sung *et al.* [166]. (d) A P-adatom trimer model proposed by Mitchell [155]. Smaller circles depict atoms in lower layers. The shaded area is the surface unit cell.

tions of the electronic density of states would be required in order to distinguish between these models.

The Fe films were deposited at RT with a deposition rate of about 1 ML/min monitored by a quartz microbalance. The pressure during Fe deposition did not exceed $7\times10^{-10}$ mbar. The chemical composition and the structure of the films were revealed immediately after growth by AES and LEED, respectively. In Fig. 8.2(a) an Auger spectrum of a 20 ML Fe film grown on {2×4}InP(001) is shown. At this level of Fe coverage the In peak of the underlying substrate is still visible. No LEED pattern has been observed from the Fe layers. The LEED pattern disappears after deposition of approximately 1 ML and doesn't reappear for thicker Fe layers. The peak-to-peak intensity of the P LMM and In KLL transitions is shown in Fig. 8.2(b) indicating that the intensity of both P and In peaks decreases as the film thickness increases. The P peak disappears after deposition of 10 ML Fe but the one of In does not vanish even after deposition of 45 ML of Fe, indicating that In floats on top of the Fe layers. Probably, this is the reason why no LEED pattern from the Fe films could be observed. Such a behavior was also reported by Zavaliche *et al.* [165]. The Auger data analysis show that the ratio of the of the P peak with respect to the In peak decreases after the deposition of the first Fe film (5 ML). It remains nearly constant for 5, 8, 9, and 10 ML films and vanishes for thicker Fe layers. The ratio of the In peak with respect to the Fe peak remains constant for films with a thickness of above 30 ML (see Fig. 8.2). We conclude that P reacts with Fe to form $\mathrm{Fe}_x\mathrm{P}_{1-x}$ compounds and In floats on top of the Fe layers.

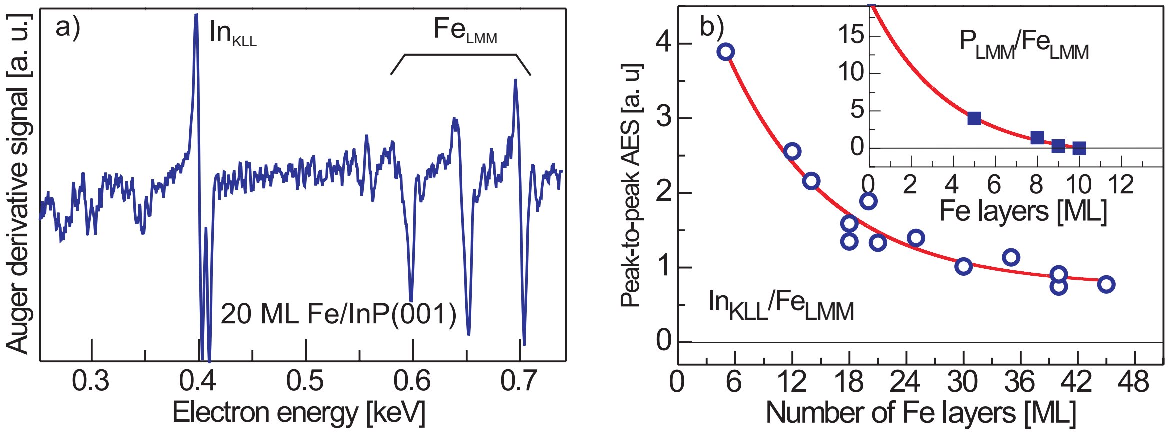

**Figure 8.2.:** (a) Auger spectrum of a 20 ML Fe grown on {2×4}InP(001) at RT. (b) Peak-to-peak intensity ratios of the $\mathrm{P}_{\mathrm{LMM}}/\mathrm{Fe}_{\mathrm{LMM}}$ and $\mathrm{In}_{\mathrm{KLL}}/\mathrm{Fe}_{\mathrm{LMM}}$ transitions normalized by the transition. The solid lines are guide to the eyes.

## 8.3. Magnetic anisotropy

FMR spectra were recorded for the polar angle range of -90° $\leq\theta\leq$90°, i.e. within the (1$\bar{1}$0)-plane at microwave frequencies of 9.3 and 4 GHz. The in-plane angular dependence measurements were performed within 42° $\leq\phi\leq$48° (±3° around the [110]-direction ) and 222° $\leq\phi\leq$228° (±3° around the $[\bar{1}\bar{1}0]$-direction) with respect to the [100]-direction at a frequency of 4 GHz. The anisotropy values were determined as described in chapter 2. The polar and azimuthal angular dependence of the resonance field of a 15 ML sample is shown in Fig. 8.3 as an example. In our analysis the $g$ factor $g = 2.09$ was assumed to be isotropic. The absolute value of the saturation magnetization $M$ was determined by performing *in situ* SQUID magnetometry on the same samples.

The FMR data indicate that the magnetization favors an in-plane alignment in the whole thickness range as can be seen from Fig 8.3(a). The easy axis of magnetization is along the [1$\bar{1}$0]-crystallographic direction of the InP(001) substrate for $d$ $<$7 ML and rotates by 45° towards the [100]-direction for thicker Fe layers.
The *in situ* SQUID data show a reduced value for the absolute value of the film magnetization compared to the Fe bulk (by 15% for a 5 ML sample and 9% for a 21 ML one). This is likely due to the formation of Fe-compounds with a lower magnetization value. The measured anisotropy terms and the magnetization of the samples are listed in Tab. 8.1.

The out-of-plane anisotropy field is found to be negative meaning that the magnetization favors an in-plane alignment for all films. After subtracting the shape anisotropy contribution, the perpendicular uniaxial anisotropy is found to be strongly thickness dependent (column 2

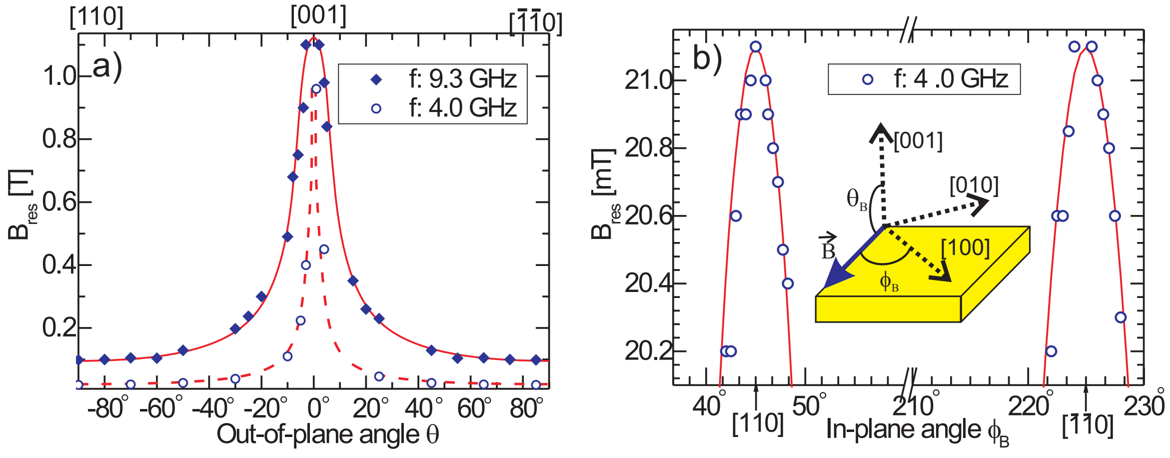

**Figure 8.3.:** Typical (a) polar and (b) azimuthal angular dependence of the FMR resonance field of 15 ML Fe on {2×4}InP(001) at RT and microwave frequencies of 4 and 9.3 GHz. The inset of (b) shows the coordinate system used in our FMR data analysis.

| Thickness (ML) | $K_{2\perp}$ ($10^5$J/m$^3$) | $K_4$ ($10^4$J/m$^3$) | $K_{2\parallel}$ ($10^4$J/m$^3$) | $M$ ($10^6$A/m) |
|---|---|---|---|---|
| 5 | 11.5 | 0.9 | 1.10 | 1.45 |
| 8 | 11.5 | 0.9 | 0.75 | 1.48 |
| 10 | 10.5 | 0.95 | 0.60 | 1.5 |
| 12 | 8.8 | 1 | 0.50 | 1.55 |
| 15 | 8 | 1 | 0.35 | 1.5 |
| 18 | 7 | 1 | 0.29 | 1.55 |
| 20 | 6 | 1.05 | 0.25 | 1.5 |
| 21 | 5.5 | 1.1 | 0.24 | 1.6 |

**Table 8.1.:** Room temperature magnetic anisotropy constants of Fe on {2×4}InP(001) for different film thicknesses determined by *in situ* FMR. The error bar in magnetic anisotropy constants and magnetization is about 5%.

Tab. 8.1). This is a rather large surface-interface value close to the one, which we found in chapter 4 for Fe films on {4×6}GaAs(001).

The cubic anisotropy $K_4$ is positive favoring an easy axis along the $\langle 100 \rangle$-directions. It is relatively small compared to the Fe cubic anisotropy and nearly constant for all Fe thicknesses.

The in-plane uniaxial anisotropy $K_{2\parallel}$ is found to favor an easy axis along the [1$\bar{1}$0]-direction and is strongly thickness dependent. This indicates that the in-plane uniaxial anisotropy originates mainly from the interface of the film and the substrate and is influenced by a tensile strain along the [1$\bar{1}$0]- and [110]-direction. Moreover, it might result from a change of the electronic structure of the Fe atoms confined to the interface. We will come back to this point in Sec. 8.5.

The interplay between $K_4$ and $K_{2\parallel}$ explains the observed spin reorientation transition from the [1$\bar{1}$0]-direction for thinner Fe layer towards the $\langle 100 \rangle$-directions for thicker ones. The equilibrium angle of magnetization (Fig. 8.4) with respect to the [100]-direction as a function of film thickness was calculated using the values of Tab. 8.1 based on the minimization of the free energy in the steady state condition when no external magnetic field is applied. Figure 8.4 shows the evolution of the easy axis of the magnetization with increase of the nominal number of Fe layers. Figure 8.4 clearly shows that the easy axis of magnetization rotates gradually from the [1$\bar{1}$0]-direction for a 5 ML Fe layer towards the [100]-direction for thicker layers. The in-plane spin reorientation transition in Fe/InP is extends over a larger thickness range than in the case of Fe/InAs (see Fig. 6.4). This is due to the difference in the thickness dependence of the anisotropy fields in these two structures.

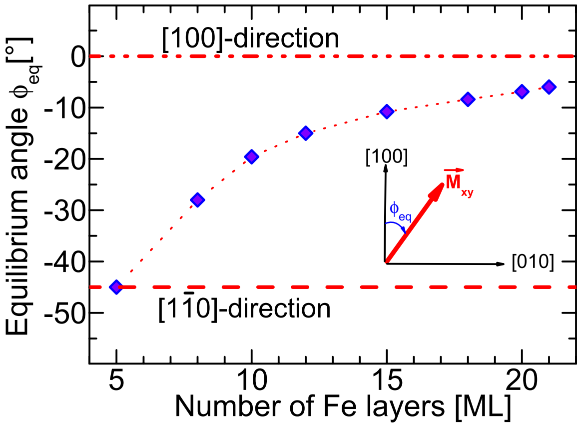

**Figure 8.4.:** Evolution of the in-plane equilibrium angle of magnetization with increasing number of Fe layers.

## 8.4. FMR dispersion relation

Figure 8.5 shows the resonance frequency versus resonance field for the magnetic field applied along the [110]-direction. The solid and dashed-dotted curves show the numerically calculated dispersion relation based on Eq. (2.23) for a 5 and a 21 ML sample, respectively. The calculated dispersion relation predicts an unsaturated branch for 5 ML below 3 GHz. At 9.3 GHz the low field (unsaturated) resonance of the 21 ML film cannot be excited due to the smaller in-plane uniaxial anisotropy. The point at $f$=24 GHz is for a 3 nm Au capped film, which has been measured *ex situ*.

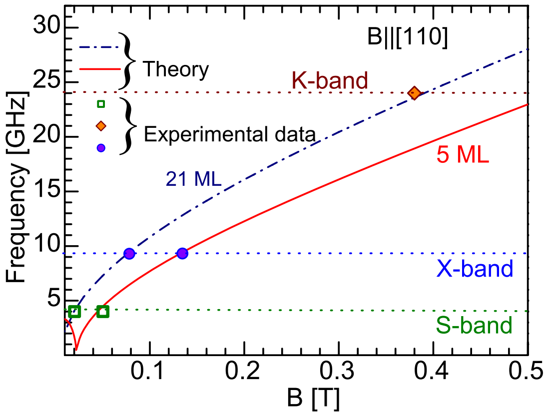

**Figure 8.5.:** Resonance frequency as a function of resonance field (dispersion relation) of a 5 and a 21 ML Fe film on {2×4}InP(001). The measurements were performed at RT with an external magnetic field applied along the [110]-direction.

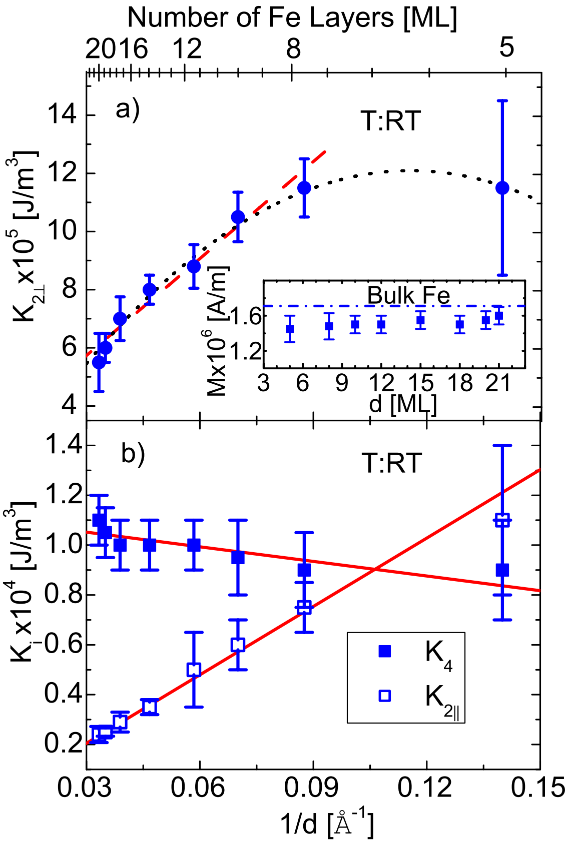

**Figure 8.6.:** (a) The perpendicular $K_{2\perp}$ and (b) cubic $K_4$ and uniaxial in-plane $K_{2\|}$ magnetic anisotropy constants of Fe/{2×4}InP(001) as a function of the reciprocal film thickness. The dashed and solid lines represent linear fits whereas the dotted line denotes a parabolic fit according to $K_{2\perp} = K^v_{2\perp} + (K^{s,\alpha}_{2\perp} + K^{s,\beta}_{2\perp}/d)/d$. The inset of (a) shows the thickness dependence of the magnetization measured by *in situ* SQUID.

## 8.5. The surface-interface & volume contributions to the magnetic anisotropy

According to the reciprocal thickness dependence of the anisotropy constants one would be able to separate the surface-interface as well as the volume contributions to the overall anisotropy constants [58]. In Fig. 8.6 the anisotropy constants are plotted as a function of the reciprocal Fe thickness and the separated volume and surface-interface contributions are listed in Tab. 8.2.

The perpendicular magnetic anisotropy $K_{2\perp}$ shows a deviation from the $d^{-1}$-dependence (see Fig. 8.6). However, if we assume that the surface anisotropy is proportional to $d^{-1}$, the data for Fe thicknesses above 8 ML can be fitted with a large surface-interface contribution $K^{\text{s, eff}}_{2\perp} = (1.1 \pm 0.1) \times 10^{-3}$ J/m$^2$ close to the value, which has been determined for Fe films

| System | $K^v_{2\perp}$ $(10^5\,\frac{\mathrm{J}}{\mathrm{m}^3})$ | $K^v_4$ $(10^4\,\frac{\mathrm{J}}{\mathrm{m}^3})$ | $K^v_{2\parallel}$ $(10^4\,\frac{\mathrm{J}}{\mathrm{m}^3})$ | $K^{\mathrm{s,eff}}_{2\perp}$ $(10^{-3}\,\frac{\mathrm{J}}{\mathrm{m}^2})$ | $K^{\mathrm{s,eff}}_4$ $(10^{-5}\,\frac{\mathrm{J}}{\mathrm{m}^2})$ | $K^{\mathrm{s,eff}}_{2\parallel}$ $(10^{-5}\,\frac{\mathrm{J}}{\mathrm{m}^2})$ |
|---|---|---|---|---|---|---|
| Fe/InP(001) | $2.4 \pm 0.1^\dagger$ | $1 \pm 0.2$ | 0 | $1.1 \pm 0.1^\dagger$ | $-0.1 \pm 0.2$ | $0.9 \pm 0.1$ |
| Fe/GaAs(001) [62] | -1.7 | 6.6 | 0 | 1.17 | -6.1 | -8.9 |

**Table 8.2.:** Surface-interface and volume contribution to the magnetic anisotropy constant of Fe films grown on {2×4}InP(001).

† By assuming a reciprocal thickness dependence for the Fe layers with a thickness of above 8 ML.

grown on {4×6}GaAs(001) ($K^{\mathrm{s,\,eff}}_{2\perp} = (1.17 \pm 0.1) \times 10^{-3}$ J/m$^2$ [62]). Its volume term ($K^v_{2\perp} = (2.4 \pm 0.1) \times 10^5$ J/m$^3$ ) is relatively small in comparison to the surface-interface term. It has been shown by Sander [53] that the in-plane strain results in a perpendicular uniaxial anisotropy. The value of the strain induced anisotropy is given by $K^{MEL}_{2\perp} = B_1(\epsilon - \epsilon_{33})$, where $\epsilon_{33}$ is the out-of-plane strain component and is related to the in-plane one $\epsilon$, $\epsilon_{33} \simeq -2\epsilon$ [52,53]. In this case $\epsilon_{33}$ is negative meaning that in contrary to bulk Fe, the first order magneto-elastic coupling constant $B_1$ should be positive, which indeed reported for Fe/GaAs [101,102]. Moreover, the thickness dependence of $K_{2\perp}$ can be expressed as $K_{2\perp} = K^v_{2\perp} + (K^{s,\alpha}_{2\perp} + K^{s,\beta}_{2\perp}/d)/d$. Here it is assumed that the strain is not linear in $d^{-1}$. This approach results in a value of $K^{s,\alpha}_{2\perp} = (2 \pm 0.5) \times 10^{-3}$J/m$^2$, $K^{s,\beta}_{2\perp} = (-9 \pm 0.5) \times 10^{-3}$J/m, and a thickness independent term being nearly zero ($K^v_{2\perp} \approx 0$). This interpretation means that the interface anisotropy changes as the nominal number of Fe layers increases. This arises from the fact the interface stress changes as the surface reconstruction changes to a new interface consisting of Fe, In, and P and their compounds with different stoichiometry.

From the linear fit in Fig. 8.6(b) the volume contribution to the cubic anisotropy is found to be $K^v_4 = (1 \pm 0.2) \times 10^4$ J/m$^3$. The positive sign indicates that the $\langle 100 \rangle$ directions are the favored easy axes, which are the bulk easy axes of Fe. The value of $K^v_4$ is more than 4 times smaller than the bulk Fe cubic anisotropy ($K^{bulk}_4 = 4.8 \times 10^4$ J/m$^3$). This is likely due to intermixing of the substrate material and formation of phosphide compounds (Fe$_x$P$_{1-x}$), as it is well known that the magnetic anisotropy and Curie temperature of Fe phosphide compounds are smaller than the ones of bulk Fe [167,168]. This is in good agreement with the fact that Fe/InP is the most reactive interface compared to the other semiconducting substrates [157]. Another reason could be the poor crystallinity of the samples as revealed by the vanishing LEED pattern, We note, however, that the surface segregation of In on Fe layer might hinder the observation of the LEED pattern, so that no clear conclusion about the crystallinity of the Fe films can be drawn.

The surface-interface contribution to the cubic anisotropy $K^{\mathrm{s,\,eff}}_4$ has been found to be approximately zero in contrary to the value which is reported in chapter 4 for Fe films grown on {4×6}GaAs ($K^{\mathrm{s,\,eff}}_4 = -6.1 \times 10^{-5}$ J/m$^2$) [62].

While the surface-interface contribution to the in-plane uniaxial anisotropy is relatively large ($K_{2\|}^{\mathrm{s,\,eff}} = 0.9 \times 10^{-5}$ J/m$^2$), the volume contribution is almost negligible. It was demonstrated that the uniaxial strain in the film plane results in an anisotropy term of uniaxial character [52,53]. By assuming a coherent strain in [110] and [1$\bar{1}$0] directions the uniaxial in-plane magneto-elastic anisotropy can be written as $K_{2\|}^{MEL} = 2B_2\epsilon_{12}$. For a further evaluation one needs the second order magneto-elastic coupling constant $B_2$, which according to our knowledge has not been measured for Fe films on InP. The lattice mismatch in Fe/InP is positive in contrary to the one of Fe/GaAs. Since the measured $K_{2\|}$ for Fe/InP is positive we conclude that the second order magneto-elastic coupling constant $B_2$ should be positive (as it is known for Fe/GaAs $B_2 = 7.2 \times 10^6$ J/m$^3$ [101,102] and bulk Fe $B_2 = 7.8 \times 10^6$ J/m$^3$ [53]). However, direct evidence of this assumption is lacking.

## 8.6. The onset of ferromagnetic order

In order to study the onset of long range ferromagnetic order sub-monolayers of Fe were grown from 1 up to 5 ML and FMR and SQUID experiments were performed as a function of nominal

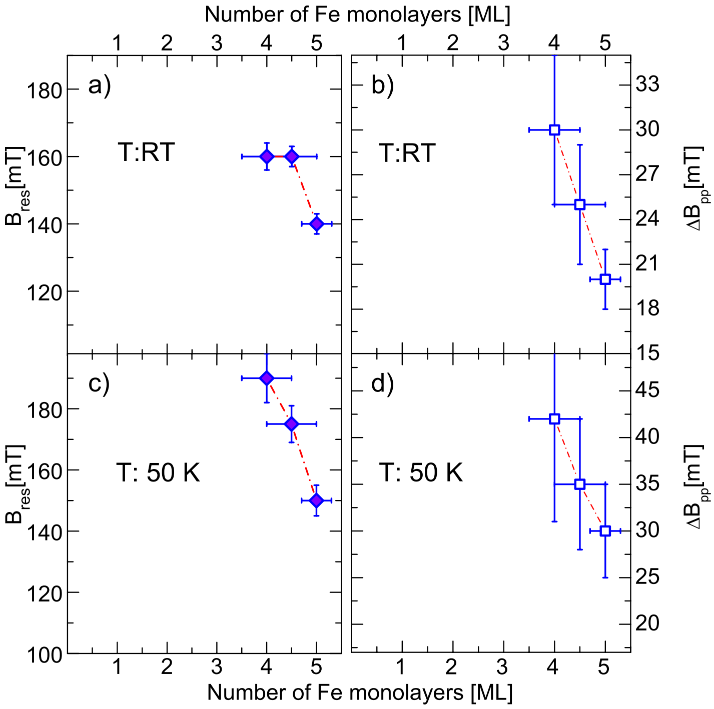

**Figure 8.7.:** Evolution of the FMR resonance field ((a) and (c)) and linewidth ((b) and (d)) with the nominal number of Fe layers recorded at RT (upper panels) and at 50 K (lower panels) with an external magnetic field applied along the [1$\bar{1}$0]-direction.

number of Fe layers at RT and at 50 K. The FMR measurements were performed at $f = 9.3$ GHz in which the external magnetic field was applied along [110]-direction. A ferromagnetic signal was detected by SQUID from 2 ML onwards at 50 K (LT) but no signal was observed by FMR up to 4 ML.

The results of the thickness dependence of the FMR resonance field and linewidth are shown in Fig. 8.7. The reason that no ferromagnetic signal could be observed by FMR for film thicknesses below 4 ML is still not clear. It can be related to the large $\Delta B_{pp}$ which results from the large size distribution of the 3D-like Fe clusters. The coalescence of Fe clusters and formation of a continuous film takes place in thicker Fe layers as reported by Zavaliche *et al.* using STM studies [165].

## 8.7. Summary

In summary the magnetic anisotropy and magnetization of 5–21 ML thick Fe films grown on $\{2\times4\}$InP were determined using *in situ* FMR and SQUID, respectively. It is found that the cubic anisotropy is not thickness dependent and has a small value in comparison to the one of bulk Fe. The surface contribution to the perpendicular uniaxial anisotropy is positive (favoring an out-of-plane magnetization direction) and strongly thickness dependent. It is very close to the measured value for Fe/GaAs.

The perpendicular and in-plane uniaxial anisotropy are related to strain due to the misfit between film and substrate.

The onset of ferromagnetic order at 50 K was found to be 4 ML by FMR, whereas the SQUID measurements shows a weak ferromagnetic signal for a 2 ML sample.

Our magnetic characterization shows that in principle Fe/InP has the capability to be used in *spintronic* devices or relevant magneto-electronic application because of ordered magnetic structure which can be achieved.

# 9. A comparison among Fe/Semiconductor structures

*In this chapter the results of the different systems are compared. The critical thickness of long-range ferromagnetic order, the easy magnetization direction, the thickness where the in-plane spin reorientation transition takes place and the measured magnetic anisotropy contributions will be compared to each other.*

In Tab. 9.1 the critical thickness for the onset of long-range ferromagnetic order at room temperature ($T$ =300 K) and $T = 50$ K, the easy magnetization direction and the critical thickness of the spin reorientation transition (SRT) of the Fe monolayers on different substrates and with different buffer and cap layers are summarized. A comparison of the critical thickness for the RT long-range ferromagnetic order of Fe layers directly grown on semiconductors shows that the RT long-range ferromagnetic order appears at approximately the same thickness for Fe/{4×6}GaAs and Fe/{4×2}InAs, but for Fe/{2×4}InP it appears at thicker layers. This is due to the fact that Fe/InAs interface is less chemically reactive than the other interfaces, whereas the

| System | $d_c^{RT}$ (ML) | $d_c^{50K}$ (ML) | Easy axis | $d_c^{SRT}$ (ML) |
|---|---|---|---|---|
| Fe/GaAs | 2.8(1) | 2.3(2) | [110] | 15(2) |
| Ag/Fe/GaAs | 3.1(1) | — | [110] | 15(2) |
| Fe/Ag/GaAs | — | — | [110] | — |
| Fe/InAs | 2.7(2) | — | $[1\bar{1}0]$ | 7(1) |
| Fe/Au/InAs | 5(1) | — | $[1\bar{1}0]$ | — |
| Au/Fe/Au/InAs | 7(1) | — | $[1\bar{1}0]$ | — |
| Fe/InP | 4(1) | 3.8(9) | $[1\bar{1}0]$ | 12(4) |

**Table 9.1.:** The critical thickness for room ($T$ =300 K) and low ($T = 50$ K) temperature long-range ferromagnetic order, the easy axis of magnetization, and the thickness of the spin reorientation transition (SRT) of the Fe monolayers in different layered structures.

most chemically reactive interface is the Fe/InP interface. A comparison among the cases with buffer layers indicates that the inter-diffusion in the Fe/Au interface is significantly stronger than the Fe/Ag interface. This means that although Au reduces the effect of band structural mismatch, the inter-diffusion of Au to the Fe layers changes the magnetic properties.

The direction of the magnetization for thin Fe layers is given by the direction of the in-plane uniaxial anisotropy. For thicker layer (thicker than a critical thickness, $d_c^{SRT}$) the direction of the easy axis will be parallel to the direction of the cubic anisotropy ([100]-direction). The largest in-plane uniaxial anisotropy was found for Fe/{4×6}GaAs followed by Fe/{2×4}InP and Fe/{4×2}InAs. The largest cubic anisotropy was found for Fe/{4×2}InAs followed by Fe/GaAs and Fe/{2×4}InP. The overcoming of the cubic anisotropy leads to a spin reorientation transition near $d_c^{SRT} \approx$=7 ML for Fe/{4×2}InAs, whereas the one of Fe/{2×4}InP and Fe/{4×6}GaAs happens at larger thicknesses ($d_c^{SRT} \approx$12 ML and $d_c^{SRT} \approx$15 ML).

Table 9.2 provides a direct comparison of the different contributions to the magnetic anisotropy constants of the Fe-base layered structures studied in this work.

In Fe/{4×6}GaAs(001), the volume contribution to the uniaxial anisotropy and a part of surface-interface uniaxial in-plane anisotropy result from the misfit induced stress in the film plane. The direction of the easy axis can be understood by the compressive stress in the film plane. A quantitative explanation of the in-plane anisotropy needs a consideration of the changes in the electronic structure at the interface.

In Fe/{4×2}InAs(001) the volume contribution to the perpendicular uniaxial anisotropy and

| System | $K^v_{2\perp}$ ($10^5 \frac{J}{m^3}$) | $K^v_4$ ($10^5 \frac{J}{m^3}$) | $K^v_{2\parallel}$ ($10^5 \frac{J}{m^3}$) | $K^{s,\mathrm{eff}}_{2\perp}$ ($10^{-3} \frac{J}{m^2}$) | $K^{s,\mathrm{eff}}_4$ ($10^{-5} \frac{J}{m^2}$) | $K^{s,\mathrm{eff}}_{2\parallel}$ ($10^{-5} \frac{J}{m^2}$) | $\epsilon$ (%) |
|---|---|---|---|---|---|---|---|
| Fe/GaAs | -1.7(8) | 0.6(1) | 0.2(2) | 1.17(10) | -6.1(1) | -8.9(4) | -1.6 |
| Ag/Fe/GaAs | -1.7(8) | 0.4(1) | 0.1(2) | 0.9(1) | -3(1) | -8.2(4) | -1.6 |
| Fe/Ag/GaAs | — | — | 0.1(2) | – | — | -6.5(4) | — |
| Fe/InAs | 3.1(7) | 0.68(5) | 0.12(5) | 0.9(1) | -4.6(5) | 0.08(5) | +5.4 |
| Fe/Au/InAs | 1.8(7) | 0 | 0.02(1) | 1.0(1) | 0 | 0 | — |
| Au/Fe/Au/InAs | — | 0 | 0 | — | 0 | 0 | — |
| Fe/InP[†] | 2.4(1) | 0.1(2) | 0 | 1.1(1) | -0.1(2) | 0.9(1) | +2.2 |

**Table 9.2.:** The surface-interface and volume contributions to the magnetocrystalline anisotropy of the Fe monolayers in different layered structures. The lattice mismatch in the last column is defined as $\epsilon = (a_{\text{substrat}} - a_{\text{film}})/a_{\text{substrat}}$.

[†] These results were obtained by assuming a linear reciprocal thickness dependence of $K_{2\perp}$, for a film thickness above 8 ML. The perpendicular uniaxial anisotropy shows, however, a deviation from the linear dependence, which is due to the thickness dependence of the strain in the film (for more details see chapter 8).

both surface-interface and volume contributions to the uniaxial in-plane anisotropy have an opposite sign in comparison to the values of Fe/{4×6}GaAs. This is related to the opposite sign of the strain in this system ($\epsilon > 0$).

Similar to the ones of Fe/{4×2}InAs(001), the volume contribution to the perpendicular anisotropy and the contributions to the uniaxial in-plane anisotropy of Fe/{2×4}InP(001) have the opposite of those of Fe/GaAs. This is also due to the fact that both Fe/InP and Fe/InAs have positive lattice mismatches whereas Fe/GaAs has a negative lattice mismatch. In contrary to the Fe/{4×6}GaAs(001) and Fe/{4×2}InAs(001) systems, in Fe/{2×4}InP the strain is thickness dependent because of the high reactivity of the Fe/InP interface and consequently formation of the $Fe_xP_{1-x}$ compounds.

Although the surface contribution to the perpendicular magnetic anisotropy in Ag/Fe/{4×6} GaAs(001) is suppressed by about 20%, the other magnetic anisotropy contributions are only slightly affected in comparison to the Fe/{4×6}GaAs system. For the Fe/Ag/{4×6}GaAs(001) system a reversed situation is governing. While the surface contribution to the magnetic anisotropy constants are unaffected, the interface uniaxial anisotropy is decreased by about 25% in comparison to Fe/{4×6}GaAs. This can be understood from the fact that the Ag layer change both stress and the electronic structure of the Fe films at the interface.

A comparison to the Fe/InAs Fe/Au/{4×2}InAs(001) and Au/Fe/Au/{4×2}InAs(001) shows no in-plane anisotropy. The volume contribution to the perpendicular magnetic anisotropy is also suppressed by 40%. These observation can be attributed to the inter-diffusion of the Au to Fe layers.

In summary, most of magnetic properties of the studied systems are directly related to the strain, structure and the nature of the interfaces, which are included in these layered structures.

# 10. Fe$_3$Si thin films on MgO(001)

*In this chapter the experimental results of the magnetic as well as structural characterization of epitaxial 4–40 nm Fe$_3$Si/MgO(001) thin films investigated by ex situ ferromagnetic resonance, superconducting quantum interference device magnetometry, and magneto-optical Kerr effect are presented. Magnetic anisotropy energy, $g$-factor, and magnetization as well as magnetic relaxation parameters were determined for different samples with Si concentrations of 20, 25, and 30 %. Additionally, different annealing procedures were applied. It was found that the films have a dominating cubic anisotropy $K_4 \approx 3 \cdot 10^3$ J/m$^3$ that is about one order of magnitude smaller than the one of bulk-Fe. The magnetization was determined to be on the order of $\mu_0 M$ ≈1 T which is less than half of the value for bulk Fe ($\mu_0 M$=2.1 T). A small uniaxial in-plane and a larger out-of-plane anisotropy of interfacial nature was detected. From frequency dependent ferromagnetic resonance measurements an isotropic $g$-factor $g = 2.075(5)$ was found which is slightly smaller than the one of bulk Fe ($g = 2.091$). For the 4 nm film a small enhancement was observed ($g = 2.080(5)$). The magnetic anisotropy fields and the $g$-factor decrease linearly as the Si concentration increases within the D0$_3$-regime. The spin and orbital magnetism of the 8 nm Fe$_{2.8}$Si$_{1.2}$, Fe$_3$Si, and Fe$_{3.2}$Si$_{0.8}$ epitaxially grown films were determined by combination of FMR and SQUID magnetometry. The effective spin and orbital moment of the stoichiometric Fe$_3$Si was found to be $\mu^{\mathit{eff}}_{S(L)} = 1.38\mu_B(0.051\mu_B)$, which is smaller than the one of bulk-Fe [$\mu^{\mathit{eff}}_{S(L)} = 2.24\mu_B(0.103\mu_B)$] by a factor of roughly two as was confirmed by our density functional theory calculations [$\mu^{\mathit{eff}}_{S(L)} = 1.75\mu_B(0.029\mu_B)$]. The reduced spin and orbital moments are due to the fact that in Fe$_3$Si the atomic orbitals are more affected (quenched) by the ligand field than in bcc bulk Fe. Two relaxation channels, i.e., isotropic intrinsic Gilbert damping and anisotropic two-magnon scattering are simultaneously identified by detailed analyses of the frequency and angular dependence of the FMR linewidth. The scattering rates for spin-waves propagating in $\langle 100 \rangle$- and $\langle 110 \rangle$-directions ($\gamma\Gamma_{\langle 100 \rangle} = 0.25(2)$ GHz and $\gamma\Gamma_{\langle 110 \rangle} = 0.04(2)$ GHz) due to two-magnon scattering at the crystallographic defects and the isotropic Gilbert damping term G=0.051(1) GHz are determined. We show that by changing the film thickness from 8 to 40 nm and by slightly modifying the Fe concentration one can tune the non-Gilbert type relaxation via changing the density of the available spin-waves with non-zero wave-vectors as well as the Gilbert relaxation via changing the spin-orbit coupling.*

## 10.1. Introduction

It has been demonstrated by theoretical as well as experimental investigations that Heusler alloys show ferromagnetic order [169–171]. It is, however, still not fully understood, how the ferromagnetism is stabilized on a microscopic level, as it is connected to a quite complex unit cell in these types of materials. There exist two classes of Heusler alloys: (i) *‘full Heusler alloys’* with the general formula $X_2YZ$ and cubic $L2_1$ structure. (ii) *’Half Heusler alloys’* with the general formula XYZ and a $C1_b$ lattice structure (X and Y denote transition metal atoms, while Z is a group II-V element). It was predicted that some of the *‘full Heusler alloys’* are fully spin polarized at the Fermi level and have half-metallic character, e. g. $Co_2MnSi$ [171–174].

$Fe_3Si$ is a binary Heusler alloy ($Fe_2FeSi$) with a cubic $D0_3$ structure. It has a spin polarization of 43% (at T=0 K) in addition to its high Curie-temperature being 820 K [26–28]. In Fig. 10.1 a schematic drawing of the $Fe_3Si$ lattice and the calculated density of states (DOS) [142] is shown. The lattice parameter is close to the one of many SC substrates (i.e. GaAs). These aspects make it a very promising candidate for applications in spintronics. Bulk-$Fe_3Si$ was intensively investigated theoretically [175–177] and experimentally [26–28,178] with respect to its magnetic and microstructural behavior. In order to realize the application of $Fe_3Si$ in future magneto-electronic and *spintronic* devices the growth of well ordered ultrathin magnetic structures is required. In contrast to bulk, the epitaxial growth and magnetic properties of $Fe_3Si$ films on semiconducting substrates have been investigated by a few groups only, i. e. $Fe_3Si$/Si(Ge) [29–34] and $Fe_3Si$/GaAs(001) [35–43]. Besides the growth on semiconductors, the growth of $Fe_3Si$ films on MgO(001) substrates is of interest in connection with the Tunnel Magnetoresistance (TMR) effect. The TMR effect results from the quantum mechanical tunnelling effect with spin-split transition probabilities. The TMR can be illustrated best by the simplest system of two ferromagnetic layers separated by an insulating spacer layer. It has been predicted [44] and later demonstrated [45–47] that the TMR effect increases just by replacing the amorphous $Al_2O_3$ insulating layer by a crystalline MgO barrier in FM/MgO/FM magnetic tunnelling junctions (MTJ).

In this chapter we report on the structural and magnetic properties of $Fe_3Si$ films epitaxially grown on MgO(001). The magnetic anisotropy as well as the $g$-factor will be quantitatively determined and discussed in terms of their dependence on (i) the film thickness, (ii) different annealing procedures, and (iii) the Si concentration close to stoichiometry. Moreover, the magnetic relaxation process will be studied in this binary Heusler structure by studying the FMR linewidth. The relaxation model by Arias and Mills [81,82,85]is experimentally tested and used to quantitatively determine the magnetic relaxation parameters.

This chapter is organized as follows: Secs. 10.2 and 10.3 provide the results of the growth and structural characterizations. The static magnetic properties such as magnetic anisotropy, $g$-factor, dispersion relation, spin and orbital magnetic moment for different film thickness,

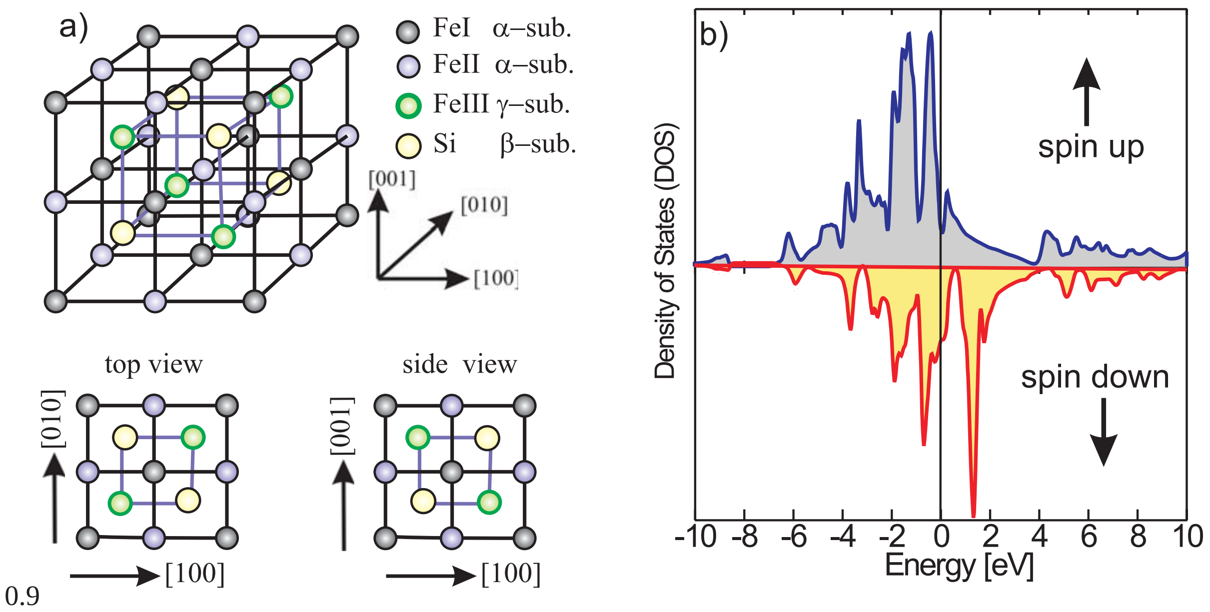

**Figure 10.1.:** (a) Schematic representation of the $D0_3$ structure of $Fe_3Si$ lattice. (b) The calculated total density of states in $Fe_3Si$ calculated by S. J. Hashemifar using Wien2k [142]. The Fermi level is marked as vertical line at E=0 eV.

different sample treatment, and different Si concentration will be presented in Secs. 10.4 to 10.6, respectively. Section 10.8 describes the dynamic magnetic properties of samples with different thickness and Si concentration.

## 10.2. Growth of $Fe_3Si$ on MgO(001)

Epitaxial 4, 8, and 40 nm $Fe_3Si$ films were grown on MgO(001) in an MBE chamber with a base pressure of about $1 \times 10^{-9}$ mbar in the group of Prof. Keune, (University of Duisburg-Essen). The MgO(001) substrate was first cleaned by isopropanol in an ultrasonic bath and afterwards transferred into the UHV chamber. Inside the UHV chamber the substrate was annealed at 1200 K for 30 min. This substrate preparation results in a clean surface. The use of MgO(001) as a substrate to grow epitaxial $Fe_3Si$ thin films is supported by the fact that there is a good match of the lattice parameters along the $Fe_3Si$ $\langle 100 \rangle$- and the MgO-$\langle 110 \rangle$-directions. Using the lattice constants for $Fe_3Si$ (0.565 nm) and MgO (0.423 nm), the atomic distance along $Fe_3Si$-[100] is 0.567 nm, while for MgO-[110] it is 0.598 nm. This leads to a lattice mismatch of 5.2% with the two lattices being rotated by 45°. The film is thus expected to be under tensile strain in the film plane. During the film deposition the substrate was kept at a constant temperature of $T_s = 485$ K, while the films were grown by co-evaporation of $^{57}$Fe and Si. The growth rate was about 1 nm/min, which was monitored using a calibrated quartz microbalance. In order to avoid any oxidation, the samples were capped with 5 nm of chromium. To verify that the chromium layer has no influence on the magnetic properties, uncapped films were also produced for comparison.

In order to investigate influence of the annealing on the magnetic properties, three samples with the thickness of 8 nm were prepared:

**Sample A:** deposited at $T_s$ =480 K.

**Sample B:** has been annealed in UHV for $1$ h at $T_a = 900$ K immediately after growth at $T_s$ =480 K.

**Sample C:** was annealed immediately after growth in UHV in steps of 100 K between $T_a = 550 - 900$ K. At each temperature step the sample was kept for 1 h.

Moreover, to study the influence of the Si concentration on the magnetic parameters, three different samples with the thickness of 8 nm were prepared:

**Sample D** with a Si concentration of 20$\%$.

**Sample E** with a Si concentration of 25$\%$.

**Sample F** with a Si concentration of 30$\%$.

All three samples (D, E, and F) were annealed immediately after deposition in UHV at $T_a = 900$ K for $1$ h in order to reach the favorable $D0_3$ structure as will be discussed in the context of the experimental results (see Sec. 10.4.2).

The structure and stoichiometry of all capped and uncapped samples were verified *ex situ* using X-ray diffraction (XRD) and energy dispersive X-ray analysis (EDX). The actual composition and the $D0_3$ and B2 chemical order parameters of the films were determined by $^{57}$Fe Mössbauer spectroscopy in combination with spectra simulations [179], and found to be 25% and 28% Si for the 8 nm and 40 nm thick films (nominally 25% Si) and 19.5% Si for the 8 nm thick film (nominally 20% Si). Moreover, the actual 28% Si content of the 40 nm sample was independently confirmed by Auger electron spectroscopy (AES) sputter profiling to be 27.7% Si [179].

## 10.3. Structural characterizations

We have performed X-ray diffraction measurements using Cu $K_\alpha$ radiation. In Fig. 10.2 the results are summarized for samples A, B, and C. One can clearly identify the MgO(200) as well as the $Fe_3Si$(200) and $Fe_3Si$(400) reflex. Note, as sample A was capped by Cr, the Cr(200) reflex leads to the shoulder on the left side of the $Fe_3Si$(400) reflex. Since no $K_\beta$ filter was used, the substrate peak has a satellite due to the $K_\beta$ radiation. The occurrence of a satellite due to W

$L_\alpha$ radiation results from a small contamination of the Cu anode. Upon comparing samples A, B, and C one observes that samples A and C present the same diffraction angles of the $Fe_3Si$ reflexes, while for sample B they have slightly higher values (this can be seen better in the inset). The vertical lattice constant that follows for sample B is $a_\perp = 5.63$ Å. As can be seen from the vertical line in the inset representing the bulk value, we conclude that samples A and C have bulk-like lattice constants (0.567 nm), whereas the lattice of sample B is slightly compressed along the film normal. This expected due to the in-plane tensile strain. Sample B shows the highest intensity of the reflexes. The full width at half maximum (FWHM) of all samples is, however, nearly the same, showing that the typical size of the crystallites is quite similar. The $Fe_3Si(400)$ reflex was fitted by a Lorentzian function (in the case of Cr-capped sample with two Lorentzian functions, one for Cr(200) and one for $Fe_3Si(400)$) and the average vertical size of the crystallites were calculated using the well-known Scherrer formula [180]

$$D = \frac{0.94 \cdot \lambda(\mathrm{Cu}_{K\alpha})}{\cos\theta \cdot \Delta\theta_{\mathrm{FWHM}}} \tag{10.1}$$

where $\Delta\theta_{FWHM}$ is the full width of the diffraction peak at half maximum, $\lambda(\mathrm{Cu}_{K\alpha})$ the wavelength of the radiation, 0.94 a factor for cubic symmetry and $\theta$ is the diffraction angle. The spectra linewidth caused by the apparatus is much smaller than 0.1° and can be neglected. Employing Eq. (10.1) leads to average sizes of $D = 6.5 \pm 0.5$ nm. The crystallite sizes are the same for all samples and nearly as large as the film thickness. The higher intensity of the Bragg re-

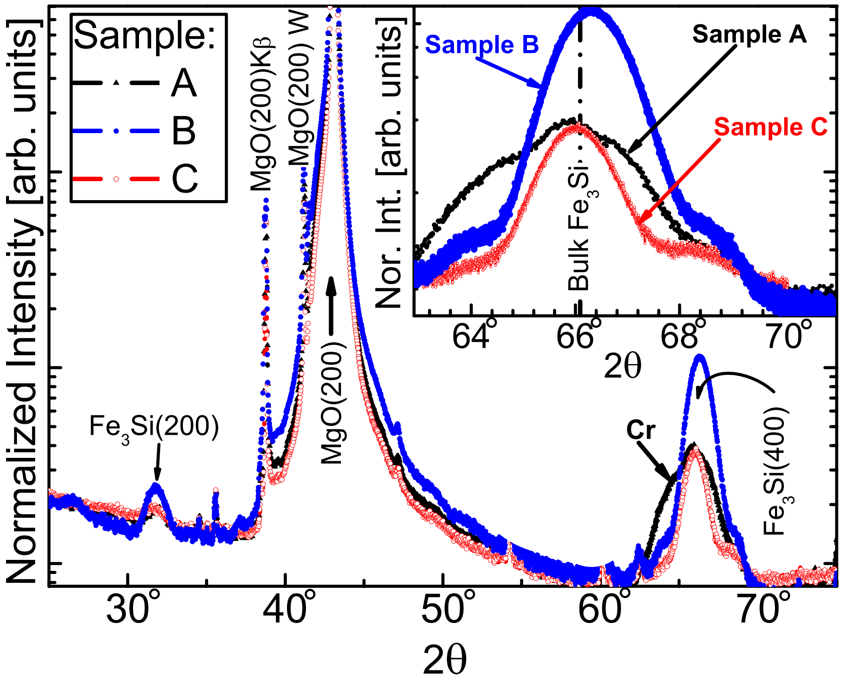

**Figure 10.2.:** XRD spectra of the samples A, B, and C (logarithmic scale). The inset shows the manifestation of the (400)-peak of $Fe_3Si$ .

flexes in the case of sample B indicates a better (100)-orientation of the crystallites and thus the film as a whole, since only the (100) lattice planes determine the intensity in the $\theta/2\theta$-geometry. This is consistent with a larger strain within sample B due to a better orientation on the substrate. To achieve the strained state one obviously needs a well-defined annealing procedure. Heating too much leads to a relief of strain as observed for sample C.

In summary, the X-ray analysis yields clear evidence that sample B has the optimum epitaxial quality (see Fig. 10.2) with an optimum (100)-orientation. This was also confirmed by conversion electron Mössbauer spectroscopy (CEMS) measurements [179].

The epitaxial growth of the Fe$_3$Si on MgO(001) manifests itself in a well-ordered magnetic structure, which will be discussed in the following. First, we present the analysis of the magnetic anisotropy fields. Then we discuss the $g$-factor and the implicit results.

## 10.4. Magnetic anisotropy

In order to determine the anisotropy fields the *ex situ* FMR experiments were carried out at a microwave frequency of 9.9 GHz. The FMR spectra were recorded as a function of the polar and azimuthal angle of the external magnetic field at RT. The absolute value of the magnetization was measured by SQUID magnetometry. In addition to this, the frequency dependence of the FMR spectra was investigated over a wide range of microwave frequencies between 1 and 70 GHz in order to precisely determine the $g$-factor and magnetic relaxation parameter. The measurements at 1, 4, 10, 24, and 35 GHz were performed using microwave cavities, while the additional measurements between 6 and 20 GHz and above 35 GHz were performed by placing the sample into a shorted waveguide termination.

MOKE studies were carried out in order to determine the coercive field as well as the magnetization reversal process. MOKE measurements were performed by F. M. Römer in longitudinal geometry, for which the applied field is oriented parallel to the plane of the incident laser beam.

The polar and azimuthal angular dependence of the resonance field recorded at a microwave frequency of 9.9 GHz for 4 and 40 nm samples (not annealed after preparation) are shown in Fig. 10.3. The fourfold (cubic) symmetry in the azimuthal angular dependence of the resonance field (right panels in Fig. 10.3) indicates that an in-plane cubic anisotropy exists with easy axes along the $\langle 100 \rangle$-directions of the Fe$_3$Si films. This cubic contribution is slightly affected by another small in-plane anisotropy term in the case of the 4 nm sample. This uniaxial anisotropy has uniaxial character and favors an easy axis along a direction which is rotated by -13° with respect to the [100]-direction. Although the origin of the uniaxial contribution could not be unambiguously extracted from the measurements, it must be of interfacial nature, as its value clearly decreases for thicker films. As no difference of the uniaxial in-plane anisotropy was

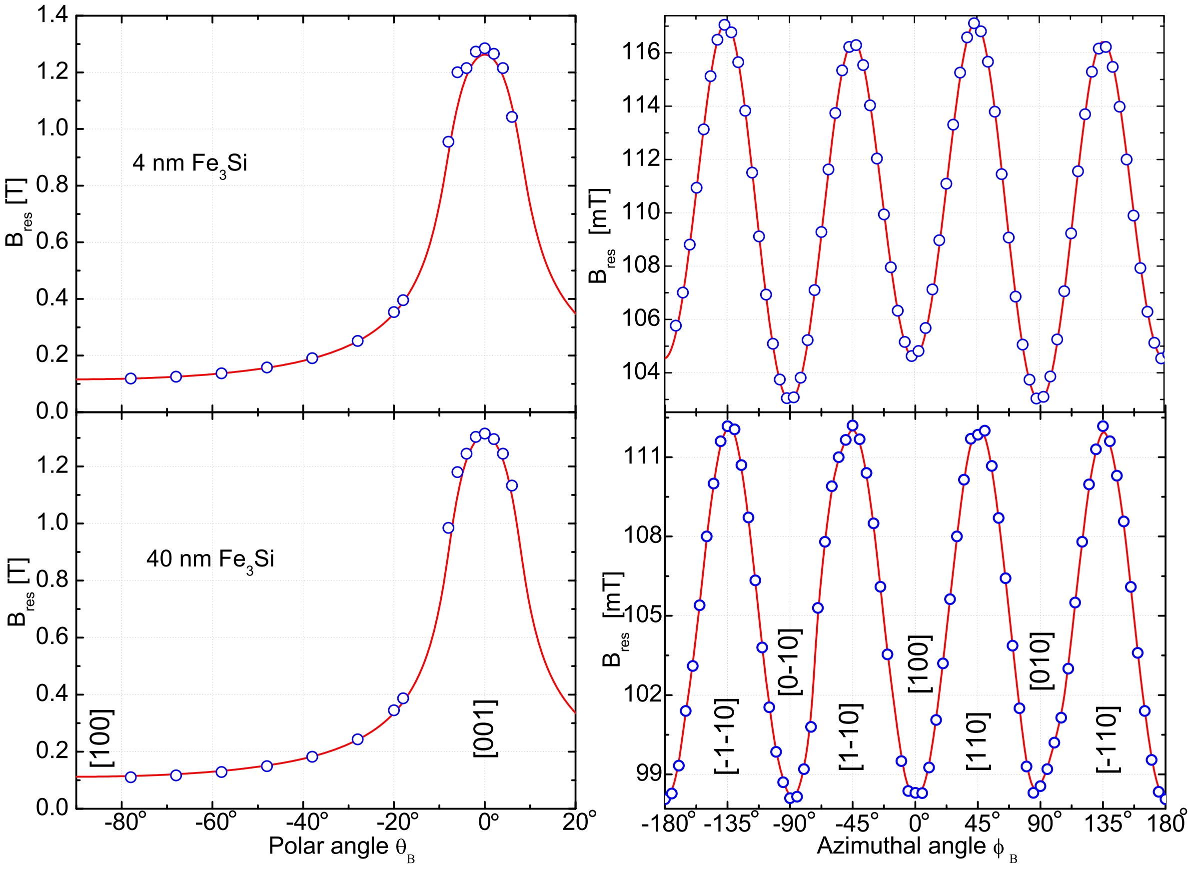

**Figure 10.3.:** Polar and azimuthal angular dependence of the resonance field of a 4 nm (upper row) and a 40 nm (lower row) Fe$_3$Si film measured at a microwave frequency of 9.9 GHz.

found between the uncapped and Cr-capped samples, the cover layer as the origin can be ruled out. We therefore propose that either a small miscut of the substrate or the deposition of Si, which is performed under an oblique angle of about 30° with respect to the film normal are possible sources. While the former leads to steps on the substrate, the latter could result in small islands with a preferential alignment parallel to the projection of the deposition beam onto the sample surface, thus leading to a uniaxial symmetry at the surface.

The anisotropy fields were determined by fitting the experimental FMR data of polar and azimuthal angular dependence of the resonance field using Eqs. (2.21) and (2.22). The anisotropy constant can be found by using the sample magnetization measured by SQUID. In this case 10% error in magnetization—caused by uncertainty of the sample volume— enters into the obtained anisotropy constant. As the anisotropy fields obtained by FMR has only a small error bar (smaller than 1%), in the following section we discuss the anisotropy field instead of the anisotropy constants.

| $d$<br>(nm) | Ref. | $\mu_0 M_{\text{eff}}$<br>(mT) | $K_4/M$<br>(mT) | $K_{2\parallel}/M$<br>(mT) | $\mu_0 M$<br>(mT) | $K_{2\perp}$<br>$(10^3\frac{\text{J}}{\text{m}^3})$ | $K_4$<br>$(10^3\frac{\text{J}}{\text{m}^3})$ | $K_{2\parallel}$<br>$(10^3\frac{\text{J}}{\text{m}^3})$ |
|---|---|---|---|---|---|---|---|---|
| **4 nm** | **[This work]** | **-941** | **3.5** | **0.45** | **1053** | **46.9** | **2.9** | **0.38** |
| **8 nm** | **[This work]** | **-958** | **3.9** | **0.08** | **1052** | **39.4** | **3.3** | **0.07** |
| **40 nm** | **[This work]** | **-978** | **3.9** | **0.00** | **1059** | **34.1** | **3.3** | **0.00** |
| Bulk | [178,181] | -1232 | 5.5 | — | 1232 | — | 5.4 | — |
| 21 nm | [37,38] | — | 4.1 | 0.06 | 931 | — | 3.1 | 0.046 |
| 39 nm | [35] | -1010 | 4.7 | 0.3 | 992 | -7 | 3.7 | 0.2 |

**Table 10.1.:** The magnetic anisotropy fields and the corresponding anisotropy constants of $Fe_3Si$ films for different film thickness. Our results are shown in the upper part while in the lower part the anisotropy fields of a 21 and a 39 nm $Fe_3Si$/GaAs(001) as well as the bulk values are listed. The error bar in anisotropy constants is about 10%, which lies mainly in the uncertainty in the sample volume used to determine the sample magnetization.

### 10.4.1. Thickness dependence of the anisotropy fields

The resulting anisotropy fields for different film thicknesses are summarized in the upper part of Tab. 10.1. whereas the cubic anisotropy field, $K_4/M$ ≈3.9 mT, was found to be almost thickness independent, the effective out-of-plane anisotropy field, $\mu_0 M_{\text{eff}}$ is slightly thickness dependent. The reciprocal thickness dependence of the anisotropy fields is shown in Fig. 10.4. No linear

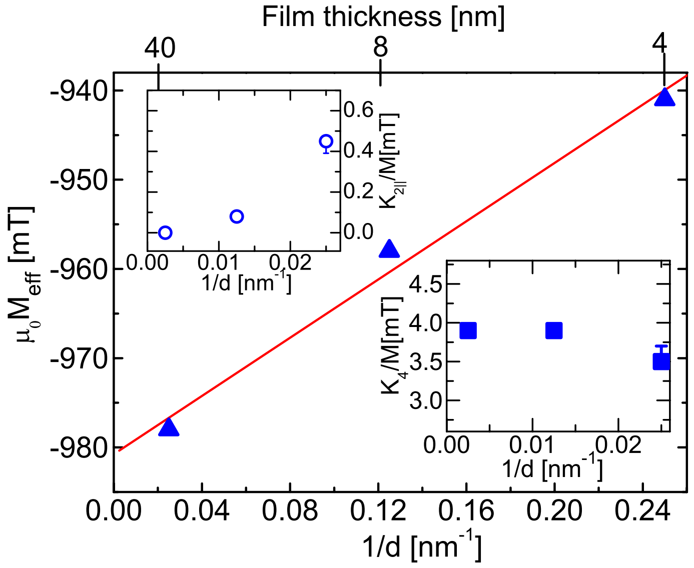

**Figure 10.4.:** The reciprocal thickness dependence of the anisotropy fields. The error bars are smaller than the symbol size.

behavior is found, which can be related to the fact that all three samples are thick enough so that interface contributions are negligible. Our values of $K_4/M$ are similar to the one measured by MOKE for a 21 nm $Fe_3Si$ film grown on GaAs(001) [37,38]. They are, however, smaller than the value of bulk $Fe_3Si$ [178] and of a 39 nm thick sample grown on GaAs(001) [35,43] (see lower part of Tab. 10.1).

$\mu_0 M_{\mathrm{eff}}$ is roughly 2 times smaller than $\mu_0 M_{\mathrm{eff}}^{Fe} = 2.15$ T for Fe bulk, which is due to the fact that the magnetization of $Fe_3Si$ is by a factor of 2 smaller than the one of Fe (the out-of-plane anisotropy field $\frac{2K_{2\perp}}{M}$ is very small in comparison to $\mu_0 M$).

$\mu_0 M_{\mathrm{eff}} = \frac{2K_{2\perp}}{M} - \mu_0 M$ was found to be slightly thickness dependent (see Fig. 10.4). The magnetization was found to be thickness independent (see Tab. 10.1) as measured by SQUID. As the absolute value of $\mu_0 M_{\mathrm{eff}}$ increases with increasing film thickness, $K_{2\perp}$ is positive and becomes larger for thinner films.

To shed light onto the origin of $K_{2\perp}$, we write the reciprocal thickness dependence of the effective out-of-plane anisotropy field in the limit of thin films as $\mu_0 M_{\mathrm{eff}} = \left(\frac{2K_{2\perp}^{\mathrm{v}}}{M} - \mu_0 M\right) + 2\frac{K_{2\perp}^{\mathrm{si}}}{dM}$, where $K_{2\perp}^{\mathrm{si}}$ ($K_{2\perp}^{\mathrm{v}}$) is the surface-interface (volume) contribution to $K_{2\perp}$ and $d$ is the film thickness. Note that a simple proportionality to $1/d$ is valid only for films with thickness independent values of $K_{2\perp}^{\mathrm{si}}$ ($K_{2\perp}^{\mathrm{v}}$), i.e. in a coherent growth regime, where no structural variations occur as discussed in Sec. 2.3. The slope and the y-axis intersection of Fig. 10.4 yields the values of $\mu_0 M - \frac{2K_{2\perp}^{\mathrm{v}}}{M} = 0.981$ T and $\frac{K_{2\perp}^{\mathrm{si}}}{M} = 0.8(2) \times 10^{-10}$ Tm. Using $\mu_0 M$ of the 40 nm sample one calculates $K_{2\perp}^{\mathrm{si}} = 6(2) \times 10^{-5}$ J/m$^2$ and a value for $K_{2\perp}^{\mathrm{v}} = 33(1) \times 10^3$ J/m$^3$.

$K_{2\perp}^{\mathrm{v}}$ and $K_{2\perp}^{\mathrm{si}}$ are very small compared to the shape anisotropy $\frac{1}{2}\mu_0 M^2 = 4.4 \times 10^5 J/m^3$. The positive sign of $K_{2\perp}^{\mathrm{v}}$ indicates that this anisotropy contribution favors an out-of-plane magnetization direction. A twofold volume anisotropy would result from a tetragonal distortion of the cubic lattice [58,62]. Indeed our X-ray analysis (see Fig. 10.2) shows a compressed vertical lattice parameter for the 8 nm sample of $a_\perp = 0.563(2)$ nm which is about 0.3% smaller than the bulk $Fe_3Si$. This indicates that the lattice is still distorted even for the 8 nm samples. Minimizing the elastic energy one expects a smaller vertical value due to the in-plane tensile strain. This is, however, surprising that the 8 nm thick film is not complectly relaxed.

The positive sign of both $K_{2\perp}^{\mathrm{si}}$ and $K_{2\perp}^{\mathrm{v}}$ means that these terms favor an out-of-plane easy magnetization axis (note that a positive sign for the perpendicular surface anisotropy is well-known for Fe films). In the very thin film limit (monolayer regime) $K_{2\perp}$ might even overcome the shape anisotropy, resulting in an out-of-plane easy axis.

## 10.4.2. Influence of thermal treatments on the anisotropy fields

The influence of the thermal treatment on the magnetic anisotropy was studied on samples A, B, and C (see Sec. 10.2). The polar and azimuthal angular dependence of the resonance field for all three samples are shown in Fig. 10.5. The anisotropy fields resulting from fittings the

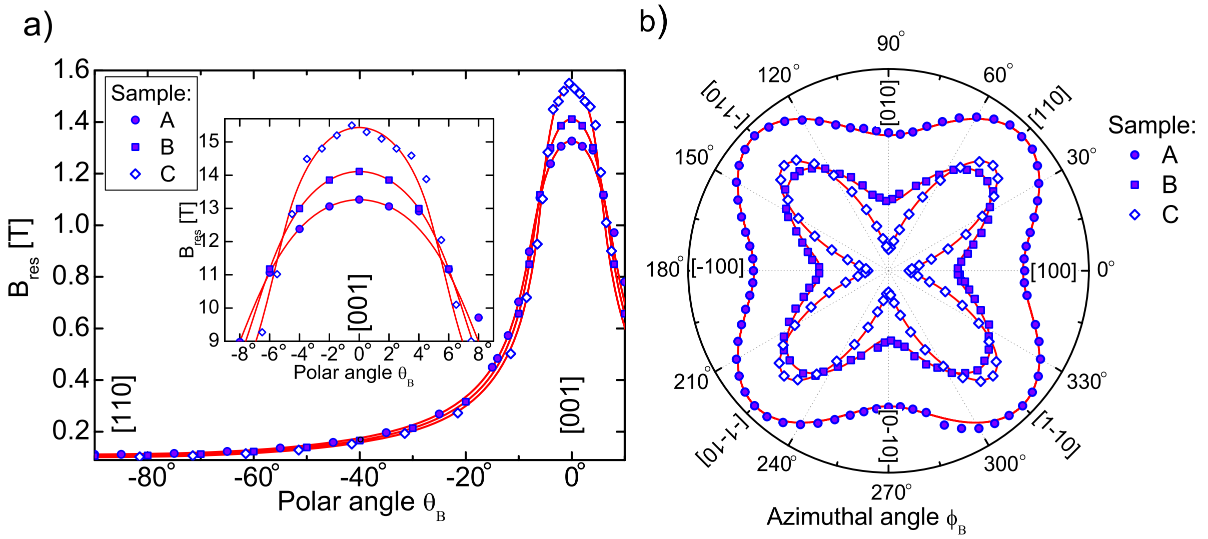

**Figure 10.5.:** (a) Polar and (b) azimuthal angular dependence of the resonance field for sample A, B and C. The resulting anisotropy fields are listed in Tab. 10.2.

| Sample | $\mu_0 M_{\mathrm{eff}}$ (mT) | $K_4/M$ (mT) | $K_{2\|}/M$ (mT) | $\mu_0 M$ (mT) |
|---|---|---|---|---|
| A | -958(7) | 3.9 | 0.008 | 1052 |
| B | -1080(1) | 4.5 | — | 1105 |
| C | -1226(7) | 8.6 | — | 1252 |

**Table 10.2.:** Magnetic anisotropy fields of $Fe_3Si$/MgO(001) prepared by three different annealing procedures. All samples have a thickness of 8 nm. The error bar of the magnetization is 10%, mainly due to uncertainty of the sample volume.
A: Without any annealing procedure,
B: Directly annealed at 900 K for 1 h,
C: Temperature raised from 550 K to 900 K in steps of 100 K (time at each step 1 h).

dependencies are listed in Tab. 10.2. A large enhancement of both, $\mu_0 M_{\mathrm{eff}}$ and $K_4/M$, was observed for the annealed samples compared to the as-prepared one (type A). Our experimental results further show that sample C has even larger anisotropy than sample B. The MOKE data for samples B and C presented in Fig. 10.6 support the finding from FMR. As can be clearly seen, sample B has a smaller saturation field along the [110]-direction compared to sample C. Assuming a coherent rotation between easy and hard in-plane direction, the saturation field along the [110] hard in-plane direction is given by $2K_4/M$. This results in anisotropy fields of $2K_4/M = 9(1)$ mT for sample B, while for sample C, $2K_4/M = 14(1)$ mT are obtained. Both values are consistent with the ones obtained by FMR (see Tab. 10.2). In addition, sample B is

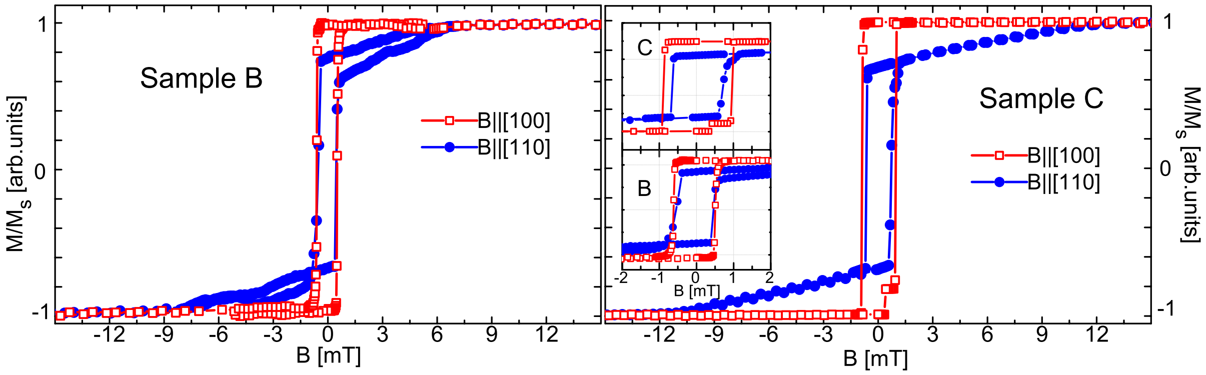

**Figure 10.6.:** MOKE hysteresis loop of sample B (left panel) and sample C (right panel) recorded at RT with the magnetic field applied along the easy $[100]$ and hard $[110]$ in-plane direction, recorded by F. M. Römer. The insets are magnifications of the low field regions.

magnetically softer, as can be seen from the smaller coercivity. This suggests—in combination with our X-ray analysis discussed in Fig. 10.2— that sample B has less structural defects than sample C, leading to an easier motion of the spins during magnetization reversal. In the bulk, all structural phases of $Fe_3Si$ are stable up to a temperature of 1500 K [26], and no temperature induced structural transformation of our samples were observed within our X-ray diffraction study (see Fig. 10.2).

## 10.4.3. Influence of the Si concentration on the anisotropy fields

It is well known that the concentration of the constituents Fe and Si within the binary Fe-Si alloy has a considerable influence on the electronic and magnetic properties [175–177,181]. In order to investigate the influence of the Si concentration on the magnetic parameters, the magnetic anisotropy of 8 nm $Fe_{80}Si_{20}$ (sample D), $Fe_{75}Si_{25}$ (sample E), and $Fe_{70}Si_{30}$ (sample F) thin films were investigated.

| Sample | Si-Con. (%) | $\mu_0 M_{\text{eff}}$ (mT) | $K_4/M$ (mT) | $K_{2\parallel}/M$ (mT) | $\mu_0 M$ (mT) |
|---|---|---|---|---|---|
| Fe-Bulk | 0 | -2150 | 28.05 | — | 2150 |
| D | 20 | -1460(2) | 9.8 | — | 1345 |
| E | 25 | -1144(3) | 5.5 | — | 1105 |
| F | 30 | -1006(7) | 3.05 | 0.12 | 971 |

**Table 10.3.:** Magnetic anisotropy fields of an 8 nm $Fe_{(1-x)}Si_x$ films with different Si concentrations of $x = 20,\ 25$, and 30% measured at RT.

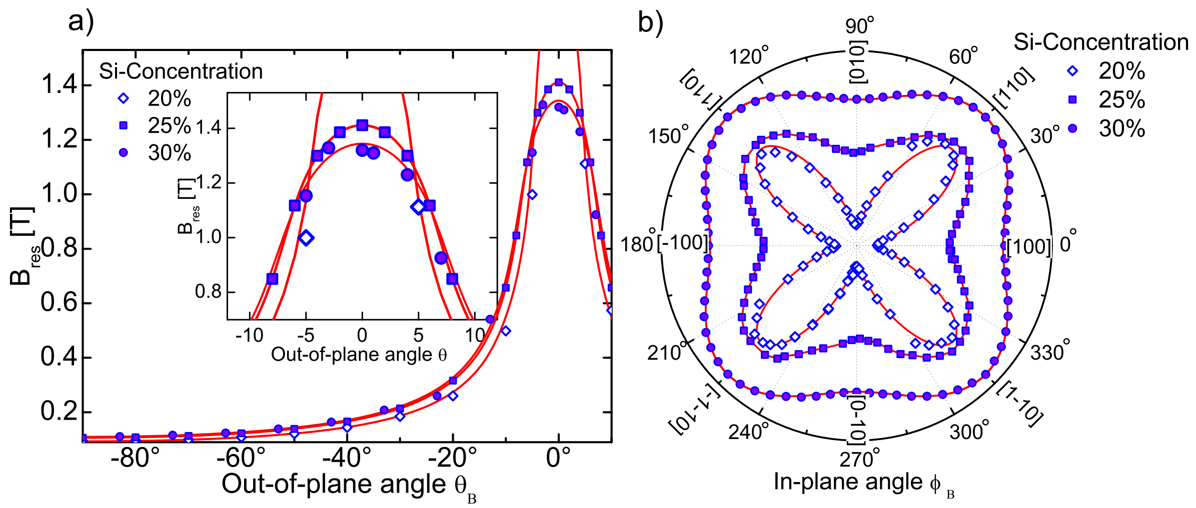

**Figure 10.7.:** (a) Polar and (b) azimuthal angular dependence of the resonance field for different Si concentrations of 20, 25, and 30%. The solid lines are fits according to Eqs. (2.21) and (2.22). The resulting anisotropy fields are listed in Tab. 10.3.

The magnetic anisotropy fields were determined by again performing polar and azimuthal angle dependent measurements. The results are shown in Fig. 10.7 for the three different samples and the resulting anisotropy constants are listed in Tab. 10.3.

Figure 10.8 shows the anisotropy fields as a function of the Si concentration. The anisotropy fields of a 33 nm thick Fe film epitaxially grown on GaAs(001) is also shown as a reference for bulk Fe. Figure 10.8 shows that both $\mu_0 M_{\text{eff}}$ and $K_4/M$ as well as the magnetization $M$ are de-

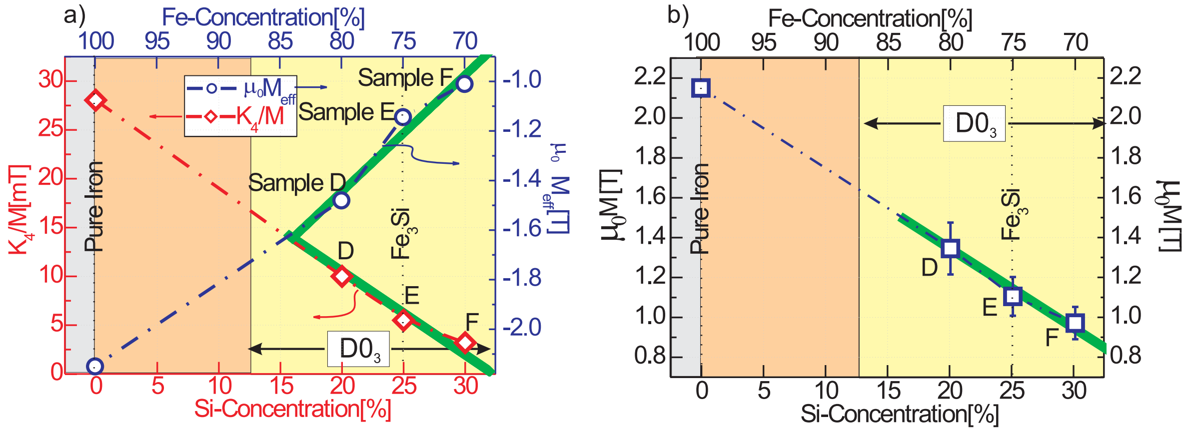

**Figure 10.8.:** (a) Magnetic anisotropy fields and (b) the magnetization as a function of Si concentration of 20, 25, and 30% (samples D, E, and F, respectively) measured at RT. The solid lines are linear fits. The error bar of the magnetization values are due to the uncertainty of the sample volume.

creased by increasing the Si concentration. The magnetization of sample F is reduced by about 30% with respect to sample D and by about 15% with respect to sample E with the optimum Fe and Si concentration (see column 6 of Tab. 10.3). One should note that from the phase diagram of $\mathrm{Fe}_{1-x}\mathrm{Si}_x$ no crystalogryphic changes are expected when varying the Si concentration by 5%, as $\mathrm{Fe}_{1-x}\mathrm{Si}_x$ stabilizes the $\mathrm{D0}_3$ structure at Si concentrations between 12.5 and 31% [26]. The fact that all three samples have $\mathrm{D0}_3$ structure is demonstrated in Fig. 10.9 where the XRD spectra of the samples are shown. As can be seen from Fig. 10.8, the anisotropy fields and magnetization are nearly linear with Si concentration even outside the regime of the $\mathrm{D0}_3$ structure. By fitting the linear behavior of the anisotropy fields within the $\mathrm{D0}_3$-regime, one obtains the concentration dependence of anisotropy fields and magnetization: $K_4/M[mT] = 0.27 - 0.7 \cdot x$, $\mu_0 M_{\text{eff}}[T] = -2.2 + 4 \cdot x$ and $\mu_0 M[T] = 2 - 4 \cdot x$ where $x$ is the Si concentration in the $\mathrm{D0}_3$-regime.

The spin moments of the Fe and Si atoms are strongly related to their positions within the $\mathrm{Fe}_3\mathrm{Si}$ lattice [177]. As it is obvious that by increasing the number of Fe atoms within the cubic $\mathrm{D0}_3$ structure of $\mathrm{Fe}_{1-x}\mathrm{Si}_x$, the configuration of nearest neighbors must change. The spin moment is thus expected to be influenced by concentration. In our $g$-factor analysis we will show that also the orbital magnetic moments decrease with increasing Si concentration and that this decrease is even stronger than the one of the spin magnetic moment. Taking the decrease of both, spin and orbital contribution into account, the spin-orbit coupling itself will be smaller, which in turn explains the smaller magnetic anisotropy of the samples with higher Si content. The main origin of the change of magnetic anisotropy should thus be related to the changes of

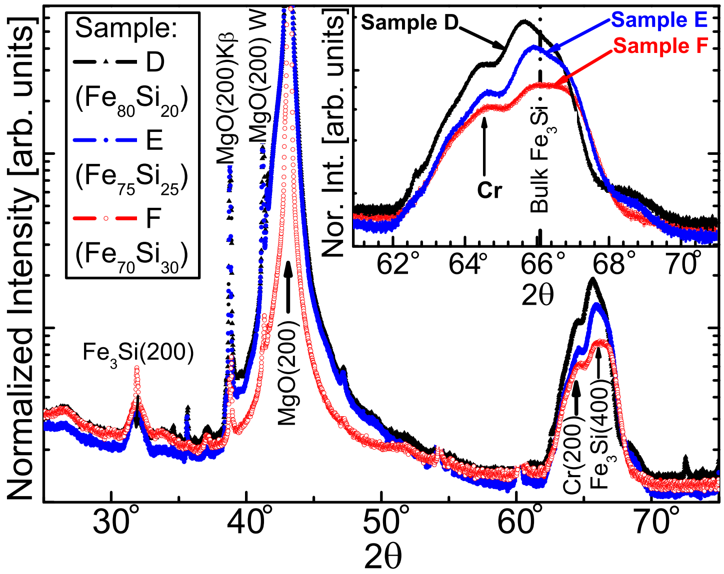

**Figure 10.9.:** XRD spectra of the samples D ($\mathrm{Fe}_{80}\mathrm{Si}_{20}$), E ($\mathrm{Fe}_{75}\mathrm{Si}_{25}$), and F ($\mathrm{Fe}_{70}\mathrm{Si}_{30}$). The inset shows the manifestation of the (400)-peak of $\mathrm{Fe}_3\mathrm{Si}$ .

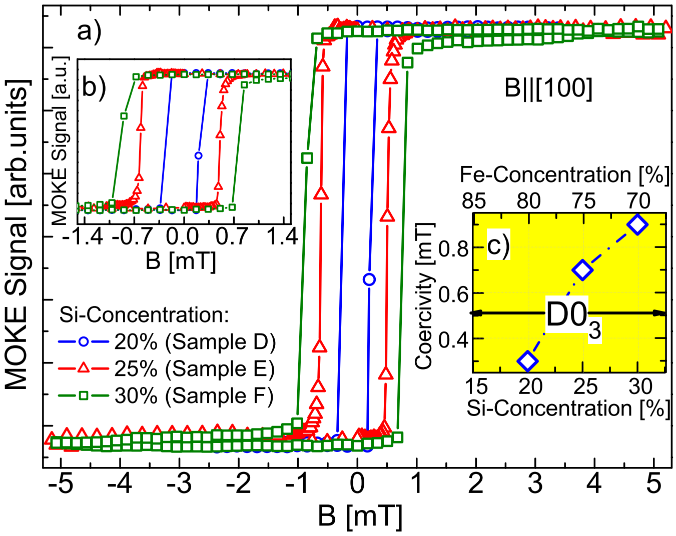

**Figure 10.10.:** (a) MOKE hysteresis loop of Fe$_{1-x}$Si$_x$ for different Si concentration of $x = 20$, 25, and 30% measured at RT (performed by F. M. Römer). The magnetic field was applied along the easy axis [100]-direction. (b) Magnifications of the low field regions. (c) Coercivity as a function of Si concentration within the D0$_3$ regime.

the magnetic moments due to the varying amount of Fe and Si.

MOKE hysteresis loops measured along the easy axis $[100]$-direction are shown in Fig. 10.10(a) indicating that with increasing Si concentration the coercivity increases from 1 mT for 20% Si to a value of about 0.3 mT for a Si concentration of 30% (see Fig. 10.10(c)). This means that as the Si concentration decreases the film becomes magnetically softer.

## 10.5. g-factor

The $g$-factor can be used to monitor the influence of the orbital contribution to the overall magnetic moments. Therefore, a careful $g$-factor determination offers a possibility to learn more about the different magnetic behavior observed for as-prepared/annealed samples and the off-stoichiometric ones. As discussed in Sec. 2.3 a precise determination of the $g$-factor requires a frequency dependent measurement. Figure 10.11 shows the square of the resonance frequency versus the resonance field for two different crystallographic directions. The data are that of the 8 nm thick Fe$_3$Si sample B that was annealed directly at 900 K for 1 h. The solid lines are fits according to Eqs. (2.24) and (2.23) using the anisotropy constants that were determined from the angle dependent measurements (see Tab. 10.1) The resonance frequency versus resonance field in perpendicular configuration ($B$ is applied parallel to the film normal) is shown in Fig. 10.11. Its linear dependence was fitted by employing Eq. (2.25). From the fits the $g$-factor can be determined. The result shows that the $g$-factor is isotropic, having a value of $g = 2.075(5)$

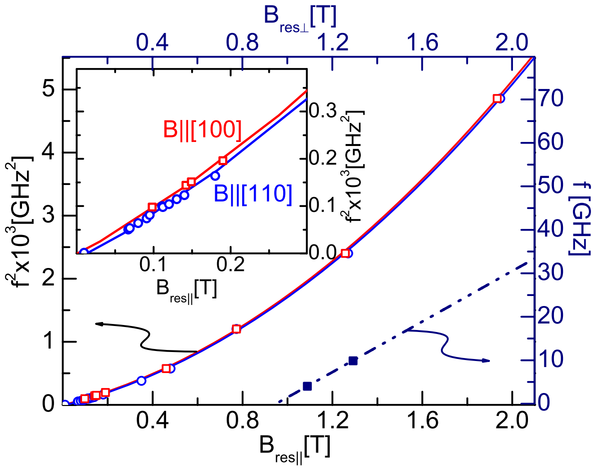

**Figure 10.11.:** The square of the resonance frequency versus the resonance field for two different in-plane configurations (left axis). The solid curves are fits according to Eqs. (2.24) and (2.23) using the anisotropy constants measured from the angular dependency of the resonance field (see Tab. 10.2). The frequency dependence of the resonance field with the external magnetic field applied along the film normal is shown as solid squares (right axis). The dash-dotted line is a fit according to Eq. (2.25). The inset shows the details below 0.3 T.

which is smaller than the pure bcc Fe value ($g_{\mathrm{Fe}} = 2.091$) and also the one of other metallic ferromagnets ($g_{\mathrm{Co}}$=2.187 and $g_{\mathrm{Ni}}$=2.183) [182]. To relate the $g$-factor to the ratio of orbital to spin magnetic moment, the well-established Kittel equation (4.4) can be used. The deviation of the $g$-factor from the value of a free electron for small orbital moment contributions is proportional to $(\mu_L/\mu_S)$, where $\mu_S$ and $\mu_L$ are the spin and orbital moment, respectively [58,183]. In our case the smaller $g$-factor thus is related to larger spin magnetic moments or smaller orbital contributions. As in our case the magnetization and therefore the spin magnetic moment is smaller than for Fe bulk, one can conclude that the smaller $g$-factor in Fe$_3$Si must stem from a reduction of the orbital magnetic moment as compared to the Fe bulk case. Indeed, we will show below that adding Si to Fe reduces the $g$-factor, which has to be related to a reduction of the orbital magnetic moment. We will come back to this point in Sec. 10.6 and a comparison to the calculated values will be presented.

## 10.5.1. Thickness dependence of the g-factor

The $g$-factor was determined for different film thicknesses as described above and in detail in Sec. 2.3. The measured $g$-factors are plotted as a function of film thickness in Fig. 10.12(a). As no thickness dependent variation of the magnetization and thus of the total magnetic moment was found (see Tab. 10.2), the small enhancement for the 4 nm-thick sample ($g = 2.080(5)$) reflects an increase of the orbital moment in the thin film regime. It is straightforward to relate

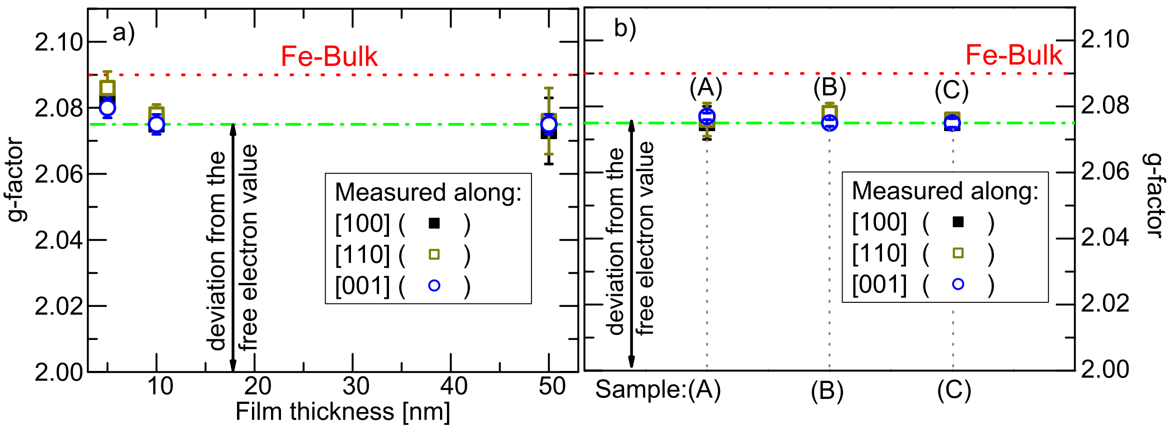

**Figure 10.12.:** . (a) $g$-factor as a function of film thickness measured at RT and along different crystallographic directions. (b) $g$-factor for samples after different annealing procedures. A, B, and C denote the annealing procedures described in the text. The dashed-dotted lines are guides to the eyes and the dotted line represents the value of Fe-bulk.

this enhancement to the increasing importance of the surface anisotropy given by $K_{2\perp}^{\mathrm{si}}$. The reduced symmetry at the surface is thus the source of the uniaxial out-of-plane anisotropy observed for the thin film. Figure 10.12(a) further demonstrates that the $g$-factor is isotropic for all film thicknesses, being almost close to the value of $2.075(5)$.

## 10.5.2. The effect of annealing on the g-factor

The $g$-factor was measured for samples A, B, and C (differently annealed samples). Our experiments indicate that within the error bar the value of the $g$-factor is almost the same for all samples and very close to 2.075(5) (see Fig. 10.12(b)). From this we conclude that the annealing reduces the number of defects rather than influences the quality of the $D0_3$ structure on an atomic level, as the latter would definitely lead to changes of the $g$-factor. This scenario is consistent with the fact that our X-ray diffraction data do not show significant changes between the differently treated samples. The enhanced intensity of (400) reflex for sample B indicates that in this case, the orientation of the crystallites are modified whereas their size is almost unchanged.

## 10.5.3. Influence of Si concentration on the g-factor

The $g$-factor was determined for samples D and F with Si concentrations of 20 and 30% as well as for the stoichiometric sample E. The results for the off-stoichiometric samples investigated at RT are shown in Fig. 10.13(a) together with the fitting curves according to Eq. (2.24) (for the [100]-direction) and Eq. (2.23) ([110]-direction). The solid squares show the resonance field de-

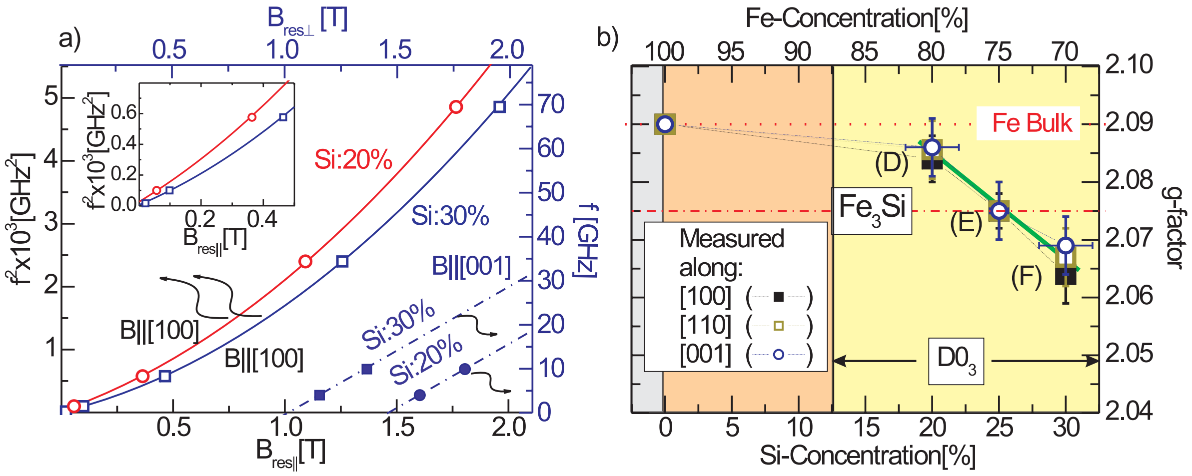

**Figure 10.13.:** (a) The square of the resonance frequency versus the resonance field for a magnetic field applied parallel to the [100]-direction. The open circles and squares denote samples D and F with Si concentrations of 20% and 30%, respectively. The solid curves are fits according to Eqs. (2.24) and (2.23). The solid squares show the resonance field dependence of the resonance frequency when the external magnetic field is applied along the film normal [001]-direction. The dashed-dotted lines are the fits according to Eq. (2.25). The inset show the details below 0.5 T. (b) $g$-factor for samples with different Si concentration.

pendence of the resonance frequency when the external magnetic field is applied along the film normal ([001]-direction). The dashed-dotted and dotted lines are fits according to Eq. (2.25). The anisotropy fields extracted from the angle dependent measurements were used for the fitting. The $g$-factor as a function of the Si concentration is presented in Fig. 10.13(b). One observes that the $g$-factor decreases as the Si concentration increases. Thus, the deviation of the $g$-factor from the free electron value decreases with increasing the Si concentration. As the magnetization was found to decrease for higher Si content, the reduced $g$-factor clearly indicates a strong reduction of the orbital magnetic moment. Furthermore, the $g$-factor dependence is linear within the concentration regime in which $\mathrm{Fe}_{1-x}\mathrm{Si}_x$ forms the $\mathrm{D}0_3$ structure. Extrapolating the $g$-factor to the one of pure Fe indicates that this trend does change outside the regime of the $\mathrm{D}0_3$ structure, which shows that the $g$-factor can also be used as a sensitive tool to monitor structural changes. By fitting the linear behavior of the $g$-factor within the $\mathrm{D}0_3$-regime, one obtains the dependence $g = 2.12 - 0.19 \cdot x$, where $x$ is the Si concentration in the $\mathrm{D}0_3$-regime.
The trend of Si to reduce the orbital moments is plausible as paramagnetic Si itself has a $g$-factor close to the free electron value of $g_{\text{electron}} = 2.0023$ [184]. We note that the reduction of the spin magnetic moment as function of the Si concentration is expected to continue on the Si rich side of the $\mathrm{D}0_3$-regime. $\mathrm{Fe}_{50}\mathrm{Si}_{50}$ is predicted to show no ferromagnetic order anymore [175].

## 10.6. Spin and orbital magnetic moments

The orbital moment of transition metals and most of their compounds is considerably smaller than the spin moment. This is due to the cubic symmetry and quenching of the orbital moment. The sum of these two quantities is the total magnetic moment. For the determination of the orbital moment FMR or XMCD can be used.

FMR can be used to probe the ratio of the orbital to the spin moment ($\mu_L^{\text{eff}}/\mu_S^{\text{eff}}$) via determination of the $g$-factor [183]. For small values of ($\mu_L^{\text{eff}}/\mu_S^{\text{eff}} \ll$1), and by neglecting the higher order terms, the $g$- factor can be expressed as [185]

$$g = g_{\text{electron}} + 2\left(\frac{\mu_L^{\text{eff}}}{\mu_S^{\text{eff}}}\right); \qquad g_{\text{electron}} = 2.002319. \tag{10.2}$$

As the ratio of the orbital to the spin moment $\mu_L^{\text{eff}}/\mu_S^{\text{eff}}$ of $Fe_3Si$ is small, the Kittel formula [185] (Eq. (10.2)) which is valid only for $\mu_L^{\text{eff}}/\mu_S^{\text{eff}} \ll 1$ can be used to extract the orbital to the spin moment ratio from the measured $g$-factor in an FMR experiment. The epitaxial growth of $Fe_3Si$ along with the applicability of the Kittel formula in this compound, make it an appropriate prototype system for the orbital moment investigation.

Inserting the measured $g$-factor into Kittel's formula [Eq. (10.2)] one simply obtains $\mu_L^{\text{eff}}/\mu_S^{\text{eff}}$=0.037(3). The SQUID measurements result in a value of $M = 0.879 \times 10^6$ A/m for the total magnetic moment per volume, which is the sum of the spin and orbital moments of all atoms ($\mu_S^{\text{eff}} + \mu_L^{\text{eff}}$, see below). In order to determine the effective moments of Fe and Si atoms information about the relative atomic contributions to the total magnetic moment in $Fe_3Si$ are required. Hence, we calculated the spin resolved electronic structure of $Fe_3Si$ in $D0_3$ structure (a schematic illustration of the structure is given in Fig. 10.1(a)) and then obtain the atomic magnetic moments in the system. Calculations were performed in the framework of our collaboration with the group of Prof. Kratzer using DFT based Wien2k computational package [142] that uses the full-potential linear augmented plane wave (FP-LAPW) method to solve the single particle Kohn-Sham equations. In the FP-LAPW method, the unit cell is partitioned into two regions, non-overlapping spheres around the nucleus (Muffin-Tin spheres) and the remaining interstitial region. In the Muffin-Tin spheres, the wave function is expanded into the atomic orbitals and lattice harmonics while in the interstitial region, plane waves are used as the basis set. The exchange-correlation energy was calculated by using the generalized gradient approximation (GGA). The relativistic spin-orbit correction was taken into account to calculate the orbital contributions to the magnetic moments.

There are two different Fe atoms in the unit cell of the $D0_3$ lattice (Fig. 10.1(a)) and we found that the local moment on FeII sites is significantly larger than the one on FeI sites in good agreement with previous theoretical [171,175,176,186,187] and experimental [28,37,38] investigations. The results show that the Fe atoms at FeI sites have a spin (orbital) moment of

$\mu_S$ =1.35 ($\mu_L$ =0.022) $\mu_B$ while at FeII sites, they have a spin (orbital) moment of $\mu_S$ =2.57 ($\mu_L$ =0.042) $\mu_B$. The spin moment of the Si atom was found to be antiparallel and very small ($\mu_S$ =-0.067 $\mu_B$) and its orbital moment was practically zero, hence its contributions to the total moment is neglected. We assume a Russel-Saunders (L-S) type coupling [188] where the effective spin (orbital) moment of Fe atoms in $D0_3$ structure of $Fe_3Si$ can be expressed as

$$\mu_{S(L)}^{\text{eff}} = \frac{\left[8\mu_{S(L),FeI} + 4\mu_{S(L),FeII}\right]}{8FeI + 4FeII}. \tag{10.3}$$

Here the denominator represents the total number of Fe atoms in the unit cell that are 8 FeI plus 4 FeII atoms. This approach leads to effective spin and orbital moments of $\mu_S^{\text{eff}} = 1.75$ $\mu_L^{\text{eff}} = 0.029\mu_B$.

Now we turn back to the experimental results of the FMR and SQUID measurements, to experimentally find out the effective spin and orbital moments. By assuming again an L-S type coupling, according to Eq. (10.3) we obtain the values of $\mu_S^{\text{eff}} = 1.38\mu_B$ and $\mu_L^{\text{eff}} = 0.051\mu_B$. We note that within this approach all Fe atoms are assumed to be equivalent and the individual moments of FeI and FeII are not distinguishable. It is observed that the obtained theoretical value of $\mu_L^{\text{eff}}$ is smaller than the measured one. For transition metals, it is rather common that LDA/GGA severely underestimates the orbital moment [189–191]. For instance, for bcc Fe, LDA finds a value of $\mu_L \sim 0.04\mu_B$ instead of the experimental value $\mu_L \sim 0.1\mu_B$ [190,191]. Although the absolute values of the calculated orbital moments are small and cannot be directly compared to the measured values the relative changes with respect to the value of the Fe-bulk are in acceptable agreement with experiment.

| System | $g$-factor | $\mu_S^{\text{eff}}[\mu_B/\text{atom}]$ | $\mu_L^{\text{eff}}[\cdot 10^{-3}\mu_B/\text{atom}]$ |
|---|---|---|---|
| | Measured | | |
| $Fe_{2.8}Si_{1.2}$ | 2.067 | 1.32 | 46 |
| $Fe_3Si$ | 2.075 | 1.38 | 51 |
| $Fe_{3.2}Si_{0.8}$ | 2.085 | 1.53 | 65 |
| Fe | 2.092 | 2.24 | 103 |
| | Calculated | | |
| FeSi | 2.002 | 0.00 | 0 |
| $Fe_3Si$ | 2.035 | 1.75 | 29 |
| Fe | 2.069 | 2.28 | 76 |

**Table 10.4.:** The measured $g$ factor, effective spin and orbital moments of the 8 nm $Fe_{3\pm\delta}Si_{1\mp\delta}$ ($\delta = 0, 0.2$) thin films (upper part). The error bar in $\mu_S^{\text{eff}}$ and $\mu_L^{\text{eff}}$ is less than 6% and mainly results form the uncertainty of the sample volume. Calculated $g$-factor, effective spin, and orbital moments of bulk FeSi, $Fe_3Si$, and Fe (lower part).

In order to shed light into the origin of the quenching of the orbital moments in $Fe_3Si$ and to find out the role of local atomic moments in the effective moments, the spin and orbital moments were calculated for two additional cases: (i) bcc Fe (ii) FeSi ordered in B2 structure using the same theoretical approach mentioned above. The calculated spin and orbital moments are listed in the lower part of Tab. 10.4.

Both experimental and theoretical results indicate that $\mu_S^{\mathrm{eff}}$ and $\mu_L^{\mathrm{eff}}$ of Fe atoms in $Fe_3Si$ are considerably smaller than the corresponding values in the bcc Fe (see Tab. 10.4). The reduction of the spin and orbital moments in the $Fe_3Si$ alloy, compared to the Fe-bulk, can be attributed to the Fe-Si bonding and hybridization that change the Fe band structure near the Fermi level (see below). Based on the calculated moments in $Fe_{50}Si_{50}$, we conclude that increasing the Si concentration to 50% completely extinguishes the ferromagnetic character of the system.

We expect that alloying with Si increases the crystal field strength and accordingly orbital quenching effects in iron. The extreme quenching was observed in the B2 structure of FeSi alloy in which every Fe atom is surrounded by 8 nearest Si neighbors. This geometry indicates high Fe-Si hybridization in this system that leads to a complete quenching of the moments.

A perfect $D0_3$ lattice of $Fe_3Si$ consists of four bcc and four B2 sublattices (twelve Fe atoms, eight FeI, four FeII and four Si atoms, see Fig. 10.1). The first argument for the direct influence of Fe-Si hybridization on orbital quenching is based on the different magnetic moments of

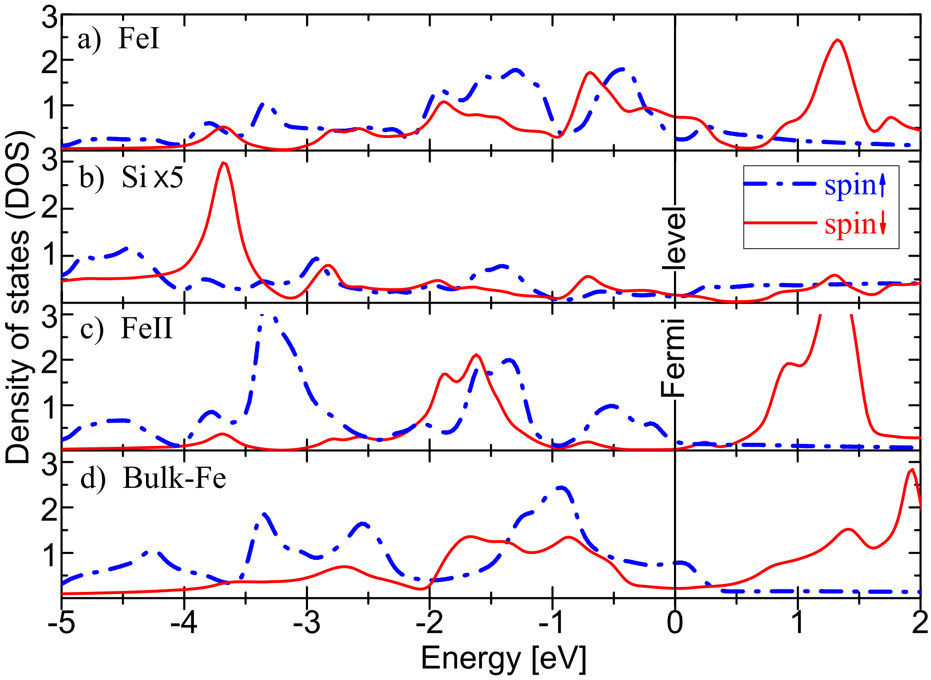

**Figure 10.14.:** Calculated spin resolved DOS of the (a) FeI, (b) Si, (c) FeII atoms in $Fe_3Si$ lattice, and (d) bulk-Fe. The solid curves represent the minority spins whereas the dashed-dotted curves represent the majority ones. Calculations were performed by S. J. Hashemifar.

FeI and FeII atoms in ordered $Fe_3Si$ alloy, which was found by our calculations. FeII in this alloy has eight Fe nearest neighbors whereas FeI has four Fe and four Si nearest neighbors and hence should be effectively hybridized with Si and consequently has a smaller magnetic moment compared to FeII. In Fig. 10.14 the spin resolved density of states (DOS) of each individual atoms in $Fe_3Si$ are shown. Figure 10.14 clearly indicates that: (i) the minority spins states in FeI are enhanced with respect to the one of bulk-Fe and (ii) the minority states are very similar to the one of Si. Since the DOS of both minority and majority spins in FeII is not affected drastically, we conclude that both changes in the DOS of FeI are direct indications of the hybridization of the d-states of FeI with the p-state of Si that strongly suppressed the FeI moments. For justification of the effect of Fe-Si hybridization on the magnetic moments we replace a Si (an Fe) atom with an Fe (a Si) atom in the unit cell that was obtained by modifying the Fe and Si concentration in $Fe_3Si$ alloy by $\pm5\%$ [5% increasing (decreasing) of Si concentration is almost equal to replacing an Fe (a Si) atom by a Si (an Fe)]. These replacements, modify the number of the nearest Si neighbors of some Fe atoms and number of Fe-Si bonds and consequently change the effective Fe moments. Following the same method used for $Fe_3Si$, we measured the effective spin and orbital moments of the off-stoichiometric samples. The results are summarized in the upper part of Tab. 10.4. Notably, the unit cell of $Fe_{3.2}Si_{0.8}$ consists of almost thirteen Fe atoms (five bcc and three B2 sublattices) whereas the one of $Fe_{2.8}Si_{1.2}$ consists of almost eleven Fe atoms (three bcc and five B2 sublattices), which have to be taken into account for the off-stoichiometric samples (see Eq. 10.3).

Table 10.4 clearly indicates that both spin and orbital moments increase as the Fe concentration increases. It means that replacing one Si atom with one Fe atom in the unit cell reduces the effective Fe-Si hybridization in the system and consequently enhances the effective atomic moment. A reversed mechanism takes place when an Fe atom is replaced by a Si, which in turn explain the decreased effective Fe moments in $Fe_{2.8}Si_{1.2}$.

In summary, we used the experimental FMR and SQUID techniques as well as the DFT based calculations to study the spin and orbital magnetism in Fe-Si alloys. In the experimental part we investigated bcc Fe, the $D0_3$ ordered $Fe_{3\pm0,0.2}Si_{1\mp0,0.2}$ thin films while in the theoretical part, in addition to the ordered stoichiometric $Fe_3Si$, FeSi, and bcc Fe were calculated. The results confirm that Fe-Si hybridization increases the crystal field effects on Fe atoms and consequently enhance the orbital quenching in $Fe_{3\pm\delta}Si_{1\mp\delta}$ binary Heusler structures.

## 10.7. FMR dispersion relation

The values of the anisotropy fields resulting from the angle dependent measurements and the $g$-factor measured by frequency dependent measurement are used to numerically calculate the dispersion relation. The calculated dispersion relation was compared to the experimentally mea-

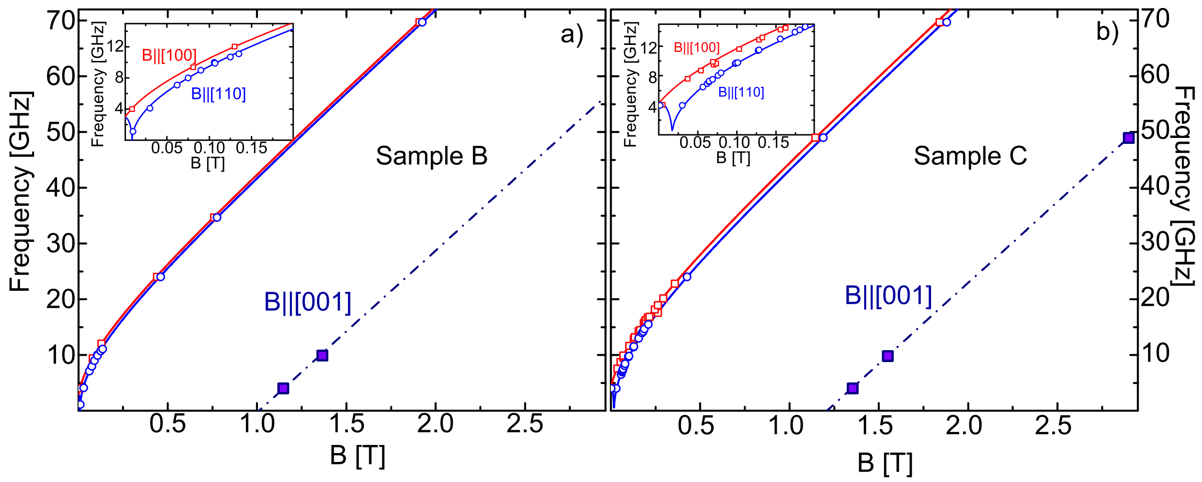

**Figure 10.15.:** The resonance frequency versus field (dispersion relation) of (a) samples B and (b) sample C measured at RT and along three different crystallographic directions. The experimental data are shown as open (for the case that the external field is applied in the film plane) and solid symbols (for the case that the external field is applied perpendicular to the film plane). The solid and dashed-dotted lines are the numerically calculated curves. The inset show the details of low frequency measurements.

sured one. In Fig. 10.15 two examples are shown. Figure 10.15 indicates that for the resonance frequencies below 3 GHz, both the unsaturated as well as saturated modes are observed when the external magnetic field is applied along $\langle 110 \rangle$-direction (see the insets). The modes overlap with each other at lower frequencies, as expected from the calculated dispersion relation.

It was observed that the unsaturated branch is going to be shifted to the higher microwave frequency and higher resonance field with decreasing the Si concentration. This can be understood by the enhanced anisotropy fields and the slight enhancement of the $g$-factor for the samples with lower Si-concentration.

## 10.8. Relaxation mechanisms

Magnetic relaxation processes are among the most interesting topics in magnetism at the nanoscale. As the dimensions of magnetic structures decrease, different kinds of magnetic phenomena appear, such as thickness-dependent Curie temperatures [192], easy axes located normal to the plane [193], or magnetic coupling mechanisms due to the confinement given by the low dimensionality [194]. Besides these *static* effects, for which the magnetization remains in its ground state, dynamic processes involving a magnetic excitation and subsequent gyroscopic vortex precession and reversal in magnetic Landau domain configurations [195] exist. Also, mechanisms leading to ultra fast magnetization reversal either by applying magnetic fields or using the torque carried by a spin-polarized current (current induced switching) are moving into the focus of many investigators. In all of these effects, understanding the different relaxation channels in magnetic damping is the most important issue. However, rather few experimental studies have addressed the microscopic origin of the relaxation processes in nano-magnets [54,135,196,197]. Usually, these processes are described by LLG phenomenology only, neglecting other physical mechanisms that contribute to the damping process in nano-magnets.

This section gives a detailed and quantitative explanation of the damping processes within thin $Fe_3Si$ films grown epitaxially on MgO(001), a system that can be viewed as a prototype system for the investigation of relaxation mechanisms. The results of extensive frequency dependent (in the range of 1 to 70 GHz) as well as angle dependent measurements of the ferromagnetic resonance (FMR) linewidth are presented. The narrow FMR linewidth allows to a precise determination of the magnetic relaxation parameters of these samples. The benefits of the $D0_3$ structure of epitaxial $Fe_3Si$ is that one can obtain different strength contributions to the FMR linewidth from the Gilbert damping constant, $G$ and other relaxation terms. We present a general model to explain the experimental results of *both* the angular and frequency dependence of the FMR linewidth yielding one set of relaxation parameters. Moreover, we show that the relative strength of the relaxation parameters can be tuned by changing the annealing temperature and also by slightly modifying the Fe content.

As it is discussed in Sec. 2.3, in general the motion of the sample magnetization $\vec{M}$ in an FMR experiment can be described by Eq. (2.8). In order to quantify the different relaxation channels, the damping of $\vec{M}$ has to be discussed in terms of linewidth contributions. The FMR linewidths measured in this work are analyzed considering four different contributions:

$$\begin{aligned}\Delta B_{pp}(\omega,\psi_B) &= \Delta B_{pp}^{\mathrm{Gilbert}}(\omega,\psi_B)+\Delta B_{pp}^{\mathrm{2mag}}(\omega,\psi_B)\\ &+ \Delta B_{pp}^{\mathrm{mosaic}}(\omega,\psi_B)+\Delta B_{pp}^{\mathrm{inhom}} \qquad (10.4)\end{aligned}$$

Here $\Delta B_{pp}$ denotes the peak-to-peak linewidth of the FMR signal. $\psi_B$ denotes the two angles $\theta_B$ and $\phi_B$, the first being the polar angle of the external field measured with respect to the film normal and the latter the azimuthal angle of $\vec{B}$ measured with respect to the in-plane [100]-direction. In the following, we briefly describe the four different contributions to the FMR linewidth within Eq. (10.4):

(i) The Gilbert contribution $\Delta B_{pp}^{\mathrm{Gilbert}}$.

In various magnetic systems, the damping can be described by the phenomenological Gilbert damping parameter $G$ [54]. Sometimes the dimensionless parameter $\alpha$ is given instead, which is related to $G$ by $\alpha = G/(\gamma M)$. If the Gilbert damping represents the entire intrinsic damping, then it follows from the Landau-Lifshitz-Gilbert equation of motion [54] that the FMR linewidth would depend linearly on the microwave frequency [135]. In order to determine $G$ or $\alpha$, frequency-dependent FMR measurements over a large range of microwave frequencies are needed. Note that the linear frequency dependence of FMR linewidth is valid *only* when the magnetization and external magnetic field are parallel to each other. Otherwise the so-called field dragging contribution has to be included. If one wants to express relaxation rates in terms of linewidths, i.e., to convert from frequency-swept to the field-swept linewidth measured by FMR, one can use the following conversion (see for example Refs. [135,198] and references therein):

$$\Delta B_{pp}(\omega,\psi_B) = \gamma \frac{dB_{\mathrm{res}}(\omega,\psi_B)}{d\omega} \cdot \Delta(\frac{\omega}{\gamma}). \tag{10.5}$$

Here $\Delta(\frac{\omega}{\gamma})$ is the frequency-swept linewidth written in magnetic field units. The suffix 'res' indicates that $dB_{\mathrm{res}}(\omega,\psi_B)/d\omega$ has to be calculated at the resonance condition. In Eq. (10.5) $\omega$ is a function of $B$ and $\psi_B(B)$, therefore Eq. (10.5) can be written as

$$\begin{aligned}\Delta B_{pp}(\omega,\psi_B) = \gamma &\frac{\partial B_{\mathrm{res}}(\omega,\psi_B \equiv \text{constant})}{\partial\omega} \cdot \Delta(\frac{\omega}{\gamma}) \\ +\gamma &\frac{\partial B_{\mathrm{res}}(\omega \equiv \text{constant},\psi_B)}{\partial\psi_B} \cdot \frac{d\psi_B}{d\omega} \cdot \Delta(\frac{\omega}{\gamma}).\end{aligned} \tag{10.6}$$

The first term in Eq. (10.6) is commonly called the field-dragging contribution, because the partial derivative gets large at angles for which the magnetization $\vec{M}$ is dragged behind $\vec{B}$ due to magnetic anisotropy effects. Along the hard and easy axes of magnetization, for which $\vec{M}$ and $\vec{B}$ are parallel, this dragging contribution vanishes. The Gilbert damping contribution in Eq. (10.4) is therefore given by (see Sec. 2.3):

$$\Delta B_{pp}^{\mathrm{Gilbert}}(\omega,\psi_B \equiv \beta) \approx \frac{2}{\sqrt{3}}\frac{\alpha}{\gamma}\frac{\omega}{\cos\beta} \tag{10.7}$$

where $\beta$ is the angle between the magnetization $\vec{M}$ and external field $\vec{B}$. For the in-plane configuration $\beta = \phi_{eq} - \phi_B$ and for the out-of-plane configuration $\beta = \theta_{eq} - \theta_B$.

(ii) Line broadening due to mosaicity ($\Delta B_{pp}^{\mathrm{mosaic}}$).

The second term in Eq. (10.6) is the so called mosaicity term. It is caused by a small spread of sample parameters on a very large scale [199]. This variation can be found in the internal fields, thickness, or orientation of crystallites within the sample. The individual regions thus have slightly different resonance fields. The overall signal will be a superposition of these local FMR lines yielding a broader linewidth. We consider the fluctuations of the *directions* of the anisotropy fields by the mosaicity contribution given by [199]:

$$\begin{aligned}&\Delta B_{pp}^{\mathrm{mosaic}}(\omega,\psi_B) = \\ &\frac{\partial B_{\mathrm{res}}(\omega,\psi_B)}{\partial\phi_B}\Delta\phi_B + \frac{\partial B_{\mathrm{res}}(\omega,\psi_B)}{\partial\theta_B}\Delta\theta_B,\end{aligned} \tag{10.8}$$

where $\Delta\phi_B$ and $\Delta\theta_B$ represent the average spread of the direction of the easy axes in the film plane and normal to the film, respectively. Note that for frequency dependent measurements along the easy and hard axes, the partial derivatives are zero and thus the mosaicity contribution vanishes.

(iii) The two-magnon scattering contribution $\Delta B_{pp}^{\mathrm{2mag}}$.
Two-magnon scattering, where the $k = 0$ magnon excited by FMR scatters into degenerate states of magnons having wave vectors $k \neq 0$ [198]. This process requires that the spin-wave dispersion allows for degenerate states, and that there are scattering centers in the sample. The geometrical separation of the scattering centers is connected to the extension of the final magnon states in real space. If long-wavelength spin-waves are involved in the relaxation process, defects of the order of several 100 nm rather than atomic defects act as scattering centers. The existence of two-magnon scattering has been demonstrated in many systems of ferrites (see Refs. [80,200,201] and references therein). While in bulk materials this is well known, it was only recently found by several groups to be of major importance also in superlattices [65,202] and ultrathin ferromagnets [199,203,204].

The linewidth $\Delta B_{pp}^{\mathrm{2mag}}$ caused by the two-magnon scattering mechanism is a measure of the scattering rate of the uniform ($k = 0$) precession magnons into other spin-wave modes ($k \neq 0$) [65,80,202,205,206]. For thin magnetic films, $\Delta B_{pp}^{\mathrm{2mag}}$ can be expressed as [81,82,85]:

$$\Delta B_{pp}^{\mathrm{2mag}}(\omega, \psi_B) = \sum_{\langle x_i \rangle} \Gamma_{\langle x_i \rangle} f(\phi_B - \phi_{\langle x_i \rangle}) \times \arcsin\left( \sqrt{\frac{\sqrt{\omega^2 + (\omega_0/2)^2} - \omega_0/2}{\sqrt{\omega^2 + (\omega_0/2)^2} + \omega_0/2}} \right) U\left(\theta_{eq} - \theta_c\right) \tag{10.9}$$

with $\omega_0 = \gamma \mu_0 M_{\mathrm{eff}} = \gamma \left(\mu_0 M - 2K_{2\perp}/M\right)$ and $\mu_0 M_{\mathrm{eff}}$ being the effective magnetization that consists of $\mu_0 M$ and the intrinsic out-of-plane anisotropy field $2K_{2\perp}/M$ that was determined in Sec. 10.4. The factor $\Gamma_{\langle x_i \rangle}$ denotes the strength of the two-magnon scattering along the principal in-plane crystallographic direction $\langle x_i \rangle$ (see Sec. 2.3). This parameter will be fitted to the experimental data. It should be noted that in Refs. [81,82,85] only the frequency-dependent part of the FMR linewidth was derived [$\Gamma \cdot \arcsin(...)$-term in Eq. (10.9)]. The additional terms added to this contribution will be explained in the following. The $f(\phi_B - \phi_{\langle x_i \rangle})$-term allows for the two-magnon contribution to depend on the in-plane direction of $\vec{B}$ relative to the principal in-plane crystallographic directions $\langle x_i \rangle$ given by the angles $\phi_{\langle x_i \rangle}$. An angle dependent two-magnon scattering may occur when the scattering centers are not isotropic within the sample. In the case that the centers are given by lattice defects, the angular dependence should reflect this lattice symmetry. In case that different contributions of two-magnon scattering along the principal crystallographic directions $\langle x_i \rangle$ occur, one has to sum up these contributions weighted by their angular dependence given by $f$. The step function $U\left(\theta_{eq} - \theta_c\right)$ in Eq. (10.9) is equal to 1 for $|\theta_{eq}| > |\theta_c|$ and zero for $|\theta_{eq}| < |\theta_c|$. It is used to describe the ‘switching off’ of the two-magnon scattering at a critical out-of-plane angle of the magnetization [207]. Theoretically, it is shown that in oblique configuration, when the magnetization is tipped out of the film plane, finite wave vector modes are degenerate with the FMR mode for $|\theta_{eq}| > |\theta_c| = 45°$. Thus the two-magnon scattering should be operative in this regime of the tipping angle, but it should shut off for $|\theta_{eq}| < |\theta_c| = 45°$ (see for example Eqs. (25-27) of Ref. [207]). Such behavior is observed very often in thin metallic ferromagnets [65,135,203,208]. We emphasize that no analytical formula for the angular dependence of the FMR linewidth due to two-magnon scattering has been reported for $|\theta_{eq}| > |\theta_c| = 45°$ and, thus, for simplification we neglect the angular dependence of the two-magnon scattering in this regime and approximate the polar angular dependence of the two-magnon scattering by a step function. There are reasons to believe that this indeed is an appropriate approximation: i) All experimental data reported so far have shown practically no change in the FMR linewidth for $|\theta_{eq}| > |\theta_c| = 45°$ (see also [65,135,203,208]) meaning that the scattering matrix is rather angle independent. ii) The overall angular dependence of the FMR linewidth in the out-of-plane configuration for which the static field is varied from the in-plane to the out-of-plane direction is governed by the mosaicity term. Moreover, Ref. [196] shows that the angular dependence due to two-magnon scattering for most cases should rather lead to a reduction of the linewidth with respect to the in-plane value. This is, however, not observed in the experiment due to the larger dragging and mosaicity contribution. Therefore, the angular dependence caused by two-magnon scattering can be neglected for $|\theta_{eq}| > 45°$. The few studies that experimentally evidence two-magnon scattering in ferromagnets base their conclusion *either* on the frequency dependence of the linewidth being not linear [65,202] *or* on the angular dependence of $\Delta B_{pp}$ at fixed frequency alone [65,199,203,204].

(iv) Although for our films, fluctuations of the thickness, and thus fluctuations of the *strength* of the anisotropy fields are small, we add a frequency and angle independent broadening term $\Delta B_{pp}^{\mathrm{inhom}}$ to Eq. (10.4) to account for them [135]. $\Delta B_{pp}^{\mathrm{inhom}}$ added to the model represents a frequency and angle independent broadening, which cannot be written in the other forms (Gilbert or two-magnon scattering term). As we will show this contribution plays a minor role in our samples.

Taking all mechanisms together the following expression for the linewidth can be formulated:

$$\begin{aligned}\Delta B_{pp}^{total}(\omega,\psi_B) &= \Delta B_{pp}^{inhom} + \frac{2}{\sqrt{3}}\frac{\alpha}{\gamma}\frac{\omega}{\cos\beta} + \frac{\partial B_{res}(\omega,\psi_B)}{\partial\phi_B}\Delta\phi_B + \frac{\partial B_{res}(\omega,\psi_B)}{\partial\theta_B}\Delta\theta_B \\ &+ \sum_{\langle x_i\rangle}\Gamma_{\langle x_i\rangle} f\left(\phi_B-\phi_{\langle x_i\rangle}\right)\cdot \arcsin\left(\sqrt{\frac{\sqrt{\omega^2+(\omega_0/2)^2}-\omega_0/2}{\sqrt{\omega^2+(\omega_0/2)^2}+\omega_0/2}}\right) U\left(\theta_{eq}-\theta_c\right) \qquad (10.10)\end{aligned}$$

In order to precisely determine the magnetic damping parameters, the frequency dependence of the FMR spectra was investigated within a wide range of microwave frequencies between 1 and 70 GHz. Furthermore, the angular dependence of the FMR linewidth was recorded at microwave frequencies of 9.9 and 24 GHz.

The frequency dependence of the FMR linewidth for an 8 nm thick Fe$_3$Si film (sample B) measured along two different in-plane directions, [100] and [110], is shown in Fig. 10.16(a). The two fit curves were obtained with the help of Eq. (10.10) using fixed angles $\theta_B = 90°$ (external field in-plane) and $\phi_B = 0°$ or $\phi_B = 45°$ (external field parallel [100]- or [110]-direction, respectively). The fitting parameters used, are $\Delta B_{pp}^{\mathrm{inhom}}$, $G$, and $\Gamma$ corresponding to a small frequency independent inhomogeneous contribution, the Gilbert damping, as well as the two-magnon scattering, respectively. The linewidth broadening due to mosaicity (see Eq. (10.8)) cannot be determined from the frequency dependence of $\Delta B_{pp}$ along principal axes ($\langle 100 \rangle$ and $\langle 110 \rangle$), because then the partial derivatives in Eq. (10.8) are zero. In Fig. 10.16 (a) one can see that the curvature along the [100]-direction is more pronounced than along the [110]-direction. This clearly indicates the presence of two-magnon scattering, as pure Gilbert-like damping would lead to a linear dependence. The fit parameter $\Gamma$ in Eq. (10.9) is a factor scaling the curve with respect to the y-axis. The precision of the fit parameters can be enhanced significantly when the in- and out-of-plane angular dependence of the FMR linewidth are fitted using Eq. (10.10) for a fixed frequency of $f = 9.9$ GHz. The azimuthal and polar angular dependencies of the FMR linewidth are shown in Figs. 10.16(b) and (c), respectively. The polar angle dependent measurement is performed by rotating the external field from the [110] towards the [001] direction. Taking only the Gilbert mechanism according to Eq. (10.7) into account one obtains the dashed curves. This clearly shows that the Gilbert mechanism alone is not sufficient to describe the relaxation within the films. In particular, the azimuthal angular dependence of the FMR linewidth should have eight maxima due to the Gilbert contribution alone. Note that due to the small value of $G$ the eight maxima can hardly be seen. In contrast to the expected behavior, the in-plane angular dependence of the FMR linewidth shows just fourfold (four maxima) symmetry [Fig. 10.16 (b)].

This observation can be explained by considering all contributions of Eq. (10.10) with the fit parameters obtained from the frequency dependence of the linewidth. There are two issues to note: (i) For all angles between the hard and easy directions, i.e. $\langle 100 \rangle$ and $\langle 110 \rangle$, field dragging effects [see Eq. (10.5)] have to be taken into account because then $\vec{M}$ and $\vec{B}$ are not aligned parallel. This is due to the large demagnetizing field, which acts as an anisotropy contribution. That broadening of the resonance line for the out-of-plane angles $-30° < \theta_B < -5°$ and $5° < \theta_B < 30°$ can be observed nicely in the dashed line of Fig. 10.16 (c). In the in-plane angular dependence, field dragging plays a minor role as depicted by the almost constant dashed line in Fig. 10.16 (b), since the in-plane anisotropy fields are small. (ii) Comparing the frequency dependencies of the linewidth taken along two distinct directions it is obvious that the two-magnon contribution is angle dependent. In fact it has the same fourfold (four maxima) symmetry in the film plane as it is observed for the angular dependence of the resonance position. Such a behavior of anisotropic two-magnon scattering was observed earlier for thin metallic ferromagnets [203,206], superlattices [65], as well as *'half Heusler'* alloy films [208].

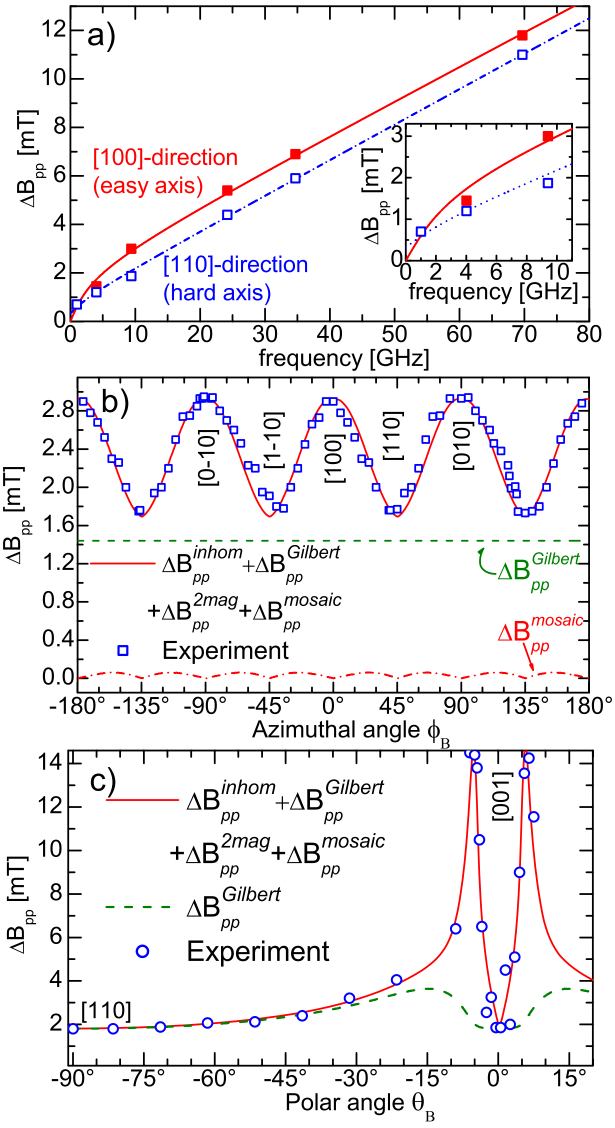

**Figure 10.16.:** (a) The frequency dependence of the FMR linewidth for an 8 nm $Fe_3Si$ directly annealed after growth (sample B). The inset shows the manifestation of the low-frequency results. (b) Azimuthal and (c) polar angular dependence of the FMR linewidth measured at a microwave frequency of 9.9 GHz. All FMR experiments were performed at ambient temperature.

In some cases this could be correlated to defect structures (e.g. dislocation lines) being oriented along distinct crystallographic directions, thus leading to an asymmetry, which is the same as the one of the crystal lattice. In such a case the Fourier component of the defects leads to a fourfold angular dependence being proportional to $f(\phi_B - \phi_{\langle x_i \rangle}) = \cos^2[2(\phi_B - \phi_{\langle x_i \rangle})]$ due to an effective channelling of scattered spin-waves (for more details see Ref. [203]). This function was also used to fit the in-plane angular dependence. Note that the fitted solid and dashed curves are not least squares fits of the frequency dependence data, but are the result of a simultaneous

| Sample | $\Delta B_{pp}^{\mathrm{inhom}}$ (mT) | $G$ ($10^7$Hz) | $\gamma\Gamma_{\langle 100\rangle}$ ($10^7$Hz) | $\gamma\Gamma_{\langle 110\rangle}$ ($10^7$Hz) | $\Delta\phi_B$ (°) | $\Delta\theta_B$ (°) |
|---|---|---|---|---|---|---|
| (a) 8 nm $Fe_3Si$ (sample B) | 0.2(2) | 5.1 | 25(2) | 4(2) | 0.09 | 0.05 |
| (b) 40 nm $Fe_3Si$ as-prepared | 0.9(1) | 5.1(1) | 53(17) | 26(2) | 0.3 | 0.15 |
| (c) 8 nm $Fe_3Si$ (sample C) | 0 | 6.0(2) | 42(8) | 16(4) | 0.3 | 0.15 |
| (d) 8 nm $Fe_{80}Si_{20}$ (sample D) | 0 | 5.8 | 7(2) | 2.65(5) | 0.2 | — |

**Table 10.5.:** Magnetic relaxation parameters for (a) 8 nm $Fe_3Si$ annealed at 900 K for 1 h (sample B), (b) 40 nm $Fe_3Si$ as-prepared, (c) 8 nm $Fe_3Si$ annealed between 550-900K for 1 $h$ in steps of 100 K (sample C). (d) 8 nm $Fe_{80}Si_{20}$ annealed at 900 K for 1 h (sample D). All samples were measured at ambient temperature.

fit to Eq. (10.10) using both, the angular *and* frequency dependence of the linewidth yielding a unique set of parameters. A detailed description of the fitting procedure and the values of the individual frequency and angle dependent fits are given in Appendix A.3.

The fits reveal a small mosaicity of the sample on the order of 0.05–0.1$^\circ$ for $\Delta\phi_B$ and $\Delta\theta_B$. In the film plane the mosaicity term is slightly bigger than along the perpendicular direction ($\Delta\phi_B > \Delta\theta_B$). This implies that the lateral variation of the anisotropy fields in the film plane (either in orientation or strength) is bigger than the one of the effective demagnetizing field along the perpendicular direction.

In summary, the frequency dependence as well as the angular dependencies for the 8 nm $Fe_3Si$ film can be explained by one set of fit parameters that are summarized in Tab. 10.5(a). The entire angular dependence can be explained by anisotropic two-magnon scattering and mosaicity effects. No angle dependent Gilbert damping parameter needs to be invoked. The measured intrinsic Gilbert parameter is slightly smaller than the bcc Fe-bulk one ($6 \times 10^7$ Hz) [209]. This is due to the fact that the spin–orbit coupling in this structure is slightly smaller than for bulk-Fe (see Sec. 10.6). The two-magnon scattering along the $\langle 100\rangle$ directions is about 5 times more effective than along the $\langle 110\rangle$ directions. Its strength is comparable to the intrinsic Gilbert damping contribution, $G$, but small in comparison to the values measured for FeV superlattices [65,202]. Indeed, earlier works employing Mössbauer spectroscopy [210] have shown that the defects in bulk $Fe_3Si$ are mainly concentrated in $\alpha$-sublattices (being oriented parallel to the $\langle 100\rangle$-directions). This scenario, which was confirmed recently by first principle density functional calculations in combination with statistical mechanics [187], naturally explains the fact that the two-magnon contribution is stronger along the $\langle 100\rangle$-directions. According to Refs. [187,210] the probability of defect formation along $\langle 100\rangle$-directions is higher than along $\langle 110\rangle$-directions. This already confirms that the $\langle 100\rangle$- and $\langle 110\rangle$-directions are not equivalent. Indeed Refs. [187,210] discuss not only point defects, but also preferential diffusion channels.

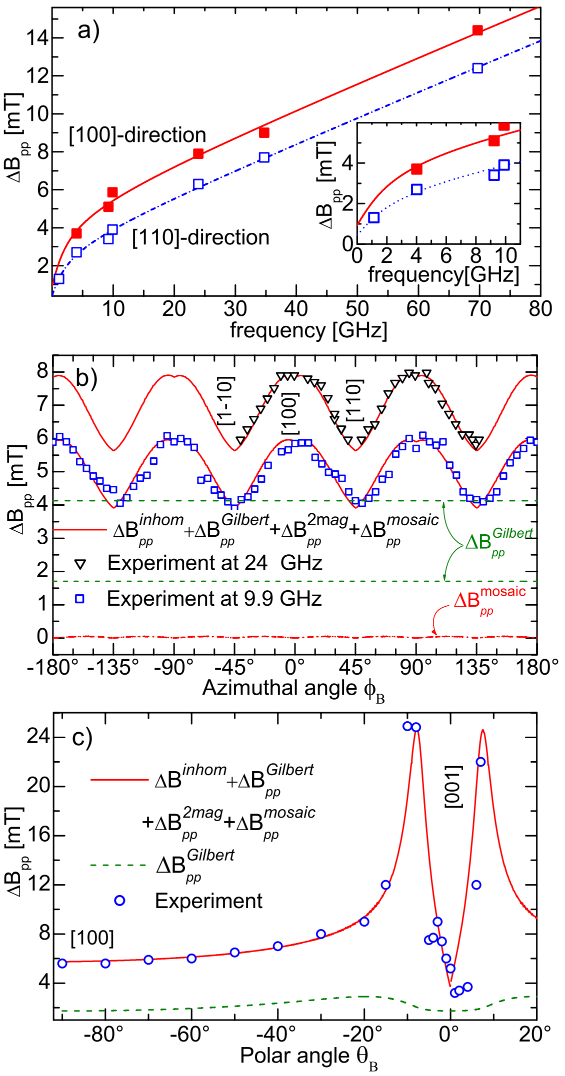

**Figure 10.17.:** (a) The frequency dependence of the FMR linewidth for 40 nm $Fe_3Si$ as-prepared. The inset shows the low-frequency results. (b) The azimuthal angular dependence of the FMR linewidth measured at microwave frequencies of 9.9 (squares) and 24 (triangles) GHz. (c) The polar angular dependence of the FMR linewidth recorded at a microwave frequency of 9.9 GHz. All experiments were performed at RT.

The latter are the ones that to our opinion might lead to large scale defects with average separation on the order of exited spin-waves (100 nm) within the film. To quantify these defects is not the goal of this thesis. We rather propose that such defects must be present.

We point out that there are other broadening mechanisms, i.e. exchange-conductivity, surface pinning or surface anisotropy effects [211]. To account for their contributions we have performed the calculations using the formulas for FMR microwave absorption obtained from the equation of motion, Maxwell and boundary equations of the linewidth contribution caused by exchange-conductivity effects and by surface spin pinning. For our case, $-\mu_0\mathrm{M}_{eff} \sim 1$ T, $g$ ∼2.075, $G = 5.1 \times 10^7$ Hz and $d$ =8–40 nm, both linewidth contributions are less than 0.1 mT for 18 to 70 GHz. Therefore, they can be neglected.

If lattice defects in the volume of the film and not at the interfaces are the origin of the two-magnon scattering, one would expect that its strength increases with film thickness when the volume part of the film becomes the dominating contribution. This is demonstrated in Fig. 10.17, where the frequency and angular dependencies of the FMR linewidth of an as-prepared (not annealed) 40 nm thick sample are plotted. The values for this film were obtained in the same way as described for the case of the 8 nm thick sample. They indeed show (see Table 10.5(b)) that the two-magnon contribution is increased along both principle in-plane directions. Although the Gilbert contribution is the same ($G$ is a material dependent constant), the two-magnon contribution has even overcome the Gilbert damping along the $\langle 100\rangle$-directions (see Table 10.5(b)).

One notices that the two magnon scattering strength for the 40 nm film is about twice that of the 8 nm. This is mainly due to the change in the available density of states for the degenerate magnons in the thicker film. This thickness dependence has been established recently in Ref. [212]. The enhanced two-magnon scattering in the 40 nm sample is another direct experimental confirmation of the theory that was recently developed by Krivosik *et al.* [212]. The authors showed that the available density of states for the degenerate magnons increases for thicker films. In addition, the larger mosaicity supports the fact that the thicker film has less structural perfection than the 8 nm thick one. We note, however, that the structural imperfection could also be related to the fact that this sample was not annealed. In the thick sample with stronger two-magnon scattering another effect can be observed in Fig. 10.17(c): The linewidth along the film normal is smaller than the one in the film plane. This is due to two-magnon scattering contribution because the dragging effect as a cause can be ruled out, as $\vec{M}$ and $\vec{B}$ are parallel in these directions (see discussion above) and also the Gilbert contribution is the same.

A possibility to raise the density of defects and dislocations within the $\mathrm{Fe_3Si}$ films stems from the fact that the film quality (for a given film thickness) strongly depends on the annealing procedure, as one can read off the broader linewidth for the as-prepared sample (compare Fig. 10.16 with Fig. 10.17). This was also verified by our conversion electron Mössbauer spectroscopy (CEMS) [179] combined with XRD measurements (see Fig. 10.2). This can be used to increase the number of scattering centers and thus two-magnon processes. Figure 10.18 shows the frequency and angle dependent linewidth of an 8 nm $\mathrm{Fe_3Si}$ film annealed between 550-900 K for 3 h in steps of 100 K, which has more defects (sample C) than the first sample (sample B) shown in Fig. 10.16. The magnetic relaxation parameters resulting from the frequency and angular dependence of the FMR linewidth of that sample are summarized in Tab. 10.5 (c).

In this case the relaxation mechanism along the [110]-direction is still dominated by

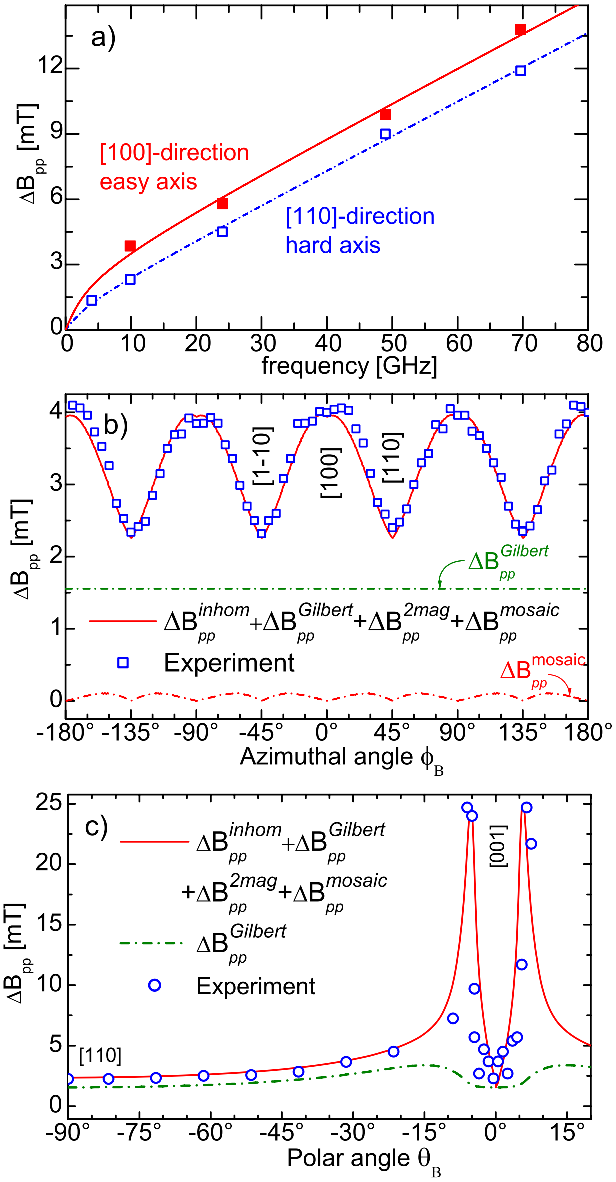

**Figure 10.18.:** (a) The frequency dependence of the FMR linewidth for an 8 nm Fe$_3$Si sample annealed between 550-900 K for 3 h in steps of 100 K (sample C). (b) The azimuthal and (c) polar angular dependences of the FMR linewidth measured at a microwave frequency of 9.9 GHz. All experiments were performed at RT.

a Gilbert-type mechanism, but the strength of the two-magnon scattering along the [100]-direction is enhanced by 33% with respect to the first sample. This indicates that the defects and dislocations within the Fe$_3$Si lattice have the tendency to form mainly along $\langle 100\rangle$ directions. Note that the $\alpha$ sublattices are oriented along these directions. This again proves in agreement with theory [187], that a preferential occupation of Fe sites by unwanted defects takes place along the $\langle 100\rangle$ directions, leading to a stronger contribution of two-magnon scattering in this direction.

As mentioned before, it was found experimentally [210] and later theoretically [187] that the defect formation energy increases with increasing Fe concentration, i.e., less defects are expected for a higher Fe concentration. In order to monitor this effect, an 8 nm $Fe_{80}Si_{20}$ film was prepared. The phase diagram of $Fe_{100-x}Si_x$ shows that the $D0_3$ structure is stable in the Si-concentration range between $12.5 < x < 31$ percent [26]. Therefore, a structural transformation due to the reduction of the Si concentration can be ruled out as it is also demonstrated by our X-ray diffraction experiments (see Fig. 10.9).

The frequency and angular dependencies of the 8 nm $Fe_{80}Si_{20}$ (sample D) film are shown in Fig. 10.19. It is obvious that the two-magnon scattering contribution is now much smaller than in the stoichiometric sample (Fig. 10.16). The in-plane angular dependence of the FMR linewidth in Fig. 10.19(b) clearly shows eight maxima, which is expected from a mosaicity driven linewidth broadening as well as for a strong field dragging contribution in the Gilbert damping. It can be seen that a smaller fourfold (four maxima) symmetry is superimposed on the eight maxima, indicating that two-magnon scattering is still present. This time its strength is much smaller than the mosaicity effect.

The magnetic relaxation parameters are listed in Tab. 10.5(d). The Gilbert parameter $G$ is found to be slightly larger than in the stoichiometric $Fe_3Si$ film, meaning a slightly larger spin–orbit coupling for this structure as expected due to the larger Fe content. We note that this enhancement is also confirmed by measurements of the $g$-factor as well as the magnetic anisotropy, which also show a slight increase with respect to the stoichiometric sample. As both quantities are related to orbital magnetism, they support the finding of a larger Gilbert parameter. According to Eq. (2.42), the Gilbert damping parameter is proportional to the deviation of the $g$-factor from the free electron value, $\Delta g$. $\Delta g$ is enhanced in $Fe_{80}Si_{20}$ as compared to $Fe_3Si$ (see

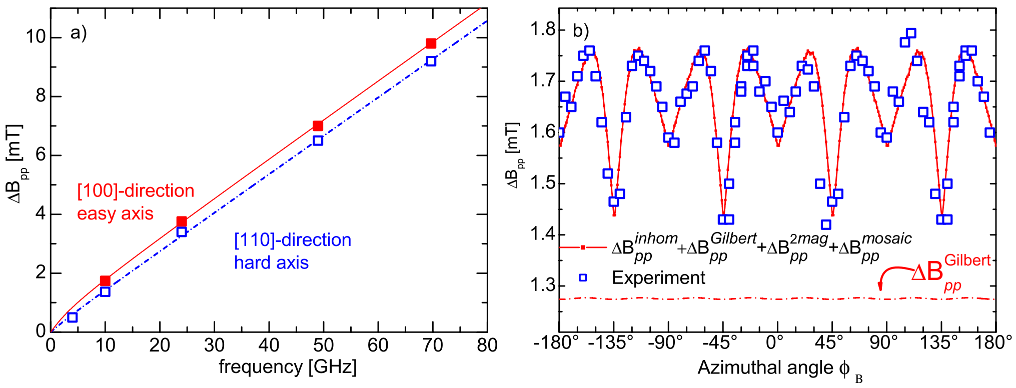

**Figure 10.19.:** (a) The frequency dependence of the FMR linewidth for an 8 nm $Fe_{80}Si_{20}$ film directly annealed at 900 K (sample D). (b) The azimuthal angular dependence of the FMR linewidth measured at a microwave frequency of 9.9 GHz. All experiments were performed at ambient temperature.

Sec. 10.6) therefore the enhanced Gilbert damping parameter is plausible.

## 10.9. Summary

In this chapter the static and dynamic magnetic properties of thin Fe$_3$Si films epitaxially grown on MgO(001) substrates were discussed. X-ray diffraction revealed that the expected cubic D0$_3$ structure is formed and that the best result was achieved upon deposition of the Fe at a temperature of $T_s = 550$ K and subsequent annealing of the film at $T = 900$ K for 1 h. The optimum deposition rate was about 0.5 nm/min.
The magnetic investigation by FMR, MOKE and SQUID magnetometry on as-prepared films with thicknesses between 4 and 40 nm at RT showed that the films have a dominating cubic anisotropy ($K_4 \approx 3 \cdot 10^3$ J/m$^3$, depending on the film treatment) that is about one order of magnitude smaller than the one of bulk Fe ($K_4 = 4.8 \cdot 10^4$ J/m$^3$). The magnetization was found to be $\mu_0 M = 1$ T which is less than half of the value for bulk Fe ($\mu_0 M = 2.1$ T).

Due to the very high sensitivity of FMR even to small anisotropy fields, a uniaxial in-plane anisotropy within the films was detected. It was shown to be of interfacial nature, so that most likely the oblique angle during Si deposition is the source.

Besides the cubic anisotropy, an out-of-plane uniaxial contribution was found that mostly results from the interface of the film. It leads to a perpendicular easy axis and plays an important role as the film thickness decreases. As the effect of shape anisotropy in the films is reduced compared to bulk Fe, one could speculate on a perpendicular orientation of the film's easy axis of magnetization in the very thin film limit. Thus, a further reduction of the film thickness beyond 4 nm is of great interest.

The $g$-factor of Fe$_3$Si could be extracted from frequency dependent FMR measurements to be $g = 2.075$, being slightly smaller than the one of bulk Fe ($g = 2.09$). The $g$-factor was found to be isotropic. A small increase was observed for the 4 nm film, possibly due to the growing importance of the out-of-plane anisotropy mentioned above. The different sample treatment, however, showed no influence on the $g$-factor.

The Si concentration dependence around the optimum concentration of 25% Si:75% Fe on the magnetic properties were investigated. The $g$-factor and magnetic anisotropy fields decrease linearly within the D0$_3$-regime.

The spin and orbital magnetism of 8 nm ordered Fe$_{2.8}$Si$_{1.2}$, Fe$_3$Si, and Fe$_{3.2}$Si$_{0.8}$ thin films were measured confirming that Fe-Si hybridization increase the crystal field effects on Fe atoms and consequently enhance the orbital quenching in Fe$_{3\pm\delta}$Si$_{1\mp\delta}$ binary Heusler structures.

The magnetic relaxation mechanisms were investigated over a wide range of microwave frequency (1-70 GHz). A general approach was proposed to quantitatively determine the relaxation mechanism in Fe$_3$Si. This model (Eq. (10.10)) is very general and can be used for all magnetic structures. The important results are: (i) In order to quantitatively disentangle the different relaxation parameters, low- as well as high-frequency FMR measurements supported by full in- and out-of-plane angular dependence at a fixed microwave frequency are needed. (ii) A precise determination of the magnetic damping parameter is possible only when all contributions to the FMR linewidth are considered. (iii) The angular dependence of the FMR linewidth is reproduced by the same set of relaxation parameters determined from the frequency dependence. No apparent inhomogeneous linewidth broadening (residual linewidth at $f$=0) is needed. (iv) The Gilbert damping parameter and the non-Gilbert type relaxation rates can be tuned by slightly modifying the Fe concentration, film thickness and annealing procedure.

# 11. Conclusion and Outlook

In this thesis a comparative study of structural and magnetic properties of Fe-based layered structures was presented. The first goal was to understand the interplay between lattice strain and magnetic anisotropy in the monolayer range, therefore, the static magnetic properties of Fe monolayers grown on the (001)-surface of different types of III-V semiconducting substrates (GaAs(001), InAs(001), and InP(001)) with different lattice mismatches were investigated. The magnetic anisotropy energy, $g$-factor, and the magnetization were determined by an unique combination of *in situ* UHV ferromagnetic resonance and SQUID magnetometry as a function of temperature and film thickness. As a second goal the static and dynamic magnetic properties of epitaxial $\mathrm{Fe_3Si}$ thin films were investigated using *ex situ* ferromagnetic resonance, SQUID magnetometry, magneto-optical Kerr effect, and X-ray diffraction as a function of film thickness, sample treatment, and Si concentration.

The main results of each system are summarized as follows:

- **Fe/{4×6}GaAs(001):** The different anisotropy contributions could be quantitatively related to misfit and reconstruction induced stress in the film plane. A magneto-elastic model was employed to explain the anisotropy contributions using the stress parameters measured *in situ* by IV-LEED analysis [59,62].
  The power-law relation between the temperature dependence of perpendicular magnetic anisotropy and magnetization was investigated, which reveals that single-ion magnetic anisotropy is the dominating microscopic origin in the Fe monolayers [213,214]. Moreover, the temperature dependence of each anisotropy contribution was determined and extrapolated to zero Kelvin, yielding $K_{2\perp}^{s,\mathrm{eff}}(T \longrightarrow 0)$=(1.26 ±0.1)$\times10^{-3}$ J/m$^2$=649 ± 36 $\mu$eV/atom and $K_{2\perp}^{v}(T \longrightarrow 0)$=(4±9)$\times10^4$ J/m$^3$=3±6.7 $\mu$eV/atom allowing quantitative comparison with first principle calculations [213,214].
  An enhanced $g$-factor observed for thin layers suggests an enhanced orbital moment, which was attributed to the reduced dimension and the changes of the electronic structure at the Fe-GaAs interface, which may modify the spin-orbit coupling of the Fe atoms confined to the interface. It was demonstrated that one monolayer of Ag increases the critical thickness for the onset of ferromagnetism from 2.8 ML for Fe/GaAs to 3.1 for 1 ML Ag /Fe/GaAs at room temperature. This can be related to the suppression of the surface contribution to the perpendicular magnetic anisotropy by about 20%. The Ag capping has

only very small effects on the in-plane magnetic anisotropy [94]. The Fe films exhibit a temperature-driven morphological transformation occurring at a temperature $T > 550$ K depending on the film thickness. During this transformation the cubic anisotropy increases by a factor of 2, whereas the perpendicular and in-plane uniaxial anisotropies decrease by about only 15 and 10%, [94].

In order to modify the interface magnetic parameters, Fe layers grown on thin buffer layers (1-5 ML) of Ag were studied since the Ag/GaAs interface is thermodynamically more stable than the Fe/GaAs interface. In addition to that, the thickness of the chosen buffer layer was thin enough (1-5 ML) to prevent the presence of electrical shunts. The interface uniaxial anisotropy is affected by a buffer layer of Ag at the interface. A single atomic layer of Ag decreases the interface uniaxial anisotropy by almost 15%. This effect becomes stronger as the thickness of the Ag layer increases; for example a 5 ML Ag layer reduces the interface uniaxial anisotropy by about 25%.

- **Fe/{4×2}InAs(001):** The different magnetic anisotropy contributions were determined and found to be related to uniaxial and biaxial strains in the films. The RT ferromagnetic long-range order in {4×2}InAs(001) appears at a film thickness of about 2.7 ML. The easy axis of magnetization is parallel to the [1$\bar{1}$0]-direction for thin Fe layers and rotates by 45° towards the [100]-direction above 7 ML.

  5 ML Au were used as a buffer layer to modify the magnetic anisotropy as well as the electronic structure at the interface. It was found that in contrary to the Fe/Ag/GaAs system the Au layer suppresses the cubic anisotropy as well as the uniaxial in-plane anisotropy by 100% and 80%, respectively. This can be related to a disordered structure or the diffusion of Au into the Fe layers. A morphological characterization of Au/InAs by STM is proposed for further verifying this hypothesis.

- **Fe/{2×4}InP(001):** The critical thickness for the onset of ferromagnetism at RT was found to be 4 ML. The magnetocrystalline anisotropy contributions and magnetization were determined and explained in terms of a magneto-elastic model. The cubic anisotropy for this structure was small and almost thickness independent, whereas the in-plane uniaxial anisotropy was strongly thickness dependent. The perpendicular uniaxial anisotropy deviates from the reciprocal thickness dependence, which was attributed to the change in the surface strain due to the formation of the new reconstructed surface of the intermixed atoms. The equilibrium angle of the magnetization was measured as a function of film thickness indicating an in-plane spin reorientation transition from the [1$\bar{1}$0]-direction for thin layers ($d$ <7 ML) towards the [100]-direction for thicker ones. The spin reorientation transition in Fe/InP extends over a larger thickness range than that of Fe/InAs. This is due to the difference in the thickness dependence of the anisotropy fields in these two systems.

- **Fe$_3$Si/MgO(001) films:** The magnetic anisotropy energy, $g$-factor, and magnetization were determined for different samples with Si concentrations of 20, 25, and 30 % for the first time. It was found that the films have a dominating cubic anisotropy ($K_4 \approx 3 \cdot 10^3$ J/m$^3$, depending on the film treatment) that is about one order of magnitude smaller than the one of bulk-Fe. The magnetization was determined to be $\mu_0 M = 0.9$ T which is less than half of the value for bulk Fe ($\mu_0 M = 2.1$ T). A small uniaxial in-plane anisotropy of interfacial nature within the films was detected. The perpendicular uniaxial anisotropy term was found to mostly result from the interface. From frequency dependent FMR measurements the $g$-factor was determined to be $g = 2.075(5)$ and isotropic. Since a small enhancement was observed for the 4 nm film ($g = 2.075(5)$), the different sample treatment showed no influence on the $g$-factor. The magnetic anisotropy fields and $g$-factor decreases linearly as the Si concentration increases within the D0$_3$-regime.
  The effective spin and orbital moment of the stoichiometric Fe$_3$Si was found to be $\mu^{\text{eff}}_{S(L)} = 1.38\mu_B\ (0.051\mu_B)$, which is smaller than the one of bulk-Fe [$\mu^{\text{eff}}_{S(L)} = 2.24\mu_B\ (0.103\mu_B)$] by a factor of roughly two as was confirmed by our density functional theory calculations [$\mu^{\text{eff}}_{S(L)} = 1.75\mu_B\ (0.029\mu_B)$]. The reduced spin and orbital moments are due to the fact that in Fe$_3$Si the atomic orbitals are more affected (quenched) by the ligand field than in bcc bulk Fe.
  It is found that in addition to the Gilbert mechanism the relaxation mechanism is altered by two-magnon scattering. The model by Arias and Mills [81,82,85] was confirmed and used to quantify the different magnetic relaxation parameters. The strength of two-magnon scattering depends on film treatment and is maximum along the $\langle 100 \rangle$-directions, while it is very small along the $\langle 110 \rangle$-directions. The intrinsic Gilbert damping parameter was found to be $G = 5.1 \cdot 10^7$ Hz and thickness independent. It was observed that as the Si concentration decreases the Gilbert damping parameter increases whereas the strength of two-magnon scattering decreases. These observations were attributed to the enhancement of spin-orbit coupling and a reduction of lattice defects.

Our investigation provides a quantitative explanation of magnetic anisotropy, $g$-factor and magnetization of Fe monolayers grown on GaAs(001), InAs(001), and InP(001) as a function of temperature and film thickness. The role of the different types of stress caused by the lattice mismatch and the surface reconstruction in the magnetic anisotropy terms is quantified. This means that strain plays a crucial role on the magnetic anisotropy in Fe films on semiconducting substrates in the monolayer regime. The magneto-elastic anisotropy depends linearly on the strain in the film and the first order magneto-elastic coupling constant has opposite sign compared to the one in bulk Fe. The Fe/InP interface was found to be the most reactive interface whereas the Fe/InAs is the less reactive one. The Fe/Ag interface is found to be much sharper

than the Fe/Au interface.
Moreover, an quantitative determination of the static and dynamic magnetic properties of epitaxial $Fe_3Si$ binary Heusler films grown on MgO(001) is presented for the first time. Two relaxation channels, i.e. dissipative, isotropic Gilbert damping as well as anisotropic two-magnon scattering are simultaneously identified and quantitatively analyzed. These results are important not only for applications in *spintronic* devices or for this particular system, but also to understand the physical principals of the spin damping mechanism in general. We showed how the relaxation parameters can be tuned by changing the film thickness and Si concentration.

The present investigation demonstrates that these kind of structures have, in principles, the capability to be used in future *spintronic* applications. For further studies we propose the investigation of the magnetic anisotropy of the Fe on other surface orientations of semiconductors (i.e. (110)- and (111)-surface), which allows one to compare the results with the results of this thesis.
While our investigation predicts a spin transition reorientation from in-plane to out-of-plane for ultrathin $Fe_3Si$ films (in monolayer regime), an investigation of the magnetic parameters of the $Fe_3Si$ monolayers grown on MgO(001) *and/or* GaAs(001) would also be very interesting.
Furthermore, a determination of the spin and orbital magnetism of $Fe_3Si$ films using XMCD and a calculation of these quantities for off stoichiometric $Fe_{3\pm\delta}Si_{1\mp\delta}$ alloys is proposed to yield valuable results.

# A. Appendix

## A.1. Conversion units

In the literature various units are used for the energy and magnetic parameters. In Tab. A.1 the conversion of energy units are given. In order to convert surface and volume anisotropy energy density Tab. A.2 can be utilized.

| | J | erg | eV |
|---|---|---|---|
| 1 J | $1$ | $10^7$ | $6.242 \cdot 10^{18}$ |
| 1 erg | $10^{-7}$ | $1$ | $6.242 \cdot 10^{11}$ |
| 1 eV | $1.602 \cdot 10^{-19}$ | $1.602 \cdot 10^{-12}$ | $1$ |

**Table A.1.:** Conversion of energy units

| | Lattice parameter (nm) | Atom/m$^3$ | $10^5$ J/cm$^3$ multiplied by | Atom/m$^2$ | $10^{-5}$ J/m$^2$ multiplied by |
|---|---|---|---|---|---|
| bcc (001) | 0.286 | $8.46 \cdot 10^{28}$ | 7.38$\mu$eV/atom | $1.21 \cdot 10^{19}$ | 5.15$\mu$eV/atom |
| fcc (001) | 0.359 | $8.65 \cdot 10^{28}$ | 7.22$\mu$eV/atom | $1.55 \cdot 10^{19}$ | 4.03$\mu$eV/atom |

**Table A.2.:** The list of bcc and fcc Iron lattice parameter, surface and volume density of atoms and proportionality constants for conversion of (eV $\longleftrightarrow$ J m$^{-3}$) and (eV $\longleftrightarrow$ J m$^{-2}$).

## A.2. Spherical harmonics

The spherical harmonics $Y_l^m(\theta,\phi)$ are the angular portion of the solution to Laplace's equation in spherical coordinates where azimuthal symmetry is not present. Some care must be taken in identifying the notational convention being used. In this entry, $\theta$ is taken as the polar (colatitudinal) coordinate with $\theta$ in [0,$\pi$], and $\phi$ as the azimuthal (longitudinal) coordinate with $\phi$ in [0,2$\pi$]. This is the convention normally used in physics, as described by Arfken [215], $\theta$ usually denotes the longitudinal coordinate and $\phi$ the colatitudinal coordinate). Spherical harmonics satisfy the spherical harmonic differential equation, which is given by the angular part of Laplace's equation in spherical coordinates.

$$Y_l^m(\theta,\phi) = \sqrt{\frac{2l+1}{4\pi}\frac{(l-m)!}{(l+m)!}}P_l^m(\cos\theta)e^{-im\phi} \tag{A.1}$$

$$Y_l^{-l}(\theta,\phi) = \frac{1}{2^l l!}\sqrt{\frac{(2l+1)!}{4\pi}}\sin^l\theta e^{-il\phi} \tag{A.2}$$

$$Y_l^0(\theta,\phi) = \sqrt{\frac{(2l+1)}{4\pi}}P_l(\cos\theta) \tag{A.3}$$

$$Y_l^{-m}(\theta,\phi) = (-1)^m Y_l^m(\theta,\phi) \tag{A.4}$$

where $P_l(\cos(\theta))$ is a Legendre polynomial. In the following some of the spherical harmonics which are needed to define the magnetic anisotropy up to the fourth order are listed.

$$Y_2^0(\theta,\phi) = \tfrac{1}{4}\sqrt{\tfrac{5}{\pi}}(3\cos^2\theta-1)$$

$$Y_2^{\pm2}(\theta,\phi) = \tfrac{1}{4}\sqrt{\tfrac{15}{2\pi}}\sin^2\theta e^{\pm2i\phi}$$

$$Y_4^0(\theta,\phi) = \sqrt{\tfrac{9}{256\pi}}(3\cos^4\theta-30\cos^2\theta+3)$$

$$Y_2^{\pm4}(\theta,\phi) = \sqrt{\tfrac{315}{512\pi}}\sin^4\theta e^{\pm4i\phi}$$

## A.3. The fit procedure of the FMR linewidth

The fitting procedure of frequency and angle dependent data was performed as follows:

(i) The frequency dependence of the FMR linewidth was fitted by Eq. (10.10) yielding the parameters $G$, $\Gamma_{\langle 100\rangle}$. $\Gamma_{\langle 110\rangle}$ and $\Delta B_{pp}^{\text{inhom}}$.

(ii) The same parameters were used to fit the angular dependence of the resonance linewidth measured at 9.9 GHz and the parameters were modified so that the best fit resulted.

(iii) These modified parameters were used to to crosscheck with the frequency dependent data again. In this step $G$ was kept constant.
Since in the frequency dependent fits the only contributions are $G$ and $\gamma\Gamma_{\langle 100\rangle}$ (or $\gamma\Gamma_{\langle 110\rangle}$), the error bar is larger than for the angle dependent fits, where all contributions have to be considered.

(iv) The fit procedures (i)–(iii) were repeated several times so that the best angle and fre-

| Sample | | $\Delta B_{pp}^{\text{inhom}}$ (mT) | $G$ ($10^7$Hz) | $\gamma\Gamma_{\langle 100\rangle}$ ($10^7$Hz) | $\gamma\Gamma_{\langle 110\rangle}$ ($10^7$Hz) | $\Delta\phi_B$ (°) | $\Delta\theta_B$ (°) |
|---|---|---|---|---|---|---|---|
| (a) | $B \parallel [100]$ | 0 | 5.1 | 25(2) | — | — | — |
| 8 nm $Fe_3$Si | $B \parallel [110]$ | 0.2(2) | 5.1 | — | 4(2) | — | — |
| annealed at | azimuthal | 0 | 5.1 | 25.6(8) | 4.4(5) | 0.09 | — |
| 900 K for 1 $h$ | polar | 0 | 5.1 | — | 4.4(5) | — | 0.05 |
| (b) | $B \parallel [100]$ | 0.9(1) | 5.1 | 53(17) | — | — | — |
| 40 nm $Fe_3$Si | $B \parallel [110]$ | 0.9(1) | 5.1 | — | 26(2) | — | — |
| not annealed | azimuthal | 1 | 5.1 | 56(2) | 26(1) | 0.3 | — |
| (as-prepared) | polar | 1 | 5.1 | 53(4) | — | — | 0.15 |
| (c) | $B \parallel [100]$ | 0 | 6.0 | 37(4) | — | — | — |
| 8 nm $Fe_3$Si | $B \parallel [110]$ | 0 | 6.0 | — | 15(4) | — | — |
| annealed between | azimuthal | 0 | 6 | 42.4(8) | 16(2) | 0.3 | — |
| 550-900 K for 3 $h$ | polar | 0 | 6 | — | 16(2) | — | 0.15 |
| (b) | $B \parallel [100]$ | 0 | 5.8 | 9(2) | — | — | — |
| 8 nm $Fe_{80}Si_{20}$ ann. | $B \parallel [110]$ | 0 | 5.8 | — | 2.65(5) | — | — |
| at 900 K for 1 $h$ | azimuthal | 0 | 5.8 | 5.6(9) | 2.65(5) | 0.2 | — |

**Table A.3.:** Magnetic relaxation parameters of (a) 8 nm $Fe_3$Si annealed at 900 K for 1 h (sample B), (b) 40 nm $Fe_3$Si as-prepared, (c) 8 nm $Fe_3$Si annealed between 550-900K for 1 h in steps of 100 K (sample C), and (d) 8 nm $Fe_{80}Si_{20}$ annealed at 900 K for 1 h (sample D). All samples were measured at ambient temperature. The parameters shown have been determined from the frequency dependencies for the two principal in-plane axes (denoted by $B \parallel [100]$ and $B \parallel [110]$, respectively), and from the angle dependent fits (denoted by *azimuthal* and *polar*).

quency dependent fits were archived. Table. A.3 lists the optimal parameters obtained from the frequency and angular dependencies of the FMR linewidth for each sample.

# List of Figures

# List of Tables

# Bibliography

[1] H. J. Zhu, M. Ramsteiner, H. Kostial, M. Wassermeier and H.-P. Schönherr, *Phys. Rev. Lett.* **87**, 016601 (2001)

[2] G. A. Prinz, *Science* **282**, 1660 (1996)

[3] Y. Ohno, D. K. Young, B. Beschoten, F. Matasukura, H. Ohno and D. D. Awschalom, *Nature* **402**, 790 (1999)

[4] K. H. Ploog, *Phys. Rev. Lett.* **87**, 016601 (2001)

[5] G. A. Prinz, G. T. Rado and J. J. Krebs, *J. Appl. Phys.* **53**, 2087 (1982)

[6] G. A. Prinz, *Science* **250**, 1092 (1990)

[7] R. Fiederling, M. Keim, G. Reuscher, W. Ossau, G. Schmidt, A. Waag and L. W. Molenkamp (1999)

[8] G. Wastlbauer and J. A. C. Bland, *Adv. Phys.* **54**, 137 (2005)

[9] R. J. Hicken, D. E. P. Eley, M. Gester, S. J. Gray, C. Daboo, A. J. R. Ives, and J. A. C. Bland, *J. Magn. Magn. Mater.* **145**, 278 (1995)

[10] M. Zölfl, M. Brockmann, M. Köhler, S. Kreuzer, T. Schweinböck, S. Miethaner, F. Bensch and G. Bayreuther, *J. Magn. Magn. Mater.* **175**, 16 (1997)

[11] A. Filipe, A. Schuhl and P. Galtier, *Appl. Phys. Lett.* **70**, 129 (1997)

[12] A. Filipe and A. Schuhl, *J. Appl. Phys.* **81**, 4359 (1997)

[13] J. M. Florczak and E. D. Dahlberg, *Phys. Rev. B* **44**, 9338 (1991)

[14] T. L. Monchesky, B. Heinrich, R. Urban, K. Myrtle, M. Klaua and J. Kirschner, *Phys. Rev. B* **60**, 10242 (1999)

[15] R. Urban, G. Woltersdorf and B. Heinrich, *Phys. Rev. Lett.* **87**, 217204 (2001)

[16] M. Madami, S. Tacchi, G. Carlotti, G. Gubbiotti and R. L. Stamps, *Phys. Rev. B* **69**, 144408 (2004)

[17] R. F. C. Farrow, S. S. P. Parkin and V. S. Speriosu, *J. Appl. Phys.* **64**, 5315 (1988)

[18] M. D. Stiles and A. Zangwill, *Phys. Rev. B* **66**, 14407 (2002)

[19] H. Dassow, R. Lehndorff, D. E. Bürgler, M. Buchmeier, P. A. Grünberg, C. M. Schneider and A. van der Hart, *Appl. Phys. Lett.* **89**, 222511 (2006)

[20] M. Zwierzycki, K. Xia, P. J. Kelly, G. E. W. Bauer and I. Turek, *Phys. Rev. B* **67**, 092401 (2003)

[21] H. Ohno, K. Yoh, K. Sueoka, K. Mukasa, A. Kawaharazuka and M. Ramsteiner, *Jap. J. Appl. Phys.* **42**, L87 (2003)

[22] Y. B. Xu, E. T. M. Kernohan, M. Tselepi, J. A. C. Bland and S. Holmes, *Appl. Phys. Lett.* **73**, 399 (1998)

[23] J. A. C. Bland, A. Hirohata, C. M. Guertler, Y. B. Xu and M. Tselepi, *J. Appl. Phys.* **89**, 6740 (2001)

[24] C. Ohler, C. Daniels, A. Förster and H. Lüth, *J. Vac. Sci. Technol. B* **15**, 702 (1997)

[25] C. H. Moeller, O. Kronenwerth, D. Grundler, W. Hansen, Ch. Heyn and D. Heitmann, *Appl. Phys. Lett.* **80**, 3988 (2002)

[26] T. B. Massalski, *Binary Alloy Phase Diagrams*, American Society for Metals, Ohio (1986)

[27] Y. Nakamura, *Landolt-Börnstein, New Series III/19c*, Springer, Berlin (1988)

[28] V. A. Niculescu, T. J. Burch, and J. I. Budnick, *J. Magn. Magn. Mater.* **39**, 223 (1983)

[29] M. Mendik, Z. Frait, H. von Känel, and N. Onda, *J. Appl. Phys.* **76**, 6897 (1994)

[30] N. Onda, H. Sirringhaus, S. Goncalves-Conto, C. Schwarz, S. Zehnder, and H. von Känel, *Appl. Surf. Sci.* **73**, 124 (1993)

[31] Z. Frait, *Private Communications* (2006)

[32] S. Adoh, M. Kumano, R. Kizuka, K. Ueda, A. Kenjo, and M. Miyao, *Appl. Phys. Lett.* **89**, 182511 (2006)

[33] T. Yoshitake, D. Nakagauchi, T. Ogawa, M. Itakura, N. Kuwano, Y. Tomokiyo, T. Kajiwara, and K. Nagayama, *Appl. Phys. Lett.* **86**, 262505 (2005)

[34] R. Nakanea, M. Tanakab and S. Sugahara, *Appl. Phys. Lett.* **89**, 192503 (2006)

[35] K. Lenz, E. Kosubek, K. Baberschke, H. Wende, J. Herfort, H.-P. Schönherr, and K. H. Ploog, *Phys. Rev. B* **72**, 144411 (2005)

[36] B. Jenichen, V. M. Kaganer, J. Herfort, D. K. Satapathy, H. P. Schönherr, W. Braun and K. H. Ploog, *Phys. Rev. B* **72**, 075329 (2005)

[37] A. Ionescu, C. A. F. Vaz, T. Trypiniotis, C. M. Gürtler, H. Garcia- Miquel, J. A. C. Bland, M. E. Vickers, R. M. Dalgliesh, S. Langridge, Y. Bugoslavsky, Y. Miyoshi, L. F. Cohen, and K. R. A. Ziebeck, *Phys. Rev. B* **71**, 094401 (2005)

[38] A. Ionescu, C. A. F. Vaz, T. Trypiniotis, C. M. Gürtler, M. E. Vickers, H. Garc'ia-Miquel, and J. A. C. Bland, *J. Magn. Magn. Mater.* **72**, 286 (2005)

[39] S. H. Liou, S. S. Malhotra, J. X. Shen, M. Hong, J. Kwo, H. S. Chen, and J. P. Mannaerts, *J. Appl. Phys.* **73**, 6766 (1993)

[40] J. Herfort, H.-P. Schönherr, and K. H. Ploog, *Appl. Phys. Lett.* **83**, 3912 (2003)

[41] J. Herfort, H.-P. Schönherr, K.-J. Friedland, and K. H. Ploog, *J. Vac. Sci. Technol. B* **22**, 2073 (2004)

[42] J. Herfort, H.-P. Schönherr, A. Kawaharazuka, M. Ramsteiner, and K. H. Ploog, *J. Cryst. Growth* **278**, 666 (2005)

[43] K. Lenz, E. Kosubek, K. Baberschke, J. Herfort, H.-P. Schönherr, and K. H. Ploog, *Phys. Stat. Sol. (c)* **2**, 122 (2006)

[44] J. Mathon and A. Umersky, *Phys. Rev. B* **63**, 220403R (2001)

[45] D. D. Djayaprawira, K. Tsunekawa, M. Nagai, H. Maehara, S. Yamagata, N. Watanabe, S. Yuasa, Y. Suzuki and K. Ando, *Appl. Phys. Lett.* **86**, 092502 (2005)

[46] S. Yuasa, T. Nagahama, A. Fukushima, Y. Suzuki, and K. Ando, *Nature Materials* **3**, 868 (2004)

[47] S. Yuasa, A. Fukushima, T. Nagahama, K. Ando, and Y. Suzuki, *Jap. J. Appl. Phys.* **43**, L 588 (2004)

[48] G. Bihlmayer, *Reduced Dimensions: Magnetic Anisotropy*, in *Magnetism goes Nano*, 36th IFF Spring School, Jülich (2005)

[49] P. Bruno, *Phys. Rev. B* **39**, 865 (1989)

[50] S. H. Vosko and L. Wilk, *Phys. Rev. B* **22**, 3812 (1980)

[51] P. Bruno, *Physical Origins and Theoretical Models of Magnetic Anisotropy*, in *Vorlesungsmanuskripte des 24.IFF-Ferienkurses im Forschungszentrum Jülich*, Forschungszentrum Jülich (1993)

[52] D. Sander, *Rep. Prog. Phys.* **62**, 1 (1999)

[53] D. Sander, *J. Phys.: Condens. Matter.* **16**, R603 (2004)

[54] T. L. Gilbert, *Phys. Rev.* **100**, 1243 (1955)

[55] Z. Frait and D. Fraitova, *Frontiers in Magnetism of Reduced Dimension Systems*, Bd. 49, NATO ASI Series 3, Kluver Acad. Publ. (Dordrecht) (1998)

[56] J. Smit and H. G. Beljers, *Phillips Res. Rep.* **10**, 113 (1955)

[57] J. Pelzl, R. Meckenstock, D. Spoddig, F. Schreiber, J. Pflaum and Z. Frait, *J. Phys.: Condens. Matter* **15**, S451 (2003)

[58] M. Farle, *Rep. Prog. Phys.* **61**, 755 (1998)

[59] Kh. Zakeri, Th. Kebe, J. Lindner, C. Antoniak, M. Farle, K. Lenz, T. Toliński and K. Baberschke, *Phase Transitions* **79**, 793 (2006)

[60] B. Heinrich and J. A. C. Bland, *Ultrathin Magnetic Structures II*, Springer, Heidelberg (1994)

[61] L. Baselgia, M. Warden, F. Waldner, L. Hutton, E. Drumheller, Y. Q. He, P. E. Wigen, M. Maryško, *Phys. Rev. B* **38**, 2237 (1988)

[62] Kh. Zakeri, Th. Kebe, J. Lindner and M. Farle, *J. Magn. Magn. Mater.* **299**, L1 (2006)

[63] C. E. Patton, *Dynamic processes in magnetic thin films. Domain wall motion and ferromagnetic resonance*, Ph. D. thesis, California Institute of technology (1967)

[64] F. Bloch, *Phys. Rev.* **70**, 460 (1946)

[65] K. Lenz, H. Wende, W. Kuch, K. Baberschke, K. Nagy, and A. Jánossy, *Phys. Rev. B* **73**, 144424 (2006)

[66] N. Bloembergen, *Phys. Rev.* **78**, 572 (1950)

[67] S. V. Vonsovski, *Ferromagnetic Resonance*, Pergamon Press, Oxford London Edinburgh New York Toronto Paris Frankfurt (1966)

[68] B. Heinrich, D. Fraitová and V. Kamberský, *Phys. Stat. Sol. (a)* **23**, 501 (1967)

[69] R. J. Elliot, *Phys. Rev.* **96**, 266 (1954)

[70] L. Piraux, S. Dubois, A. Fert, and L. Belliard, *Euro. Phys. J. B* **4**, 413 (1998)

[71] S. D. Steenwyk, S. Y. Hsu, R. Loloee, J. Bass and W. P. Pratt, *J. Magn. Magn. Mater.* **170**, L1 (1997)

[72] S. Dubois, L. Piraux, J. M. George, K. Ounadjela, J. L. Duvail and A. Fert, *Phys. Rev. B* **60**, 477 (1999)

[73] R. Kobu, M. Toda and N. Hashitsume, *Statistical Physics II Nonequilibrium Statistical Mechanics*, Springer, Heidelberg (1992)

[74] V. Kambersky, *Can. J. Phys.* **48**, 2906 (1970)

[75] V. Kambersky, *Czech. J. Phys B* **26**, 1366 (1976)

[76] M. Sparks, R. Louden and C. Kittel, *Phys. Rev.* **122**, 791 (1961)

[77] E. Schlömann, *J. Phys. Chem. Solids* **6**, 242 (1958)

[78] C. E. Patton, C. H. Wilts, and F. B. Humphrey, *J. Appl. Phys.* **38**, 1358 (67)

[79] R. LeCraw, E. G. Spencer and C. S. Porter, *Phys. Rev.* **110**, 1311 (1958)

[80] M. J. Hurben and C. E. Patton, *J. Appl. Phys.* **83**, 4344 (1998)

[81] R. Arias and D. L. Mills, *Phys. Rev. B* **60**, 7395 (1999)

[82] R. Arias and D. L. Mills, *J. Appl. Phys.* **87**, 5455 (2000)

[83] R. D. McMichael, M. D. Stiles, P. J. Chen, and W. F. Egelhoff, *J. Appl. Phys.* **83**, 7037 (1998)

[84] R. P. Erickson and D. L. Mills, *Phys. Rev. B* **46**, 861 (1992)

[85] D. L. Mills and R. Arias, *Physica B* **384**, 147 (2006)

[86] R. Ramchal, *In situ magnetic domain imaging at the spin-reorientation transition of ultrathin Ni- an Fe/Ni-films*, Ph. D. thesis, Universität Duisburg-Essen (2004)

[87] L. E. Davis, N. C. MacDonald and P. W. Palmberg, *Handbook of Auger Electron Spectroscopy*, Eden Prairie (1978)

[88] C. Kittel, *Introduction to solid state physics*, John Wiley & Sons, Inc. (1996)

[89] F. Jonat, J. A. Strozier Jr, and W. S. Yang, *J. Appl. Phys.* **45**, 527 (1982)

[90] B. Heinrich and J. F. Cochran, *Adv. Phys.* **42**, 523 (1993)

[91] Th. Kebe, *SQUID-magnetometry on Fe monolayers on GaAs(001) in UHV*, Ph. D. thesis, Universität Duisburg-Essen (2006)

[92] Th. Kebe, Kh. Zakeri, J. Lindner, M. Spasova and M. Farle, *J. Phys.: Condens. Matter* **18**, 8791 (2006)

[93] A. Ney, P. Poulopoulos, M. Farle and K. Baberschke, *Phys. Rev. B* **62**, 11336 (2000)

[94] Kh. Zakeri, Th. Kebe, J. Lindner, and M. Farle, *Superlattices and Microstructures* **41**, 116 (2007)

[95] Y. B. Xu, E. T. M. Kernohan, D. J. Freeland, M. Tselepi, A. Ercole and J. A. C. Bland, *J. Magn. Magn. Mater.* **198-199**, 703 (1999)

[96] K. Sano and T. Miyagawa, *J. Appl. Phys.* **30**, 1434 (1991)

[97] K. Sano and T. Miyagawa, *Surf. Sci.* **60/61**, 813 (1992)

[98] F. Bensch, G. Garreau, R. Moosbühler, G. Bayreuther and E. Beaurepaire, *J. Appl. Phys.* **89**, 7133 (2001)

[99] D. J. Freeland, Y. B. Xu, E. T. M. Kernohan, M. Tselepi and J. A. C. Bland, *Thin Solid Films* **343-344**, 210 (2001)

[100] W. C. Lin, C. C. Kuo, C. L. Chio and Minn-Tsong. Li, *Surf. Sci.* **478**, 9 (2001)

[101] G. Wedler, B. Wassermann, R. Nötzel and R. Koch, *Appl. Phys. Lett.* **78**, 1270 (2001)

[102] G. Wedler, B. Wassermann and R. Koch, *Phys. Rev. B* **66**, 064415 (2002)

[103] V. Kumar and B. S. R. Sastry, *Cryst. Res. Technol.* **36**, 565 (2001), and references therein

[104] R. Mahesh, D. Sander, S. M. Zharkov and J. Kirschner, *Phys. Rev. B* **68**, 045416 (2003)

[105] D. E. Bürgler, C. M. Schmidt, D. M. Schaller, F. Meisinger, R. Hofer and H.-J. Güntherodt, *Phys. Rev. B* **56**, 4149 (1997)

[106] K. B. Urquhart, B. Heinrich, J. F. Cochran, A. S. Arrott, and K. Myrtle, *Adv. Phys.* **64**, 5334 (1998)

[107] D. Sander and H. Ibach, *Physics of Covered Solid Surfaces*, in *New Series, Group III* (2002)

[108] Q. Xue, T. Hashizume, J. M. Zhou, T. Sakata, T. Ohno and T. Sakurai, *Phys. Rev. Lett.* **74**, 3177 (1995)

[109] S. McPhail, C. M. Gürtler, F. Montaigne. Y. B. Yu, M. Tselepi and J. A. C. Bland, *Phys. Rev. B* **67**, 24409 (2003)

[110] R. Urban, *Electron Tunnelling and Spin Dynamics and Transport in Crystalline Magnetic Multilayers*, Ph. D. thesis, Department of Physics, Simon Fraser University, Canada (2003)

[111] M. Brockmann, M. Zölfl, S. Miethaner and G. Bayreuther, *J. Magn. Magn. Mater.* **198-199**, 384 (1999)

[112] G.W. Anderson, M.C. Hanf, P.R. Norton, M. Kowalewski, K. Myrtle and B. Heinrich, *J. Appl. Phys.* **79**, 4954 (1996)

[113] W. Platow, A. Anisimov, M. Farle and K. Baberschke, *Phys. Stat. Sol. (a)* **173**, 145 (1999)

[114] B. Heinrich and J.F. Cochran, *Adv. Phys.* **42**, 523 (1993)

[115] R. Moosbühler, F. Bensch, M. Dumm and G. Bayreuther, *J. Appl. Phys.* **91**, 8757 (2002)

[116] R. A. Gordon, E. D. Crozier, D.-T. Jiang, T. L. Monchesky and B. Heinrich, *Phys. Rev. B* **62**, 2151 (2000)

[117] M. Kŏsuth, V. Popescu, H. Ebert and G. Bayreuther, *Europhys. Lett.* **72**, 816 (2005)

[118] F. Bensch, R. Mossbühler and G. Bayreuther, *J. Appl. Phys.* **91**, 8754 (2002)

[119] S. J. Steinmuller, M. Tselepi, V. Strom, and J. A. C. Bland, *J. Appl. Phys.* **91**, 8679 (2002)

[120] B. Actas, B. Heinrich, G. Woltersdorf, R. Urban, L. R. Tagirov, F. Yildiz, K. Özdogan, M. Özdemir, O. Yalçin, B. Z. Rameev, *Nanostructured Magnetic Materials and their Applications*, Bd. 143 von *NATO Science Series II Mathematics, Physics and Chemistry*, Springer-Verlag, Berlin (2004)

[121] H. B. Callen and E. Callen, *J. Phys. Chem. Solids* **27**, 1271 (1966)

[122] J. G. Gay and R. Richter, *J. Appl. Phys.* **61**, 3362 (1987)

[123] P. J. Jensen and K. H. Bennemann, *Phys. Rev. B* **42**, 849 (1990)

[124] A. Kashuba and V. L. Pokrovsky, *Phys. Rev. Lett.* **70**, 3155 (1993)

[125] A. Ecker, P. Fröbrich, P. J. Jensen and P. J. Kuntz, *J. Phys.: Condens. Matter* **11**, 1557 (1999)

[126] D. P. Pappas, *J. Vac. Sci. Technol.* **14**, 3203 (1996)

[127] O. Fruchart, J. -P. Nozieres and D. Givord, *J. Magn. Magn. Mater.* **165**, 508 (1997)

[128] S. Okamoto, N. Kikuchi, O. Kitakami, T. Miyazaki, Y. Shimada and K. Fukamichi, *Phys. Rev. B* **66**, 024413 (2002)

[129] J. -U. Thiele, K. R. Coffey, M. F. Toney, J. A. Hedstrom and A. J. Kellock, *J. Appl. Phys.* **91**, 6595 (2002)

[130] O. N. Mryasov, U. Nowak, K. Y. Guslienko and R. W. Chantrell, *Europhys. Lett.* **69**, 805 (2005)

[131] J. B. Staunton, S. Ostanin, S. S. A. Razee, B. L. Gyorffy, L. Szunyogh, B. Ginatempo and E. Bruno, *Phys. Rev. Lett.* **93**, 257204 (2004)

[132] J. M. Shaw, S. Park and C. M. Falco, *J. Appl. Phys.* **95**, 6552 (2004)

[133] J. M. Shaw and C. M. Falco, *J. Magn. Magn. Mater.* **286**, 420 (2005)

[134] B. Lépine, S. Ababuo, A. Guivarc'h, G. Jézéqule, S. Députier, R. Guérin, A. Filipe, A. Schuhl, F. Abel, C. Cohen, A. Rocher, and J. Crestou, *J. Appl. Phys.* **83**, 3077 (1998)

[135] J. A. C. Bland and B. Heinrich, *Ultrathin Magnetic Structures III*, Springer-Verlag, Berlin Heidelberg (2005)

[136] J. Camarero, J. J. de Miguel, R. Miranda, V. Raposo and A. Hernando, *Phys. Rev. B* **83**, 4344 (1998)

[137] P. Poulopoulos, J. Lindner, M. Farle and K. Baberschke, *Surf. Sci.* **437**, 277 (1999)

[138] P. Bruno, *J. Appl. Phys.* **64**, 3153 (1988)

[139] P. Bruno, *J. Phys. F: Met. Phys.* **18**, 1291 (1988)

[140] H. J. Elmers, *Magnetometrische Untersuchungen an ultradünnen Ni- und Fe- Epitaxie-Schichten*, Ph. D. thesis, Department of Physics, Technische Universität Clausthal (1989)

[141] H. J. Elmers and U. Gradmann, *J. Appl. Phys.* **64**, 5328 (1988)

[142] WIEN2k, An Augmented Plane Wave+Local Orbitals Program for Calculating Crystal Properties, P. Blaha, K. Schwarz, G. K. H. Madsen, D. Kvasnicka, and J. Luitz, 2001, Techn. Universität Wien, Austria, (www.wien2k.at)

[143] J. S. Claydon,Y. B. Xu, M. Tselepi, J. A. C. Bland and G. van der Laan, *J. Appl. Phys.* **95**, 6543 (2006)

[144] A. T. Hanbicki, O. M. J. van't Erve, R. Magno, G. Kioseoglou, C. H. Li, B. T. Jonker, G. Itskos, R. Mallory, M. Yasar and A. Petrou, *Appl. Phys. Lett.* **82**, 4092 (2003)

[145] H. Ohno, K. Yoh, T. Doi, A. Subagyo, K. Sueoka and K. Mukasa, *J. Vac. Sci. Technol. B* **19**, 2280 (2001)

[146] L. Ruppel, G. Witte, Ch. Wöll, T. Last, S. F. Fischer and U. Kunze, *Phys. Rev. B* **66**, 255307 (2002)

[147] P. Schieffer, B. Lépine and G. Jézéqule, *Surf. Sci.* **497**, 341 (2002)

[148] C. M. Teodorescu, F. Chevrier, C. Richter, V. Ilakovac, O. Heckmann, L. Lechevalier, R. Brochier, R. L. Johnson and K. Hricovini, *Appl. Surf. Sci.* **166**, 137 (2000)

[149] M. Kneppe, M. Berse and U. Köhler, *App. Phys. A* **79**, 1935 (2004)

[150] C. M. Teodorescu, F. Chevrier, R. Brochier, C. Richter, O. Heckmann, V. Ilakovac, P. De Padova and K. Hricovini, *Surf. Sci.* **482-485**, 1004 (2001)

[151] C. M. Teodorescu and D. Luca, *Surf. Sci.* **600**, 4200 (2006)

[152] C. M. Teodorescu , F. Chevrier , R. Brochier , C. Richter , V. Ilakovac , O. Heckmann , P. De Padova and K. Hricovini, *The European Physical Journal B* **28**, 305 (2002)

[153] H. Yamaguchi and Y. Horikoshi, *Phys. Rev. B* **51**, 9836 (1995)

[154] Y. B. Xu, D. J. Freeland, M. Tselepi and J. A. C. Bland, *Phys. Rev. B* **62**, 1167 (2000)

[155] C. E. J. Mitchell, *Structural and electronic peoperties of clean (2x4) reconstructed and Sulphur-pasivated InP(100)*, Ph. D. thesis, Queen's University (1996)

[156] T. Toliński, K. Lenz, J. Lindner, E. Kosubek, K. Baberschke, D. Spoddig and R. Meckenstock, *Sol. Stat. Comm.* **128**, 385 (2003)

[157] C. D. Damsgaard, H. P. Gunnlaugsson, G. Weyer, J. Bindslev Hansen C. S. Jacobden, J. L. Skov, I. Rasmussen and S. Morup, *Solid State Commun.* **133**, 579 (2005)

[158] Y.-L. He and G. -C. Wang, *Phys. Rev. Lett.* **71**, 3834 (1993)

[159] A. M. Begley, S. K. Kim, J. Quinn, F. Jona, H. Over and P. M. Marcus, *Phys. Rev. B* **48**, 1779 (1993)

[160] R. Belkhou, R. Flammini, M. Marsi, A. Taleb-Ibrahimi, L. Gregoratti, A. Barinov, M. Kiskinova, *Surf. Sci.* **532-535**, 63 (2003)

[161] M. M. J. Bischoff, T. Yamada, A. J. Quinn, R. G. P. van der Kraan and H. van Kempen, *Phys. Rev. Lett.* **87**, 246102 (2001)

[162] T. Zhang, M. Spangenberg, N. Takahashi, T. -H. Shen, D. Greig, J. A. D. Matthew and E. A. Seddon **191**, 211 (2002)

[163] C. M. Aldoa, I. M. Vitomirov, F. Xu and J. H. Weaver, *Phys. Rev. B* **37**, 6019 (1988)

[164] T. W. Kim, D. U. Lee, Y. S. Yoon, Y. H. Shin and C. O. Kim, *Thin Solid Films* **338**, 161 (1999)

[165] F. Zavaliche, W. Wulfhekel, and J. Kirschner, *Phys. Rev. B* **65**, 245317 (2002), F. Zavaliche, M. Przybylski, W. Wulfhekel, J. Grabowski, R. Scholz and J. Kirschner, *Surf. Sci.* **507-510**, 560 (2002)

[166] M. M. Sung, C. Kim, H. Bu, D. S. Karpuzov and J. W. Rabalais, *Surf. Sci.* **322**, 116 (1995)

[167] S. J. Pearton, C. R. Abernathy, D. P. Norton, A. F. Hebard, Y. D. Park, L. A. Boatner and J. D. Budai, *Materials Science and Engineering R* **40**, 137 (2003)

[168] E. J. Lisherfs, C. Wilkinsont, T. Ericssonx, L. Haggstromx, L. Lundgrent and R. Wappling, *J. Phys. C: Solid State Phys.* **7**, 1344 (1974)

[169] I. Galanakis, P. H. Dederichs, and N. Papanikolaou, *Phys. Rev. B* **66**, 174429 (2002)

[170] S. Picozzi, A. Continenza, and A. J. Freeman, *Phys. Rev. B* **66**, 094421 (2002)

[171] S. Fujii, S. Ishida and S. Asano, *Journal of the Physics Society* **64**, 185 (1995)

[172] R. de Groot, F. Mueller, P. van Engen, and K. Buschow, *Phys. Rev. Lett.* **50**, 2024 (1983)

[173] S. Ishida, T. Masaki, S. Fujii, and S. Asano, *Physica B* **245**, 1 (1998)

[174] P. Webster, *J. Phys. Chem. Solids* **32**, 1221 (1971)

[175] E. G. Moroni, W. Wolf, J. Hafner, and R. Podloucky, *Phys. Rev. B* **59**, 12860 (1999)

[176] A. Bansil, S. Kaprzyk, P. E. Mijnarends, and J. Tobola, *Phys. Rev. B* **59**, 13396 (1999)

[177] J. Kudrnovsky, N. E. Christensen, and O. K. Andersen, *Phys. Rev. B* **43**, 5924 (1991)

[178] M. Goto and T. Kamimori, *J. Phys. Soc. Jpn.* **52**, 3710 (1983)

[179] W. Keune, *Private Communications* (2006)

[180] B. E. Warren, *X-ray Diffraction*, Dover Publications: New York (1990)

[181] W. A. Hines, A. H. Menotti, J. I. Budnick, T. J. Burch, T. Litrenta, V. Niculescu, and K. Raj, *Phys. Rev. B* **13**, 4060 (1976)

[182] R. A. Reck and D. L. Fry, *Phys. Rev.* **184**, 492 (1969)

[183] Anisimov, M. Farle, P. Poulopoulos, W. Platow, K. Baberschke, P. Isberg, R. Wäppling, A. M. N. Niklasson, and O. Eriksson, *Phys. Rev. Lett.* **82**, 2390 (1999)

[184] H. Malissa, W. Jantsch, M. Mühlberger, F. Schäffler, Z. Wilamowski, M. Draxler and P. Bauer, *J. Appl. Phys.* **85**, 1739 (2004)

[185] C. Kittel, *Phys. Rev.* **76**, 743 (1949), A. J. P. Meyer and G. Asch, *J. Appl. Phys.* **32**, 330S (1961), and references therein

[186] N. I. Kulikov, D. Fristot, J. Hugel, and A. V. Postnikov, *Phys. Rev. B* **66**, 014206 (2002)

[187] S. Dennler and J. Hafner, *Phys. Rev. B* **73**, 174303 (2006)

[188] S. Blundell, *Magnetism in Condensed Matter*, Oxdord University Press Inc., New York (2001)

[189] S. Cottenier, *Private Communications* (2006)

[190] O. Eriksson, B. Johansson, R. C. Albers, A. M. Boring, M. S. S. Brooks, *Phys. Rev. B* **42**, 2707 (1990)

[191] O. Eriksson, L. Nordström, A. Pohl, L. Severin, A. M. Boring, B. Johansson, *Phys. Rev. B* **41**, 11807 (1990)

[192] U. Gradmann„ *Handbook of Magnetic Materials*, Bd. 17, Elsevier Science Publishers (1993)

[193] P. Poulopoulos and K. Baberschke, *Phase Transitions in Coupled Two-Dimensional Ferromagnetic Layers*, in *Band-Ferromagnetism, Ground-State and Finite-Temperature Phenomena*, Hrsg. K. Baberschke, M. Donath and W. Nolting, Lecture Notes in Physics, Springer, Berlin Heidelberg New York (2001)

[194] B. Hillebrands, K. Ounadiela (Eds), in *Spin Dynamics in Confined Magnetic Structures III*, Bd. 83 von *Topics in Applied Physics*, Springer, Berlin, Heidelberg, New York (2003)

[195] B. Van Waeyenberge, A. Puzic, H. Stoll, K. W. Chou, T. Tyliszczak, R. Hertel, M. Fähnle, H. Brückl, K. Rott, G. Reiss, I. Neudecker, D. Weiss, C. H. Back and G. Schütz, **444**, 461 (2006)

[196] R. D. McMichael and P. Krivosik, *IEEE Trans. Magn.* **10**, 2 (2004)

[197] B. J. Kuanr, R. E. Camley, and Z. Celinski, *J. Appl. Phys.* **95**, 6610 (2004)

[198] M. Sparks, *Ferromagnetic-Relaxation Theory*, McGraw-Hill, New York (1964)

[199] R. D. McMichael, D. J. Twisselmann and A. Kunz, *Phys. Rev. Lett.* **90**, 227601 (2001)

[200] A. V. Nazarov, D. Menard, J. J. Green, C. E. Patton, G. M. Argentina and H. J. Van Hook, *J. Appl. Phys.* **94**, 7228 (2003)

[201] N. Mo, Y. -Y. Song and C. E. Patton, *J. Appl. Phys.* **97**, 093901 (2005)

[202] J. Lindner, K. Lenz, E. Kosubek, K. Baberschke, D. Spoddig, R. Meckenstock, J. Pelzl, Z. Frait, and D. L. Mills, *Phys. Rev. B* **68**, 060102 (2003)

[203] G. Woltersdorf and B. Heinrich, *Phys. Rev. B* **69**, 184417 (2004)

[204] A. Butera, J. Gómez, J. L. Weston, and J. A. Barnard, *J. Appl. Phys.* **98**, 033901 (2005)

[205] K. Lenz, T. Toliński, J. Lindner, E. Kosubek, and K. Baberschke, *Phys. Rev. B* **69**, 144422 (2004)

[206] R. Urban, G. Woltersdorf and B. Heinrich, *Phys. Rev. Lett.* **87**, 217204 (2001)

[207] D. L. Mills and S. M. Rezende, *Spin dynamics in confined magnetic structures II*, Springer-Verlag Berlin, Heidelberg, New York (2003)

[208] B. Heinrich, G. Woltersdorf, R. Urban, O. Mosendz, G. Schmidt, P. Bach, L. Molenkamp and E. Rozenberg, *J. App. Phys.* **95**, 7462 (2004)

[209] Z. Frait and D. Fraitova, *J. Magn. Magn. Mater.* **15-18**, 1081 (1980)

[210] B. Sepiol and G. Vogl, *Phys. Rev. Lett.* **71**, 731 (1993)

[211] Z. Frait and H. MacFaden, *Phys. Rev.* **139**, 0A1173 (1965)

[212] P. Krivosik, N. Mo, S. Kalarickal and C. E. Patton, *J. Appl. Phys.* **101**, 083901 (2007)

[213] Kh. Zakeri, Th. Kebe, J. Lindner and M. Farle, *J. Magn. Magn. Mater.* **316**, e334 (2007)

[214] Kh. Zakeri, Th. Kebe, J. Lindner and M. Farle, *Phys. Rev. B* **73**, 052405 (2006)

[215] G. Arfken, *Mathematical Methods for Physicists*, Academic Press (1985)

# List of publications

## I. Publications in refereed journals

**1) Kh. Zakeri**, J. Lindner, and M. Farle
*Thickness dependent reorientation of the magnetization of Fe monolayers on InP(001)*
submitted to Europhys. Lett. (2007), reference number: EPL G19696

**2) Kh. Zakeri**, S. J. Hashemifar, J. Lindner, I. Barsukov, R. Meckenstock, P. Kratzer, Z. Frait and M. Farle
*Spin and orbital magnetism in orderd* $Fe_{3\pm\delta}Si_{1\mp\delta}$ *thin binary Heusler structures*
submitted to Phys. Rev. B (2007), reference number: LK11280BJ.

**3) Kh. Zakeri**, I. Barsukov, J. Lindner, R. Meckenstock, M. Farle, U. von Hörsten, H. Wende, W. Keune, J. Rocker, S. S. Kalarickal, K. Lenz, W. Kuch, K. Baberschke and Z. Frait
*Spin damping mechanisms in metallic ferromagnets*
in preparation (2007).

**4) Kh. Zakeri**, J. Lindner, I. Barsukov, R. Meckenstock, M. Farle, U. von Hörsten, H. Wende, W. Keune, J. Rocker, S. S. Kalarickal, K. Lenz, W. Kuch, K. Baberschke and Z. Frait
*Spin dynamics in ferromagnets:Gilbert damping and two-magnon scattering*
Phys. Rev. B, **76**, 104416 (2007).

**5) Kh. Zakeri**, I. Barsukov, F. M. Römer, J. Lindner, R. Meckenstock, M. Farle, N. K. Utochkina, U. von Hörsten, H. Wende, W. Keune, S. S. Kalarickal, K. Lenz, and Z. Frait
*Magnetic properties of epitaxial* $Fe_3Si$*/MgO(001) thin films*
Phys. Rev. B, **76** (2007) in press, reference number: BE10895.

**6) Kh. Zakeri**, C. Urban, Th. Kebe, J. Lindner, U. Köhler and M. Farle
*Temperature-driven change of morphology and magnetic anisotropy of Fe monolayers on GaAs(001)*
Appl. Phys. A. (2007) in press, DOI: 10.1007/s00339-007-4310-4.

**7) Kh. Zakeri**, Th. Kebe, J. Lindner, and M. Farle
*Temperature dependent correlation of magnetic anisotropy and magnetization in Fe monolayers on {4×6}GaAs(001)*
J. Magn. Magn. Mater. **316**, 334e (2007).

**8) Kh. Zakeri**, Th. Kebe, J. Lindner, and M. Farle
*Correlation between structure and magnetism in epitaxial Fe monolayers on GaAs(001)*
Superlattices and Microstructures **41**, 116 (2007).

**9) Kh. Zakeri**, Th. Kebe, J. Lindner, C. Antoniak, M. Farle, K. Lenz, T. Toliński and K. Baberschke
*Magnetic anisotropy in nanoscaled materials probed by ferromagnetic resonance*
Phase Transitions **793**, 793 (2006).

**10) Kh. Zakeri**, Th. Kebe, J. Lindner and M. Farle
*Power-law behavior of the temperature dependence of magnetic anisotropy of uncapped ultrathin Fe films on GaAs(001)*
Phys. Rev. B **73**, 052405 (2006).

**11)** Th. Kebe, **Kh. Zakeri**, J. Lindner, M. Spasova and M. Farle
*Magnetization and magnetic mnisotropy mnergy of Fe monolayers on GaAs(001) exposed to oxygen*
J. Phys.: Condens. Matter, (2006) **18**, 8791 (2006).

**12) Kh. Zakeri**, Th. Kebe, J. Lindner and M. Farle
*Magnetic anisotropy of Fe/GaAs(001) ultrathin films investigated by in situ ferromagnetic resonance*
J. Magn. Magn. Mater. **299**, L1 (2006).

The following publication are not included in this thesis:

**13) Kh. Zakeri** and R. Alizad
*Current density in the intermediate state of superconductors*
Supercond. Sci. Technol., **17**, 1189 (2004).

**14) Kh. Zakeri** and A. Dashti

*Monte Carlo simulation of temperature programmed desorption* $CO_2$*/Cu(100) and CO/Cu(110) systems*

Surf. Rev. Lett., **11**, 137 (2004).

**15)** A. Z. Moshfegh and **Kh. Zakeri**

*The kinetic study of* $H_2S$ *formation and desorption on S/Pt(111) surface by computer simulation*

Surf. Rev. Lett. **10**, 745 (2003).

**16) Kh. Zakeri** and A. Z. Moshfegh

*A desorption study of* $H_2S$*/Pt (111) system by TPD simulation*

Proceeding book of National Conference on Condensed Matter Physics (2003) pp 99-103.

**17) Kh. Zakeri** and A. Z. Moshfegh

*Abstraction sulfur with atomic hydrogen from Pt(111) surface by computer simulation*

Proceeding book of National Surface Science and Engineering Conference (2003) pp 512-522.

## II. Contributions to conferences

### II. (a) Talks

**1) Kh. Zakeri**, Th. Kebe, J. Lindner and M. Farle

*Temperature and thickness dependence of the magnetic parameters of uncapped Fe monolayers on {4×6}GaAs(001)*

magnetism section European Physical Society, May 2006 Dresden-Germany

**2) Kh. Zakeri**, Th. Kebe, J. Lindner and M. Farle

*Magnetic surface anisotropy of Fe monolayers on GaAs(001)*

Magnetism section German Physical Society, May 2005 Berlin-Germany

**3) Kh. Zakeri** and A. Z. Moshfegh

*A desorption study of* $H_2S$*/Pt(111) system by TPD simulation*

Sixth National Conference on Condensed Matter Physics, February 2003 Yazd-Iran

**4) Kh. Zakeri** and A. Z. Moshfegh

*Abstraction sulfur with atomic hydrogen from Pt(111) surface by computer simulation*

Fifth National Surface Science & Engineering Conference May 2003 Tehran-Iran

**II. (b) Posters**

**1) Kh. Zakeri**, Th. Kebe, J. Lindner and M. Farle
*Magnetic anisotropy and magnetization of epitaxial Fe monolayers grown on InP(001) and InAs(001)*
381. WE-Heraeus-Seminar Spin-Polarized Currents in Magnetic Nanostructures 03 - 05 January 2007 Bad Honnef-Germany

**2) Kh. Zakeri**, Th. Kebe, J. Lindner and M. Farle
*Temperature dependent correlation of magnetic anisotropy and magnetization in Fe monolayers on {4×6}GaAs(001)*
Spintronics in Ultrasmooth Films, Summer School 9-14 July 2006 Durham-UK

**3) Kh. Zakeri**, Th. Kebe, J. Lindner and M. Farle
*Growth and magnetic characterization of Fe/InP(001) hybrid structures*
Spintronics in Ultrasmooth Films, Summer School, 9-14 July 2006 Durham-UK

**4) Kh. Zakeri**, Th. Kebe, J. Lindner and M. Farle
*Temperature dependent correlation of magnetic anisotropy and magnetization in Fe monolayers on {4×6}GaAs(001)*
III Joint European Magnetic Symposia, 26-30 June 2006 San Sebastian-Spain

**5) Kh. Zakeri**, Th. Kebe, J. Lindner and M. Farle
*Correlation between structure and magnetism in epitaxial Fe monolayers on GaAs(001)*
International symposium, Physics in low dimensions, Structure meet magnetism, 5-7 April 2006 Bochum-Germany

**6)** Th. Kebe, **Kh. Zakeri**, J. Lindner and M. Farle
*Magnetization and magnetic anisotropy energy of Fe monolayers on GaAs(001) exposed to oxygen*
International symposium, Physics in low dimensions, Structure meet magnetism, 5-7 April 2006 Bochum-Germany

**7) Kh. Zakeri**, Th. Kebe, J. Lindner and M. Farle
*Magnetic anisotropy and magnetization of Fe monolayers on 4×6 GaAs(001)*
364. Heraeus-Seminar, Nanoscale Magnets - Top-down meets Bottom-up, 5-7 January 2006 Bad Honnef-Germany

**8) Kh. Zakeri**, Th. Kebe, J. Lindner and M. Farle
*Magnetic anisotropy and magnetization of Fe monolayers on 4×6 GaAs(001)* International workshop in Magnetic imaging, 5-6 December 2005 Bochum-Germany

**9) Kh. Zakeri**, J. Lindner and M. Farle
*Interface magnetic properties of Fe/GaAs(001)Films*
Nanomagnetism: New Insights with Synchrotron Radiation (3Kg2005), 5-7 January 2005 Bad Honnef-Germany

# Curriculum vitae

**I. Personal data**

Name: Khalil Zakeri Lori
Nationality: Iranian
Date & Place of Birth: 23.09.1979, Sirjan, Iran
Address: Universität Duisburg-Essen
Fachbereich Physik, Experimentalphysik
AG Farle and Center for Nanointegration (CeNIDE)
Lotharstr. 1, 47048 Duisburg.
Tel.: +49-203-379 4412, Fax.: +49-203-379 2098,
E-mail: zakeri@agfarle.uni-duisburg.de

**II. Educational Background**

| | |
|---|---|
| Dec. 2003-present | Ph. D candidate, Department of Physics<br>University of Duisburg-Essen, Duisburg, Germany |
| Feb. 2003 - Dec. 2003 | Ph. D courses, Department of Physics<br>Sharif University of Technology, Tehran, Iran |
| Feb. 2003 | Master of Science in Physics |
| Sept. 2001 - Feb. 2003 | Master student, Department of Physics<br>Sharif University of Technology, Tehran, Iran<br>Thesis title: *"An investigation of thermal desorption of* $H_2S/Pt(111)$ *system by temperature programmed desorption technique"* |
| Jun. 2001 | Bachelor of Science in Physics |
| Sept. 1997 - Jun. 2001 | Bachelor student, Department of Physics<br>Shahid Bahonar University of Kerman, Kerman, Iran<br>B.Sc. Project: *"Construction and study of an Optical Fiber Interferometer System"* |
| Jun. 1997 | High School Diploma |

**III. Honors**

| | |
|---|---|
| 2001 | Ranked 42nd in M. Sc. Qualification Exam (10,000 participants) |

| | |
|---|---|
| 2000 | Acknowledgment letter of excellence<br>issued by the canceller Shahid Bahonar University of Kerman |
| 1999 | Acknowledgment letter of excellence<br>issued by the canceller Shahid Bahonar University of Kerman |
| 1998 | Acknowledgment letter of excellence<br>issued by the canceller Shahid Bahonar University of Kerman |

# Acknowledgments

This thesis was financially supported by the Deutsche Forschungsgemeinschaft, *Sfb 491 TPA9*. At this point, I would like to thank all the persons who contributed in various ways in the realization of this thesis.

First of all, I thank my supervisor *Prof. Dr. M. Farle*, who gave me the opportunity to do my Ph. D. in his group and supervised this work with great enthusiasm throughout the last three years. It is a honor for me to express all my gratitude to him. He is not only a good supervisor but also a very good friend in difficulties. His mentality to help and support the young researchers, all over the world, is really outstanding.

Moreover, my thanks go to:

*Dr. J. Lindner*, who was all the time ready to discuss the experimental results. His helpful guidance and insightful comments really helped me interpret the results.

*Dr. Th. Kebe*, for his friendly help during experiments within the MBE chamber and profitable discussions about magnetism in general. We have spend a grate time together in our laboratory.

*C. Tomaz* and *F. M. Römer* for their constant assistance during experiments.

*Prof. U. Köhler* and *C. Urban* for the STM experiments.

*I. Barsukov* for high-frequency FMR measurements.

*Dr. R. Meckenstock* for beneficial discussions and frequency dependent FMR measurements.

*D. Schädel* for the construction of all the small and big tools and devices. Without him the UHV-equipment would not have been complete in time.

*H. Zähres* for valuable suggestions and discussions about the technical problems.

Team assistants: *S. Grubba, G. Cioleck, H. Mund* and *T. Friedrich* for their friendly help with ordering the materials and UHV components.

*Prof. K. Baberschke*, for beneficial discussions about the magnetic relaxation mechanisms in ultrathin magnetic structures.

*Dr. K. Lenz, S. S. Kalarichkal* and *J. Rocker* for L- and Q-band FMR-measurements, helpful discussions. I would like to express my deep appreciations to *Dr. K. Lenz* for his dedicated work on proofreading the manuscript.

*Prof. P. Kratzer and Dr. S. J. Hashemifar* for performing the DFT calculations and beneficial discussions.

*Prof. W. Keune, U. von Hörsten* and *U. K. Utochkina* for perpetration of $Fe_3Si$ samples and

useful discussions.
*Prof. H. Wende* for beneficial discussions.
*Prof. M. Acet* for his help during the SQUID and XRD measurements and his profitable discussions about the results.
*Prof. Z. Frait* for high-frequency FMR measurements.
*Dr. A. Ney* for beneficial discussions.
*J. Cortez* for proofreading of the manuscript.
*Dr. R. Ramchal*, *Dr. U. Wildwald*, *Dr. C. Raeder* and *C. Antoniak* for their friendly guidance to operate some of experimental equipment in the beginning of my Ph. D.
*B. Stahlmecke*, *Dr. E. Duman* and *Dr. T. Kerenke* for the friendly atmosphere and helpful guidance.

And last but not least I am very grateful to the kindest people of my life, my dear parents *S. and M. Zakeri Lori*, the ones who resisted the difficulties of life to make me not fear, resisted to make me get comforted, resisted to make me learn and resisted to make me resist. Their countless sacrifices and unconditional love have always been a source of motivation and encouragement for me. My brothers and sisters *Z., N., J., F., and A.R. Zakeri Lori* who are a source of hope and encouragement in my life.